

Spin transport in topological insulator-based nanostructures

THÈSE N° 7585 (2017)

PRÉSENTÉE LE 11 AVRIL 2017

À LA FACULTÉ DES SCIENCES DE BASE
LABORATOIRE DE SCIENCE À L'ÉCHELLE NANOMÉTRIQUE
PROGRAMME DOCTORAL EN PHYSIQUE

ÉCOLE POLYTECHNIQUE FÉDÉRALE DE LAUSANNE

POUR L'OBTENTION DU GRADE DE DOCTEUR ÈS SCIENCES

PAR

Kristina VAKLINOVA

acceptée sur proposition du jury:

Prof. V. Savona, président du jury
Prof. K. Kern, Dr M. Burghard, directeurs de thèse
Dr F. Calleja, rapporteur
Prof. L. Hueso, rapporteur
Prof. L. Forró, rapporteur



ÉCOLE POLYTECHNIQUE
FÉDÉRALE DE LAUSANNE

Suisse
2017

“Character cannot be developed in ease and quiet.
Only through experience of trial and suffering
can the soul be strengthened, ambition inspired,
and success achieved.”
— Helen Keller

Abstract

With the advent of spintronics, significant research effort is made to realize efficient injection, transport, manipulation, and detection of spin. The material platforms and device architectures suitable for this purpose have steadily evolved towards novel materials whose properties are governed by spin-orbit (SO) coupling. Three-dimensional topological insulators (3D TIs) are a class of Dirac materials, which possess two-dimensional (2D) spin-polarized helical surface states due to their strong SO coupling. This property makes them an exciting material platform that offers research possibilities in several directions, specifically (i) to gain a deeper understanding of the electronic properties of massless Dirac fermions hosted by the surface states; (ii) to exploit the spin-momentum locking of the surface states towards efficient spin-charge conversion; and (iii) to investigate the interplay of the surface states with magnetic materials, superconductors, and 2D materials that could lead to the discovery of new surface and interface phenomena with exciting technological prospects.

The main challenge in the field of 3D TIs is posed by the difficulty to selectively access the surface states in electrical transport experiments. This issue arises from the intrinsic doping of the bulk, which leads to a sizable contribution of the bulk states to the conductivity. Furthermore, while they are prospective as efficient spin current generators, the efficiency of the electrical detection of spin currents is limited due to pronounced spin relaxation and dephasing. This motivates the realization of 3D TIs with improved properties in order to address the bulk conductance issue and to engineer 3D TI-2D material heterostructures, whose interfaces would enable efficient spin-charge manipulation.

The present thesis aims at the characterization of various Dirac materials by magnetotransport experiments at low temperatures, as well as the nanofabrication and investigation of spintronic devices based on 3D TIs. In the first experimental part, the electronic properties of four different 3D TIs are investigated – antimony telluride (Sb_2Te_3) and bismuth telluride selenide ($\text{Bi}_2\text{Te}_2\text{Se}$), which are grown in a vapor-solid process, zirconium pentatelluride (ZrTe_5), grown as single crystals in a Czochralski process, and finally the naturally occurring mineral Aleksite ($\text{PbBi}_2\text{Te}_2\text{S}_2$).

In the second part, $\text{Bi}_2\text{Te}_2\text{Se}$ is chosen for the fabrication of lateral spin valve devices, in which electrical detection of charge current-induced spin polarization due to the spin-momentum locking of the 2D TI surface states is demonstrated. Spin transport measurements are performed for devices with different coupling strength between the ferromagnetic current detector and the TI transport channel. Subsequently, the spin transport is investigated for the first time in the presence of a hBN tunnel barrier. An inversion of the spin signal is observed,

which depends on the resistance of the hBN/FM/TI interface.

The third experimental part addresses the spin generation properties of Bi₂Te₂Se in a van der Waals TI/graphene heterostructure, in which the TI acts as a spin injector, while the injected spin propagates within the graphene channel underneath and is detected non-locally by a ferromagnetic electrode on top of the graphene. This is a first-time demonstration of spin injection and detection in a heterostructure, which combines the best properties of two Dirac materials, determined by the presence of SO coupling in the TI and the lack thereof in graphene. These results are examples of emergent phenomena on 2D surfaces and interfaces, which could be further investigated in vertical and lateral heterostructures utilizing the spin Hall, Rashba, or Edelstein effect for efficient spin-charge conversion towards all-spin-based information technology.

Key words: topological insulators, graphene, vapor-solid growth, heterostructures, magneto-transport, spintronics

Zusammenfassung

Mit dem Aufkommen der Spintronik begannen auch intensive wissenschaftliche Bestrebungen zur Realisierung und Effizienzsteigerung von Spin-Injektion, -Transport, -Manipulation und Detektion. Die unterschiedlichen Materialien und experimentellen Methoden, die sich für diesen Zweck eignen, wurden stetig weiterentwickelt; hauptsächlich in Richtung neuartiger Materialien, deren Eigenschaften von starker Spin-Bahn-Kopplung bestimmt werden. Dreidimensionale topologische Isolatoren (3D TI) sind Dirac Materialien, die zweidimensionale spinpolarisierte helikale Oberflächenzustände aufweisen, die von der starken Spin-Bahn-Kopplung herrühren. Aufgrund dieser Eigenschaft bieten 3D TI faszinierende Möglichkeiten in der experimentellen Forschung, im Besonderen (i) ein tieferes Verständnis der elektronischen Eigenschaften von masselosen Dirac-Fermionen, die mit den Oberflächenzuständen assoziiert sind, zu erlangen, (ii) die Spin-Impuls-Kopplung der Oberflächenzustände zu nutzen, um effizient Signale von Spin und elektrischer Ladung ineinander umzuwandeln und (iii) das Zusammenspiel von Oberflächenzuständen und magnetischen, supraleitenden und zweidimensionalen Materialien zu untersuchen. Dieses Forschungsfeld könnte zu der Entdeckung neuer Ober- und Grenzflächenphänomene führen die neuartige technologischen Anwendungsperspektiven bieten.

Eine wesentliche Herausforderung bei der experimentellen Erforschung von 3D TI besteht in der Schwierigkeit, in Transportexperimenten selektiv die Oberflächenzustände nachzuweisen. Ursache ist die intrinsische Dotierung der Bulk-Zustände, die einen beträchtlichen Beitrag zur Leitfähigkeit leisten. Darüber hinaus ist – obwohl 3D TI als effiziente Spin-Generatoren dienen könnten – die Effizienz der elektrischen Detektion von Spin-Strömen aufgrund ausgeprägter Spin-Relaxation und Phasenverlust limitiert. Dies führt zu der Bestrebung, 3D TI mit verbesserten Eigenschaften zu entwickeln, um das Problem der Bulk-Leitfähigkeit zu beheben. Zusätzlich sind Heterostrukturen aus 3D TI-2D Materialien von Interesse, deren Grenzflächen eine effizientere Spin-Ladung-Umwandlung ermöglichen könnten.

Die vorliegende Dissertation beschäftigt sich mit der Charakterisierung verschiedener Dirac-Materialien in Tieftemperatur-Magnetotransport-Experimenten sowie mit der Nanofabrikation und Untersuchung von Spintronik-Bauelementen, die auf 3D TI basieren.

Im ersten Teil werden die elektronischen Eigenschaften von vier unterschiedlichen 3D TI untersucht: Antimontellurid (Sb_2Te_3) und Bismuttelluridselenid ($\text{Bi}_2\text{Te}_2\text{Se}$), die in einem chemischen Gasphasenabscheidungsprozess hergestellt werden; Zirkonumpentatellurid (ZrTe_5), das als Einkristall im Czochralski-Verfahren hergestellt wird und schließlich das natürliche Mineral Aleksit ($\text{PbBi}_2\text{Te}_2\text{S}_2$).

Im zweiten Teil werden $\text{Bi}_2\text{Te}_2\text{Se}$ -basierte laterale Spin-Valves hergestellt, in den Strom-induzierte Spin-Polarisation, die von der Spin-Impuls-Kopplung der TI-Oberflächenzustände hervorgerufen wird, elektrisch detektiert wird. Die Spin-Transport-Messungen werden mit Bauelementen unterschiedlicher Kopplungsstärke zwischen der ferromagnetischen Detektor-Elektrode und dem TI-Kanal durchgeführt. Daraufhin wird erstmalig der Spin-Transport in Anwesenheit einer hBN-Tunnelbarriere untersucht. Es wird eine Inversion der Spin-Signale nachgewiesen, die vom Widerstand der hBN/FM/TI-Grenzfläche abhängig ist.

Der dritte Teil dieser Arbeit beschäftigt sich mit der Spin-Generation mittels $\text{Bi}_2\text{Te}_2\text{Se}$ in van-der-Waals TI/Graphen-basierten Heterostrukturen, in denen der TI die Rolle des Spin-Injektors übernimmt, während der injizierte Spin entlang des Graphen-Kanals transportiert und anschließend von einer FM-Elektrode auf dem Graphen nicht-lokal detektiert wird. Dies ist die erste Demonstration von Spin-Injektion und Detektion in einer Heterostruktur, die die besten Eigenschaften zweier Dirac-Materialien vereint, nämlich die Spin-Generation im TI und die Spin-Konservierung in Graphen. Diese Ergebnisse sind Beispiele neuartiger Phänomene an 2D-Oberflächen und Grenzflächen. Diese sollten in Zukunft in vertikalen und lateralen Heterostrukturen näher untersucht werden, um eine effiziente Spin-Ladung-Umwandlung mittels des Spin-Hall-, Rashba- und Edelstein-Effekts zu erzielen, und somit neue Anwendungen in der Spin-basierten Informationstechnologie zu eröffnen.

Stichwörter: Topologische Isolatoren, Graphen, chemische Gasphasenabscheidung, Heterostrukturen, Magnetotransport, Spintronik

Contents

Abstract (English/Deutsch)	i
List of figures	ix
1 Introduction	1
2 Theory of electronic and spin transport in topological insulators	7
2.1 Theoretical background of topological insulators	7
2.1.1 From the insulating state to a new quantum state of matter	7
2.1.2 Band gap states and topological protection	11
2.1.3 3D topological insulators	13
2.1.4 Engineering topological insulator materials	15
2.2 Electronic transport	18
2.2.1 Characteristic lengths	18
2.2.2 Diffusive quantum transport	19
2.3 Spin transport	22
2.3.1 All-electric spintronics	23
2.3.2 Spin current injection, accumulation, and detection	24
2.3.3 Spin relaxation and dephasing mechanisms	28
2.3.4 Spin-charge conversion	32
2.3.5 Graphene in spintronics	39
2.3.6 Topological insulators in spintronics	40
3 Experimental techniques	43
3.1 Chemical vapor deposition	43
3.2 Atomic force microscopy	45
3.3 Electron beam lithography and scanning electron microscopy	46
3.4 Raman spectroscopy	48

Contents

3.5	Cryogenic transport measurements	49
3.6	Electrical measurement geometries	50
3.7	TI device fabrication	53
4	Electronic transport in single-component TI devices	57
4.1	Chemically synthesized ZrTe ₅	58
4.1.1	Synthesis, initial characterization and device fabrication	58
4.1.2	Magnetotransport properties	60
4.2	Aleksite as natural topological insulator	64
4.2.1	Initial characterization and device fabrication	64
4.2.2	Magnetotransport properties	65
4.3	CVD-grown Sb ₂ Te ₃	70
4.3.1	Van der Waals epitaxial growth	70
4.3.2	Device fabrication	72
4.3.3	Magnetotransport properties	72
4.4	CVD-grown Bi ₂ Te ₂ Se	74
4.4.1	Van der Waals epitaxial growth and initial characterization	74
4.4.2	Magnetotransport studies	77
5	Spin transport in lateral spin valves based on Bi₂Te₂Se	81
5.1	Spin valves with Bi ₂ Te ₂ Se wires and transparent contacts	81
5.1.1	Device fabrication and initial characterization	82
5.1.2	Spin transport behavior	82
5.2	Spin valves with Bi ₂ Te ₂ Se platelets and tunneling contacts	86
5.2.1	Device fabrication and initial characterization	87
5.2.2	Spin filter effect of hBN/Co detector electrodes	88
6	Spin-polarized currents in van der Waals graphene/Bi₂Te₂Se heterostructures	95
6.1	Concept and device fabrication	95
6.2	Current-induced spin polarization	99
6.3	Hanle spin precession measurements	104
7	Summary and Outlook	109
7.1	Spin-charge conversion properties of TI/2D material interfaces	110
7.2	Spin detection in TI/graphene heterostructures with NM electrodes	111
7.3	Proximity-induced SO coupling in TI/graphene heterostructures	112

7.4 The TI/graphene heterostructure for optospintronic experiments	116
A Recipes	117
A.1 CVD graphene/CVD hBN wet etching and transfer process	117
A.2 Flipping of epitaxial Bi ₂ Te ₂ Se/graphene stacks	118
Bibliography	141
Acknowledgements	141

List of Figures

1.1	Charge and spin currents in a spintronic device.	2
1.2	2D surface states in spintronics.	3
2.1	Schematic band dispersion within the Brillouin zone based on the band theory of solids.	8
2.2	The Quantum Hall effect and 1D edge states.	10
2.3	A topological perspective.	11
2.4	Protected states in the energy bandgap.	12
2.5	Helical edge states and the 3D TI.	13
2.6	The spin quantum Hall effect.	14
2.7	TI surface states observed in ARPES measurements.	16
2.8	Methods for the synthesis of TI materials.	17
2.9	Characteristic lengths.	19
2.10	Quantum corrections to the conductance in diffusive systems.	21
2.11	Universal conductance fluctuations.	22
2.12	FM-NM-FM CPP junction.	25
2.13	Lateral spin valve measurement geometries.	26
2.14	SO coupling and crystal asymmetries.	29
2.15	Spin relaxation mechanisms.	31
2.16	Hanle spin precession.	32
2.17	Spin-charge conversion principles.	34
2.18	Band structure of 2D surfaces and interfaces with SO coupling.	36
2.19	Edelstein effects.	38
2.20	TIs in spintronics.	41
3.1	Chemical vapor deposition.	44
3.2	Atomic force microscopy.	46

List of Figures

3.3	Electron beam lithography.	47
3.4	Raman spectroscopy	48
3.5	Low-temperature measurement insert.	49
3.6	Electrical measurement geometries	51
3.7	Hall bar and van der Pauw transport measurement geometries.	52
3.8	In situ contact preparation.	55
4.1	Initial characterization of ZrTe ₅ single crystals.	59
4.2	Temperature and angle dependent magnetotransport in ZrTe ₅ for negative gate voltage.	61
4.3	Temperature and angle dependent magnetotransport in ZrTe ₅ for positive gate voltage.	63
4.4	Initial characterization of Aleksite thin crystals.	65
4.5	1D magnetotransport in a narrow Aleksite ribbon.	67
4.6	2D magnetotransport in a wider Aleksite ribbon.	69
4.7	Crystal, band structure, and initial characterization of CVD-grown Sb ₂ Te ₃	70
4.8	CVD-grown Sb ₂ Te ₃ on different substrates.	71
4.9	Initial electrical measurements on Sb ₂ Te ₃ devices.	73
4.10	Transport measurements on thinner Sb ₂ Te ₃ platelets.	73
4.11	Crystal structure and Raman spectrum of Bi ₂ Te ₂ Se.	74
4.12	CVD-grown Bi ₂ Te ₂ Se in different morphologies on SiO ₂ and mica.	75
4.13	Growth of Bi ₂ Te ₂ Se on CVD-graphene and exfoliated graphene.	76
4.14	Initial electrical characterization of Bi ₂ Te ₂ Se.	77
4.15	Temperature and angle dependence of the magnetoconductance of Bi ₂ Te ₂ Se.	78
5.1	Ferromagnetic switching of a Cobalt channel.	83
5.2	Spin transport in Bi ₂ Te ₂ Se wires with all-FM coupled contacts.	84
5.3	Spin transport in Bi ₂ Te ₂ Se wires with NM-FM coupled contacts.	85
5.4	Fabrication of Bi ₂ Te ₂ Se lateral spin valve devices with hBN tunnel barriers.	87
5.5	Spin transport in a Bi ₂ Te ₂ Se spin valve with low resistance hBN/Co tunnel contacts.	89
5.6	Spin transport in Bi ₂ Te ₂ Se spin valve with high resistance hBN/Co tunnel contacts.	90
5.7	Temperature and angle dependence of the spin signal.	92
6.1	Experimental concept and device structure.	96
6.2	The Bi ₂ Te ₂ Se/graphene heterostructure.	98
6.3	Spin injection into graphene by Co contacts.	100

6.4	Electrical detection of spin currents in graphene injected from $\text{Bi}_2\text{Te}_2\text{Se}$ as spin polarizer.	103
6.5	Spin signal dependencies.	104
6.6	Hanle spin precession.	106
7.1	Lateral spin valve geometry patterned onto a $\text{Bi}_2\text{Te}_2\text{Se}$ /graphene heterostructure.	112
7.2	Towards enhanced SO coupling in graphene.	113
7.3	First electronic transport measurements of $\text{Bi}_2\text{Te}_2\text{Se}$ /graphene Hall bar structures.	114
A.1	Flipping of a TI/graphene heterostructure via PDMS stamping.	118

1 Introduction

Technological advance is essential to modern society and the inevitable challenges it poses to the scientific community stimulate a plethora of research directions in fundamental and applied physics. Interdisciplinary research combining physics, materials science, and chemistry plays a major role towards achieving higher performance information storage devices and overcoming the limitations of downscaling. As proposed by Moore in 1965 [1], the exponential increase of the number of transistor on integrated circuits is accompanied by improved computing efficiency and higher memory density leading to increased storage capacity for minimized production and storage costs. Data processing is built upon the concept of binary bits, which encode information. Thus, computational power depends on the number of transistors having an "on" and "off" state, i.e., representing the bits "1" or "0". While the first Intel processor fabricated in 1971 contained 2300 transistors, in modern processors this number exceeds staggering 7 billion transistors. Downscaling of electronic devices, which has contributed to tremendous technological progress, has reached the limits of classical physics. Thus, as devices become smaller, the realm of quantum physics becomes increasingly important in the playground of innovation.

Gate leakage, high current densities, and heat dissipation lead to decreased device performance and energy loss. In order to address these issues, fundamental physics research aims to utilize an additional degree of freedom provided by the electron's spin and utilize the quantum effects associated with it, which has given rise to the vast field of spintronics. A holy grail of spintronics is the realization of a quantum computer, in which the classical binary bits are replaced by the two possible states of the spin – "up" and "down" – and importantly, as governed by the laws of quantum mechanics, a linear superposition of the two. The resulting "qubits" would unfold unprecedented computational power on the order of trillions of floating

point operations per second due to their inherent ability to perform computational tasks in parallel, while a conventional computer does one at a time.

The long way towards the implementation of quantum computation was initiated by the attempt to understand and control the electron's spin in solid state devices. The idea of spin transport refers not only to spin-polarized charge current, but also to pure spin current, which can be generated in a material and can propagate independently from charge. On this basis, modern spintronics research aims at: (i) engineering of materials with improved properties, which can generate and host spin currents by providing high spin polarization and long spin coherence times; (ii) achieving efficient charge-spin conversion via utilizing quantum phenomena such as spin transfer torques, or the spin Hall and Edelstein effect; (iii) developing and optimizing all-electric techniques to create and manipulate spin accumulation. Achieving progress in these directions can revolutionize current technologies towards all-spin-based information processing (**Fig. 1.1**).

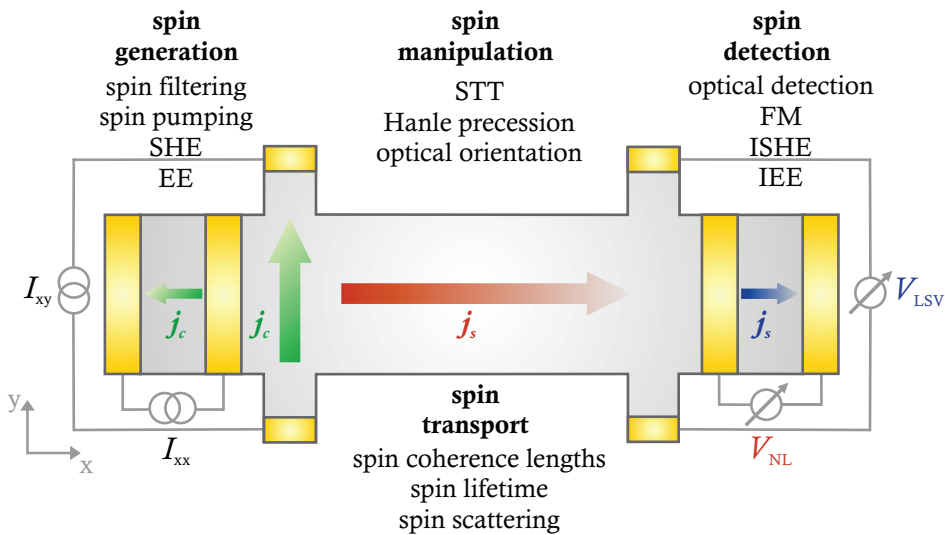


Figure 1.1 – Charge and spin currents in a spintronic device. Schematic representation of a spintronic device with the four fundamental concepts of spintronics, namely spin generation (spin filtering, spin pumping, spin Hall effect (SHE), Edelstein effect (EE), manipulation (spin transfer torque (STT), Hanle precession, optical orientation), transport (spin coherence lengths, spin lifetime, spin scattering), and detection (optical detection, ferromagnetism (FM), inverse spin Hall effect (ISHE), inverse Edelstein effect (IEE). Additionally, two measurement configurations are illustrated, namely the lateral spin valve and non-local H-bar together with several available techniques and material parameters for achieving efficient spin control.

Historically, the dawn of classical spintronics research was marked by the experimental realization of metallic heterostructures, composed of ferromagnetic/non-magnetic and ferromagnetic/insulating layers, in which the control over the direction of magnetization of the

ferromagnet gives rise to spin-dependent transport based on the giant magnetoresistance (GMR) [2] [3], or the tunnel magnetoresistance (TMR) [4] effect, respectively. The latter constitutes the operation principle of the magnetoresistive random access memory (MRAM), which consists of magnetic tunnel junctions (MTJ) arrays, wherein each MTJ serves as a bit whose resistance state encodes a "0" or a "1". Subsequently, Johnson and Silsbee [5] demonstrated the first metallic spin valve device, in which spin-polarized current is injected from a ferromagnetic (FM) into a non-magnetic (NM) material, where it persists up to a material-dependent diffusion length. A diffusion theory of spin-dependent conduction has been proposed by Fert and Valet [6] in order to elucidate the spin transport in FM–NM metallic devices.

Recently, further progress has been achieved in non-volatile memory storage by exploiting an effect called spin-transfer torque [7] [8] [9], which involves the reorientation of the magnetization direction of a thin ferromagnetic layer by angular momentum transfer from a flowing spin-polarized current. In a GMR metallic structure, the magnetic state of a FM layer can be switched by this torque back and forth, depending on the polarity of the applied current. The magnetic state and thus the resistance of the junction can be manipulated by an entirely electrical means with GHz fast magnetization dynamics, which renders an efficient memory unit.

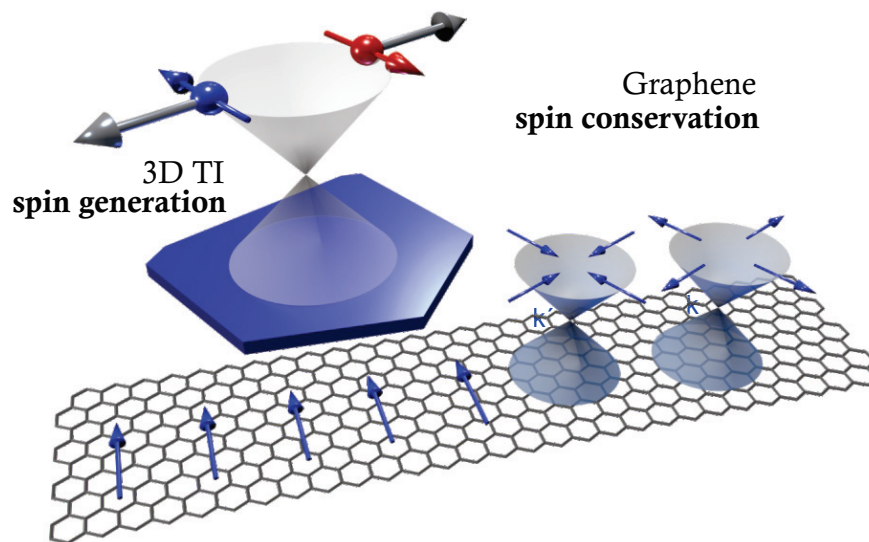


Figure 1.2 – 2D surface states in spintronics. 3D topological insulators and graphene host 2D surface states, which possess spin generation and spin conservation properties, respectively, and can be used in spintronic devices.

Beyond the realization of all-metallic spintronic devices, more efficient spin injection and much higher spin diffusion lengths have been attained with semiconductors (SC), whose

carrier concentration can be tuned via electrostatic gating or doping, and which are furthermore compatible with state-of-the-art complementary metal-oxide-semiconductor (CMOS) technology. Electrical injection of spin-polarized current into GaAs [10] and Si [11] [12] has been demonstrated, where the spin injection efficiency depends sensitively on the properties of the FM-SC interface. Large spin accumulation, as probed by Hanle precession measurements, has been observed at room temperature and a spin life time dependence on the charge carrier density established. The combined capability to inject, manipulate and detect spin polarization in semiconductors is a promising milestone towards utilizing spin for practical applications.

A major research attempt to find novel materials, which hold the potential to complement or even replace semiconductor technology, has been directed towards two-dimensional (2D) materials, motivated by the experimental discovery of graphene in 2004 by Geim and Novoselov [13]. Due to its extraordinary electronic and structural properties, graphene has been actively investigated as a rich experimental platform not only from a fundamental science point of view, but also with the realistic aim of industrial applications and commercialization. Following the rise of graphene, a plethora of 2D materials [14] [15] has emerged in the recent years, such as transition metal dichalcogenides (TMDs), phosphorene, hexagonal boron nitride (hBN), and complex oxides, whose electronic, magnetic, optical and mechanical properties make them promising candidates for applications in novel electronic and spintronic devices.

The 2016 Nobel prize in physics has been awarded to Haldane, Thouless and Kosterlitz for their pioneering theoretical work on topological phase transitions and topological phases of matter. Topology has first entered the world of solid state physics in the early 1970s in order to shed light onto phase transitions in 2D surfaces and more specifically onto the formation and behavior of spin vortices that can be described by topological order. About a decade later, the quantum Hall effect discovered by Klaus von Klitzing [16] was viewed within the framework of non-trivial topological states and the term "topological protection" has emerged to explain the precise quantization of the Hall resistance [17].

Systems characterized by a non-trivial topological invariant have been first theoretically predicted in 2005 [18] and then actively investigated, after Hsieh et al. [19] confirmed experimentally in photoemission spectroscopy experiments the existence of 2D surface states in three-dimensional (3D) topological insulators (TIs) in 2009. What distinguishes a TI from a trivial band insulator is the presence of electronic states connecting the bulk bands while crossing inside the bulk band gap. What makes these states topologically non-trivial and the

charge and spin transport in them "topologically" protected, is their helicity, i.e., they have a linear dispersion relation, called a Dirac cone, on which each momentum vector is associated with a spin locked perpendicularly to it in the surface plane. This spin-momentum locking results in spin-polarized helical states, in which backscattering not involving a spin-flip is prohibited. The emergence of the 2D surface states in 3D TIs is a direct consequence of band inversion caused by strong spin-orbit (SO) coupling in these heavy atom materials. On this basis, it is expected that a TI can act as an efficient spin generator, in contrast to graphene, whose low SO coupling makes it an efficient spin transport material [20]. TI-based spin current generation can be achieved electrically due to the spin-momentum locking (**Fig. 1.2**).

The present thesis aims to explore the magnetotransport properties of different 3D TIs, in order to characterize the surface state contribution to the electronic transport. Furthermore, it aims at demonstrating the suitability of 3D TIs as spin generators in spintronics devices based on either a single TI material, or a heterostructure comprising a TI/graphene interface.

The thesis is organized as follows:

Chapter 2 provides a brief overview of 3D TIs and the fundamental physics underlying their electronic and spin properties, and highlights state-of-the-art experimental studies of related magnetotransport phenomena and applications in spintronics.

Chapter 3 outlines the experimental methods employed in this work and provides details on TI device fabrication, measurement techniques and geometries.

Chapter 4 presents the results of the magnetotransport experiments on four different Dirac materials, namely the natural 3D TI $\text{PbBi}_2\text{Te}_2\text{S}_2$, the Dirac semimetal ZrTe_5 , and the CVD-grown 3D TIs Sb_2Te_3 and $\text{Bi}_2\text{Te}_2\text{Se}$.

Chapter 5 describes the nanofabrication and the characterization of spintronic devices, based on the 3D TI compound $\text{Bi}_2\text{Te}_2\text{Se}$. Two types of lateral $\text{Bi}_2\text{Te}_2\text{Se}$ -based spin valve (LSV) devices are investigated, specifically with strongly coupled Cobalt contacts and with hexagonal boron nitride (hBN)/Cobalt tunneling contacts, respectively.

Chapter 6 deals with the fabrication and spin transport in a TI/graphene heterostructure, in which spin-polarized current generated in the TI is transferred via the epitaxial interface to the graphene channel, where it is detected using both a LSV and a Hanle configuration.

Chapter 7 concludes this thesis with a short summary of results and provides an outline of possible future experiments.

2 Theory of electronic and spin transport in topological insulators

2.1 Theoretical background of topological insulators

The significance of topology in the field of solid state physics was realized with the discovery of the quantum Hall effect in 1980 by Klaus v. Klitzing [16] and its subsequent interpretation within the scope of topological invariants by Thouless, Kohmoto, Nightingale, and den Nijs [17]. Almost 25 years later, Kane and Mele postulated a theory regarding a new kind of band insulator with non-trivial topology, while theoretically investigating a model graphene system in the presence of SO coupling [21]. This new topological phase was found to have novel electronic properties, which are protected due to symmetry considerations. The term "topological insulator" first emerged in 2007 [22] in order to describe a new quantum phase of matter, in which an insulating bulk coexists with conductive edge or surface states that are robust and protected by time reversal symmetry (TRS). The following is a brief introduction to the concept of topological materials and their electronic properties.

2.1.1 From the insulating state to a new quantum state of matter

Band theory of solids In order to understand and classify solids, one has to describe the properties of electrons interacting with a crystal lattice [23]. The free electron model is modified in order to account for the influence of the periodic crystal potential on the electron motion and describe the electronic properties of metals, semiconductors, and insulators. For electrons in a crystal lattice, the solutions of the Schrödinger equation are given by the periodic Bloch functions with the important consequence that electrons in solids are allowed to occupy certain energy bands, while not being allowed to possess energy in forbidden regions, called

band gaps. The nearly-free electron model yields the dispersion of energy bands in reciprocal k -space, such that the electronic structure of a given material can be described within the Brillouin zone, i.e., within one period of the reciprocal lattice in k -space, centered around $k = 0$. In the presence of an energy band gap, the conduction properties are determined by the occupation of the valence and the conduction bands and the position of the Fermi energy E_F . **Fig. 2.1a** illustrates E_F located inside the band gap, in which case either insulating or semiconducting behavior occurs, depending on the size of the gap. Metallic behavior occurs when E_F lies within a bulk band and separates the highest occupied and the lowest unoccupied energy state (**Fig. 2.1b**).

Apart from the obvious technological applications of insulating materials, their electronic properties are trivial. It turns out, however, that under special circumstances exciting physics can occur in the band gap due to the emergence of stable gap states with quite fascinating properties.

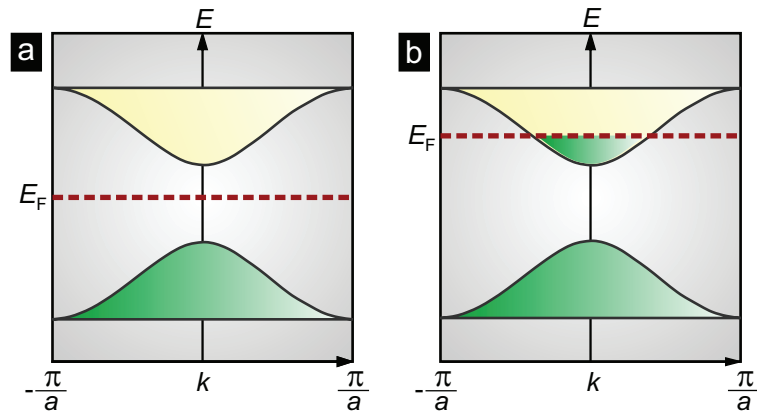


Figure 2.1 – Schematic band dispersion within the Brillouin zone based on the band theory of solids. a) Band structure of an insulator with the Fermi energy lying in the band gap and a completely filled valence band. **b)** Band structure with a filled valence band and a partially filled conduction band, i.e. E_F is located inside the conduction band, corresponding to metallic behavior.

The quantum Hall effect (QHE) A prominent example is the case of a 2D electron gas (2DEG) with an external magnetic field applied normal to the substrate plane, as schematically depicted in **Fig. 2.2a**. Naturally, the electrons start precessing around it with the cyclotron frequency, $\omega_c = \frac{eB}{m^*}$, which gives rise to discrete energy levels, called Landau levels, given by $E_n = \hbar \omega_c (n + \frac{1}{2})$. These levels are populated by electrons and can be filled or depleted as a function of the magnetic field's strength, such that similar to the insulating state, there are filled and empty states, separated by energy gaps (**Fig. 2.2c,d**). If the 2DEG is patterned into a

2.1. Theoretical background of topological insulators

Hall bar geometry and a current I_{xx} is applied, the resulting voltage drop is measured in both the longitudinal (V_{xx}) and transverse direction (V_{xy}). The associated Hall resistance R_{xy} , plotted as a function of magnetic field, exhibits staircase-like plateaus, which are quantized in steps of $\frac{h}{Ne^2}$, where N is an integer and $\frac{h}{e^2} = 25.8128 \text{ k}\Omega$ represents the resistance quantum. The plateaus in the Hall resistance correspond to regions of zero longitudinal resistance occurring when the Fermi energy is located in a density of states minimum between two Landau levels (**Fig. 2.2b**).

The QHE is an unprecedented example for a quantum state which exhibits no symmetry breaking and does not depend on the sample's properties, such as type of 2D material or its geometry. The quantization of the Hall resistance and the emergence of chiral edge states carrying dissipationless current, i.e., states which allow a single direction of charge carrier propagation, can be explained in terms of topology. In a thought experiment by Laughlin in 1981 [24], the QHE is interpreted within the scheme of a quantum pump. The 2DEG system assumes the form of a loop and the external magnetic field threads it perpendicularly, as schematically depicted in **Fig. 2.3a**. Charge transfer takes place between two electrodes connecting both edges of the loop when the magnetic flux penetrating the loop changes by a flux quantum (as a consequence of Faraday's principle). Each flux quantum increase defines one pump cycle, in which the transferred charge is equivalent to the quantized Hall conductance.

In order to explain why the charge transferred in one pump cycle is an integer multiple of the elementary charge, or alternatively why the Hall conductance is quantized in integer steps, one has to introduce the concept of topological invariants, also known as Chern numbers.

Berry phase and Chern numbers The charge transfer in Laughlin's pump is quantized due to gauge invariance, i.e., each consequent cycle maps the quantum state of the pump onto itself and an integer number of electrons are transferred. By contrast, mapping a quantum system onto itself is associated with gaining a phase, known as Berry phase [25]. This phase is related to the notion of parallel transport on a sphere, as schematically shown in **Fig. 2.3b**. The vector moving parallel to itself on a closed path points at a different direction when it arrives back at the starting point, i.e, there is always an angular mismatch due to curvature when a closed path is transversed. The link between curvature and topological numbers is provided by the Gauss-Bonnet formula: $\frac{1}{2\pi} \int_S K dA = 2(1 - g)$, where the left-hand side is the angular mismatch integrated over the whole surface, K is the curvature and dA represents the transversed closed path. This integral is related to the topology of the surface on the

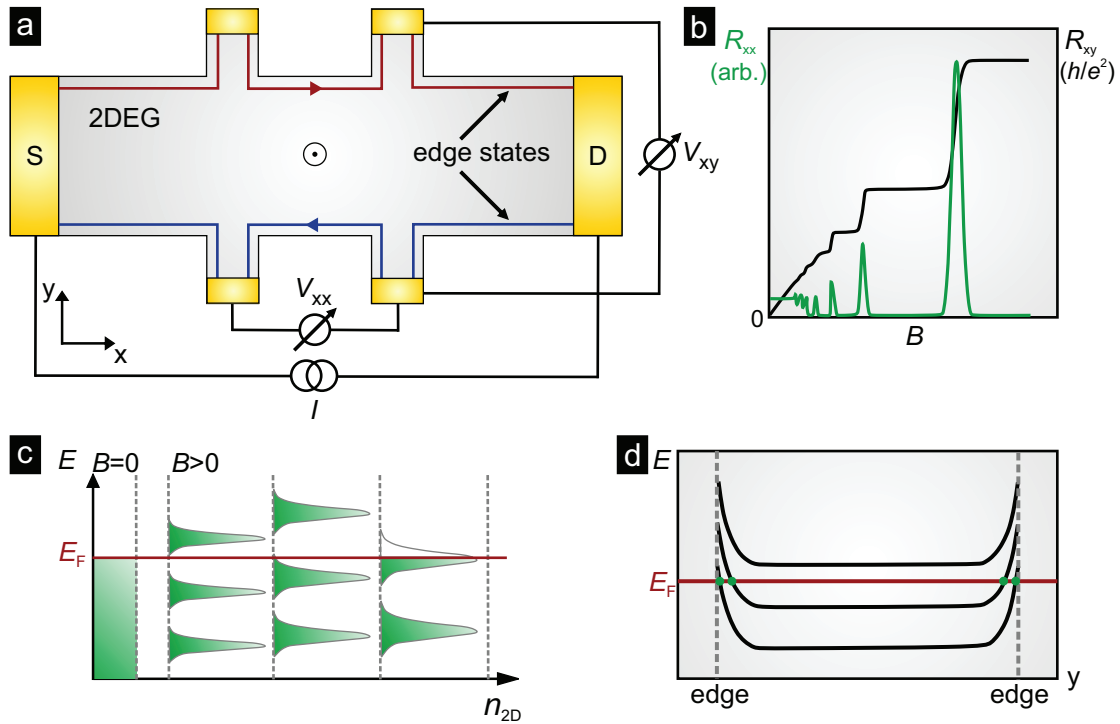


Figure 2.2 – The Quantum Hall effect and 1D edge states. **a)** 2DEG patterned in Hall bar geometry, where current is applied between the source and drain electrodes in the presence of externally applied magnetic field normal to the surface. **b)** The longitudinal (R_{xx}) and the transversal (R_{xy}) resistance measured as a function of magnetic field. The edge states give rise to the quantization of R_{xy} , while R_{xx} exhibits oscillating behavior. **c)** The electron motion in external magnetic field gives rise to discrete Landau levels in the density of states. The plateaus of R_{xy} correspond to a E_F located between two Landau levels. **d)** Bulk insulating behavior originates from the E_F being located between two Landau levels, while at the edges, it is pinned to a conductive channel giving rise to the Hall plateaus.

right-hand side of the equation, where the integer g corresponds to the number of holes the surface has (for instance, a sphere has zero holes, therefore $g = 0$; a torus has one hole, i.e., $g = 1$). From a geometrical point of view, as long as the curvature is only smoothly deformed without introducing a further hole into the surface, i.e., without changing g , the system does not change topologically (**Fig. 2.3c**). Since the conductance of a quantum Hall system can also be thought of in terms of curvature, the above formula also applies to the eigenstates of its Hamiltonian and the value of the integral is the Chern number $n \in \mathbb{Z}$, where \mathbb{Z} denotes the set of all integers. Since the Chern number is an integer, it cannot change continuously with small variations of the Hamiltonian, which makes it topologically invariant. According to the adiabatic theorem, this means that when the system is placed in a non-degenerate eigenstate and the Hamiltonian parameters are varied slowly, the system would remain in this state. For

2.1. Theoretical background of topological insulators

larger variation, however, the system's state may cross over to a next eigenstate and create a level crossing, where the two eigenstates are degenerate. This causes the local curvature to diverge and the Chern number to be no longer defined. Thus, it is only possible to change it in a step-like manner when the system is at such a level crossing and in this manner, the exact quantization of the Hall conductance becomes evident.

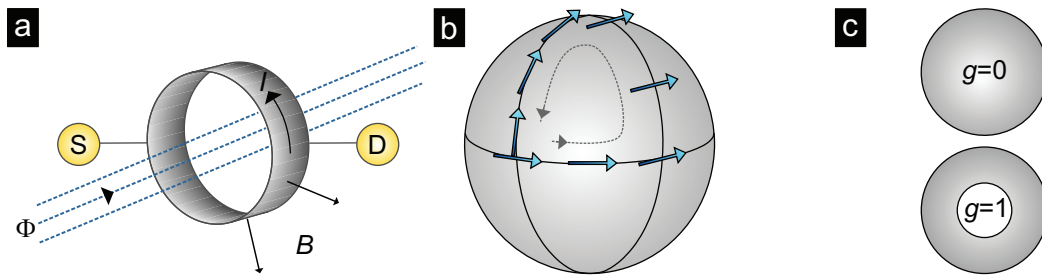


Figure 2.3 – A topological perspective. **a)** Laughlin's gauge argument relating the quantum Hall conductance to an electron pump thought experiment, in which a quantized number of electrons are transported during each pump cycle from source to drain connecting the two edges of the loop. **b)** Parallel transport on a sphere - after completing a full closed cycle, the difference between the initial and final direction of the vector corresponds to the gained Berry phase (here 90°). **c)** Topologically distinct systems defined by the number of holes g in the surface, i.e., by discontinuous deformation of the system's Hamiltonian.

2.1.2 Band gap states and topological protection

\mathbb{Z}_2 topological insulator The QHE is the most prominent example for the existence of chiral edge states at the boundary of two topologically distinct systems. In order for such a state to occur, the topological invariant needs to change, which corresponds to closing the energy gap, or "bridging" the two bulk bands with an edge state (**Fig. 2.4a**). Since such states only exist at the edges, they are dissipationless, as there are no available states to allow for backscattering. In this sense, the edge states are topologically protected.

So far, it has been shown that a topological invariant of the Bloch bands can only change when the energy gap closes and reopens. Topologically non-trivial systems with broken time-reversal symmetry (TRS) are classified by a non-zero integer Chern number and possess gapless chiral edge states. SO coupling, however, gives rise to another class of topologically distinct insulators with preserved TRS. The shape of the edge state dispersion within the band gap can be deformed, such that it crosses the Fermi energy more than once and its slope at the crossing defines the group velocity. On this basis, the difference in Chern number is defined as the difference between the number of positive and negative slopes, also known as bulk-boundary correspondence (**Fig. 2.4b**). **Fig. 2.4c,d** show the band dispersion of a 2D

time-invariant insulator in the positive half of the Brillouin zone with two different possibilities for edge states to occur. According to Kramers theorem, they need to be two-fold degenerate, i.e., at $k = 0$ (Γ_a) and $k = \frac{\pi}{a}$ (Γ_b). If the two degenerate points are connected such that the edge states cross the Fermi energy an even number of times (panel **c**), they are topologically trivial. With odd number of crossings, they remain robust and topologically protected (panel **d**). A time reversal invariant (TRI) system is characterized by an additional topological invariant \mathbb{Z}_2 , which is directly related to the number of crossings [18]. As a consequence, even when the Chern number is zero, the topological invariant \mathbb{Z}_2 is $\nu = 0$ or $\nu = 1$ ($\nu \in \mathbb{Z}_2$), corresponding to a trivial and a non-trivial band structure, respectively.

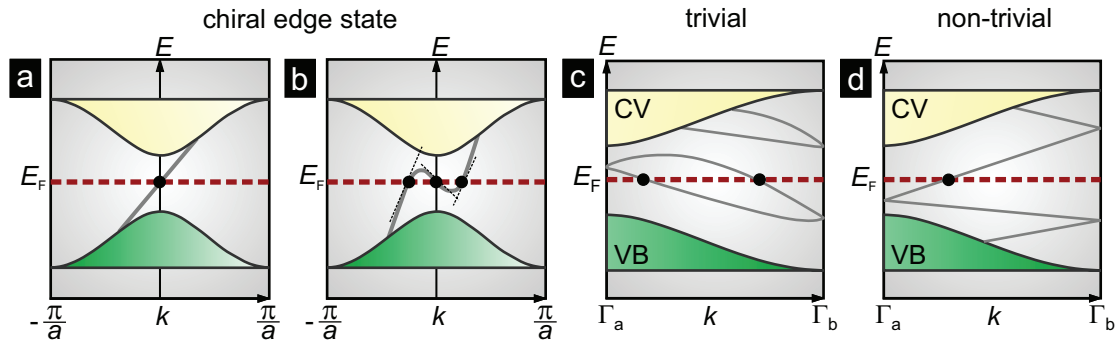


Figure 2.4 – Protected states in the energy band gap. **a)** Band dispersion in the first Brillouin zone showing a single edge state connecting the conduction and valence bands. **b)** While the number of crossings is defined by the changes in the surface Hamiltonian, the topology does not change as long as the number of left and right propagating modes, i.e., the slope of the group velocity at the E_F -surface state crossings, does not change. **c,d)** Band dispersions in the positive half of the first Brillouin zone, with even and odd number of crossings, respectively, illustrating that topological robustness is ensured only when the states cannot be pushed out of the band gap.

From quantum Hall to quantum spin Hall state A strong magnetic field is needed to break TRS and give rise to non-trivial quantum Hall edge states. The presence of SO coupling in a TRI system, however, leads to a splitting of each edge states into two components, specifically one for spin-up and another for spin-down [18] [26]. Such spin-resolved edge states are protected against backscattering by TRS, provided that there is an odd number of edge state pairs, such that there are no two states with the same spin orientation that would allow scattering between each other, just as described above for the bulk-boundary correspondence and the \mathbb{Z}_2 invariant. The fact that the spin is connected to the direction of propagation of the edge state makes these states helical, i.e. spin and momentum of an electron propagating along an edge state are coupled. These robust metallic states are topologically protected against

2.1. Theoretical background of topological insulators

scattering and cannot be localized, unless TRS is broken by an external magnetic field or a magnetic impurity. **Fig. 2.5a** shows the schematic band structure of two spin-filtered edge states crossing at $k = 0$.

In order to experimentally observe the quantum spin Hall effect (QSHE), a material system with strong SO coupling is needed. In 2006, Bernevig, Hughes, and Zhang [26] investigated a quantum well comprised of HgTe sandwiched between two layers of CdTe, both compounds being semiconductors with strong SO coupling (**Fig. 2.6b**). In this heterostructure, the SO coupling causes an inversion of the p- and s-bands in the HgTe, if the HgTe layer exceeds a critical thickness d_c , thereby inducing a quantum phase transition from a topologically trivial system to a QSH system. The corresponding longitudinal resistance R_{xx} recorded from devices fabricated in the Hall bar geometry by König et al. [27], reflects this topological phase transition (**Fig. 2.6a**). As shown in **Fig. 2.6c**, when $d < d_c$, a large R_{xx} is measured, indicative of a trivial insulating state of the system. For $d > d_c$, however, the resistance drops by more than three orders of magnitude, reaching ballistic transport with $R_{xx} = \frac{h}{2e^2}$. The quantized resistance reflects dissipationless conduction in the helical edge states of the system. The factor $\frac{1}{2}$ arises from the conductance contribution of both sets of edge states.

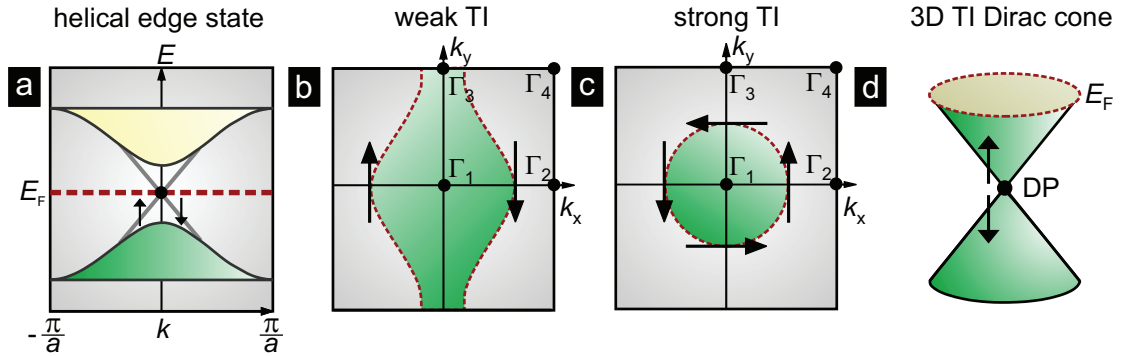


Figure 2.5 – Helical edge states and the 3D TI. **a)** Surface state dispersion indicating the opposite direction of propagation for different spin helicities. **b)** Fermi contour enclosing two TRI points, indicating an even number of E_F crossings and the emergence of a weak TI, whose surface states are only protected by TRS in the absence of disorder. **c)** Emergence of a strong TI when the Fermi contour encloses an odd number of TRI points (here: one). **d)** Dirac cone of a 3D TI with helical surface states crossing at the charge neutrality point (Dirac point, DP).

2.1.3 3D topological insulators

The theory of the 2D QSH insulator can be extended into 3D, as proposed by Fu, Kane, and Mele [22], Moore and Balents [28], and Roy [29]. The 1D edge states of 2D systems become 2D surface states (SS) in 3D TIs. In 2008, Hsieh et al. [30] observed for the first time helical surface

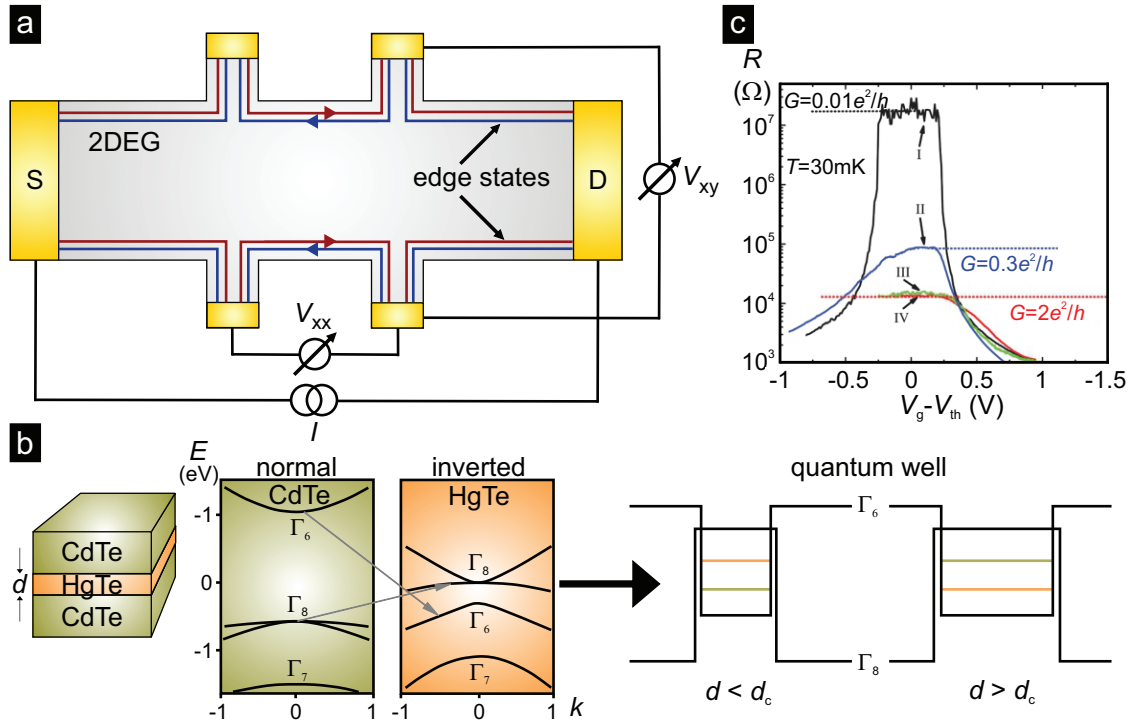


Figure 2.6 – The spin quantum Hall effect. a) Scheme of an electronic device patterned into Hall bar geometry based on the HgTe quantum well system. Similarly to the QHE, the longitudinal and transversal resistance is recorded, but in the absence of an externally applied magnetic field. b) The non-trivial band topology of HgTe is a consequence of the presence of SO coupling, which inverts the Γ_6 and Γ_8 bands given a minimum critical thickness of the HgTe layer. c) Electronic transport measurements (adapted from [27]) reveal ballistic conductance with a quantized value of $\sigma_{xx} = 2e^2/h$, which arises from the spin-polarized edge states.

states in angle-resolved photoemission spectroscopy (ARPES) measurements of $\text{Bi}_{1-x}\text{Sb}_x$, followed by the family of Bi_2Se_3 in 2009, as reported by Xia et al. [31] for Bi_2Se_3 and by Chen et al. [32] for Bi_2Te_3 . In order to visualize the surface states in a band diagram, it is helpful to look at the 2D Brillouin zone in the k_x - k_y plane. The Brillouin zone contains four distinct points, Γ_{1-4} , which are TRS invariant and degenerate according to Kramers theorem. At these points, the surface states cross, and away from them, their degeneracy is lifted by the pronounced SO coupling. The four \mathbb{Z}_2 invariants again distinguish between topologically trivial and non-trivial cases, corresponding to an even or odd number of crossings between the Fermi surface and the lines connecting each pair of Γ points.

It might be expected that creating a stack of 2D QSH systems will result in a 3D topological insulator, which is indeed the case, as seen in Fig. 2.5b. One possibility is that the Fermi surface encloses two of the Γ points, in which case the surface states are not protected by TRS and are hence sensitive to disorder – a phase known as weak topological insulator. If a single Γ

point is enclosed, a strong topological insulator emerges (**Fig. 2.5c**). The 2D Fermi surface can be extended to 3D, since it is simply a slab cut out in the x-y crystal momentum plane from the 3D band dispersion, called Dirac cone, as illustrated in **Fig. 2.5d**.

2.1.4 Engineering topological insulator materials

A large number of 3D TIs have been experimentally demonstrated by ARPES, which probes the occupied electronic states of solid state systems. Such measurements provide a map of the dispersion and the Fermi surfaces of these states in energy-momentum space. Of particular interest are the size of the band gap, the position of the charge neutrality point (Dirac point), and the location of the Fermi level. For favorable doping levels, the dispersion of the surface states within the bulk gap is clearly visible (**Fig. 2.7a,b**).

The Bi_2Se_3 family of 3D TIs form crystals with tetradymite structure, consisting of covalently bonded quintuple layers that are weakly coupled by van der Waal forces. In these compounds, a single Dirac cone centered at the Γ -point features helical spin surface states. The large band gap (300 meV) of Bi_2Se_3 and its simple band structure, as compared to Sb_2Te_3 , triggered strong interest in the properties of these materials. To this end, not only numerous ARPES experiments, but also electrical transport measurements have been performed.

In 2010, the first ternary dichalcogenides were theoretically predicted to host topological surface states. This property could be experimentally confirmed for TlBiSe_2 by Sato et al. [33], and TlBiTe_2 by Chen et al. [34]. The ternary compound $\text{Bi}_2\text{Te}_2\text{Se}$ gained a lot of interest after Ren et al. [35] reported its high bulk resistivity and tunable Fermi energy, paving the way for more detailed charge transport studies of the TI properties. Neupane et al. [36] have further investigated the electronic structure of TIs from the family of ternary compounds using ARPES, in order to aid the interpretation of optical, transport, and thermoelectric measurements.

Complementary investigations by spin-polarized ARPES have directly revealed the spin texture of the surface states in TIs. Along these lines, Hsieh et al. [19] and Nishide et al. [37] observed the spin texture in $\text{Bi}_{1-x}\text{Sb}_x$ (**Fig. 2.7c**), thereby confirming that the surface states are characterized by the $\nu_0 = 1$ topological class and that the spin polarization lies in the surface plane (**Fig. 2.7d**). Spin-integrated ARPES intensity map of Bi_2Se_3 and the corresponding map of the spin polarization P_y are illustrated in **Fig. 2.7e** [38].

Real-world TI materials, however, pose a challenging problem for the further investigation of their electronic properties by charge transport experiments, namely doping. The latter typically arises due to the presence of vacancies or anti-sites in the crystal lattice, and causes

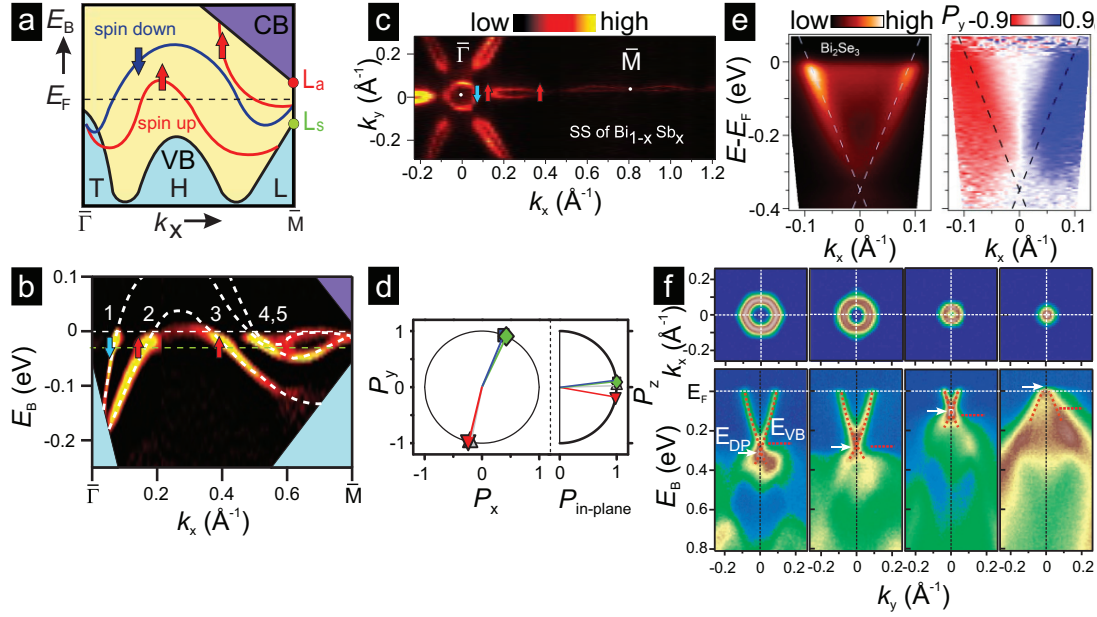


Figure 2.7 – TI surface states observed in ARPES measurements. **a)** Theoretical band structure of $\text{Bi}_{1-x}\text{Sb}_x$ from first principles calculations. **b)** Experimental ARPES data for the same compound ($x = 0.1$), showing five surface state crossings between the TRI points Γ and M. **c)** 2D momentum plane intensity map of the surface states at the E_F obtained with spin-integrated ARPES in the (111)-direction, from which a Berry phase of π can be extracted. **d)** Spin polarization of the surface state in the 2D momentum plane indicating in-plane spin alignment along the y-axis, while the out-of-plane spin polarization is close to zero (adapted from [19]). **e)** ARPES and spin-polarized ARPES of the Bi_2Se_3 surface states along k_x (adapted from [38]). **f)** Dirac cone engineering in the tetradymite $\text{Bi}_{2-x}\text{Sb}_x\text{Te}_{3-y}\text{Se}_y$ showing the Fermi surface dispersions and the Dirac point shift for varying concentrations of the individual components (adapted from [39]).

a shift of the Fermi level towards the conduction band (n-doping) or the valence band (p-doping), such that there is an increased contribution of bulk states to the overall conductivity of the material. Furthermore, exposure to ambient can result in surface oxidation and formation of surface charges. For high carrier concentrations, the formation of impurity bands within the band gap has been proposed [35]. In this model, the wave functions of the electrons bonded to impurity sites overlap and form extended states, which also contribute to the conductivity. Ideally, the Fermi level would be situated in the bulk band gap, such that the surface states can be probed exclusively. To achieve this goal, gate voltage can be applied, with the aim of shifting the Fermi level from the bulk band to the band gap. Modification of the surface using molecular dopants [40] [41], or the increase of the surface-to-bulk ratio by growing thin and laterally large films [42] [43] are further strategies that have been followed. Ultimately, the aim is to achieve high-quality crystals with minimized doping and high mobilities in order to

2.1. Theoretical background of topological insulators

detect surface-related effects unaffected by the bulk. TI materials exhibiting bulk-insulating behavior and a tunable Dirac cone (Fig. 2.7f) have been successfully engineered by precise control of the crystal stoichiometry and elemental doping [39] [44].

Studying the electronic properties and various quantum effects in TIs requires reliable and reproducible synthesis methods for high-quality TI single crystals, like the Bridgman method [45], chemical synthesis [46], pulsed laser deposition [47] [48], molecular beam epitaxy [49] [50], and chemical vapor deposition [51] [52].

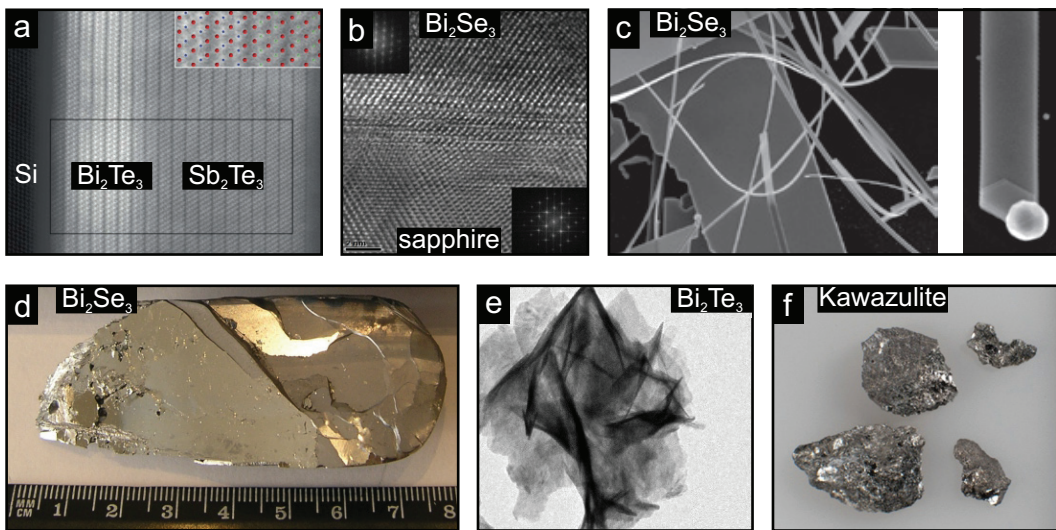


Figure 2.8 – Methods for the synthesis of TI materials. a) MBE-grown heterostructure of 15 QL Sb₂Te₃/6 QL Bi₂Te₃ [53]. b) Epitaxial Bi₂Se₃ thin film grown by PLD [54]. c) LVS-grown Bi₂Se₃ nanowires and nanoribbons [55]. d) Large crystal of Bi₂Se₃, grown by the Bridgman method. e) Surfactant-assisted wet chemical synthesis of Bi₂Te₃ nanosheets [56]. f) The natural TI Kawazulite [57].

One of the most common methods for high-quality single crystal growth is the Bridgman method, which is typically followed by mechanical cleavage of the crystal for the preparation of thin film electronic devices. Typically, high-purity elements are placed in a quartz tube, sealed and heated to their melting temperature. The tube is then allowed to cool down to about 500 °C, whereupon crystal growth takes place, and is subsequently heated to the same temperature over a certain period of time. Finally, the crystals are cooled down to room temperature and cleaved for further investigation. This technique also allows incorporating elemental dopants in well-defined stoichiometry in order to reduce the charge carrier density [58].

TIs have also been synthesized by chemical solution growth, which renders thin platelets. The presence of disorder in the latter often results in relatively poor mobilities, which hinders their usage for advanced charge and spin transport experiments.

Molecular beam epitaxy (MBE) is a well-established technique for epitaxial growth of chalcogenide-based TI thin films with large surface-to-bulk ratio and high crystal quality. In the MBE process, the TI film is grown layer-by-layer, which is monitored by reflection high-energy electron diffraction (RHEED). STM measurements have provided evidence for a low defect density in as-grown TI films [59]. A low growth temperature of 200-300 °C degrees and a slow growth rate ensures a high flatness of the TI film, which can be only a few quintuple layers. Alternatively, atomically flat TI films can be grown by pulsed laser deposition (PLD) [60] [61].

Gehring et al. have demonstrated for the first time TI electronic properties of the naturally occurring minerals Kawazulite, $\text{Bi}_2(\text{Te,Se})_2(\text{Se,S})$ [57] and Alekseite, $\text{PbBi}_2\text{Te}_2\text{S}_2$ [62], which exhibit relatively high mobilities and interesting quantum transport phenomena.

Band structure engineering has been demonstrated via MBE growth of TI thin films in a van der Waals heterostructure with other materials, e.g. Bi(111). Due to hybridization at the interface, the energy dispersion of the surface states can be modified [63]. Furthermore, epitaxial heterostructures of TI and graphene [64] or TI and hexagonal boron nitride (hBN) [65] open new avenues towards electronic and spintronic devices that allow for detecting novel interface and surface effects.

2.2 Electronic transport

2.2.1 Characteristic lengths

In order to understand electronic transport phenomena in TI materials, one needs to consider a number of length scales in relation to the system's dimensions. The characteristic length, which dominates the transport behavior is usually the smallest one and the investigated systems can be classified accordingly, as schematically shown in **Fig. 2.9**. Obviously, one needs to reduce the sample size (length L , width W) in order to observe a transition from classical to quantum behavior. In disordered systems electron scattering gives rise to localization effects, described by the localization length ε . The elastic mean free path L_e defines the distance between two elastic scattering events of an electron interacting with lattice phonons or lattice impurities. In the quantum regime, the electronic wavefunction, defined by the Fermi wavelength λ_F , contains phase information, which is susceptible to decoherence and is described by the phase coherence length L_ϕ .

Two length scale regimes are relevant for the investigated TI systems, in which charge carriers can exhibit classical and quantum behavior. In the classical regime, the electron motion is

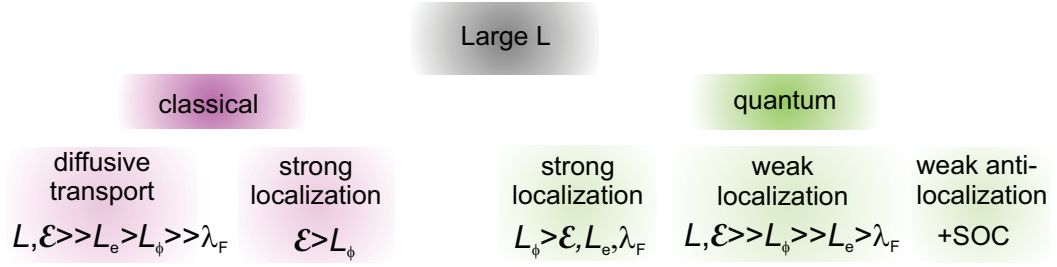


Figure 2.9 – Characteristic lengths. Classification of electronic transport regimes in diffusive conductors according to the characteristic length scales, where L and W are the sample length and width, respectively, ε is the localization length, L_e is the elastic mean free path, λ_F is the Fermi wavelength, and L_ϕ is the phase coherence length.

well described by the Drude model and there is no quantum correction to the conductivity. In the presence of strong disorder, the localization length is much larger than the phase coherence length and the conductivity is characterized by hopping transport. In the quantum limit, quantum diffusion behavior describes the electron motion and quantum interference of electronic phase information leads to a weak localization correction to the conductance. Also here strong disorder leads to strong localization and hopping behavior with a quantum correction to the conductance arising from the interference of hopping paths. Systems whose dimensions are in the range of the phase coherence length or smaller are categorized as mesoscopic and can be described in different dimensionalities depending on the relation between L , W , and L_ϕ . Accordingly, their transport properties fall into the diffusive, ballistic or quasi-ballistic regime.

2.2.2 Diffusive quantum transport

The electronic band structure of a 3D TI is described by a Dirac cone, where the bulk bands are connected by gapless states with linear dispersion. These 2D surface states are characterized by lifted spin degeneracy and spin-momentum locking describing the spin helicity. Charge carriers propagating along the surface states acquire a non-trivial Berry phase, which influences the magnetotransport properties. In a 2D electron gas system, the presence of disorder results in localization of the electrons, but in the presence of strong SO coupling, the gained electron phase results in a positive quantum correction to the conductivity, called weak anti-localization (WAL), which can be observed as long as TRS is preserved. Despite the surface state robustness, 3D TI materials exhibit relatively low mobilities and thus the nature of electronic transport is that of a diffusive conductor.

Chapter 2. Theory of electronic and spin transport in topological insulators

A TI platelet has a top and bottom surface, each featuring a Dirac cone of opposite spin helicity. In charge transport measurements, both surfaces can in principle contribute to the conductance, depending on the strength of their coupling. The latter is quantified by the parameter α , which can be extracted from the fitting of magnetoconductance data with a 2D model for diffusive transport. It assumes a value of -1 or $-1/2$ for contributions from both or only one surface, respectively.

Weak localization (WL) In classical diffusive transport where the sample size is larger than the phase coherence length, the quantum corrections to the conductivity arise from multiple phase-coherent scattering events. **Fig. 2.10a** depicts a possible path an electron takes between consecutive scattering events, along with the time-reversed path. The probability that the electron will return to the starting point corresponds to backscattering (constructive interference of the two paths). The probability is given by $P = |A^+ + A^-|^2 = |A^+|^2 + |A^-|^2 + A^+ A^{-*} + A^{+*} A^-$, where the first two terms correspond to the classical contribution to backscattering and the last two to interference effects. According to TRS, $A^+ = A^- = A$, which means that the classical probability of backscattering is $P_c = 2|A|^2$, but the additional quantum contribution increases it to $P_q = 4|A|^2$. This factor of two correction is detected in the magnetoresistance, which emerges at small magnetic fields and has its maximum at $B = 0$. As the B-field increases, TRS is broken and the quantum correction vanishes. The magnitude of the WL peak depends on the ratio between the phase coherence length and the mean free path of the electrons, as shown in **Fig. 2.10b**. The effect is maximum at low temperature and decreases as L_e becomes larger than L_ϕ for higher temperatures.

Weak anti-localization (WAL) The SO coupling in TIs has an important consequence for the magnetoresistance. As the electrons traverse diffusive closed paths, randomization of the spin direction takes place in the scattering process, which means that the initial spin direction is modified by each scattering event and becomes completely random after a characteristic time τ_{SO} , which is inversely proportional to the SO coupling strength. When many interfering paths are averaged, the destructive interference is predominant and the backscattering probability is reduced to half of the classical one, leading to an anti-localization correction dip at zero B-field (**Fig. 2.10c**). In a sense, the WAL correction is analogous to the backscattering protection observed in the edge states of a 2D QSH insulator. The magnetoconductance at low B-fields

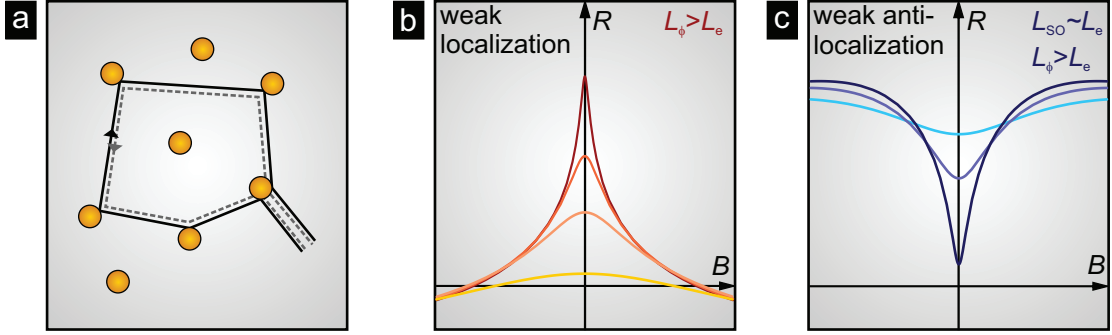


Figure 2.10 – Quantum corrections to the conductance in diffusive systems. a) Schematic representation of a 2D diffusive sample with a possible electron time-reversed scattering path. Depending on the sample’s properties, in the presence of a magnetic field, the paths interfere either constructively or destructively leading to quantum corrections to the classical magnetoresistance. b) Weak localization peak at zero magnetic field, whose shape is determined by the ratio L_ϕ/L_e . c) Weak anti-localization peak, which becomes sharper for larger L_ϕ .

can be fitted with the Hikami-Larkin-Nagaoka (HLN) model [66]:

$$\Delta\sigma(B) = \alpha \frac{e^2}{h} \left[\ln\left(\frac{B_\phi}{B}\right) - \Psi\left(\frac{1}{2} + \frac{B_\phi}{B}\right) \right], \quad (2.1)$$

which yields the phase coherence length L_{phi} and the parameter α . Here Ψ is the digamma function, $B_\phi = \frac{\hbar}{4e l_\phi^2}$, where the phase coherence length $l_\phi = \sqrt{D\tau_\phi}$. The parameter α describes the number of channels contributing to the conductance, as explained above. The value of α , however, strongly depends on the material’s doping, i.e., the position of the Fermi energy, the coupling of the two surfaces, as well as the bulk contribution. The importance of these factors are still a topic of ongoing discussion.

Universal conductance fluctuations (UCFs) In a small sample, for which $L_\phi > L, W$ and $L, W > L_e$, the transport properties are characteristic of the mesoscopic diffusive regime. Coherent interference of electronic phases gives rise to periodic Aharonov-Bohm oscillations (AB) [55, 67, 68] and aperiodic universal conductance fluctuations (UCFs) [69] in the magnetoresistance. The latter have been observed in TI samples at low temperatures, when the system is in the WAL regime [70–72]. They are sample-specific and well reproducible, exhibiting decreasing magnitude with increasing temperature, suggesting that the electronic wavefunctions are largely phase coherent. The UCF amplitude ΔG is on the order of e^2/h at $T = 0$ and independent of the sample dimensions, shape, and scattering center distribution. $\Delta G = \sqrt{\langle (G - \langle G \rangle)^2 \rangle}$ signifies the averaging over multiple mesoscopic systems with different

impurity configuration. If a two-terminal geometry is considered (Fig. 2.11a), the transmission amplitude of an electron moving on diffusive paths in a random walk manner and the amplitude of the conductance oscillations depends on the reflection amplitude of the scattering events as long as $L \gg L_e$. The variation of the impurity configuration among different samples has the same effect on the conductance as an external magnetic field, which adds an additional phase to the electron's trajectories between scattering events. As the oscillation periodicity depends on the area of each loop, the conductance, as a superposition of the oscillating ensemble of loops, fluctuates aperiodically. This manifests itself in magnetoresistance oscillations as shown in Fig. 2.11b [73].

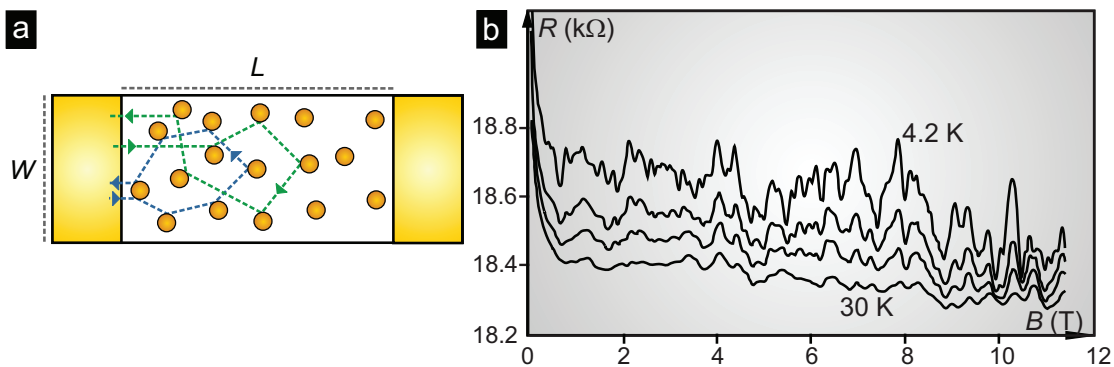


Figure 2.11 – Universal conductance fluctuations. a) Schematic illustration of scattering centers in a conductor and two possible electron path loops that lead to reflection. A magnetic field applied normal to the surface causes a phase shift in each loop, leading to an interference pattern and conduction oscillations. b) UCFs in the magnetoresistance with temperature-dependent magnitude oscillate aperiodically due to their loop-specific phases and periods (adapted from [73]).

2.3 Spin transport

The main goal of spintronics is to utilize the spin degree of freedom in order to achieve more efficient information processing and storage. For this purpose, the properties and behavior of spin ensembles or single spins need to be investigated in solid state systems. Furthermore, a distinction has to be made between spin-polarized charge current and pure spin current, which propagates independently of charge. Information transmission utilizing pure spin currents would take place without energy dissipation due to Joule heating. However, for practical applications, a better understanding of spin transport in different electronic materials and the spin dynamics in those systems is still required.

The discovery of the giant magnetoresistance (GMR) in ferromagnetic-nonmagnetic layered

structures in 1988 by Fert [2] and Grünberg [3] represents a milestone in the field of spintronics. In a GMR device, due to spin orientation dependent scattering, there exist a low and a high resistance state that can be used to convert magnetic information into electric one, providing an imminent technological application for the data storage industry. Shortly afterwards, the first metallic spin valves were realized and the injection of spin-polarized current from a ferromagnetic into a paramagnetic material was demonstrated for the first time [5]. In an attempt to increase the magnetoresistance signal in a GMR device, Miyazaki [74] and Moodera [75] discovered the tunneling magnetoresistance effect, which occurs when the paramagnetic layer is replaced by a thin insulating layer, ultimately resulting in as much as 70% increase of the resistance for anti-parallel orientations of the magnetization of the ferromagnetic layers at room temperature. Naturally, this led to the development of a new type of non-volatile memory devices, namely the magnetoresistive random access memory (MRAM).

Spin injection has also been achieved via ferromagnetic resonance spin pumping [76] [77] and switching of magnetization has been demonstrated via the spin transfer torque effect [9], which has already found application in the device storage industry as the underlying mechanism of novel MRAM devices [78] [79]. Furthermore, electrical control of magnetism has been achieved in ferromagnetic oxide semiconductors at room temperature. Optically, spins can be controlled via ultrafast laser light, whose helicity is used for spin direction reversal and also by combining magnetic resonance techniques with optically active NV-centers in a diamond [80].

2.3.1 All-electric spintronics

The necessity of downscaling in size while having to apply external magnetic fields in order to induce spin-current polarization or spin switching poses a challenge for state-of-the-art technology, which exploits both charge and spin for device applications. Quantum processes on the nanoscale, as well as spurious magnetoresistance and Hall effects arising from ferromagnetic components at contact interfaces, can introduce unwanted contributions to the measured signals and decrease the efficiency of spintronic devices.

To overcome these limitations, an all-electric control over the spin degree of freedom in the absence of magnetic components is desirable. Combining the concept of all-electric manipulation of spin currents with the existing semiconductor technology, as well as with novel materials, surfaces, and interfaces has opened a plethora of research direction towards gaining a better understanding of spin-related processes and mechanisms on a fundamental science

level, as well as from a technological point of view.

A major research effort within this field involves the use of materials with strong SO coupling, which enables spin manipulation without magnetic fields via spin-charge conversion governed by the Rashba, spin Hall, and Edelstein effects in materials with reduced dimensionality and non-trivial topology. Current-induced spin polarization in semiconductors [81–84], graphene [85] [86], and TIs [87–93] has been recently experimentally demonstrated. Emergent phenomena based on 2D interfaces and surfaces with strong SO coupling are being actively investigated, including chiral and helical spin-polarized edge and surface states in thin films and heterostructures [94].

2.3.2 Spin current injection, accumulation, and detection

Reliable information processing in a spintronic device depends on efficient spin injection, spin accumulation, spin transfer, and spin detection. It has been demonstrated that spin-polarized currents can be injected from a ferromagnetic material into a conductor, semiconductor, or superconductor, such that a non-equilibrium spin accumulation can be detected in those non-magnetic materials. When a FM and a NM material form a junction, spin-polarized electrons are driven from the FM to the NM, leading to spin accumulation close to the interface, which diffuses into the NM, while its magnitude decreases on the scale of the spin diffusion length. The spin-polarized electrons have spin-dependent electrochemical potentials, $\mu_{\uparrow\downarrow}$, such that the spin accumulation is given by $\mu_s = \frac{1}{2}(\mu_{\uparrow} - \mu_{\downarrow})$ [95] and its dynamics can be described by the relation

$$\frac{d\vec{\mu}_s}{dt} = D\nabla^2\vec{\mu}_s - \frac{\vec{\mu}_s}{\tau} + \vec{\omega}_L + \vec{\mu}_s \quad (2.2)$$

where D is the spin diffusion coefficient, τ is the spin relaxation time, and ω_L is the Larmor precession frequency. Thus, when there is no external magnetic field applied normal to the junction, the spin accumulation decays exponentially away from the interface with the spin diffusion length $\lambda = \sqrt{D\tau}$. In the presence of a magnetic field, by contrast, the spin dynamics is governed by Hanle spin precession.

Local spin valve In a local spin valve geometry, a NM transport channel is electrically contacted by two FM electrodes, acting as spin injector and spin detector, respectively. The spin transport in such a device can be described by the two-current model proposed by Valet and Fert [6], which assumes that spin-up and spin-down electrons possess different conductivities

in the FM material, in which both spin directions have a different density of states at the Fermi level. Thus, the spin-dependent conductivity is given by $\sigma_{\uparrow,\downarrow} = De^2\nu_{\uparrow,\downarrow}(E_F)$. The magnetization of the two FM electrodes is controlled by an external in-plane B-field applied along their easy axis. Due to their lateral widths, their magnetization switches at different coercive fields. When the two electrodes have parallel magnetizations, one spin species experiences low and the other one high resistance (Fig. 2.12a). For antiparallel orientation, both spin species experience low resistance in one of the electrodes, and high resistance in the other one (Fig. 2.12b). Hence, when a voltage is applied between the FM electrodes, a parallel orientation of their magnetizations effectively results in a low measured resistance, while the antiparallel one results in a high-resistance state.

In a lateral local spin valve, the measured resistance is influenced by both spin and charge currents, which coexist in the transport channel (Fig. 2.13a). Thus, a local measurement can contain co-planar spurious effects associated with the charge current, such as Hall effects or anisotropic magnetoresistance, which might mimic the real spin valve signal. Additionally, the detection of small spin-related signals can prove challenging in the presence of a larger charge current contribution, which decreases the signal-to-noise ratio significantly.

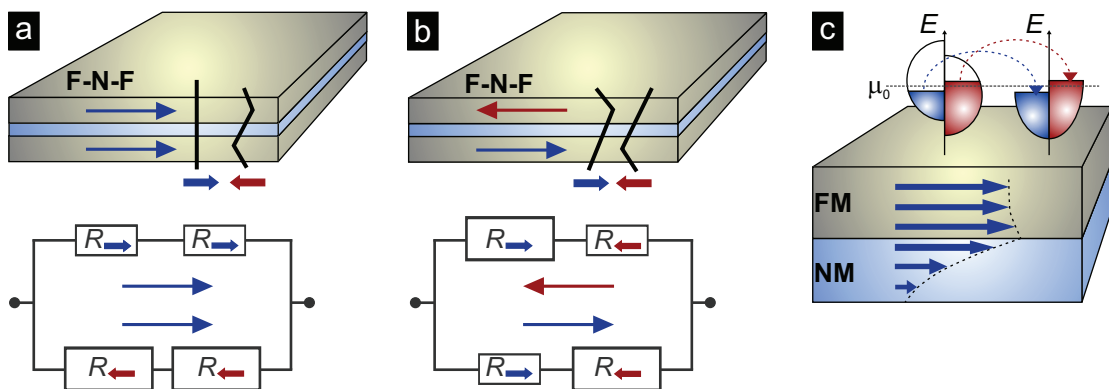


Figure 2.12 – FM-NM-FM CPP junction. Schematic representation of a NM sandwiched between two FM layers and current applied perpendicular to the junction. The spin-dependent conductivity results in low resistance for parallel FM magnetizations in **a)** and antiparallel magnetizations in **b)**. The corresponding electrical circuits represent the resistances of the two FM layers connected in series, depending on the magnetization orientations. **c)** Spin injection and diffusion at a FM-NM interface (horizontal blue arrows) and respective densities of states for the two spin species close to the Fermi level.

Non-local spin valve In order to avoid the above mentioned problems that might occur in a local spin valve, spin injection and detection measurements are usually performed in a non-local geometry, in which the spin signal is detected by electrodes placed outside of the

charge current path [96], as illustrated in **Fig. 2.13b**. This geometry was proposed for the first time by Silsbee et al. [97]. The spin accumulation in the NM can be probed by detecting a non-local voltage at the second FM. This voltage arises from the non-equilibrium spin density in the channel. In order to generate the non-local spin signal, current is applied via a pair of electrodes, at least one being a FM, and a voltage drop is detected with the second pair, such that the FM electrode in close proximity to the injector acts as detector. In this way, the spins diffusing towards the detector can be probed, and by varying the distance between the two FM electrode, the spin diffusion length of the transport channel can be determined. The non-local voltage is thus the difference between the spin potentials probed at the respective positions of the non-local voltage probe electrodes. Since this is a constant current experiment, the non-local voltage V_{NL} is often normalized by the current, resulting in a non-local resistance $R_{NL} = \frac{V_{NL}}{I}$.

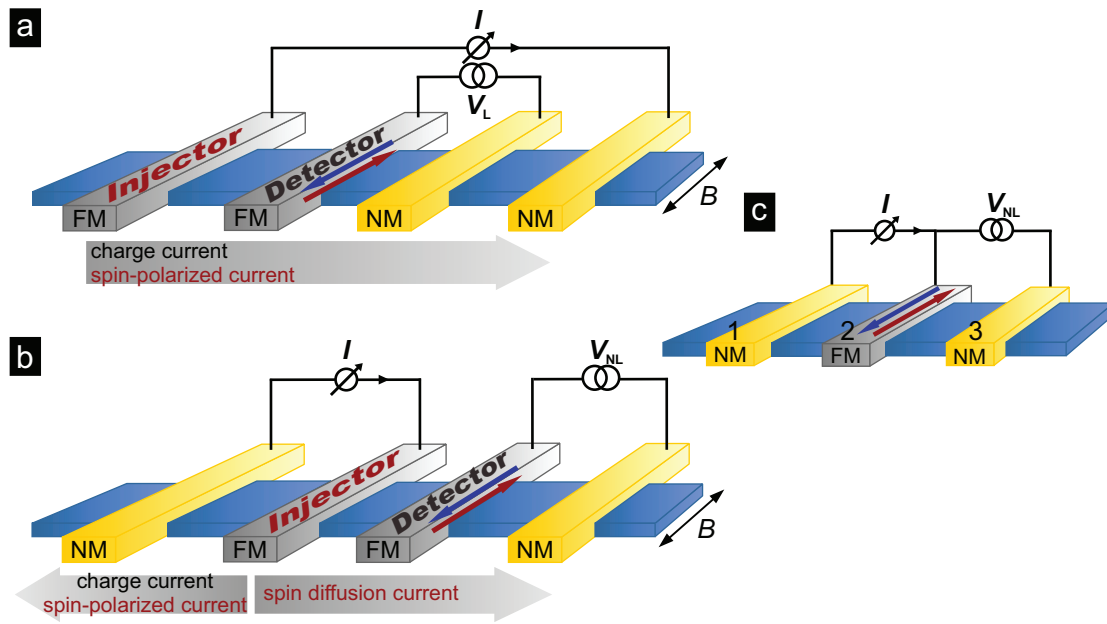


Figure 2.13 – Lateral spin valve measurement geometries. **a)** Local geometry, in which charge current and spin-polarized current are detected simultaneously. In both cases, the magnetization of the FM electrodes is switched via external in-plane magnetic field. **b)** Non-local geometry, in which the injected spin-polarized current diffuses away from the FM electrode towards the detecting FM electrode located outside of the charge current path. **c)** Three-terminal geometry, in which the spin accumulation underneath the central FM electrode can be probed.

Three-terminal non-local spin valve A similar approach to spin injection and detection is the three-terminal spin valve, where a single FM electrode is used to inject and extract spins

into and from the NM material. On this basis Dash et al. [98] demonstrated electrical creation of spin polarization in silicon at room temperature, followed by Li et al. [99] who detected spin signals in silicon even at 500 K. The geometry of a three-terminal spin valve experiment, as illustrated in **Fig. 2.13c**, comprises a single FM-NM interface, where spin accumulation in the NM is created by applying a constant current between electrodes 1-2 and detected as a voltage drop between electrodes 2-3. To increase the strength of the spin signal, a tunnel barrier is incorporated, such that spin-polarized tunnel current flows from the FM to the NM and produces a spin imbalance described by a net spin accumulation $\Delta\mu = \mu_{\uparrow} - \mu_{\downarrow}$, which is maximal at the interface and decays exponentially away from it (**Fig. 2.12c**). Its orientation is parallel to the interface and determined by the magnetization direction of the FM electrode. The spin accumulation in the NM can be influenced by applying a small magnetic field normal to the surface and detecting the Hanle effect (see **Section 2.3.3**). The spin life time and spin diffusion length can then be obtained by fitting the Hanle curves. The properties of the tunnel barrier at the FM electrode play a crucial role in the spin injection-detection process and a lot of effort has been put into optimizing its composition [100] [98], thickness [101] [5], and crystallinity [102] in order to obtain reproducible results. The expected magnitude of the spin signal in a three-terminal geometry is still controversial, as spin signals which exceed the theoretically predicted ones by several orders of magnitude have been experimentally detected [5] [99] [103]. Different mechanisms have been proposed to account for this discrepancy, including a two-step tunneling process [104], an inhomogeneous tunnel current density model [105], and an impurity-assisted tunneling magnetoresistance [106].

Conductivity mismatch problem and the role of the contacts An crucial factor that influences the efficiency of spin injection from a FM into a NM material is the interface between the two materials. The detected spin accumulation depends strongly on the interface between the injector material and the transport channel material, and more specifically on whether the junction is an Ohmic or tunneling contact. A fundamental problem is the conductivity mismatch, especially in the case of a FM-semiconductor (SC) junction, which arises due to the difference in resistivity between the two materials and leads to decreased spin polarization in the semiconductor transport channel [107]. The proposed experimental solution involves the implementation of a tunnel barrier at the FM-SC junction [108] [109]. The tunneling probability and thus the spin-dependent resistance depends on the density of states of both spin-up and spin-down electrons on both sides of the tunnel barrier. A spin-dependent interface resistance, whose value exceeds a threshold resistance given by the product of the SC

resistivity and spin diffusion length, $R_T > \rho L_{sf}$, enables the detection of a much larger spin polarization in the SC [109]. The spin polarization of the current in the SC channel is given by

$$P_J = \frac{P_F R_F + P_C R_C}{R_F + R_\lambda + R_C} \quad (2.3)$$

where P_F is the spin polarization in the FM, P_C is the interface polarization, R_C is the tunnel barrier resistance, and R_F and R_λ are the spin resistances of the FM and the SC, respectively. In the case of no tunnel barrier, $R_C = 0$ and the polarization of the spin current in the SC is given by $P_J = \frac{R_F P_F}{R_\lambda + R_F}$. When the FM and SC resistances are comparable, the polarization in the SC channel is not reduced. When the SC resistance is higher than that of the FM, i.e., $R_\lambda > R_F$, the spin polarization is reduced to $P_J = \frac{R_F}{R_\lambda} P_F$. In the presence of a tunnel barrier when $R_C > R_\lambda > R_F$, the spin polarization is proportional to the interface polarization, $P_J = P_C$. For very large R_C , however, the average time a spin-polarized electron resides in the channel exceeds the spin-relaxation time and the current polarization is again decreased.

Han et al. [110] have investigated spin transport in monolayer graphene for three different contact regimes, specifically tunnel (decoupled), pin-hole (intermediate), and transparent (highly coupled) contacts. For MgO- and TiO₂-based tunnel contacts, they found long spin lifetimes, attributable to a reduced contact-induced spin relaxation. In the other two cases, spin signals are still observed, albeit with reduced magnitude and correspondingly shorter spin lifetimes. Increased contact resistance can also be achieved by reducing the contact area, e.g. with the aid of MgO masking layers [111]. Furthermore, spin injection has also been demonstrated in the presence of a Schottky barrier, which increases the contact resistance at the FM-SC interface and affects the spin accumulation depending on the barrier's profile [11].

2.3.3 Spin relaxation and dephasing mechanisms

Band structure and SO interaction SO coupling in solids originates from relativistic effects in the rest frame of reference of an electron interacting with the crystal lattice. In this frame, the electron experiences an effective electric field gradient $\mathbf{E} = \nabla V(\mathbf{r})$ generated by the lattice, which gives rise to magnetic field $\mathbf{B} = \frac{1}{mc^2} \mathbf{E} \times \mathbf{p}$ coupling to the electron's spin. The direction of this magnetic field is perpendicular to the electron's orbital motion and to the electric field. The SO Hamiltonian can be written as

$$H_{SO} = \frac{1}{2} g \mu_B \mathbf{B} \cdot \mathbf{S} = \frac{g \mu_B}{2mc^2} (\nabla V(\mathbf{r}) \times \mathbf{p}) \cdot \mathbf{S}, \quad (2.4)$$

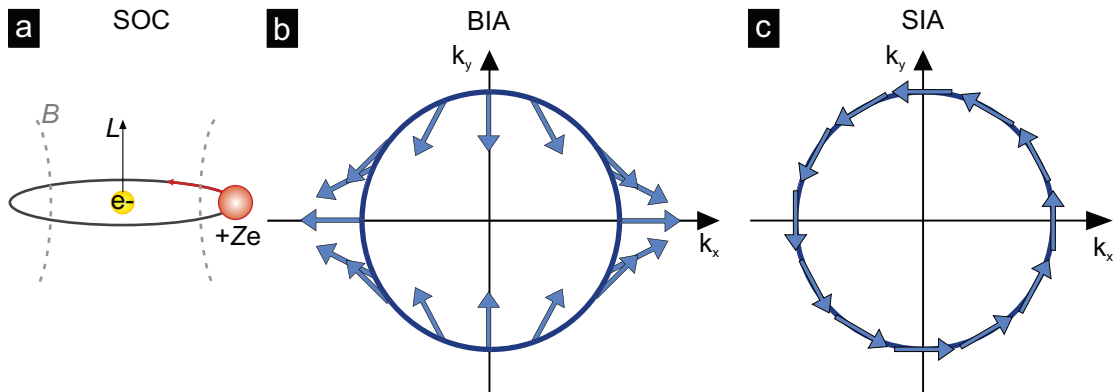


Figure 2.14 – SO coupling and crystal asymmetries. **a)** Schematic diagram illustrating the origin of SO coupling, in the electron's rest frame. The positively charge nucleus orbiting around it generates magnetic field, which couples with the electron's magnetic moment. **b)** An intrinsic electric field in crystals with bulk inversion asymmetry (BIA) gives rise to an effective magnetic field, resulting in a Dresselhaus SO coupling term. **c)** An externally applied electric field gives rise to a helical spin texture in crystals with structural inversion asymmetry (SIA), resulting in a Rashba SO coupling term.

where g is the spin gyromagnetic ratio of the electron, $\mu_B = e\hbar/2m$ is the Bohr magneton, $\mathbf{p} = m_e\mathbf{v}$ is the electron's momentum, and \mathbf{S} is the spin angular momentum vector. The gradient of the potential seen by the electron determines the SO coupling strength, which is the reason why sizable SO coupling occurs in heavy atom elements whose large number of protons is able to generate strong electric fields. By contrast, light elements and the materials composed of them, have only weak SO coupling, as exemplified by carbon and graphene. SO coupling can modify the band structure by splitting and energetically shifting bulk bands, one example being the formation of heavy and light hole valence bands in some heavy element semiconductors.

Another term in the SO Hamiltonian, known as Dresselhaus contribution, arises from the presence of bulk inversion asymmetry (BIA) in a crystal, resulting in lifting of the $E_1(k) = E_1(k)$ degeneracy [112] [113]. Furthermore, when the effect of SO coupling is combined with asymmetric potentials normal to the surface of 2D surfaces and heterostructures, another term is added to the Hamiltonian, which lifts the structural inversion asymmetry (SIA), called Rashba term. In a 2D quantum well structure, the strength of the linear BIA-induced spin splitting stems from crystal fields and depends on the quantum well's width, the temperature, and the electron density. The SIA term originates from the confining potential and can be modulated via a gate electric field.

Spin relaxation and dephasing Understanding the mechanisms of spin relaxation and dephasing is crucial for spintronic applications. Information processing based upon spin-states relies on long spin coherence times, to ensure that spin-encoded information can be transported over a sizable distance. On the other hand, short spin relaxation times are required for fast-switching applications [114].

Spin relaxation and dephasing are described by the characteristic times T_1 and T_2 , respectively, which can be derived via the equations governing spin precession, diffusion and decay of spins in magnetic field [115] [116]. T_1 , the longitudinal coherence time, is a measure of the time it takes for the longitudinal magnetization to relax back to equilibrium. T_2 is the phase coherence time for an ensemble of precessing spins, which dephase due to variations in the individual precessing frequencies.

The two major spin relaxation mechanisms are the Elliot-Yaffet (EY) [117] [118] [119] and D'yakonov-Perel (DP) [120] mechanism. The EY mechanism describes the spin state mixing during the interaction with lattice impurities and phonons, given the presence of SO interaction. The spin-up and spin-down states, which have the same momenta, couple in the presence of a SO potential, which gives rise to SO scattering leading to spin relaxation with the characteristic spin relaxation time τ_s (**Fig. 2.15a**). The phonon-induced spin relaxation is also relevant at low temperature, in the case that the heavy ion-induced SO potential is modified by phonons. The EY mechanism can be modeled with an equation involving a spin-flip function $F(\omega)$, which takes into account the phonon distribution as a function of frequency (**Eqn. 2.5**). It also involves a spin-flipping matrix element α_s , which contains the SO interaction potential, the ion mass, and the population change of spin-up and spin-down electrons $\frac{dN_{\uparrow\downarrow}}{dT}$. Obviously, low-mass elements, such as Si and C, would exhibit weak SO-induced spin relaxation, resulting in longer spin coherence times, in contrast to topological insulators.

$$\frac{1}{\tau_s} = 8\pi T \int_0^\infty F(\omega) \alpha_s^2 \frac{dN_{\uparrow\downarrow}}{dT} d\omega \quad (2.5)$$

The DP mechanism describes spin relaxation in systems with SO coupling and inversion asymmetry, in which case the degeneracy of spin-up and spin-down momentum states is lifted. Inversion asymmetry also arises at interfaces and surfaces in the presence of asymmetric confining potentials, as mentioned above. It results in an intrinsic momentum-dependent magnetic field and spin precession with the Larmor frequency. The spin dephasing is characterized by the momentum relaxation time τ_p , during which the intrinsic magnetic field fluctuates in magnitude and direction between scattering events (**Fig. 2.15b**). Thus, after τ_p , the spin would precess with a different frequency and direction, such that its phase evolves in

a random walk manner.

From the above, it follows that the EY and the DP mechanisms have opposite dependence on the momentum relaxation time. EY describes spin dephasing during the scattering process, such that it is proportional to the number of scattering events. DP, on the other hand, describes spin phase randomization between consecutive collisions, determined by momentum-dependent scattering.

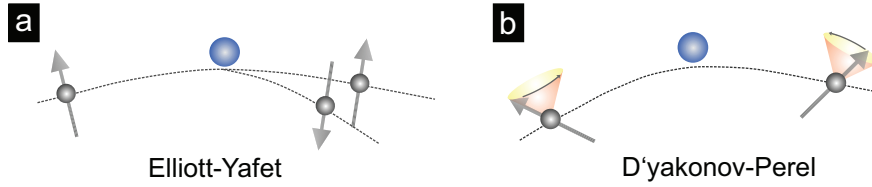


Figure 2.15 – Spin relaxation mechanisms. Scattering of the electron spin (grey arrows) at or between scattering centers (blue dots). **a)** The Elliott-Yafet mechanism describes spin relaxation, which occurs during a scattering event and involves a spin flip. **b)** The D'yakonov-Perel mechanism describes spin relaxation, which occurs between scattering events and involves Larmor precession.

Probing spin relaxation experimentally In a lateral spin valve, the spin lifetime and diffusion length can be probed by detecting the Hanle effect (**Fig. 2.16a**). In such a measurement, after the ferromagnetic injector and detector electrodes are magnetized by an external in-plane B-field, the substrate is tilted perpendicularly to the field direction, such that the B-field is normal to the direction of current flow. The injected spins now propagate away from the injector and as long as they arrive parallel to the detector's direction of magnetization, maximum signal is detected. When the field is swept, the spins in the channel start precessing with the Larmor frequency ω_L , while propagating towards the detector, and the measured signal decreases as it becomes a function of the projection of the spin direction onto the magnetization direction of the detector. The precession angle is given by $\theta = \omega_L \cdot \frac{L}{v}$, where L is the distance between the two electrodes and v is the electron velocity. The measured resistance displays a peak at zero B-field and exhibits oscillatory behavior as the field increases, with decreasing amplitude for higher fields since the angle θ depends on the averaged electron velocity. In order to extract the spin diffusion length and spin lifetime, the non-local resistance R_{NL} is recorded in a non-local spin valve configuration and the following equation is used:

$$R_{NL} \propto \int_0^{\infty} \frac{1}{\sqrt{4\pi Dt}} e^{-\frac{L^2}{4Dt}} \cos(\omega_L t) e^{-\frac{t}{\tau_s}} dt \quad (2.6)$$

where τ_s is the spin lifetime, and $D = \frac{\sigma}{e^2 N}$ is the spin diffusion constant. The spin relaxation length can also be estimated by recording R_{NL} for different injector-detector distances, and fitting the gained dependence with an exponential decay model, according to:

$$R_{NL} = \frac{\Delta V}{I} = \pm \frac{1}{2} p^2 \frac{\lambda_{sf}}{\sigma A} e^{-\frac{L}{\lambda_{sf}}}, \quad (2.7)$$

with $\lambda_{sf} = \sqrt{D\tau_{sf}}$, where λ_{sf} is the spin-flip length and τ_{sf} is the spin-flip time.

The efficiency of spin injection into a NM can also be determined by three-terminal non-local Hanle measurements (Fig. 2.16b). After the spin polarized current is injected, the perpendicular magnetic field leads to precession of the spins in the NM layer underneath the injector, which in turn reduces the spin accumulation. The measured voltage V_{3T} is proportional to the spin accumulation [11]

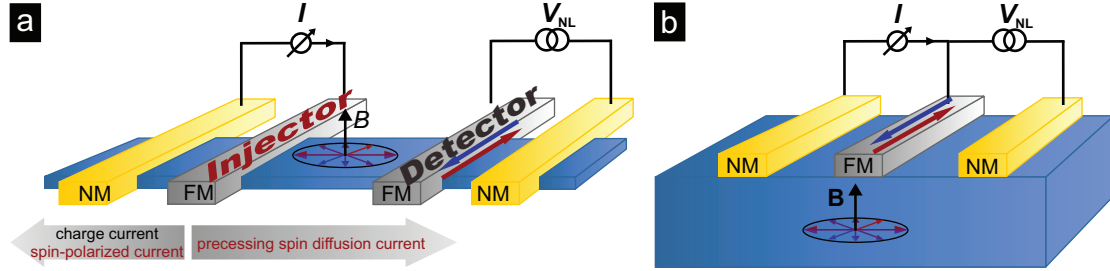


Figure 2.16 – Hanle spin precession. **a)** Precession of the injected spins in external magnetic field applied normal to the surface for a non-local four-terminal configuration. The non-local spin signal exhibits a maximum at zero B-field and decreases as the spin orientation misaligns with the detector’s magnetization during precession. **b)** Hanle precession of spins in a non-local three-terminal geometry, probing the spin accumulation underneath the central FM electrode.

2.3.4 Spin-charge conversion

Spin current can propagate independently of charge, allowing for information to be transmitted without energy dissipation due to Jule heating. A pure spin current is spin-dependent electron motion, in which spin-up and spin-down electrons propagate in opposite directions such that there is no net charge current. Thus, a main goal of spintronics is to create and detect spin currents via spin-charge conversion. Metallic interfaces, layered oxides, transition metal dichalcogenides with strong SO coupling are promising material platforms for the generation and detection of spin currents. At their 2D interfaces and surfaces, charge current can be converted to spin current via the spin Hall effect, and spin polarization can be generated from an applied electric current via the Edelstein effect. According to the Onsager reciprocity

relation, each of these effects possesses a counter effect, which does the reverse conversion and together they constitute powerful tools for spintronic applications.

Spin Hall effect (SHE) and inverse spin Hall effect (ISHE) One possible strategy for spin-charge conversion is to use materials with strong SO coupling. A prominent example is the SHE, wherein pure spin current is propagating towards the sample's edges, as a response to an applied electric current. There are two distinct mechanisms for SHE, namely an extrinsic SHE, which arises due to asymmetric scattering of spin-up and spin-down carriers, and an intrinsic SHE, induced by the topology of the band structure. The charge-spin conversion efficiency is assessed in terms of spin current per unit charge current and expressed as the spin Hall angle (SHA). **Fig. 2.17a** is a schematic representation of the SHE mechanism. An electric field is applied along the y -direction, resulting in out-of-plane spin-up and spin-down currents propagating perpendicular to the field towards the opposite edges. The spin current pointing out-of-plane is a direct consequence of the torque exerted onto the spins by a Zeeman field originating from the SO coupling. Since spin current is even under the application of the time reversal operator, it does not break TRS.

The reciprocal mechanism is the ISHE, shown in **Fig. 2.17b**, where spin current is injected and SO coupling induces a transversal electrical current perpendicular to the spin direction. **Fig. 2.17c** is a schematic representation of the Fermi contour displacement along the x -direction and the out-of-plane tilting of spin in response to the SO-induced torque.

In semiconductors, the SHE is usually detected by optical methods, such as Kerr rotation, in which linearly polarized light is reflected off the sample and the angle of rotation of the polarization plane is proportional to the out-of-plane spin Hall current. By doing this position-dependent, a spatial map of the spin distribution is obtained, which confirms spin accumulation along the edges of the sample [121].

In metals, spin-polarized current is usually injected into a paramagnetic material via a ferromagnetic electrode in a non-local geometry and the spins propagate in a diffusive manner. The transverse electrical signal induced by those spins can be detected as a voltage drop with the aid of two non-local voltage probes, as shown in **Fig. 2.17c**. Another spin injection method involves spin pumping. Under externally applied magnetic field, the magnetization of the ferromagnetic material precesses in a ferromagnetic resonance regime. The transfer of angular momentum from the precessing spins to the conduction electrons leads to spin diffusion into the NM material. The electrical signal due to the ISHE is then detected, which is possible even at room temperature for large SO coupling materials [122].

The SHE effect detected in a non-local geometry provides convincing evidence for the existence of helical edge states in a QSH system [123]. The non-local measurements are performed in a H-bar geometry without externally applied magnetic field and with NM contacts, as illustrated in Fig. 2.17d. Current is applied between contacts 1-2, and the non-local voltage drop is measured between contacts 3-4. In order to prove that the helical edge states are spin-polarized as well, a H-bar geometry can again be utilized, as demonstrated by Brüne et al. for a HgTe quantum well [124]. The carrier concentration of the HgTe underneath each pair of contacts can be tuned separately by gate voltage, such that the area underneath contacts 1-2 is in the metallic regime, while the area underneath contacts 3-4 is in the QSH insulating regime. When current is applied between 1-2, charge carriers of opposite spin separate due to the intrinsic SHE. The spin species which arrives at the metal-QSHI interface is transported by the edge state that is spin-polarized in the same direction. Thus, an electric potential difference arises between contacts 3-4, which provides an unambiguous proof of edge state spin-polarization in the QSH regime.

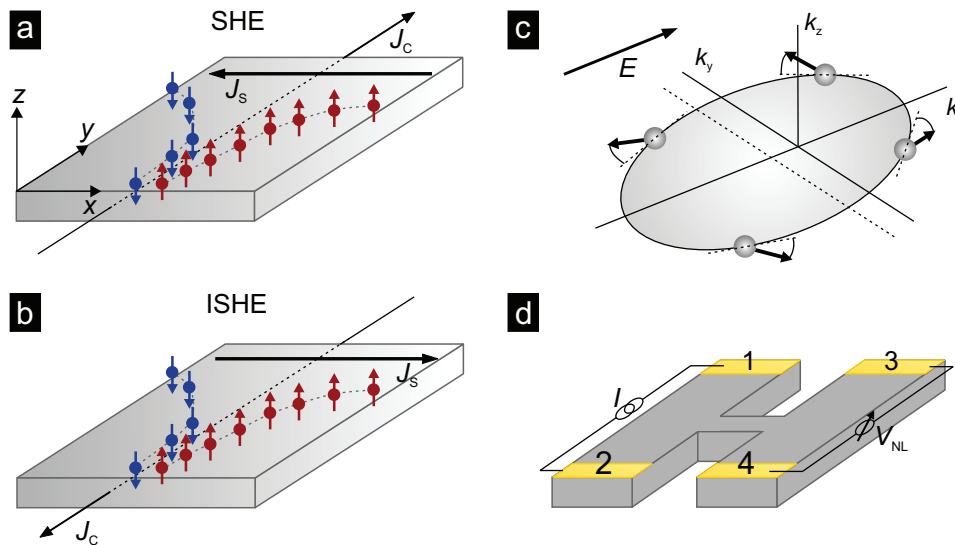


Figure 2.17 – Spin-charge conversion principles. **a)** Schematic diagram of the spin Hall effect. A charge current applied along the y -direction generates a pure spin current in the transversal direction due to spin-dependent separation of charges in the presence of SO coupling. **b)** In the inverse spin Hall effect the injection of spin current gives rise to a transverse charge current. **c)** In the presence of an electric field the Fermi surface is displaced and while moving in momentum space, the electrons experience an effective torque which tilts the spins up for $p_y > 0$ and down for $p_y < 0$, creating a net spin polarization in the z -direction. **d)** H-bar geometry for the transport measurements of SHE-related phenomena with NM electrodes, where current is applied via one pair of electrodes and the non-local voltage drop associated with a net spin imbalance is detected.

Rashba interfaces and TI surface states The presence of SO coupling in materials and at interfaces with broken inversion symmetry opens up new possibilities to generate and detect spin currents via spin-current conversion. The Rashba SO coupling in the presence of structural inversion asymmetry leads to momentum-dependent spin splitting of the band structure, as schematically shown in **Fig. 2.18a**. In a 2DEG with no external magnetic field applied, the Hamiltonian describing the electron motion is given by $H = \frac{p^2}{2m^*}$ and the momentum-dependent energy is $E(k) = \frac{\hbar^2 k^2}{2m^*}$. $E(k) = E(-k)$ in a system lacking inversion symmetry, whereas $E_{\uparrow}(k) = E_{\downarrow}(k)$ when time inversion symmetry holds. Thus, the energy eigenstates $E_{\uparrow\downarrow}(k)$ are two-fold degenerate, i.e., $E_{\uparrow}(k) = E_{\downarrow}(k)$, as long as the system's inversion symmetries are not broken. In the presence of external electric field, SO coupling gives rise to SIA Rashba or Bychikov-Rashba spin splitting of the 2D surface states [125], [126] with the Hamiltonian $H_R = \frac{\hbar^2 k^2}{2m^*} + \alpha_R \sigma (k \times E_z)$, where α_R is the Rashba parameter and σ is given by the Pauli spin matrices. The strength of this splitting depends on the SO coupling strength, which scales quadratically with the atomic number. Rashba-split states have been observed in ARPES experiments on the surfaces of noble metals, e.g. Au(111) [38] (**Fig. 2.18b**), heavy metal surfaces, e.g. Bi(111) [127], ferromagnetic metal surfaces, e.g. Gd(0001) [128], and metallic interfaces, e.g. Bi/Ag(111) [129].

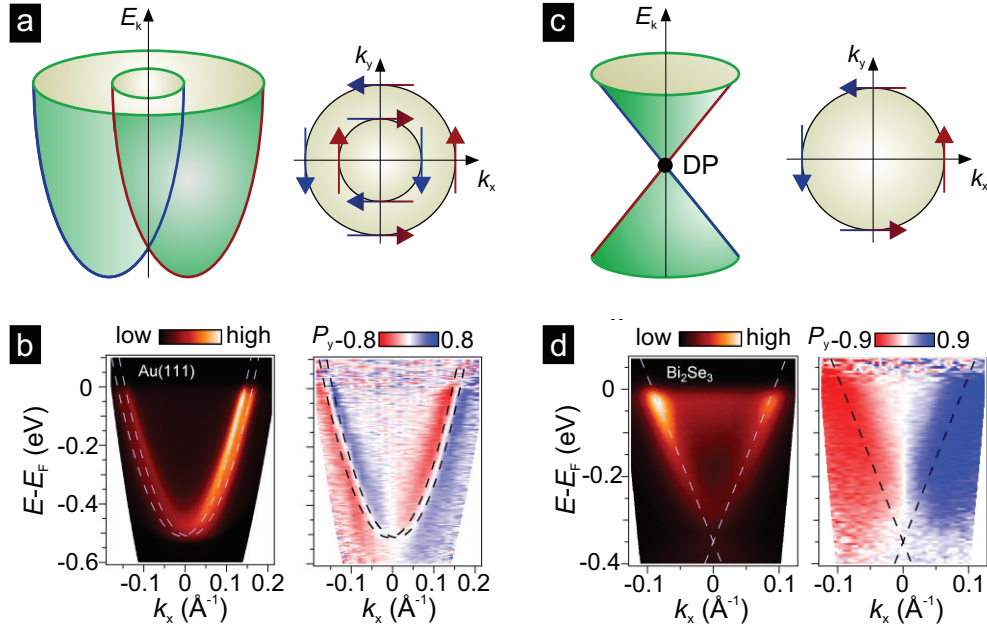


Figure 2.18 – Band structure of 2D surfaces and interfaces with SO coupling. **a)** Parabolic energy dispersion in a Rashba system, where there are two Fermi contours with opposite spin helicities. **b)** Rashba-split parabolic dispersion of the Au(111) surface and the corresponding spin-resolved ARPES measurement of the in-plane spin. **c)** Spin-polarized helical 3D TI surface states crossing in the band gap to form a Dirac cone. The Fermi contour (right) in the x-y momentum plane shows that spin is always locked to the momentum. **d)** Experimental ARPES measurement of the surface states for the 3D TI Bi_2Se_3 (left) and the spin-resolved surface states (right).

On the other hand, the TRS-protected surface states of 3D TIs also exhibit spin-momentum locking, as described by a Hamiltonian of Rashba type, $H = \hbar v_F(k_x \sigma_y - k_y \sigma_x)$, with a linear dispersion given by $E^\pm(k) = \pm \hbar v_k k$. However, unlike the spin-split parabolic bands of metallic surfaces, where back-scattering is permitted, the topology of the TI Dirac cone forbids backscattering involving a spin flip (**Fig. 2.18c**). Given spin-momentum locking of the surface states, electrically induced spin-polarization can be generated within a TI material, which allows for spin generation in the absence of a ferromagnetic injector. In an optical experiment, circularly polarized light can couple to the surface state momentum in order to generate a spin-polarized photocurrent, whose direction can be controlled by the light helicity [130]. TI surface state dispersions have been recorded in (spin-resolved) ARPES experiments, one example being the compound Bi_2Se_3 (**Fig. 2.18d**).

Edelstein effect (EE) and inverse-Edelstein effect (IEE) The conversion between spin and charge currents can be realized at 2D Rashba and 3D TI surfaces via the Edelstein and the inverse Edelstein effects (**Fig. 2.19**). According to Edelstein's theory, a current j_x carried by a helical surface state gives rise to a non-equilibrium spin accumulation σ_y in the transverse direction [131] [132]. An external electric field driving a charge current along the x-direction induces a shift Δk_x of the Fermi contour in the same direction. Due to SO coupling, spin accumulates in the k_y -direction.

In the spin-split Rashba band, the free electron parabola is split into two parabolas, which are shifted with respect to $k = 0$. The constant energy contours are two concentric circles in the k_x - k_y plane, where the spins are always perpendicular to the k -vectors in the 2D plane and the two circles have opposite helicities. The expectation value of the total spin is obtained by summing over all expectation values for all occupied states, such that there is a partial compensation arising from the opposite helicity of the two contributing Fermi circles. The larger radius of the outer circle enables the emergence of a non-zero in-plane net spin density perpendicular to the applied electric field (**Fig. 2.19a**).

In a TI, there is a single Fermi circle shifting in k -space (**Fig. 2.19b**), such that there is no partial compensation of the induced spin density and therefore a large Edelstein effect is expected here compared to a Rashba system. The underlying mechanism of spin generation is similar to the one in a Rashba system, with the exception of the factor $\hbar v_F$ that replaces the Rashba factor α_R . The sign of the spin density is determined by the chirality of the surface state carriers. The larger magnitude of the EE expected for TIs is not only due to the difference in magnitude of the Rashba factor and TI Fermi velocity factor, but also to the different Fermi circle contributions in each system. In a small k -vector approximation, the TI Fermi contour can be viewed as equivalent to the inner circle of a Rashba system. Due to the fact that in the latter, there is scattering within the inner circle, as well as between the inner and the outer circles, a larger effect is expected in TIs. The spin density in a TI should hence be Fermi energy independent, while the one arising from the Rashba inner circle is not [133]. In general, the charge-spin conversion process is characterized by the inverse length parameter q_{ICS} , which relates the 3D spin density in units of volume to the applied 2D current density in units of area [134]. For a TI system, $q_{ICS} = (v_F \tau)^{-1}$, where τ is the relaxation time of the non-equilibrium surface state population. Experimentally, the EE has been observed in Bi/Ag metallic interfaces [135] [136] (Rashba type) and in several TIs [137] [87] [90]. The inverse Edelstein effect (IEE) is defined as EE's Onsager reciprocal and involves the emergence of an electric current in the 2D k -plane perpendicular to the orientation of an existing non-

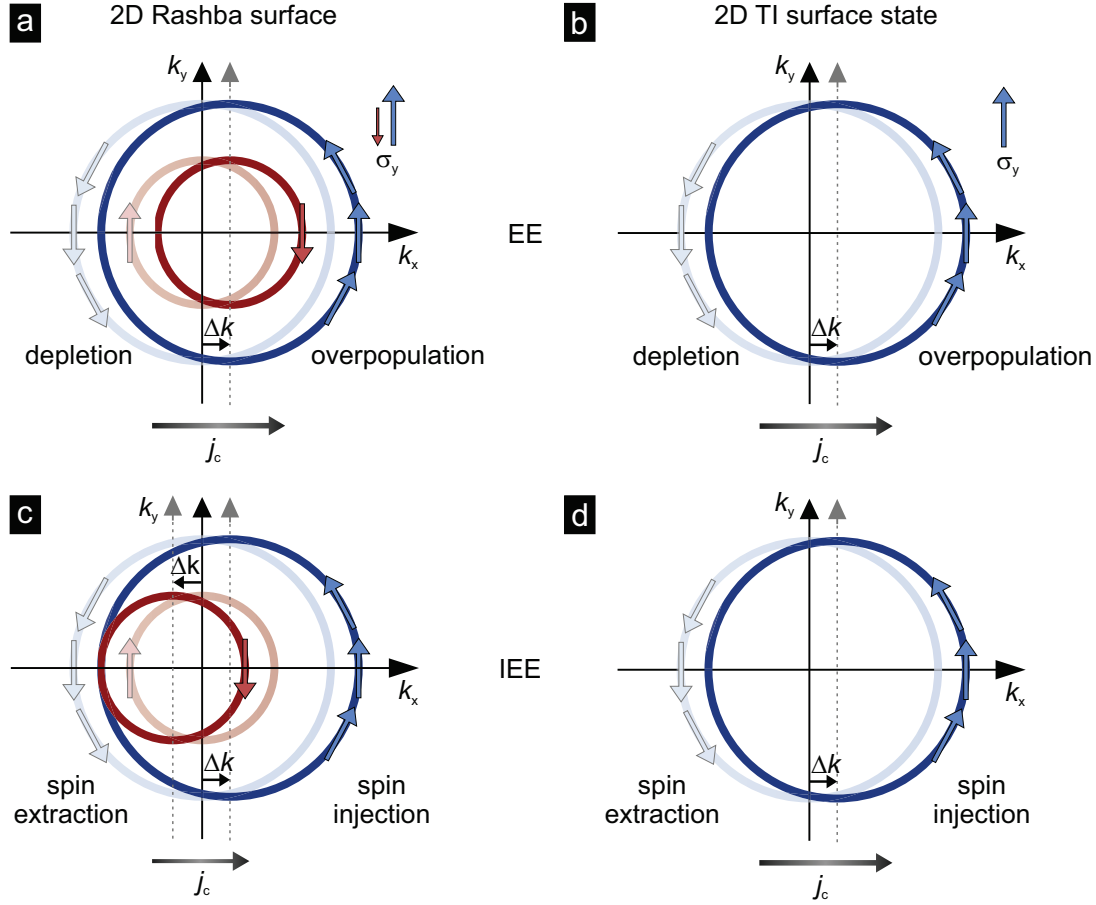


Figure 2.19 – Edelstein effects. **a)** EE in the 2D Rashba surface: A flow of electrons j_c along k_x is associated with a shift δk of the two Fermi contours and gives rise to an overpopulation of spin σ_y along k_y . **b)** EE in the 2D TI surface states: A flow of electrons j_c along k_x is associated with a shift δk of the Fermi contour and gives rise to an extra population of spin σ_y along k_y . **c)** IEE in the 2D Rashba surface: Injection of a spin current density σ_y induces a shift of the two Fermi contours (along the $\pm x$ -direction), and therefore a charge current density j_c . **d)** IEE in the 2D TI surface states: Injection of a spin current density σ_y induces a shift of the Fermi contour (along the x -direction), and accordingly a charge current density j_c .

equilibrium spin accumulation. This means that if a net spin polarization is injected into a Rashba or a TI material, it would drive a detectable electric current (**Fig. 2.19c,d**). This spin-charge conversion process directly relates the charge and spin densities to each other, via $j_c^{2D} = \alpha_{\text{IEE}} j_s^{3D}$, where α_{IEE} is the IEE length relating the 2D current density in units of area to a 3D spin density in units of volume [138] [139]. For a TI system, $\alpha_{\text{IEE}} = \nu_F \tau$, while for a Rashba system, $\alpha_{\text{IEE}} = \frac{\alpha_R \tau}{\hbar}$.

The IEE has been observed experimentally for the elemental TI α -Sn, where spin-charge conversion is achieved by ferromagnetic resonant (FMR) spin-pumping in a Sn-Ag-Fe-Au

heterostructure [122], and also by tunneling spin injection into Bi_2Se_3 [93].

2.3.5 Graphene in spintronics

Graphene-based electronics has been intensely developed since the discovery of the 2D material in 2004 [13] [140]. Graphene's dimensionality, high mobility, and charge carrier concentration tunability render it a suitable component for various electronic devices. These properties make graphene very attractive for spintronic applications as well. Spin injection into graphene has been demonstrated by numerous experiments [141] [111] [142] [143] [144] [145], along with long spin diffusion lengths [146] and long spin lifetimes [147] [148], also at room temperature [149] [150]. Spin transport has been studied in lateral spin valve structures with FM electrodes as spin injectors and detectors, while the graphene strip serves as a transport channel for the spin current. The spin signals are greatly enhanced by incorporating a tunnel barrier at the FM contacts, which increases the spin injection efficiency [108] [110]. Spin injection with transparent contacts, which are strongly coupled to the graphene channel has lower efficiency due to the conductivity mismatch problem and contact-induced relaxation processes, such as interfacial spin scattering or inhomogeneous spin injection and dephasing [151]. Apart from the contact influence, further sources of spin relaxation are defects and impurities, which lead to a greatly decreased experimental values of the spin lifetime on the order of hundreds of picoseconds to few nanoseconds, as compared to the theoretical prediction on the order of a microsecond. The origin of spin relaxation in graphene is still a subject of ongoing research, where the role of contacts is still to be investigated in more detail, including studying the spin life time dependence on contact separation and the presence of spin relaxation anisotropy. Unambiguous proof for spin injection in graphene is the detection of the Hanle effect [152] [148] [144].

Graphene-based spintronic devices with improved performance have been realized based on large-area high-mobility graphene [153], hBN-encapsulated graphene offering the advantage of clean interfaces [154] [145] [155], and suspended graphene where the substrate influence is eliminated [156]. These devices exhibit larger spin diffusion lengths on the order of several microns and longer spin lifetimes on the order of nanoseconds. Spin injection and detection in graphene have also been achieved via spin pumping [157] and non-linear spin detection without FM electrodes [158], respectively.

Owing to the fact that graphene is made up of light carbon atoms and the negligible coupling between π and σ electrons at the Fermi level, it possesses only weak SO coupling on the

order of a few μeV , which derives from π electron hopping between neighboring carbon atoms. Attempts to enhance graphene's intrinsically small SO interaction aim at realizing the quantum spin Hall phase or utilizing the spin Hall effect. One approach towards SO coupling enhancement is to weakly hydrogenate or fluorinate graphene [159]. Alternatively, the proximity of another layered material with strong SO coupling, such as transition metal dichalcogenides, has been shown to enhance the SOC in graphene [160]. Moreover, the decoration of graphene with heavy adatoms has been proposed to enhance the intrinsic-like SO coupling, whereupon a band gap is opened and graphene enters a QSHI regime featuring gapless edge states [161]. Alternatively, a Rashba-like SO coupling could be induced, which in combination with an exchange field might give rise to the quantum anomalous Hall effect (QAHE) [162] [163].

2.3.6 Topological insulators in spintronics

As opposed to graphene, whose weak SO coupling turns it into a very efficient "spin conserver", the strong SO coupling in TIs makes them relevant as "spin generators". In total, there are three spintronics-relevant distinctions between graphene and TIs. Comparing the two Dirac cones, it is clear that in a TI each momentum is associated with a single conduction and valence band surface state, whereas in graphene, there are four distinct states, associated with spin and valley degrees of freedom. Furthermore, the Fermi energy in graphene is effectively tunable via a gate field, in contrast to most TI materials, which exhibit a large bulk conductivity due to doping effects. Finally, in graphene momentum couples to the pseudo-spin, whereas TIs exhibit strong spin-momentum locking, underlining their potential as spin generators. The SO coupling in the surface states of a 3D TI gives rise to a SO field, which is larger than the elastic spin scattering rate, such that the spin-relaxation time is comparable to the transport scattering time, which is less than a nanosecond [20].

Besides the spin-momentum locking in TIs, which can give rise to current-induced spin polarization, the strong SO coupling can be utilized in order to electrically generate spin-polarization via the spin Hall effect. The magnitude of the SHE is determined by the diffusive transport in the 2D surface states. [164] [165] [166]. A larger SHE signal is expected when the spin current generated by the TI can flow into a low SO coupling material via the proximity effect.

In the past couple of years, TIs have been actively investigated as components of spintronic devices. Current-induced spin polarization has been experimentally shown in Bi_2Se_3 [87] in

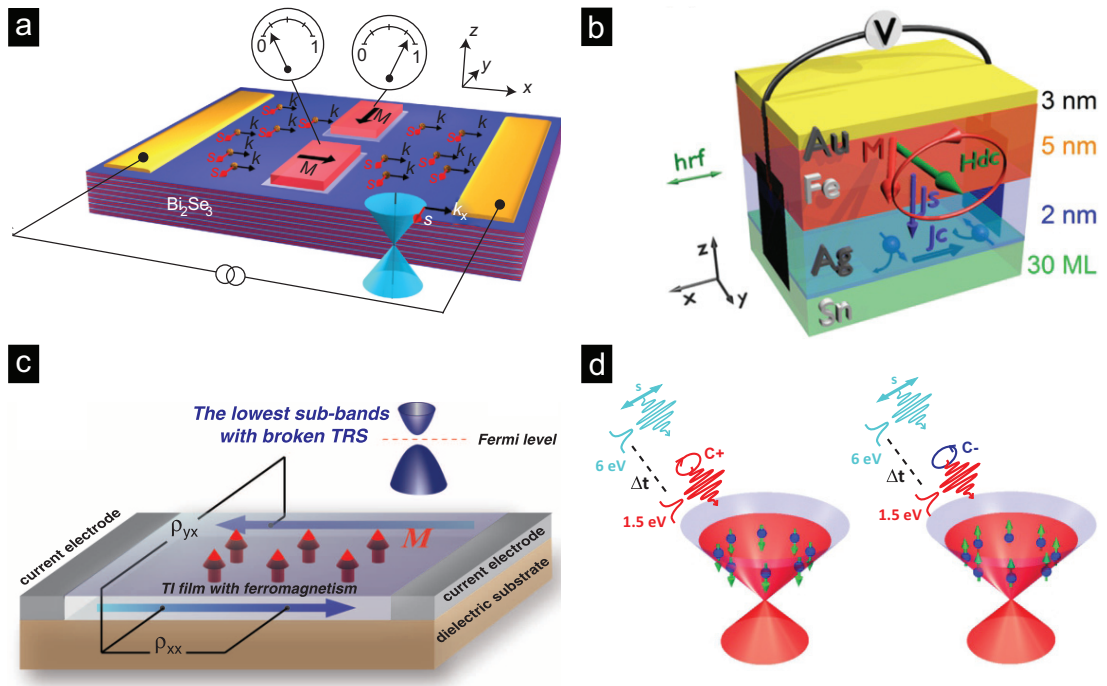


Figure 2.20 – TIs in spintronics. **a)** Electrically-induced spin polarization in the surface states of Bi_2Se_3 (adapted from [87]). **b)** Room temperature spin-charge conversion via FMR spin pumping in $\alpha\text{-Sn}$ (adapted from [122]). **c)** QAHE measured in Cr-doped $(\text{BiSb})_2\text{Te}_3$ (adapted from [167]). **d)** Ultrafast laser pulse switching of spin orientation in the surface states of Sb_2Te_3 (adapted from [168])

2014 (**Fig. 2.20a**). This has been followed by further TI materials [89] [90] and the detection of spin signals persisting up to room temperature [92]. In these experiments, lateral spin valve devices are used, wherein a TI material is contacted by normal and ferromagnetic electrodes. Owing to spin-momentum coupling of the surface states, no ferromagnetic injector is needed. Instead, current is applied between two normal metal electrodes and the voltage drop arising from spin-polarized current is detected as a function of the magnetization direction of a single ferromagnetic detector.

By utilizing the intrinsic SO coupling in TIs, efficient spin-charge conversion has been demonstrated in $\alpha\text{-Sn}$ as an elemental TI [122] (**Fig. 2.20b**). A net spin polarization is injected into the TI via FMR spin pumping and is converted via the IEE into 2D charge current.

The QAHE had been predicted to exist in magnetically doped TIs and later experimentally observed in Cr-doped $(\text{BiSb})_2\text{Te}_3$ [167] (**Fig. 2.20c**). The prospect to develop low power consumption electronics has inspired further investigations of magnetic TIs aiming at observing the effect at higher temperatures [169].

Recently, control of the spin-polarized surface states has been demonstrated by using fem-

Chapter 2. Theory of electronic and spin transport in topological insulators

to second laser pulses in order to achieve ultrafast optical orientation of the spins [168] (Fig. 2.20d).

3 Experimental techniques

3.1 Chemical vapor deposition

For the synthesis of topological insulator compounds and heterostructures including them, a chemical vapor deposition (CVD) furnace has been set up and optimized to achieve different growth morphologies (**Fig. 3.1**). The CVD-grown TI compounds explored in this thesis belong to the family of layered metal chalcogenides, like Bi_2Se_3 , Bi_2Te_3 , and Sb_2Te_3 , where quintuple layers are covalently bonded and weakly held together by van der Waals forces. These compounds have been successfully synthesized in a vapor-solid (VS) process as single-crystalline platelets, ribbons, and nanowires.

In a VS process, ultra-pure crystal powder sources were placed in the hot zone of a quartz tube furnace and heated up to their sublimation temperature. Pure Argon gas (6N) carried the evaporated materials downstream towards the growth substrates, which were placed in the colder region of the furnace, with the temperature gradient being used as an important growth parameter. The transport direction was governed by the temperatures of the sources and the deposition substrates and in the case of endothermic reactions, the source vapor was transferred from the hotter to the colder region. This direction was determined by the sign of the reaction enthalpy [170]. The pressure in the furnace was kept constant by the Argon flow rate and the pumping rate. As the evaporated material reached the colder substrates, it nucleated there to form high-quality single crystals with various morphologies. By comparison, a vapor-liquid-solid (VLS) process involves a catalytic metal, which is deposited as a thin layer onto the growth substrates and forms nanodroplets as the substrates are heated up. The droplets act as seeds for the growth of nanowires or nanoribbons.

A primary goal in the synthesis of TI compounds is the proper stoichiometry of the crystals,

Chapter 3. Experimental techniques

which ensures the topological properties. The VS growth of Bi_2Se_3 , for example, is based on decomposition sublimation, involving stoichiometric species of BiSe and Se_2 in the gas phase which crystallize as Bi_2Se_3 onto the colder substrates in a congruent manner. The accessible growth morphologies depend strongly on a set of growth parameters, as outlined in the following.

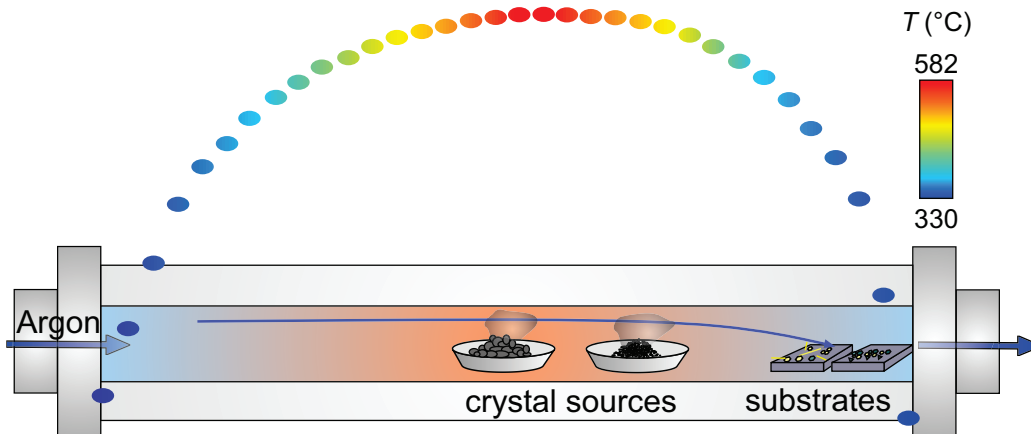


Figure 3.1 – Chemical vapor deposition. Schematic diagram of the CVD furnace setup illustrating the VS growth process. The temperature profile (colored dots) is obtained for $T = 582\text{ °C}$ and $p = 80\text{ mbar}$ and shows the temperature gradient between the source and substrate positions.

Temperature of source and substrates The source temperature determines the sublimation rate of the crystal source, while the temperature of the growth substrates influences the morphology of the deposited material.

Carrier gas flow rate and pressure The amount of transported vapor material is a function of carrier gas flow and the pressure in the quartz tube. For high pressures, the gas flows in diffusive manner, whereas at lower pressures, its flow is laminar. The amount of transported material depends on the partial pressure gradient.

Heating rate The optimal heating rates for the VS growth have been experimentally optimized, such that the heating from room to growth temperature takes place in three steps, namely 25 °C/min for $\text{RT} \rightarrow 100\text{ °C}$; 80 °C/min for $100\text{ °C} \rightarrow 400\text{ °C}$; 25 °C/min for $400\text{ °C} \rightarrow 582\text{ °C}$. Finer tuning of the growth in terms of flake density and thicknesses has been achieved through variation of the third ramp.

Growth time The thickness and lateral dimensions of the grown TI platelets/ribbons are also a function of the growth time. Typical for the used setup is the longer growth time required for nanowires and ribbons, as compared to nanoplatelets.

Type of growth substrate Although VS growth of TI compounds has been reported on amorphous substrates, the quality of single crystals can be improved by the choice of an appropriate substrate. Ideally, its lattice parameter should be close to that of the material to be grown, in order to minimize the lattice mismatch. Epitaxial growth has been achieved on graphene, hexagonal boron nitride (hBN), and mica. For the electrical contacting of single TI platelets, ribbons, and nanowires, Si substrates coated by 300 nm SiO₂ are used. The structures were mechanically transferred from the growth substrate to marker substrates for further device fabrication.

3.2 Atomic force microscopy

In order to investigate the topography of thin film surfaces, atomic force microscopy (AFM) is often employed. In a typical AFM experimental setup, a cantilever is oscillated slightly below its resonant frequency by a piezo-crystal and raster-scanned in close proximity to the sample surface. In this process, a feedback loop maintains a constant oscillation amplitude, and adjusts the distance between the probe and the surface accordingly. As the cantilever is "tapping" onto the surface, a laser beam is reflected off it and collected by a photodiode, thus providing information on the vertical height of the sample surface (**Fig. 3.2a**). In this manner, a topographical image of the sample surface is obtained in a non-invasive manner. **Fig. 3.2b** illustrates the tip-sample interaction on an atomic scale, as well as the force, which depends on the distance between the two. Depending on the force range, three accessible AFM scanning regimes, namely contact, non-contact, and tapping mode, are defined. Additionally, the cantilever's oscillation amplitude and the phase of the cantilever relative to the drive signal are also recorded, as shown in **Fig. 3.2c**. All AFM images in the present work were taken in tapping mode using a Dimension Icon Scanning Probe Microscope by Bruker.

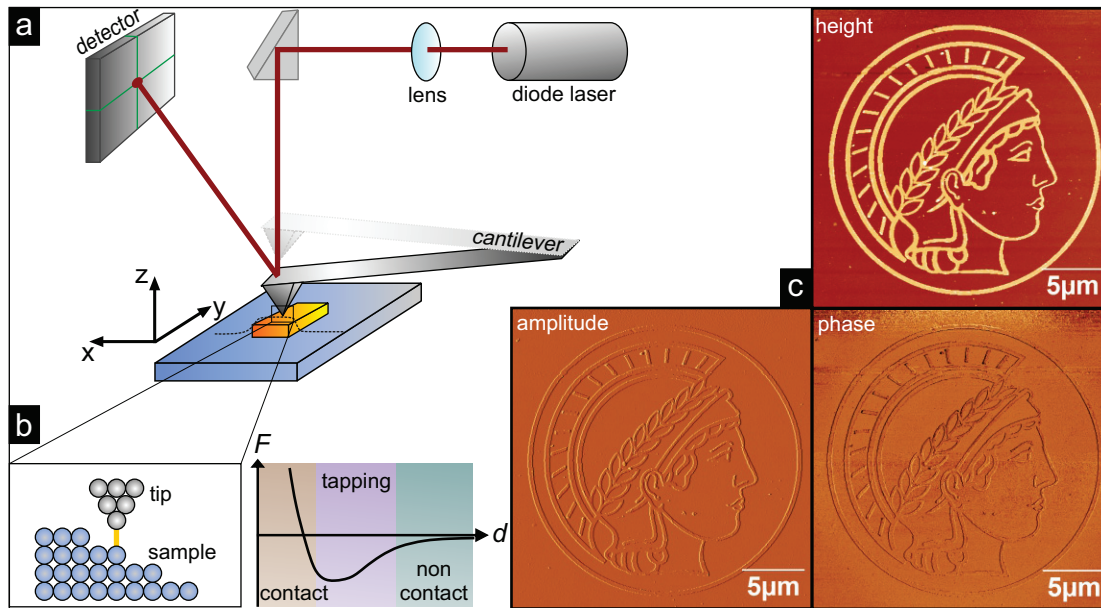


Figure 3.2 – Atomic force microscopy. **a)** Principle of operation. **b)** Zoom into the tip-sample interaction on the atomic level (left) and tip-sample interaction force as a function of tip-surface distance (right). **c)** Height profile corresponding to the change in height required to maintain a constant cantilever amplitude. Amplitude profile reflecting the change in amplitude, i.e., the probe deflection, relative to the amplitude setpoint. Phase image, displaying the cantilever’s phase relative to the driving oscillator, visualizing surface areas with different chemical properties.

3.3 Electron beam lithography and scanning electron microscopy

Electron beam lithography (EBL) is used to define electrical contacts to the investigated nanostructures. It consists of several components, specifically an electron source, optical setup for electron beam guidance, a deflection unit, a pattern generator, and a laser interferometer controlled stage, as shown in **Fig. 3.3a**. With their small mass-to-charge ratio, electrons can be easily focused in a stable beam, which is able to penetrate a thick layer of resist without introducing atomic displacements. An advantage of EBL over optical lithography for small structures is the smaller wavelength on the order of picometers, which is several orders of magnitude smaller than the size of the structures written and thus diffraction artifacts are avoided. In order to do this, the substrate is covered with a positive resist, which is chemically modified by the e-beam in the exposed areas into a predefined pattern and is subsequently removed in a developer solvent. Metallic contacts are thermally evaporated onto this mask and after the lift-off process, the deposited metal sticks to the substrate in the exposed areas, while the rest of the underlying resist is removed.

3.3. Electron beam lithography and scanning electron microscopy

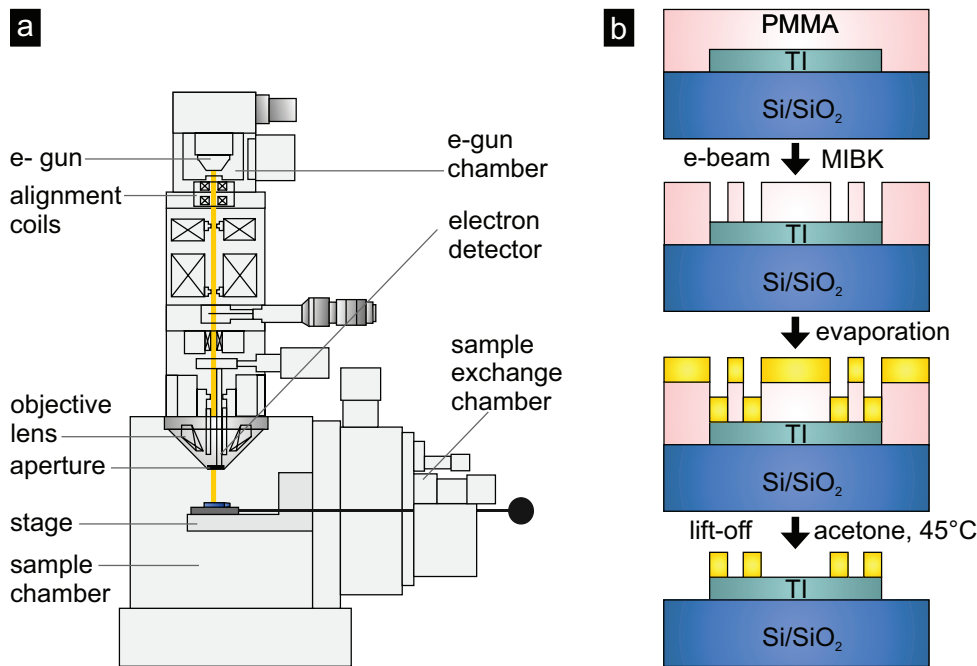


Figure 3.3 – Electron beam lithography. a) E-beam writer. **b)** A generalized step-by-step EBL fabrication process for the electrical contacting of TI structures.

The e-beam writing process is schematically illustrated in **Fig. 3.3b**. In this work, polymethyl methacrylate (PMMA) resist dissolved in chlorobenzene is used. It is available in a wide range of molecular weights (50 K-950 K), which yield a variety of resist thicknesses and a high resolution in the e-beam writing process. PMMA is spin-coated onto the substrate and baked at 160 °C. The polymer chains of the positive resist are fragmented by the e-beam and subsequently removed by a methyl isobutyl ketone (MIBK) - isopropanol (IPA) mixture (1/3, v/v). In order to determine the optimal dose (in units of $\mu\text{C}/\text{cm}^2$), a dose test is performed as a first step of the process optimization. Significant overexposure could lead to crosslinking of the polymer chains, whereby the resist is transformed into a negative one. A further technique involves spin-coating of a bilayer PMMA system where a low molecular PMMA is spin-coated first, followed by a high molecular one on top. The short chains of the lower layer are more sensitive to the e-beam and an undercut is formed, which enables an easier lift-off.

An e-beam writer can also be used as an imaging tool (i.e., a scanning electron microscope, SEM). The beam is scanned across the sample surface and secondary and backscattered electrons are collected by a detector, yielding a surface image with high spatial resolution and excellent topographic contrast. A SEM is used for the investigation of 3D TI thin films and nanostructures investigated within this work.

3.4 Raman spectroscopy

Raman spectroscopy is a powerful, non-invasive technique for material characterization based on inelastic photon scattering. **Fig. 3.4a** schematically depicts a confocal Raman setup. The laser light of a chosen wavelength illuminates the sample locally (beam spot of ~ 500 nm) through a microscope objective and the scattered light is analyzed by a monochromator and collected by a CCD camera. The obtained Raman spectrum consists of a series of peaks, whose position indicates the frequency shift of the scattered photons as a chemical and structural fingerprint of a given material. The position, shape, and relative intensity of the Raman peaks provide valuable information on crystallinity and grain boundaries, the presence of lattice defects, contaminations or doping, strain, and the number of layers. By scanning the sample in the x - y plane, a Raman map is obtained, which is composed of one spectrum per pixel and provides information on the spatial variation of each Raman peak in the form of intensity contrast. Three distinct scattering events usually occur upon laser illumination of the sample, as schematically illustrated in **Fig. 3.4b**. Molecules without Raman-active vibrational modes interact elastically with the photons and no Raman shift is observed in what is called Rayleigh scattering. Molecules in the ground state interact inelastically with the incoming photons, such that the scattered photons are shifted to lower frequency. This gives rise to the so-called Stokes peaks. Molecules in an excited vibrational state lose energy to the photons, such that the photons are frequency shifted in the opposite direction, giving rise to anti-Stokes peaks.

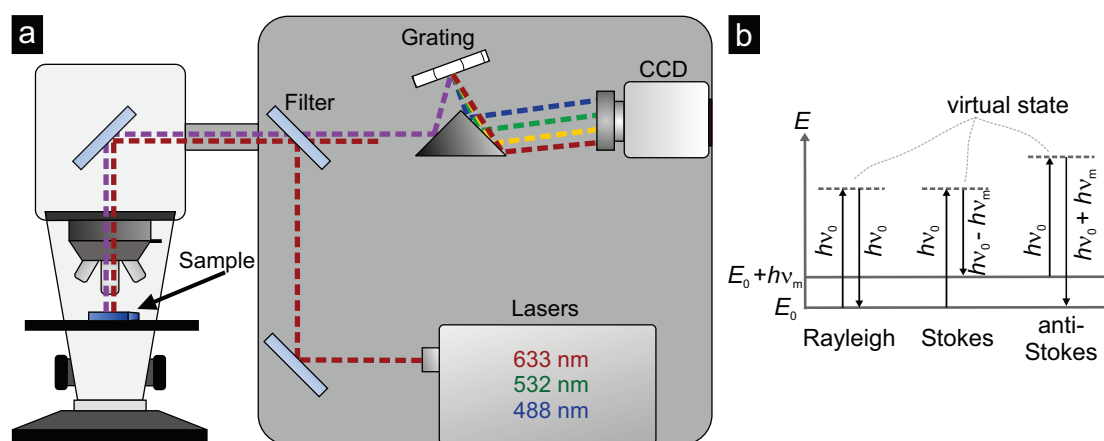


Figure 3.4 – Raman spectroscopy. Schematic diagram of the Raman spectroscopy setup, comprised of an optical microscope, lasers of different wavelengths, a monochromator, and a CCD camera (left). Quantum energy transitions for elastic Rayleigh and inelastic Raman scattering (right).

3.5 Cryogenic transport measurements

The electrical transport measurements presented in Chapter 5 and 7 are performed in an Oxford superconducting magnet system (up to 17 T) and a sorption pumped HelioxVL ^3He rotatable insert (**Fig. 3.5**) with a base temperature of 230 mK. The cryostat has an outer liquid Nitrogen shell and a ^4He inner dewar. In order to cool the sample to 4.2 K, it is mounted to the sample holder and the inner vacuum chamber (IVC) of the insert is pumped down to 8×10^{-6} mbar. The insert is then slowly lowered directly into the ^4He bath, while the He needle valve is continuously flushed with He gas to prevent it from freezing. By pumping on the ^4He reservoir, the temperature decreases further to 1.4 K. In order to reach base temperature, the sorp is heated to 30 K for about 30 min, during which time ^3He gas condenses at the 1 K pot and the sample is further cooled down as all ^3He is liquid in the ^3He pot. As soon as the sorp starts cooling down, the vapor pressure above the liquid ^3He gas is reduced and the sample reaches 230 mK, which remains stable for 2-3 days.

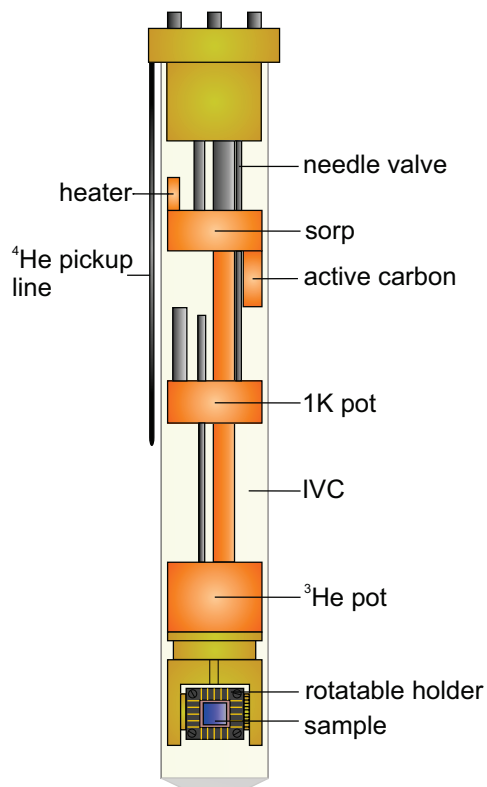


Figure 3.5 – Low-temperature measurement insert. Schematic diagram of the HelioxVL ^3He insert with rotatable chip socket.

Chapter 3. Experimental techniques

The rotatable head of the insert is equipped with 20 metal pins, one of which is electrically connected with the metalized bottom side of the sample and thus back gate voltage can be applied. In order to minimize vibrational noise transmitted along the long cables, a breakout box is mounted directly onto the insert. Low-noise coaxial cables (MCX to BNC) with an additional semiconducting layer between the insulation and the shield provide the electrical connection between the breakout box and the amplifier stage.

The amplifier stage consists of individual modules, which are connected and operated by a bus board transmitting the control and measurement signals from and to the computer. The voltage-source module provides voltages in the ranges 100 mV/V, 10 mV/V, 1 mV/V, and 100 μ V/V over the DC BNC input. This signal can be modulated by an AC-amplitude provided as the AC BNC input, which can additionally be scaled down by a factor of 10 or 100 in order to increase the signal-to-noise ratio. The same holds for the current-source, which provides current in the ranges 1 mA/V, 100 μ A/V, 10 μ A/V, 1 μ A/V, 100 nA/V und 10 nA/V and can be offset by a DC bias, which is provided by a Keithley 2400 connected to the DC BNC input. A differential amplifier module measures the voltage drop and provides high impedance signal amplification before digitalization with gains in the range of 1-1000. A separate current-meter module measures the signal with the help of a high-resistance, low-noise operational amplifier, which provides the feedback resistance for the set current range. Gate voltage can be applied either with a Keithley 2400 source-meter, or the gate voltage module, supplying ± 100 V with 3 mV resolution.

The electrical transport measurements presented in Chapter 4 and 6 are performed in an Oxford cryostat equipped with a 12 T magnet and a rotatable variable range insert for measurements in the range of 1.3-300 K. The low frequency AC-signal is applied via a 7265 dual phase DSP lock-in amplifier and preamplified using a SRS 560 (Stanford) before digitalization. It can be additionally combined with a Keithley 2400 DC-input via a home-built differential operational amplifier module running on batteries, while the current is monitored by a DLPCA 200 (FEMTO).

All electrical measurements are controlled and recorded via a LabView interface. The important measurement geometries are outlined in the following section.

3.6 Electrical measurement geometries

Two-, three-, and four-terminal resistance Two-terminal resistance is a sum of the device's resistance R_{ch} (channel resistance) and the contact resistance R_{c} , since current and voltage are

applied and measured, respectively, via the same electrode pair, as depicted in **Fig. 3.6a**. For low resistance measurements, where R_{ch} and R_{c} are comparable, this introduces a significant source of error. This problem is avoided by performing the measurements in a four-terminal configuration (**Fig. 3.6b**), in which current is applied via the outer electrode pair and voltage is measured with the inner pair, called sense leads. Since no current flows through the sense leads, there is essentially no voltage drop between them and the measured voltage $R_{4\text{T}}$ is equivalent to the voltage drop across R_{ch} .

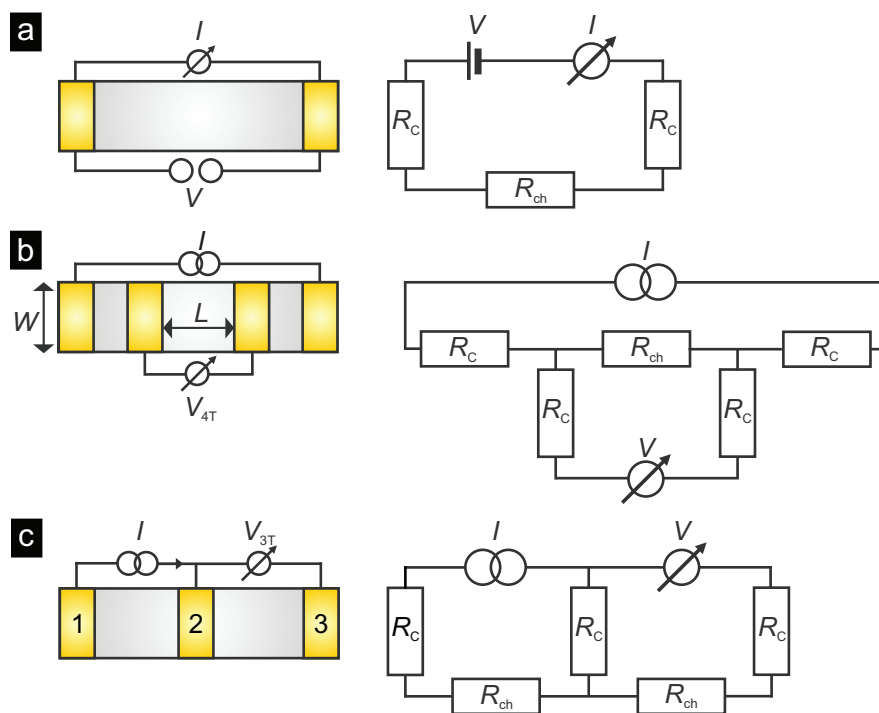


Figure 3.6 – Electrical measurement geometries. **a)** Two-terminal configuration, in which the measured resistance is a sum of the channel and the contact resistance. **b)** Four-terminal configuration, in which the measured resistance corresponds to the channel resistance. **c)** Three-terminal resistance, in which the contact resistance of the middle contact is determined.

The three-terminal resistance measurement is usually employed to characterize the channel-contact interface, for instance in the case of tunneling contacts. As shown in **Fig. 3.6c**, in order to characterize contact 2, current is applied between electrodes 1 and 2, while the voltage drop is measured between electrodes 2 and 3. The measured resistance $R_{3\text{T}}$ is the sum of the contact resistance R_{c} and the metal leads' resistance. The latter is usually on the order of several tens to hundreds of Ohms and can be neglected, such that $R_{3\text{T}} = R_{\text{c}}$.

Magnetotransport geometries Electrical measurements under external magnetic field are performed for characterizing new materials in terms of charge carrier density, doping level, mobility, as well as magnetoresistance effects. The most common device configurations employed, depending on the dimensionality and the geometry of the sample, are the Hall bar and van der Pauw geometry. A Hall bar offers the advantage of recording the longitudinal and the transversal magnetoresistance simultaneously in a single measurement when applying current to the source and drain leads (**Fig. 3.7a**). The longitudinal and the transverse tensor components of the resistivity are $\rho_{xx} = \frac{V_{xx} W}{I_x L}$ and $\rho_{xy} = \frac{V_{xy}}{I_{xx}}$, respectively, where V_{xy} is the Hall voltage.

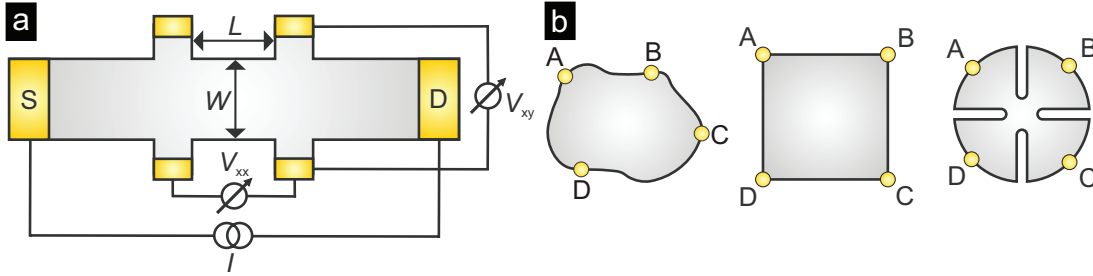


Figure 3.7 – Hall bar and van der Pauw transport measurement geometries. a) Hall bar device. b) Different geometries of the van der Pauw method.

In the case of a sample with an arbitrary shape (as often encountered for mechanically cleaved flakes or CVD-grown platelets), the electrical contacts are arranged in a van der Pauw configuration. In order to determine the sheet and Hall resistance (**Fig. 3.7b**) two sets of measurements are required to account for geometrical errors and possible material anisotropies. The sheet resistance is $R_s = \frac{\rho_{xx}}{d}$, where d is the sample's thickness and the conductivity σ_{xx} is calculated numerically by solving the equation

$$e^{-\pi R_{AB,DC} \sigma_{xx}} + e^{-\pi R_{BC,AD} \sigma_{xx}} = 1. \quad (3.1)$$

The Hall resistance is measured by applying an external magnetic field perpendicular to the sample plane, which is again performed in two contact configurations: $R_{AC,BD}$ and $R_{BD,CA}$. The Hall resistivity can be calculated from the equation

$$\rho_{xy} = \frac{R_{AC,BD}(B) - R_{AC,BD}(0) + R_{BD,CA}(B) - R_{BD,CA}(0)}{2}. \quad (3.2)$$

The four-terminal geometry (**Fig. 3.6c**) yields only the longitudinal resistance, which is multiplied by the width-to-length ratio of the channel between the sense leads in order to derive

the sheet resistance of the material.

Spin measurement geometries All spin measurements are performed in a constant current mode, provided either by the constant current source of the amplification box, or by using a voltage divider, with the device connected in series with a much larger resistance (at least 2 orders of magnitude). In this manner, small changes in the measured voltage can be detected, which comprise the spin signal.

To probe the spin transport in the measured devices, a lateral spin valve geometry is employed. Here, one distinguishes between local and non-local configurations, as depicted in **Fig. 2.13**. In the local one, charge and spin current coexist and hence effects such as non-uniform spin injection or stray magnetic fields arising from the ferromagnetic contacts can give rise to in-plane magnetoresistance and Hall effects, which are co-linear with the spin signal. In the non-local geometry, the detector electrodes are placed outside of the electrical current path. Thus, only diffusing spins propagate between injector and detector and the measured voltage drop originates from the spin current only. When one-and-the-same electrode is used as both injector and detector in a non-local, three-terminal measurement (similar to the one used for determining contact resistance in **Fig. 3.6c**), the spin accumulation underneath is effectively probed.

3.7 TI device fabrication

In the following, details of the fabrication steps are described, which are of utmost importance for obtaining reproducible electrical contacts on TIs.

(i) CVD-grown TI structures are mechanically transferred onto Si/SiO₂ substrates, which are pretreated with oxygen plasma (100 W, 0.3 mTorr, 10 min) and heated up to 130 °C in order to obtain a clean surface and improve the adhesion of the TI structures.

(ii) For the EBL process, a double layer of PMMA resist is spin-coated onto the substrate (200 K, 3.5% followed by 950 K, 2.5%), in order to create an undercut while retaining high resolution and stability against argon or oxygen plasma treatment. The substrate is baked at 160 °C after each spin-coating step. The EBL process has been developed to ensure reproducibility for all fabricated samples. The positive PMMA resist is irradiated with the e-beam through a 10 μm aperture at 20 kV acceleration voltage. A larger aperture of 120 μm is used for

Chapter 3. Experimental techniques

large structures, such as large leads and bonding pads. The exposed sample is subsequently developed in MIBK and IPA in accordance to the thickness of the PMMA layers.

(iii) Treatment of the contact area prior to metal evaporation has proven crucial for obtaining Ohmic contacts. Several methods have been tested, which have led to varying degree of reproducibility. Originally, the contact area has been treated by dipping the substrate in a solution of 36% HCl for a couple of minutes or by exposing it to Argon plasma (200 W, 0.3 mTorr) for 50 sec. In both cases, the sample is glued to a sample holder and transferred quickly to the evaporation chamber after the pretreatment. In this case, contact resistances on the order of 1-20 k Ω have been obtained. Later on, an Argon milling process has been developed followed by metal evaporation in-situ without breaking the vacuum in a new evaporation chamber with a low base pressure of 3×10^{-8} mbar (**Fig. 3.8**). This protocol has immensely increased the reproducibility of the electrical contacts and contact resistances within 1 k Ω have been achieved, as well as a certain degree of contact resistance tunability by exposing the contact area to O₂ atmosphere in-situ after the Argon milling step and prior to the metal evaporation.

(iv) For the spin valve devices, a reliable and reproducible fabrication of ferromagnetic electrodes is crucial. Their quality and properties are strongly influenced by the evaporation pressure in the vacuum chamber, specifically the presence of cross-contaminations and adsorbed water and oxygen. In order to ensure the cleanest possible environment, Titanium can be evaporated against the shutter in order to trap water and oxygen released while the sample stage is heated up to 70 °C. After evaporation of the ferromagnetic contacts (e.g., Co) at the lowest possible pressure of 6×10^{-8} mbar, they are capped by 10 nm of Au in order to prevent their oxidation under ambient atmosphere.

(v) For the graphene/TI heterostructure devices, the graphene film is patterned into a laterally narrow channel by means of reactive ion etching (RIE), which requires an additional EBL step. For etching, the sample is exposed to a directed Argon/Oxygen plasma (Ar flow of 100 sccm, O₂ flow of 11 sccm, power of 48 W, and process pressure of 0.05 mbar) in three 5 second cycles, while allowing the substrate to cool down for 15 min after each cycle.

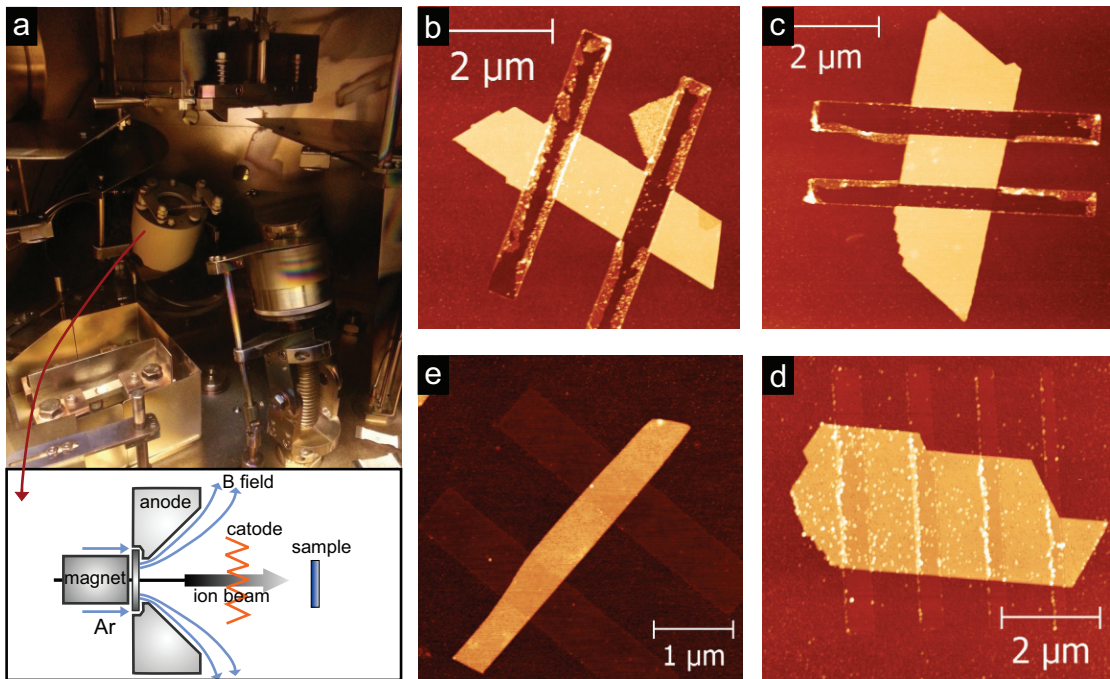


Figure 3.8 – In situ contact preparation. a) Evaporation vacuum chamber equipped with thermal evaporation sources and Argon ion source. The sample is mounted onto the angular piece attached to the sample holder, whose temperature and rotation can be controlled. At the bottom, a schematic diagram of the ion source and its principle of operation is shown. b-d) AFM images for the optimization of an Argon milling process for *in situ* contact pretreatment prior to metal evaporation with varying parameters – $V = 170\text{ V}$, $I = 1.5\text{ A}$ (b); $V = 150\text{ V}$, $I = 1\text{ A}$ (c); $V = 100\text{ V}$, $I = 0.5\text{ A}$ (d); $V = 80\text{ V}$, $I = 0.4\text{ A}$ (e).

4 Electronic transport in single-component TI devices

Complementary to ARPES and spin-resolved ARPES, the electronic properties of 3D TIs need to be evaluated by electrical transport experiments. So far, this task has proven challenging, due to imperfections in real TI materials that hinder the observation of surface state related phenomena in the presence of interfering bulk state contributions. Since Bi-based chalcogenides have been identified as 3D TIs, more complex TI materials have been predicted and it has been subsequently shown that their Dirac cone properties can be tuned via chemical doping and improved synthesis methods. Currently available 3D TIs offer a rich experimental platform for fundamental science and as new methods are developed to access the full potential of their exotic electronic properties, they emerge as promising components of novel spintronic devices.

Within the scope of this work, different Dirac materials have been investigated with the prospect of incorporating at least one of them into a spin valve device. Two CVD furnaces have been setup for the vapor-solid (VS) growth of Sb_2Te_3 and $\text{Bi}_2\text{Te}_2\text{Se}$. These two compounds are p- and n-doped, respectively, which also opens up the possibility to use heteroepitaxy in order to grow vertical or lateral heterostructures and to fabricate TI p-n junctions [171].

Another Dirac material studied here is ZrTe_5 , whose electronic properties have been investigated by magnetotransport experiments. Its layered structure makes it possible to obtain ZrTe_5 monolayers which theory predicts to be a 2D TI with 1D edge states.

Finally, a naturally occurring TI, Alekseite, has been studied, in particular the dependence of its electronic properties on the dimensionality of the exfoliated nanostructures.

4.1 Chemically synthesized ZrTe₅

In contrast to the thoroughly studied 3D TIs, only few examples of 2D TIs have been investigated. 2D TIs are QSH insulators, which host spin-polarized edge states allowing for dissipationless transport when TRS is preserved [18]. Graphene has been used as a model system for the theoretical description of the QSH state, but its small SO coupling on the order of a few μeV does not permit the observation of the QSHE in pristine graphene [21]. So far, the QSH effect has been experimentally observed in HgTe/CdTe [27] and InAs/GaSb [172] [173] quantum wells, which requires considerable fabrication effort and very low temperatures. Materials hosting 1D edge channels should ideally be layered materials with a large band gap and large SO coupling. Recently, a monolayer of ZrTe₅ with a large band gap on the order of 100 meV and a layered crystal structure has been predicted to satisfy these requirements [174]. Theoretical studies of its band structure furthermore suggest that 3D ZrTe₅ crystals lie at the boundary between weak and strong TIs.

4.1.1 Synthesis, initial characterization and device fabrication

ZrTe₅ forms layered orthorhombic crystals in the $Cmcm(D_{2h}^{17})$ point group [175]. ZrTe₃ chains and zig-zag Te chains are linked along the c-direction such that ZrTe₅ planes stack along the b-direction and are weakly bound by van der Waals forces. The 2D sheets of ZrTe₅ are formed in the a-c plane, as apparent from the top view in **Fig. 4.1a**.

The compound has been synthesized by Dr. L. Schoop at the Nanochemistry department of the Max Planck Institute for Solid State Research. Long needle-like crystals of ZrTe₅ from a Zr-Te melt, which is left to cool down to room temperature. They are stored under vacuum in order to prevent oxidation and before exfoliation, the Si/SiO₂ substrates are pretreated by O₂-plasma, as shown in **Fig. 4.1b**. This layered material with weak interlayer bonding can be easily exfoliated into thin flat ribbons, with a height of 8–50 nm and lateral sizes of 50–500 nm, as concluded from AFM topographical measurements (**Fig. 4.1c**).

After mechanical exfoliation of the crystals onto Si/SiO₂ substrates and AFM height characterization, Raman spectroscopy has been performed in order to confirm the stoichiometry of the compound, as shown in **Fig. 4.1d**. All Raman spectra ($\lambda = 532 \text{ nm}$) have been obtained immediately after exfoliation in order to prevent surface oxidation or altering of the surface in ambient conditions. In the experimentally accessible range, eight characteristic Raman peaks of ZrTe₅ are observed. The peaks corresponding to the A_g symmetry group are located at 179 cm^{-1} , 144 cm^{-1} , 117.65 cm^{-1} , 114.2 cm^{-1} , and 39 cm^{-1} . The peaks corresponding to

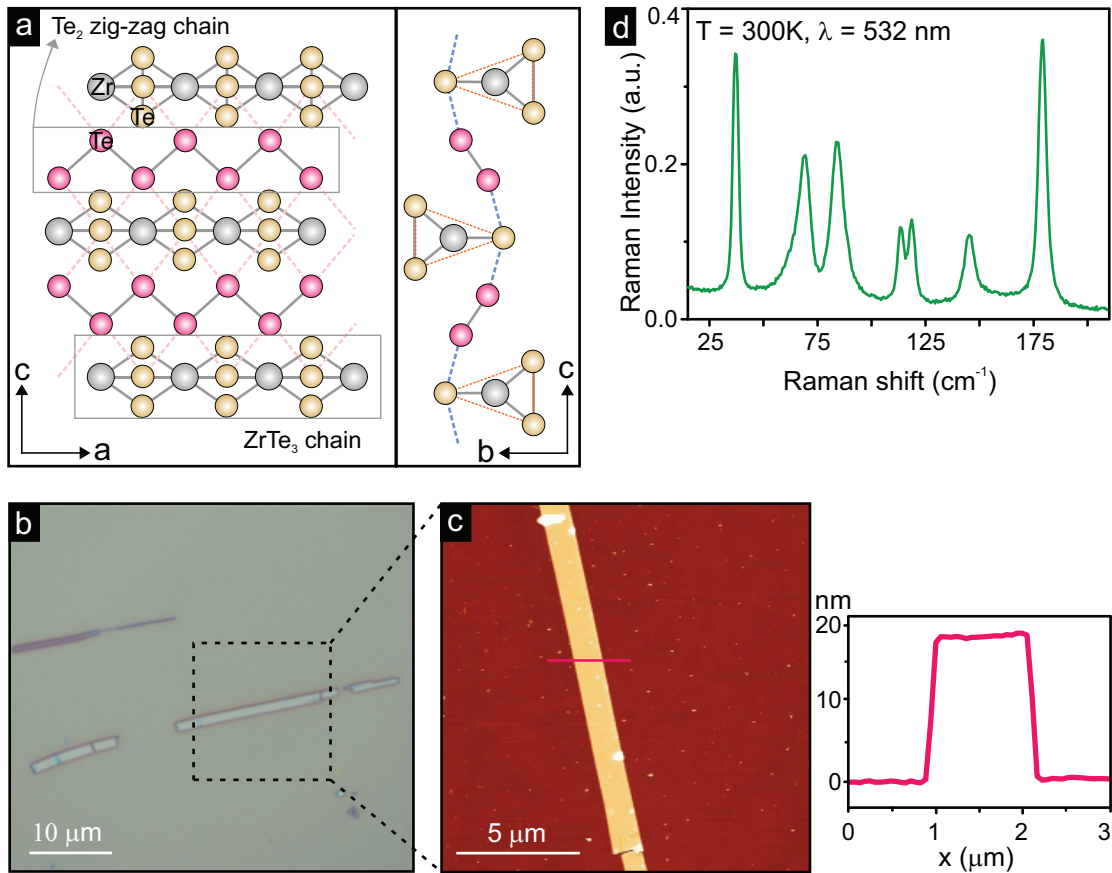


Figure 4.1 – Initial characterization of ZrTe₅ single crystals. **a)** Schematic representation of the projection of the 3D crystal structure onto the a-c plane (top view) and onto the b-c plane (side view), where the b-axis corresponds to the stacking direction. **b)** Optical micrograph of mechanically cleaved ZrTe₅ thin ribbons on SiO₂. **c)** AFM image and height profile of a 19 nm thick ribbon, revealing a smoothly cleaved surface. **d)** Raman spectrum of ZrTe₅ obtained at room temperature with 532 nm laser light. The characteristic peaks confirm the crystal stoichiometry.

the B_{2g} symmetry group are located at 84 cm⁻¹ and 69.2 cm⁻¹, and belong to the shearing mode of the Te(II) pairs and to the zig-zag chains of Te(III) atoms, which are displaced along the c-axis. They are ascribed to the 1D character of the pentatelluride family of compounds. All peak energies are in good agreement with previously published Raman data [176].

For investigating the electronic transport properties of ZrTe₅, devices have been fabricated by electrically contacting thin sheets/ribbons of the exfoliated material. Importantly, the material is found to be temperature sensitive and to lose its structural stability, as apparent from the increased surface roughness and bubble formation above 110 °C. Therefore, the EBL resist is baked at only 90 °C. The electrical contacts consist of thermally evaporated Ti(2 nm)/Au(50 nm) and are arranged in a Hall bar geometry. The contact areas are pre-treated by an Ar-milling

process *in-situ* prior to metal evaporation.

4.1.2 Magnetotransport properties

In order to characterize ZrTe₅, magnetotransport measurements are performed on an exfoliated 19 nm thin ribbon electrically contacted in a Hall bar geometry (see **Fig. 4.2a**). The Hall resistance indicates n-doping of the material at low temperature ($T = 1.3$ K), consistent with previous reports [177]. Moreover, a charge carrier density $n_{3D} = 4.5 \times 10^{18} \text{ cm}^{-3}$ is extracted from the Hall slope. The sheet resistance yields a high mobility $\mu = 3720 \text{ cm}^2/\text{Vs}$.

Two sets of magnetoconductance data are obtained for the device in **Fig. 4.2a**, corresponding to positive and negative back gate voltage. As seen in **Fig. 4.3f**, the gate voltage changes the magnetoconductance characteristic, i.e., for $V_g = +60$ V it is roughly parabolic, while for $V_g = -60$ V, it approaches a linear behavior.

For negative gate voltage, the low-temperature magnetoconductance exhibits a WAL effect at low B-fields, which is studied as a function of tilting angle and temperature. In order to probe the WAL dimensionality, the sample is tilted in magnetic field, such that $\theta = 0^\circ$ corresponds to in-plane magnetic field and $\theta = 90^\circ$ to out-of-plane magnetic field. The WAL peak is most pronounced under normal B-field, and almost disappears for in-plane B-field, as seen in **Fig. 4.2b**. The magnetoconductance plotted as a function of the normal field component in **Fig. 4.2c** reveals that all angle-dependent curves fall closely on top of one another, indicating a 2D character of the WAL effect, i.e., a sizable contribution from the surface states.

The magnetoconductance data in **Fig. 4.2d**, obtained up to ± 12 T, exhibits a linear behavior, in analogy to previous studies on Bi₂Se₃ [178] and Bi₂Te₃ [179], for which it has been attributed to the topological surface states and in some cases could be tuned by the gate voltage [180]. At lower B-fields, pronounced oscillations attributable to universal conductance fluctuations (UCF) have been observed. The low-field magnetoconductance data could be well-fitted by the HLN model for 2D localization (**Eqn. 2.1**). From the fits at different temperatures (**Fig. 4.2e**), a phase coherence length of 238 nm at 1.3 K and alpha factor $\alpha = -0.51$ have been extracted, the latter value pointing toward only one surface channel contributing to the overall conductance (see **Section 2.2.2**). As apparent from **Fig. 4.2f**, the phase coherence length decreases with increasing temperature, which can be ascribed to enhanced electron-phonon and electron-electron interactions [71]. A data fit by a power law yields $L_\phi \propto T^{-0.58}$, which further supports the 2D nature of the WAL in the measured samples.

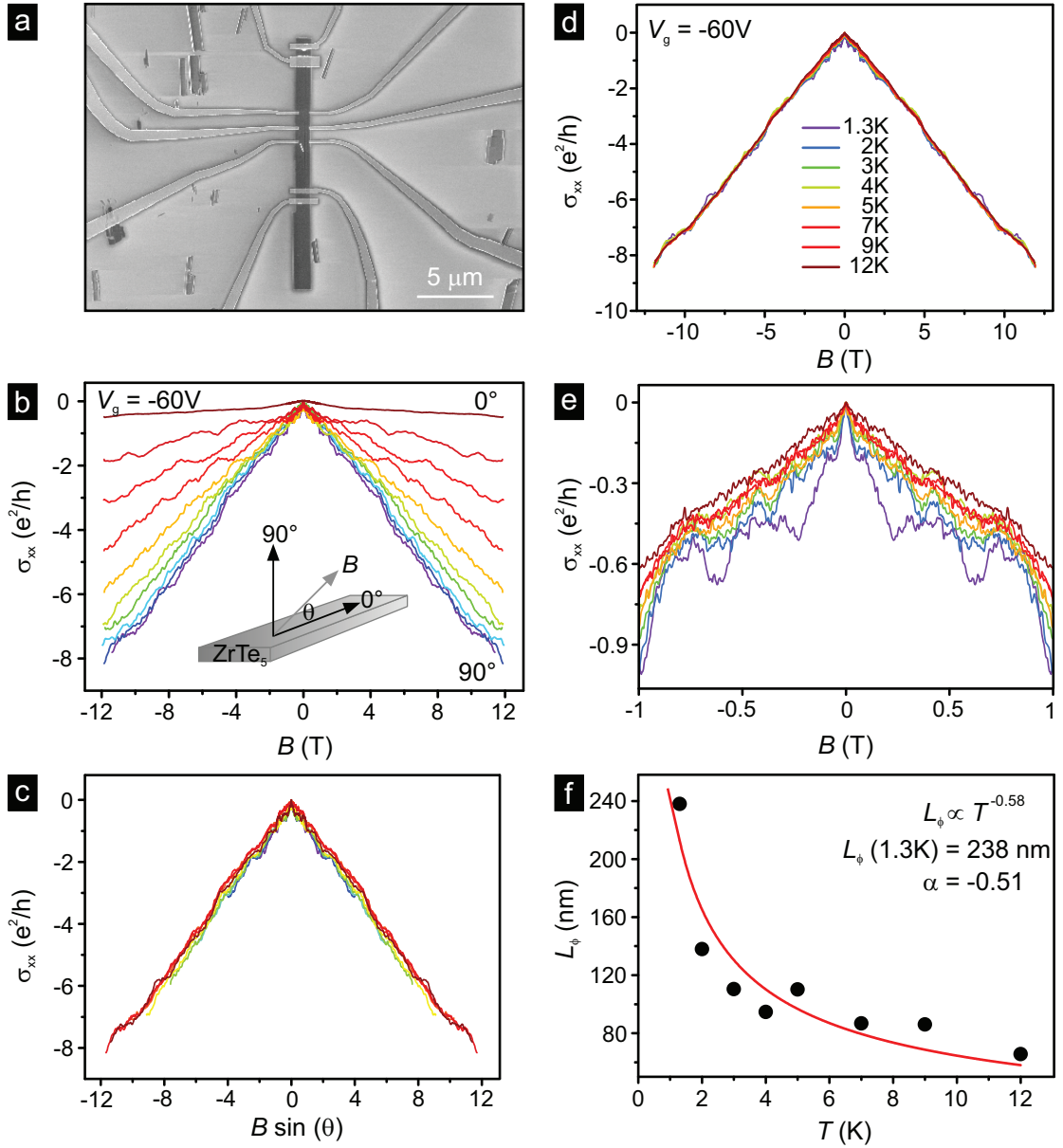


Figure 4.2 – Temperature and angle dependent magnetotransport in ZrTe₅ for negative gate voltage. **a)** SEM image of one of the measured devices, comprised of a 19 nm thin ribbon, contacted in a Hall bar geometry with Ti/Au electrodes. **b)** Angle-dependent magnetoconductance in the range ± 12 T. The inset is a schematic diagram of the tilting angle of the sample. **c)** Overlapping of the angle-dependent curves, which are plotted as a function of the normal field component. **d)** Temperature-dependent magnetoconductance up to $T = 12$ K, which exhibits a nearly linear behavior at $V_g = -60$ V, indicative of surface state contribution. **e)** Pronounced WAL effect at low B-fields, which is fitted by the HLN model for 2D localization. **f)** Phase coherence length extracted from the WAL fits plotted as a function of temperature. The temperature dependence closely follows a power law, yielding $L_\phi = 238$ nm at $T = 1.3$ K and $\alpha = -0.51$.

Chapter 4. Electronic transport in single-component TI devices

The second set of magnetoconductance data was obtained for the same device at $V_g = +60$ V. Here WAL up to $T = 35$ K was recorded and fitted with the HNL model, resulting in a phase coherence length $L_\phi = 279$ nm at $T = 1.3$ K, and an alpha factor $\alpha = -0.48$ (**Fig. 4.3b,c**). Tilting the sample in B-field and plotting the magnetoconductance as a function of the magnetic field component normal to the surface (**Fig. 4.3d,e**) again results in a close overlap for all angles, reflecting a 2D surface state contribution. The quantum oscillations here are observed even at higher fields and can be attributed to overlapping UCFs [71] and SdH oscillations [181].

The magnetotransport study of ZrTe_5 provides a promising perspective along several directions. The relatively large mobility, compared to the other investigated TI materials, might be further enhanced for example by optimizing the exfoliation method and by transferring the material onto an atomically flat substrate, such as hBN. This could enable the observation of well-developed SdH oscillations, whose angular dependence in magnetic field along different crystal axes may provide access to the shape of the Fermi surface and yield further proof for the 2D transport mediated by Dirac fermions [177].

Furthermore, it has been demonstrated that the charge carrier type in ZrTe_5 can be tuned via temperature, changing from n-type at low temperature to p-type at higher temperatures [177]. Thus, the two doping regimes could be further explored by performing temperature-dependent magnetotransport measurements up to room temperature. In such experiments, electrostatic gating of ultra-thin ZrTe_5 sheets could be attempted via a global back gate or locally via a top gate. The film thickness could prove essential, as it has been predicted that a ZrTe_5 monolayer hosts 1D edge states, which may enable observation of the QSHE [174]. Recently, scanning tunneling microscopy experiments have provided evidence for the presence of topological edge states and a large band gap of 80-100 meV in ZrTe_5 [182] [183].

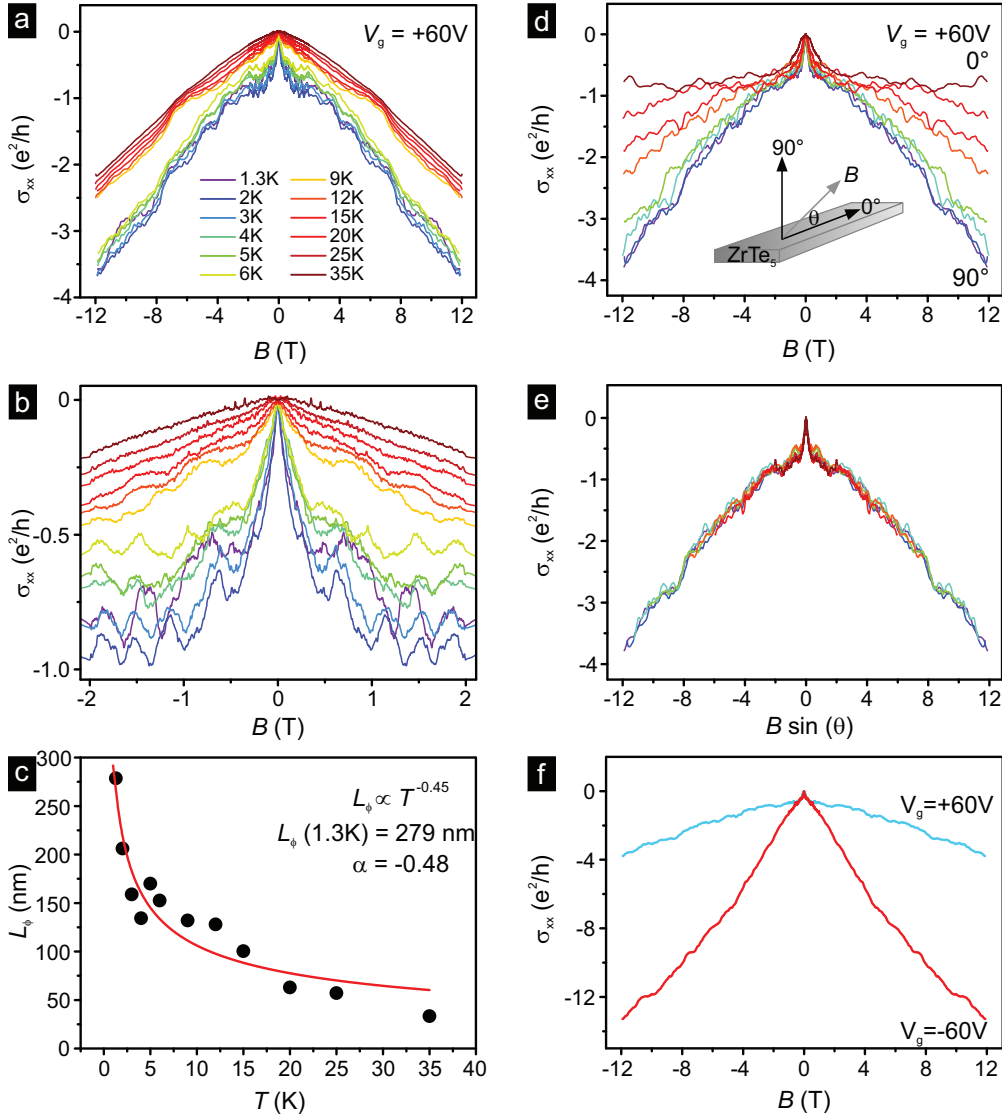


Figure 4.3 – Temperature and angle dependent magnetotransport in ZrTe₅ for positive gate voltage. **a)** Temperature-dependent magnetoconductance up to $T = 35$ K. **b)** Pronounced WAL effect at low fields for the same temperature range, which is fitted by HLN model for 2D localization. **c)** Phase coherence length extracted from the WAL fits plotted as a function of temperature. Its temperature dependence can be well described by a power law, yielding $L_\phi = 279$ nm at $T = 1.3$ K and $\alpha = -0.48$. **d)** Angle-dependent magnetoconductance in the range ± 12 T. The inset is a schematic diagram of the tilting angle of the sample. **e)** Overlapping of the angle-dependent curves, which are plotted as a function of the normal B-field component. **f)** Tuning of the high-field magnetoconductance with gate voltage and transition from parabolic (positive gate) to linear (negative gate) behavior.

4.2 Aleksite as natural topological insulator

In 2013, topological properties have been identified for the first time in a naturally occurring mineral, called Kawazulite [57]. The crystal contains heavy elements, specifically Bi, Te and Se, which give rise to strong SO coupling that imparts a topologically non-trivial band structure. The mineral was characterized by photoemission and magnetotransport measurements in order to investigate its surface state properties and determine whether a naturally occurring TI might offer certain advantages when compared to artificially synthesized materials, such as the presence of less defects in the crystal structure, which would lead to more pronounced surface-related effects and reduced bulk contribution to the conduction. Further candidates are the minerals belonging to the Tetradymite and the Aleksite group. Theoretical studies of the Aleksite family, comprising quaternary minerals with layered structure, predict large band gaps and large spin polarization [184]. Here, the electronic properties of one of these materials are investigated, namely Aleksite with the chemical formula $\text{PbBi}_2\text{Te}_2\text{S}_2$.

4.2.1 Initial characterization and device fabrication

As distinguished from other TI materials investigated, the crystal structure of Aleksite belongs to the $P\bar{3}m1$ space group and contains blocks of seven layers, rather than quintuple ones, that are weakly bonded by van der Waals forces. **Fig. 4.4a** shows the schematic crystal structure of such a seven-layer block, composed of Te–Bi–S–Pb–S–Bi–Te atomic planes. In order to investigate the properties of Aleksite, the microcrystal was mechanically exfoliated onto Si/SiO₂ substrates and the as-obtained thin flakes were examined by AFM. **Fig. 4.4b,c** show the topography and the height profile, respectively, of a 28 nm thick ribbon.

In order to confirm the existence of gapless surface states, ARPES measurements have been performed on a freshly cleaved crystal at 100 K in UHV. In **Fig. 4.4d**, a diagram of the predicted band structure is shown (partially adapted from [184]), together with the experimental band structure, as recorded in the photoemission experiment (**Fig. 4.4e**). The rather weak signal is due to the small sample size, as only tiny micro-crystals of the material were available. A Dirac cone shaped band structure between two bulk bands could be nevertheless identified and a band gap of about 300 meV estimated. Also evident from the experimental ARPES data was the position of the Fermi level within the conduction band.

Atomic resolution of the crystal lattice is provided by scanning tunneling electron microscopy (STEM) measurements. To this end, Aleksite thin flakes are exfoliated and transferred to a STEM carbon grid. The obtained diffraction pattern, shown in **Fig. 4.4f**, signifies a single crys-

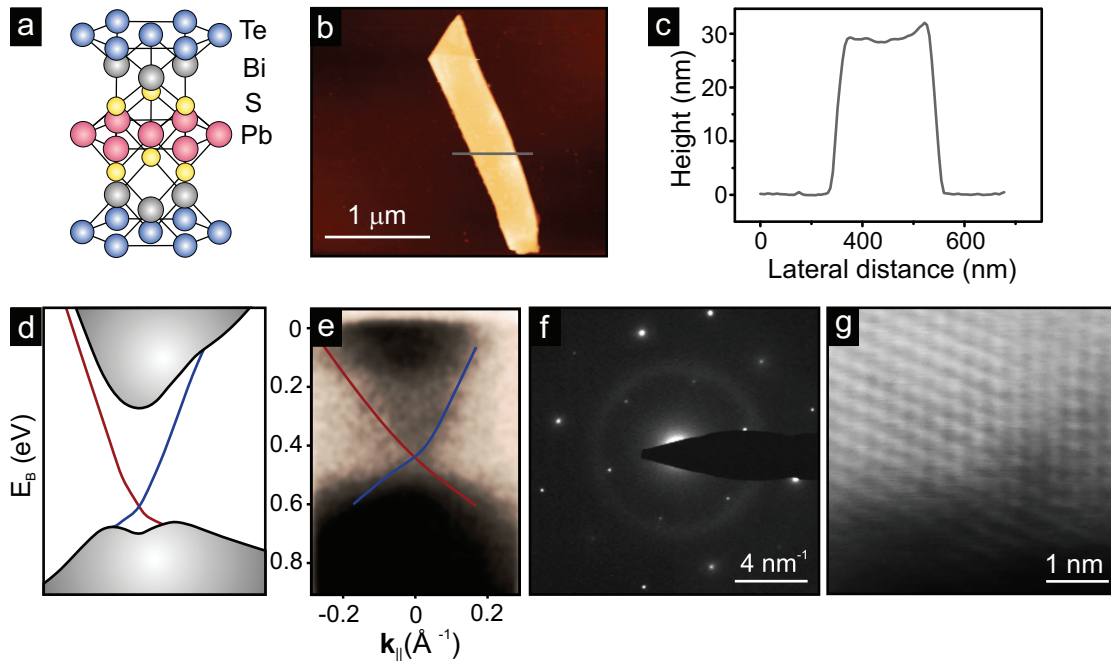


Figure 4.4 – Initial characterization of Aleksite thin crystals. **a)** Schematic depiction of a seven-layer stack composed of Te-Bi-S-Pb atomic planes bonded by weak van der Waals forces. **b)** AFM topography of a mechanically exfoliated 28 nm thin Aleksite flake. **c)** AFM height profile taken along the grey line in panel **b**. **d)** Schematic band structure of Aleksite. **e)** Experimental ARPES data revealing the presence of surface states inside the bulk band gap. **f)** STEM measurement of a cleaved thin Aleksite flake rendering an electron diffraction pattern of a hexagonal crystal structure. **g)** High resolution STEM image of a thin Aleksite flake.

tal with hexagonal symmetry. The orientation-dependent lattice spacings of 1.34, 1.72, 1.83, 2.76, and 3.01 Å were extracted, which agree reasonably well with previously reported values gained from X-ray diffraction experiments [185] and theoretical calculations [184]. **Fig. 4.4g** presents an atomic resolution STEM image of a thin region of an Aleksite flake, revealing a poly-crystalline structure with multiple crystal orientations.

In order to perform magnetotransport measurements on Aleksite, the microcrystal was mechanically cleaved and transferred onto Si/SiO₂ substrates for device fabrication. The structures were electrically contacted with Ti(4 nm)/Au(60 nm) electrodes thermally evaporated after contact area pretreatment with 50 s Argon plasma (as described in **Section 3.7**).

4.2.2 Magnetotransport properties

The exfoliated thin Aleksite films have been electrically contacted in four-terminal or van der Pauw geometry. An averaged Hall mobility on the order of $\mu = 900 \text{ cm}^2/\text{Vs}$ and a carrier

density $n_{3D} = 3.9 \times 10^{19} \text{ cm}^{-3}$ are found at $T = 1.4 \text{ K}$. The sign of the Hall coefficient and the high charge carrier density [62] indicate strong n-doping of the material, consistent with the position of the Fermi level in the ARPES measurements.

The electrical measurements of thin Aleksite flakes reveal a very low channel resistance on the order of several Ohms at low temperature. Such low-Ohmic devices are extremely sensitive and moreover the magnitude of the magnetoresistance effects is very small and hence difficult to detect. In order to increase the overall channel resistance thin ribbons are contacted in a four-terminal geometry with maximized spacing between the voltage probe contacts. Such a device is shown in **Fig. 4.5a**, while the AFM topography of the contacted 19 nm thin and 240 nm wide ribbon is presented in **Fig. 4.5b**. The corrected low-field magnetoconductance $\Delta\sigma_{xx} = \sigma_{xx}(B) - \sigma_{xx}(0)$ exhibits a pronounced WAL effect and is recorded in dependence of temperature for several Aleksite ribbons of different lateral width. The most important observation relates to how well the WAL peak can be fitted with the standard HNL equation for 2D transport. For the ribbons with lateral widths larger than 250 nm, the fit works well, whereas for ribbons less than 250 nm wide, the model is unable to fit the data, as follows from the lack of physical significance of the obtained large values of the alpha factor. Furthermore, the extracted values for the phase coherence length exceed the physical width of those ribbons, further implying that transport of lower dimensionality occurs. Two groups of devices are thus investigated, based on the width threshold $W = 250 \text{ nm}$ in order to confirm a possible dimensional crossover from 2D to 1D transport in Aleksite. For fitting the magnetoconductance in **Fig. 4.5c**, an alternative model for 1D transport is employed, which has been proposed by Altshuler et al. [186]:

$$\Delta\sigma = \frac{e^2}{\sqrt{2\pi\hbar}} \frac{L_n}{W} \left\{ \frac{\text{Ai}(x)}{\text{Ai}'(x)} \left[2 \frac{L_n^2}{L_\phi^2} \right] - \frac{\text{Ai}(x)}{\text{Ai}'(x)} \left[2 \frac{L_n^2}{L_\phi^2} + \frac{2}{3} L_n^2 \left(\frac{eWB}{\hbar} \right)^2 \right] \right\} \quad (4.1)$$

where W is the width of the ribbon, L_n is the Niquist dephasing length, L_ϕ is the phase coherence length, and Ai and Ai' are the Airy function and its first derivative, respectively. From the 1D fits of the WAL peaks, as shown in **Fig. 4.5c**, a phase coherence length $L_\phi = 914 \text{ nm}$ and a Niquist length $L_n = 410 \text{ nm}$ are extracted. They are plotted as a function of temperature in **Fig. 4.5d** and fitted with a power law, which indicates $L_\phi \propto T^{-0.3}$ and $L_n \propto T^{-0.34}$. According to theory, the coherence lengths should scale as $T^{-1/2}$ in a 2D system and as $T^{-1/3}$ in a 1D system [187] [69]. The latter dependence is consistent with the experimental observations for all devices with width below 250 nm.

To further support the 1D nature of the magnetotransport in the narrow Aleksite nanoribbons, the high field magnetoconductance is recorded and after background subtraction, the temper-

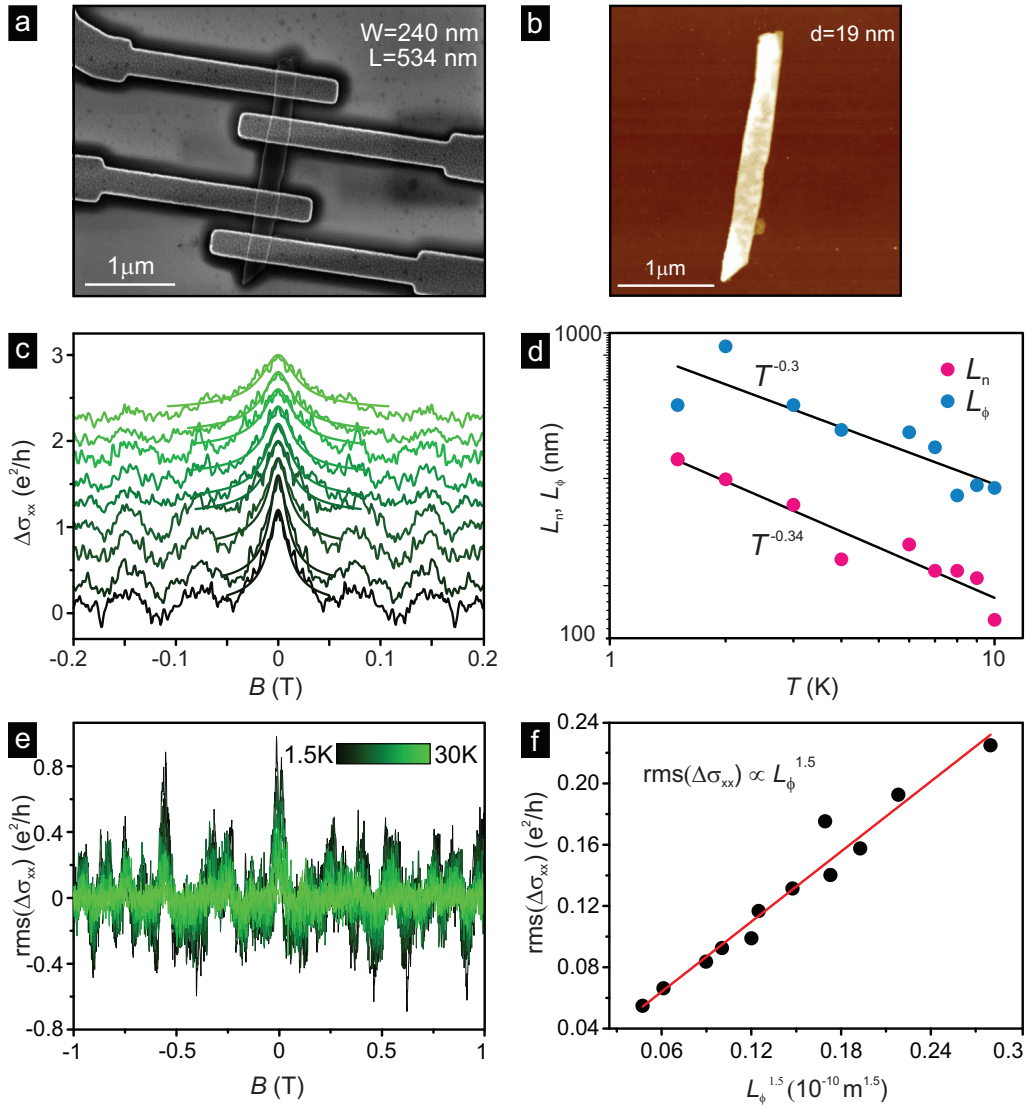


Figure 4.5 – 1D magnetotransport in a thin Aleksite ribbon. **a)** SEM image of a mechanically exfoliated and electrically contacted ribbon. **b)** AFM topography of the same 19 nm thick and 240 nm wide ribbon. **c)** Corrected low-field magnetoconductance fitted by a 1D model for diffusive transport. The curves are offset for clarity. **d)** Temperature dependence of the characteristic scattering lengths, which scale with temperature consistently for transport in a 1D system. **e)** Universal conductance fluctuations (UCFs) in the magnetoconductance after background subtraction plotted for a range of temperatures. The UCF amplitude is seen to decrease with increasing temperature. **f)** Root mean square (rms) of the UCFs as a function of the phase coherence length extracted from the 1D fits of the WAL peaks.

ature dependent amplitude of the universal conductance fluctuations (UCFs) is analyzed, as illustrated in **Fig. 4.5e**. The relationship between the root mean square of the UCFs and the phase coherence length reflects the dimensionality d of the observed effects and is given by

$$\text{rms}(\Delta\sigma_{xx}) \propto L_{\phi}^{(4-d)/2} \quad (4.2)$$

Fig. 4.5f shows this relationship, which can be well fitted linearly ($\text{rms}(\Delta\sigma_{xx}) \propto L_{\phi}^{1.5}$). According to **Eqn. 4.2**, this corresponds to $d = 1$, thus confirming the 1D character of the system.

One of the devices whose lateral width $W = 476$ nm exceeds the threshold is shown in **Fig. 4.6a**. The AFM analysis shows a similar thickness of 18 nm like for the ribbon in **Fig. 4.5**. In the present case, the corrected low-field magnetoconductance $\Delta\sigma_{xx}$ can be well fitted with the HLN model, rendering $L_{\phi} = 493$ nm at $T = 1.4$ K and $\alpha = -1.3$. The latter value points towards the participation of two transport channels. The phase coherence length follows a $T^{-0.44}$ dependence on temperature, confirming the genuine 2D nature of the WAL effect.

The analysis of the UCF oscillations reveals that their amplitude is slightly smaller than the one found for the narrow ribbon devices, and their root mean square scales linearly with the phase coherence length, consistent with 2D transport, as apparent from **Eqn. 4.2**.

In conclusion, the magnetotransport properties of thin Aleksite samples are of a diffusive conductor whose surface state contribution to the conductance is evident from the presence and characteristics of the WAL effect, as well as the pronounced UCFs. Importantly, the nature of the transport changes from 2D to 1D when the physical size of the sample is reduced beneath a certain sample width, in which case coherence lengths well above the sample width are found.

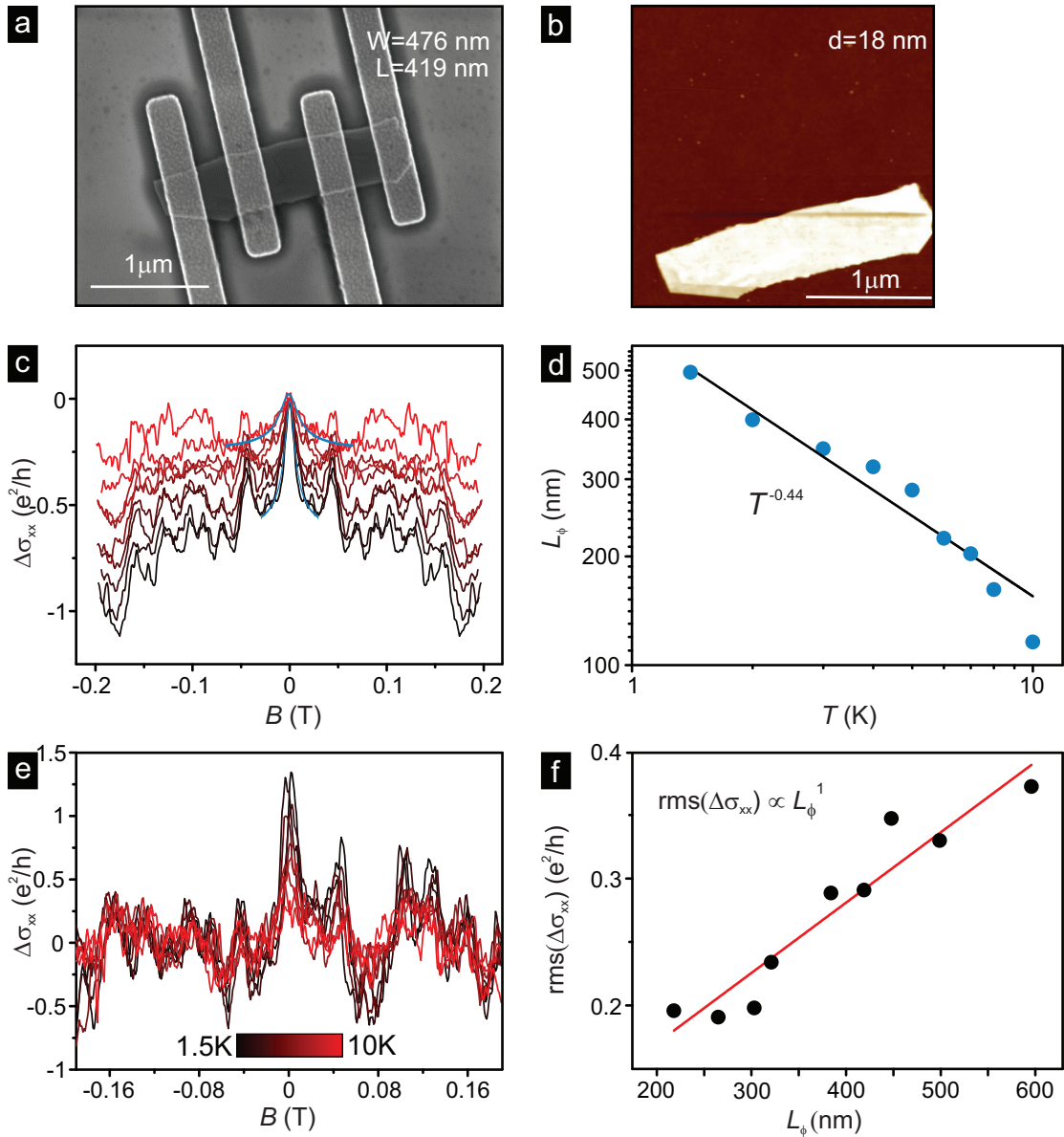


Figure 4.6 – 2D magnetotransport in a wider Aleksite ribbon. **a)** SEM image of a mechanically exfoliated and electrically contacted ribbon, whose lateral width is larger than 250 nm. **b)** AFM topography of the same 18 nm thick and 476 nm wide ribbon. **c)** Corrected low-field magnetoconductance fitted by the HLN model for 2D diffusive transport. **d)** Temperature dependence of the extracted phase coherence length, which scales with temperature consistently for transport in a 2D system. **e)** Universal conductance fluctuations (UCFs) in the magnetoconductance after background subtraction plotted for a range of temperatures. The UCF amplitude decreases with rising temperature. **f)** Root mean square (rms) of the UCFs as a function of the phase coherence length extracted from the HLN fits of the WAL peaks.

4.3 CVD-grown Sb_2Te_3

4.3.1 Van der Waals epitaxial growth

A new two-zone horizontal tube furnace with a 1-inch quartz tube has been set up, which has a stable temperature profile with reproducible heating rates and offers precise control of the substrate temperature. The chalcogenide Sb_2Te_3 is chosen as a starting material in order to establish the initial growth parameters. Its topological surface states were observed in ARPES measurements by Zhang et al. [188] Due to Sb–Te anti-site defects in the rhombohedral crystal structure, the compound is usually strongly p-doped and the E_F crosses the double valence band (Fig. 4.7a). The crystal structure is composed of Te–Sb–Te–Sb–Te quintuple layers (Fig. 4.7b), which are weakly connected by van der Waals forces, such that thin layers of Sb_2Te_3 crystals can be easily cleaved or mechanically transferred from a growth substrate and investigated in transport experiments.

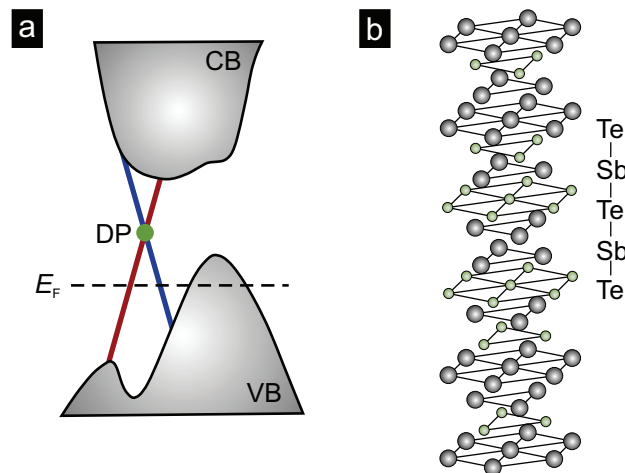


Figure 4.7 – Crystal, band structure, and initial characterization of CVD-grown Sb_2Te_3 . **a)** Electronic band structure of Sb_2Te_3 , where the Fermi energy crosses both the surface states and the bulk valence band, indicating p-doping. **b)** Crystal structure of Sb_2Te_3 illustrating the van der Waals bonded quintuple layers Te-Sb-Te-Sb-Te.

Sb_2Te_3 thin platelets are synthesized by a catalyst-free VS process. Ultra-pure Sb_2Te_3 crystal source (99.999 % purity, Alfa Aesar) is placed in the hot zone of the furnace, while the substrates are located in the colder region downstream. The growth is strongly dependent on the precise temperature control. The best results are achieved for a two-ramp process, in which the source and the growth substrates can be heated separately, namely: RT-300 °C with 40 °/min and 300-550 °C with 50 °/min (source); RT-300 °C with 40 °/min and 300-450 with 20 °/min (substrates)

and a growth time of 30 min. A constant ultra-pure Argon flow carries the evaporated material to the substrates where single crystals form. **Fig. 4.8a,b** shows the representative results of a catalyst-free VS growth of single crystalline thin platelets on SiO_2 (a) and on graphene (b). Typical platelet thicknesses are in the range of 6-100 nm and their lateral sizes reach up to $20\ \mu\text{m}$ on SiO_2 . In order to confirm the stoichiometry, Raman spectra have been acquired. **Fig. 4.8c** shows the spectrum of a representative sub-50 nm thick Sb_2Te_3 platelet excited with 633 nm laser light. It displays the E_g peak at $112\ \text{cm}^{-1}$ and the A_{1g} peak at $165\ \text{cm}^{-1}$, both in accordance with the report by Richter et al. [189].

The X-ray diffractogram in **Fig. 4.8d** of a Sb_2Te_3 film exhibits peaks corresponding to the (001) planes, which is an indication for c-axis oriented growth, in agreement with previous reports [190] [191]. The reflection peaks are indexed based on Sb_2Te_3 with a rhombohedral structure.

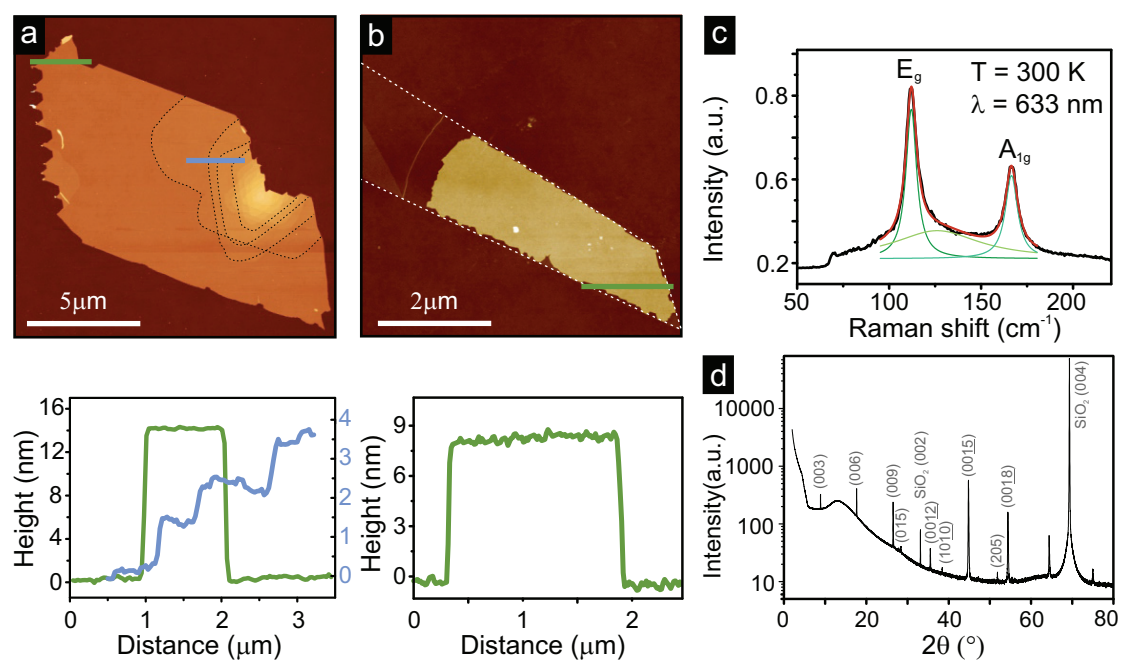


Figure 4.8 – CVD-grown Sb_2Te_3 on different substrates. **a)** AFM image of a 14 nm thick Sb_2Te_3 platelet on SiO_2 . **b)** AFM image of a $6\ \mu\text{m}$ long and 8 nm thick Sb_2Te_3 platelet on a graphene monolayer. The dashed lines indicate the edges of the Sb_2Te_3 epitaxial terraces and the graphene strip, respectively. The corresponding height profiles are shown at the bottom. **c)** Raman spectrum of a sub-50 nm Sb_2Te_3 platelet at 633 nm laser excitation, displaying the E_g peak at $112\ \text{cm}^{-1}$ and the A_{1g} peak at $165\ \text{cm}^{-1}$. **d)** XRD pattern of the synthesized platelets on SiO_2 . The reflections from the (00l) planes indicate c-axis growth of the Sb_2Te_3 .

4.3.2 Device fabrication

Growth substrates covered by Sb_2Te_3 platelets are manually pressed onto Si/SiO₂ (300 nm) substrates, on which an array of markers (Ti(10 nm)/AuPd(30 nm)) has been defined. If needed, the substrates are sonicated at low power for a couple of seconds in order to remove larger structures from the surface. The transferred platelets are investigated by optical and atomic force microscopy, and thin flat platelets are chosen for electrical contacting in Hall bar or van der Pauw geometry. The electrical contacts are defined by EBL patterning, followed by Argon milling in order to remove surface oxide, resist residues, or adsorbates, and finally evaporation of Ti (2 nm)/Au (50 nm) and lift-off in acetone at 45 °C. The contact area pretreatment and metal evaporation are done *in-situ* without breaking the vacuum, as described in **Section 3.7**.

4.3.3 Magnetotransport properties

Charge transport measurements have been performed at 1.4 K with external magnetic field applied normal to the sample surface. The first CVD grown flakes are found to have thicknesses in the range 40–150 nm. Hall bars have been fabricated, as exemplified by the optical micrograph in **Fig. 4.9a**. The longitudinal resistance R_{xx} is seen to decrease as the sample is cooled down, which indicates metallic behavior and correspondingly strong doping of the Sb_2Te_3 sheets (**Fig. 4.9b**). The magnetoresistance exhibits conventional parabolic behavior without quantum correction at zero magnetic field. The slightly non-linear Hall resistance (**Fig. 4.9c**) suggests two parallel surface and bulk transport channels, as expected from the band structure of the compound. It is difficult to tune the position of the Fermi level via electrostatic gating, as evidenced by the Hall resistance curves obtained for different back gate voltages.

By further optimization of the CVD growth parameters, thinner platelets have been obtained, as depicted in **Fig. 4.10a**. The Hall and magnetoresistance, shown in **Fig. 4.10b,c**, yield a charge carrier density on the order of 10^{19} cm^{-3} . Fermi level pinning in the valence band is concluded from the gate voltage dependent magnetoconductance, which remains unchanged up to $V_g = +110 \text{ V}$. However, at low magnetic fields, a WAL peak appears (**Fig. 4.10c (inset)**). **Fig. 4.10d,e** show the temperature dependence of the WAL peak up to $T = 20 \text{ K}$ (panel **d**) and the phase coherence length (panel **e**), which is extracted from the HLN model fits of the WAL peaks and scales as $L_\phi \propto T^{-0.52}$, suggesting a 2D contribution to the conductance.

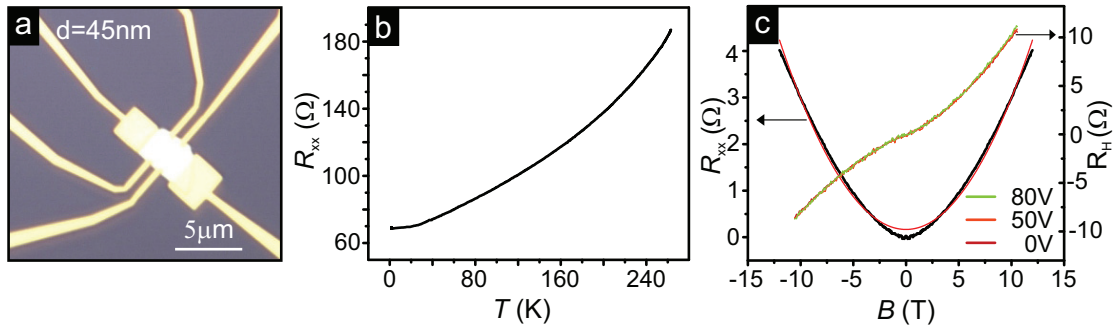


Figure 4.9 – First electric measurements of Sb_2Te_3 devices. **a)** A 45 nm thin platelet electrically contacted in a Hall bar geometry. **b)** Decreasing longitudinal resistance upon cooling, indicating metallic behavior and hence strong p-doping of the Sb_2Te_3 . **c)** Magnetoresistance exhibiting conventional parabolic behavior ($R_{xx} \propto (\mu B)^2$) indicative of a strong bulk contribution. The slightly non-linear Hall resistance for different gate voltages suggests two parallel transport channels. A mobility of $600 \text{ cm}^2/\text{Vs}$ and a charge carrier density $n_{3D} = 10^{19} \text{ cm}^{-3}$ are extracted.

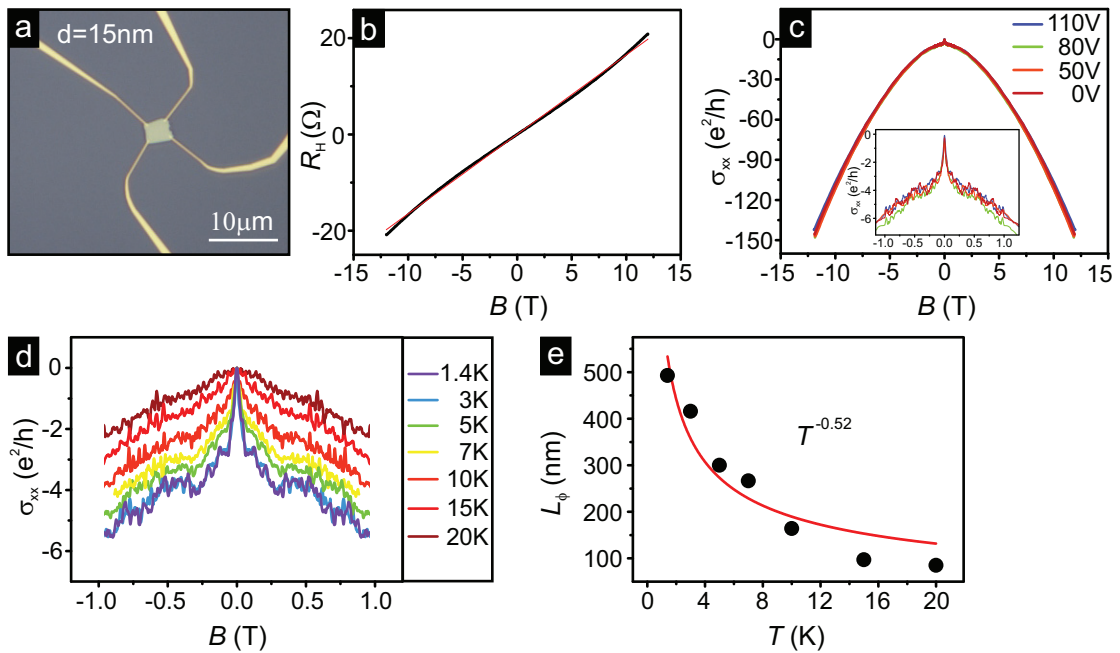


Figure 4.10 – Transport measurements on thinner Sb_2Te_3 platelets. **a)** Optical image of a 15 nm thick platelet contacted in van der Pauw geometry. **b)** Hall resistance indicating strong p-doping. **c)** Magnetoconductance exhibiting parabolic behavior for different gate voltages and a WAL correction peak at low fields (inset). **d)** Temperature dependence of the WAL peak in the range of 1.4-20 K at low B-fields. **e)** Temperature dependence of the phase coherence length extracted using the 2D HLN model.

4.4 CVD-grown $\text{Bi}_2\text{Te}_2\text{Se}$

4.4.1 Van der Waals epitaxial growth and initial characterization

The ternary tetradymite $\text{Bi}_2\text{Te}_2\text{Se}$ forms layered rhombohedral single crystals in the $R\bar{3}m$ space group, which consist of Te–Bi–Se–Bi–Te quintuple layers, weakly bonded by van der Waals forces. **Fig. 4.11a** schematically illustrates the crystal structures of Bi_2Se_3 and Bi_2Te_3 , which are used as sources for the crystal growth of $\text{Bi}_2\text{Te}_2\text{Se}$. The resulting compound is n-doped with the Fermi level located at the bottom of the conduction band (schematically shown in **Fig. 4.11b**), such that it is possible to shift E_F into the band gap via electrostatic gating by applying large negative gate voltages [192] or chemical doping with Sb [193] in order to reduce the density of Se vacancies and hence the n-doping.

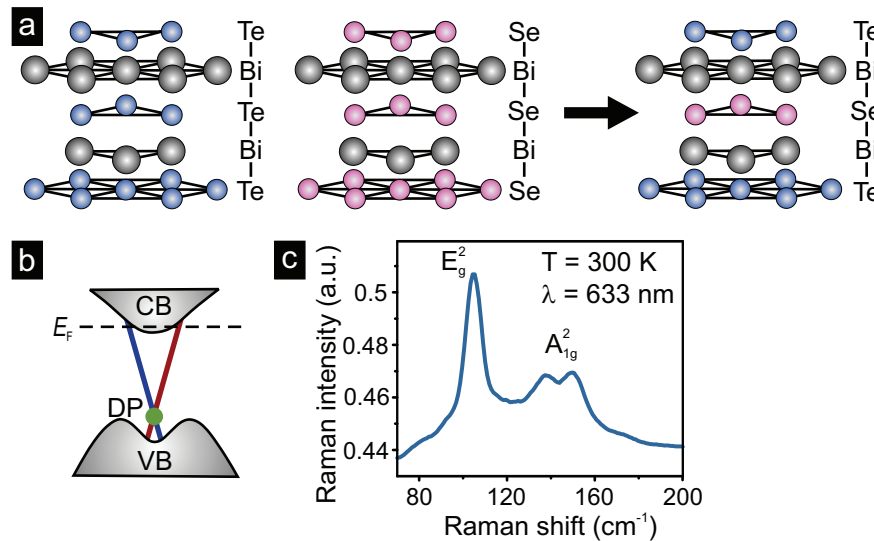


Figure 4.11 – Crystal structure and Raman spectrum of $\text{Bi}_2\text{Te}_2\text{Se}$. **a)** Quintuple layer stacking in the crystal structures of Bi_2Se_3 , Bi_2Te_3 , and $\text{Bi}_2\text{Te}_2\text{Se}$. **b)** Schematic band diagram of $\text{Bi}_2\text{Te}_2\text{Se}$, where E_F lies at the bottom of the conduction band, indicating n-doping. **c)** Raman spectrum of $\text{Bi}_2\text{Te}_2\text{Se}$ taken at room temperature with a laser wavelength of 633 nm, displaying the E_g^2 and A_{1g}^2 characteristic peaks.

To confirm the chemical composition, the crystals are transferred from the growth substrate to a Si/SiO₂ substrate and a Raman spectrum is recorded with 633 nm laser light. **Fig. 4.11c** shows the Raman spectrum of a representative $\text{Bi}_2\text{Te}_2\text{Se}$ platelet. Two characteristic peaks are observed, namely the E_g^2 peak at 106.8 cm^{-1} , and the A_{1g}^2 peak which is split into two components located at 137.8 cm^{-1} and 153.8 cm^{-1} . The stoichiometry is estimated based upon the data published by Richter et al. [189] to be $\text{Bi}_2(\text{Te}_{1-x}\text{Se}_x)_3$ with $0.34 < x < 0.42$ for a range

of Bi₂Te₂Se platelets.

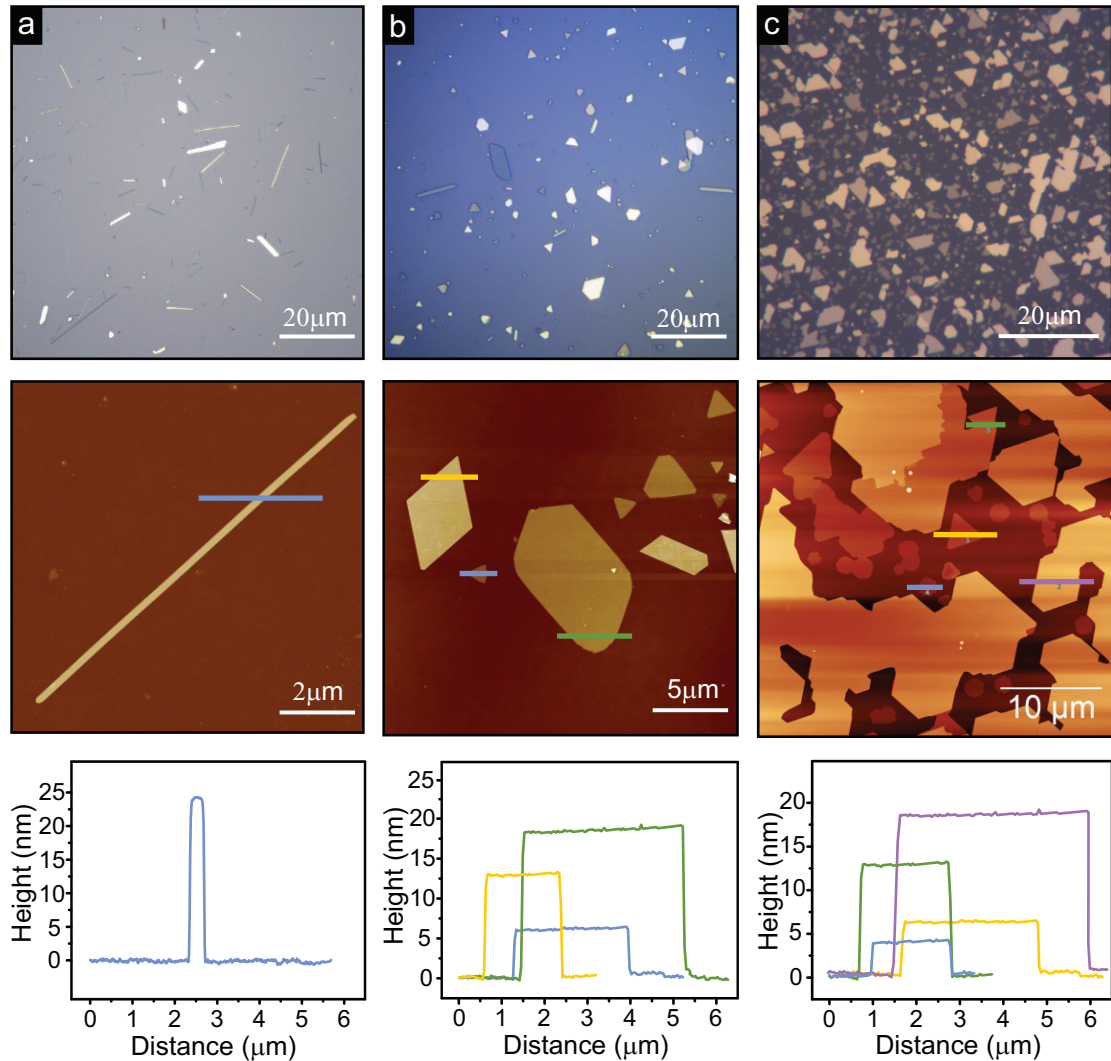


Figure 4.12 – CVD-grown Bi₂Te₂Se in different morphologies on SiO₂ and mica. Optical micrographs (top row) of Bi₂Te₂Se on **a,b**) SiO₂ and **c**) mica and corresponding AFM topography, revealing different growth morphologies, more specifically nanoribbons, nanowires, thin platelets, and large films. The height profiles (bottom row) of these structures are extracted along the colored lines in the AFM images (middle row).

Bi₂Te₂Se nanowires are grown by a catalyst-free VS method on Si/SiO₂ (300 nm) substrates following the procedure of Gehring et al. [192]. Bi₂Se₃ and Bi₂Te₃ crystal sources (99.999% purity) are heated up to 582 °C in a quartz tube furnace. Ultrapure Argon gas (6N) transports the evaporated material to the growth substrates, which kept at 450-480 °C during a growth time of 30 min. The pressure in the furnace is maintained at 75-85 mbar at an Argon flow rate of 150 sccm. Thus obtained nanowires and nanoribbons (**Fig. 4.12a**) have a length in the

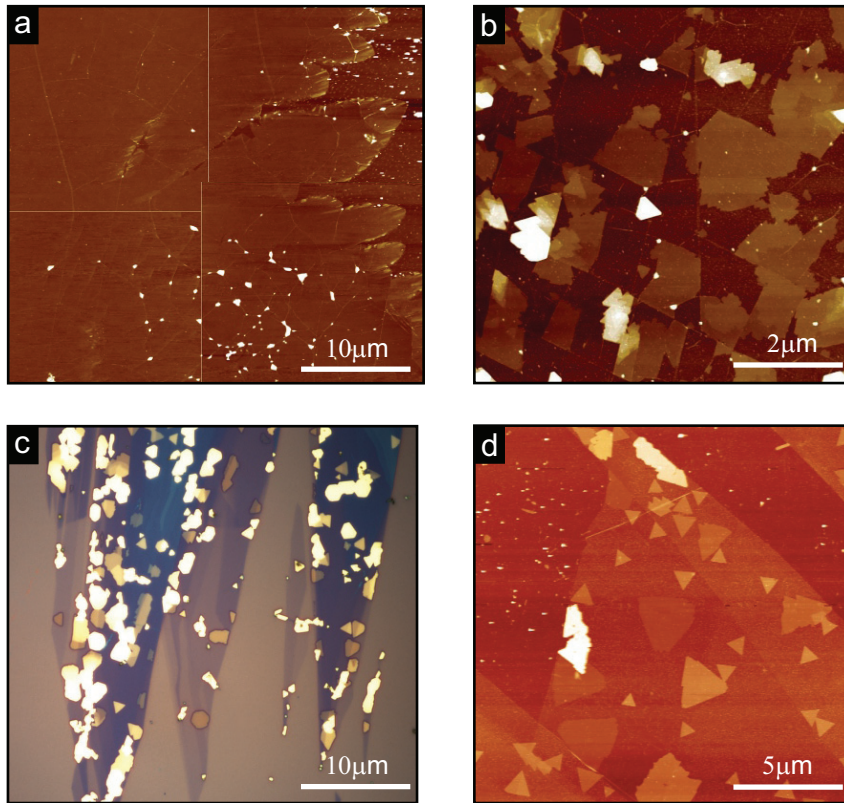


Figure 4.13 – Growth of $\text{Bi}_2\text{Te}_2\text{Se}$ on CVD-graphene and exfoliated graphene. **a)** AFM image of a CVD-graphene monolayer transferred from Cu onto SiO_2 in a wet etching process. **b)** AFM topography of $\text{Bi}_2\text{Te}_2\text{Se}$ grown on top of the CVD graphene. Regular growth is limited by domain boundaries and resist residues. **c)** Optical micrograph of $\text{Bi}_2\text{Te}_2\text{Se}$ grown on exfoliated graphene and **d)** corresponding AFM topography.

range of 5-60 μm , a lateral width of 0.05-1 μm , and a thickness of 15-200 nm. On the colder substrates (450-470 $^\circ\text{C}$), thin platelets are formed with lateral sizes of 0.5-15 μm and thickness in the range of 5-100 nm (**Fig. 4.12b**).

Van der Waals epitaxial growth is also demonstrated on layered substrates, such as hBN, mica, and graphene. The crystal growth on mechanically exfoliated insulating hBN sheets is highly oriented and electronic transport measurements have shown increased mobilities, enabling the observation of gate-tunable Shubnikov-de-Haas (SdH) oscillations [65]. On mica substrates, $\text{Bi}_2\text{Te}_2\text{Se}$ grows in a similarly oriented manner, with the growth time determining the thickness and lateral size of the film (**Fig. 4.12c**). The growth of $\text{Bi}_2\text{Te}_2\text{Se}$ on HOPG or graphene allows combining two materials into an epitaxial heterostructure [64] in order to investigate emergent interface phenomena. To this end, the growth on CVD graphene and on exfoliated graphene has been investigated. **Fig. 4.13a** shows the AFM topography of graphene

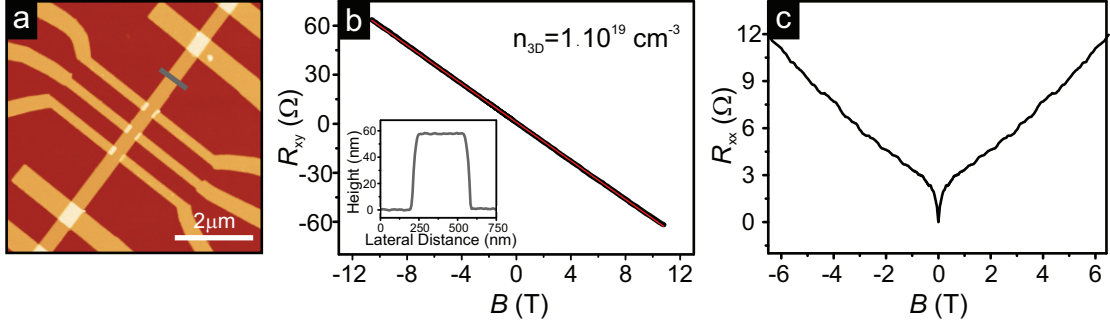


Figure 4.14 – Initial electrical characterization of Bi₂Te₂Se. **a)** AFM topographical image of a 55 nm thick and 400 nm wide Bi₂Te₂Se nanoribbon, contacted in Hall bar geometry. **b)** Linear Hall resistance R_{xy} , from which an electron density on the order of 10^{19} cm^{-3} is extracted. (inset: Height profile of the Bi₂Te₂Se nanoribbon taken along the grey line in the AFM image). **c)** The magnetoresistance R_{xx} exhibits a pronounced WAL dip at zero B-field at $T = 1.3 \text{ K}$.

grown on Cu-foil and subsequently transferred onto a Si/SiO₂ substrate, as described in Appendix A1. Bi₂Te₂Se grows epitaxially on top, although the lateral size of the nanoplatelet is limited by domain boundaries in the CVD graphene and resist residues on its surface (Fig. 4.13b). A cleaner and more reproducible growth has been achieved with mechanically exfoliated graphene, as demonstrated in Fig. 4.13c,d. In this case, larger platelets are formed with thicknesses as low as 4 nm.

4.4.2 Magnetotransport studies

For the fabrication of devices for electric transport measurements, Bi₂Te₂Se thin platelets and ribbons are transferred onto a Si/SiO₂ substrate and individual structures are electrically contacted via EBL, contact area pre-treatment, thermal evaporation and lift-off, similar to the procedure followed for the materials previously discussed. The as-obtained contacts are Ohmic ($R_c < 1 \text{ k}\Omega$), owing to the Argon milling treatment performed *in-situ* and the evaporation of a thinner Titanium adhesion layer of only 1.5-2 nm thickness. Devices in Hall bar geometry (Fig. 4.14a) allow for simultaneously recording the longitudinal and Hall resistance at low temperatures, from which a carrier density on the order of $1 \times 10^{19} \text{ cm}^{-3}$ and an average mobility on the order of $300 \text{ cm}^2/\text{Vs}$ are extracted (Fig. 4.14b,c). These values are comparable to previously published ones [194]. The magnetoconductance has been measured in dependence of temperature and titling angle, as shown in Fig. 4.15a,c. It is calculated from the magnetoresistance by taking into account the thickness of the sample d , the distance between the voltage probe contacts L , and the width of the Bi₂Te₂Se channel W . On this basis, the corrected magnetoconductance $\Delta\sigma_{xx} = \sigma_{xx}(B) - \sigma_{xx}(B = 0)$ is plotted in units of e^2/h . At low

temperature ($T = 1.4$ K), $\Delta\sigma_{xx}$ exhibits a prominent WAL peak and well-pronounced oscillations, which are attributed to UCFs, in accordance with previous observations [72]. The data is fitted with a 2D localization HLN model (Eqn. 2.1) and two parameters are extracted from the fits – the phase coherence length L_ϕ and the coefficient α . For strong SO coupling, as in the case of TIs, one expects $\alpha = -0.5$ for a single transport channel, i.e., one surface contributing to the conductance, whereas $\alpha = -1$ is associated with contribution from both surfaces. For the present samples, $\alpha = -0.5$. The dependence of the coherence length on temperature is shown in Fig. 4.15b in the range of 1.4–30 K.

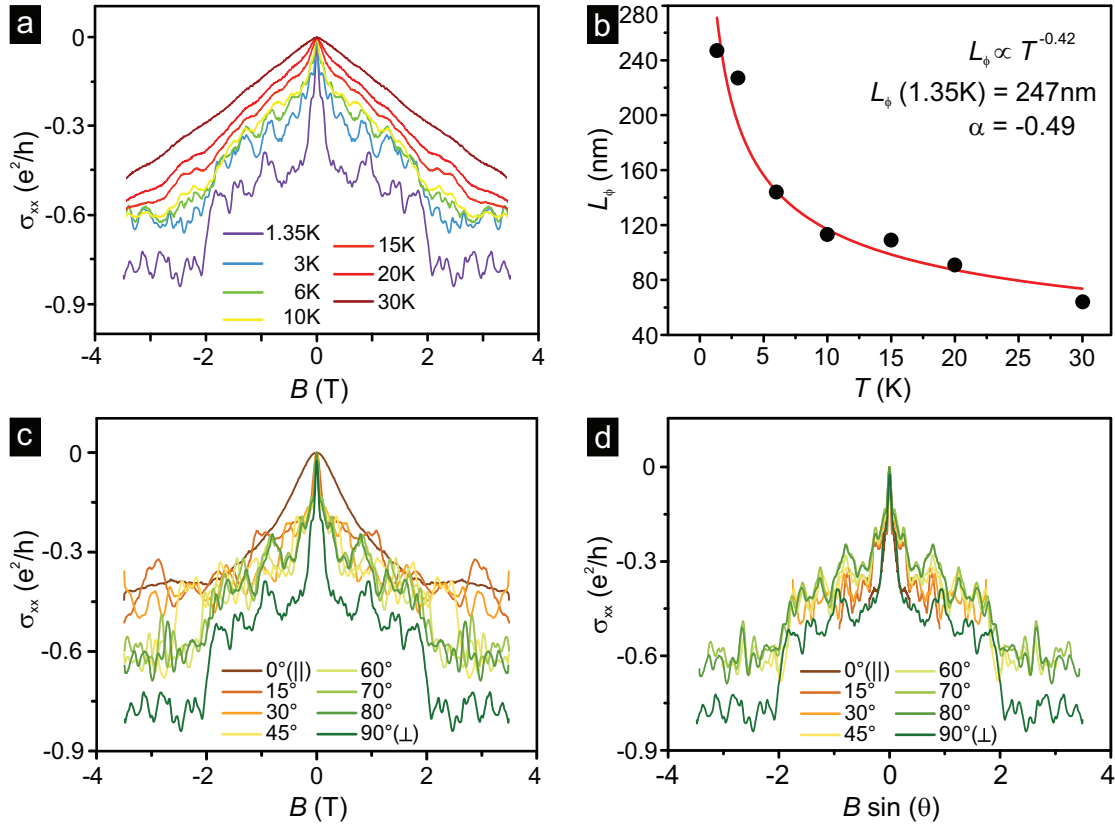


Figure 4.15 – Temperature and angle dependence of the magnetoconductance of Bi₂Te₂Se.

a) Temperature-dependent magnetoconductance in Bi₂Te₂Se exhibiting WAL at low fields and quantum oscillations, the magnitude of both decreasing with increasing temperature. **b)** Temperature-dependence of the phase coherence length, which can be well fitted with a power law dependence. **c)** Magnetoconductance for different tilting angles. **d)** The magnetoconductance, plotted as a function of the perpendicular component of the magnetic field. All curves fall onto one another, indicating a 2D origin of the WAL effect.

It can be well fitted by a power law, rendering $L_\phi \propto T^{-0.49}$. According to theory, this dependence is related to the dimensionality of the system, such that $L_\phi \propto T^{-1/2}$ for a 2D system and $L_\phi \propto T^{-3/4}$ for a 3D system [186]. Thus, the observed power law dependence is characteristic

of a 2D system and indicates that the WAL observed at low B-fields originates from the TI surface states.

In order to further investigate the WAL origin, which can contain both surface and bulk contributions, the sample is tilted in magnetic field in order to highlight the effect, which depends only on the component of the magnetic field that is perpendicular to the sample plane. The peak is most pronounced for $\theta = 90^\circ$ (out-of-plane) and weakens as θ approaches 0° (in-plane), as seen in **Fig. 4.15c**. The fact that WAL is still observable under in-plane B-field is an indication for partial bulk contribution to the conductance. The corrected conductance is plotted as a function of the normal component of the magnetic field, $B \cdot \sin(\theta)$, in order to subtract the bulk contribution. All angle-dependent curves fall onto a single curve for low B-fields, evidencing a surface state-related WAL effect (**Fig. 4.15d**).

The successful CVD growth of Bi₂Te₂Se in various morphologies and its magnetotransport properties pointing towards surface state contribution to the conductance despite the interfering bulk make this compound a promising spintronic device component. Furthermore, the spin-momentum locking of the surface states and the successful epitaxial growth of Bi₂Te₂Se on various low-dimensional substrates, like graphene or hBN, make it possible to investigate Bi₂Te₂Se as a possible spin generator, in order to inject spin polarized current into a non-magnetic material in direct proximity to it, for example in a van der Waals heterostructure. In order to decrease the compound's carrier concentration, antimony doping could be introduced into the CVD growth process, such that the Fermi level can be more easily shifted via electrostatic gating. On the other hand, the problem of low mobility may be addressed by growing Bi₂Te₂Se on atomically flat hBN or mica insulating substrates, which has been documented to increase the surface-related mobility and gate tunability of the compound [65]. Bi₂Te₂Se growth on mica yields closed films, which could be used for ARPES experiments or nonlinear plasmonic experiments when combined with an array of lithographically defined nano-antennas.

Finally, it would be interesting to explore emergent interface phenomena in a Bi₂Te₂Se/graphene heterostructure using tunneling spectroscopy in order to determine the interaction mechanisms of the TI surface states with the Dirac cone of graphene, and to study elastic or inelastic tunneling processes at the interface. The temperature dependence of the resistivity may also reveal charge transport mechanisms, like thermal activation, tunneling, etc.

5 Spin transport in lateral spin valves based on $\text{Bi}_2\text{Te}_2\text{Se}$

Owing to the spin-momentum locking of their 2D surface states, 3D TIs represent promising components of spintronic devices. In particular, they show great potential as spin generators, wherein the amplitude and direction of the resulting net spin polarization should be controllable through the amplitude and direction of the applied charge current. Charge current-induced spin-polarized currents have been successfully demonstrated in Bi_2Se_3 [87] [92], $\text{Bi}_2\text{Te}_2\text{Se}$ [89], $\text{Bi}_{1.5}\text{Sb}_{0.5}\text{Te}_{1.7}\text{Se}_{1.3}$ [91], and $(\text{Bi}_{0.53}\text{Sb}_{0.47})_2\text{Te}_3$ [90] with the aid of ferromagnetic contacts in different configurations. In an alternative approach to confirm spin-momentum locking in a 3D TI, vertical spin-polarized tunnel junctions have been utilized to demonstrate charge-spin conversion in Bi_2Se_3 and $(\text{Bi}_{0.5}\text{Sb}_{0.5})_2\text{Te}_3$ [93]. Furthermore, by using a microwave-based detection approach, it has been shown that a charge current flowing within a 3D TI exerts a spin-transfer torque onto an adjacent ferromagnetic metal film [137].

5.1 Spin valves with $\text{Bi}_2\text{Te}_2\text{Se}$ wires and transparent contacts

Spin injection and detection are largely dependent on the type and the quality of the contact interface between the electrodes and the transport channel. In a TI-based LSV, bias current can be applied with the aid of non-ferromagnetic metal contacts (e.g., Ti/Au) and spin detection accomplished through a ferromagnetic contact that is decoupled from the TI by a tunneling barrier composed of Al_2O_3 [87] [89], MgO [93], TiO_2 [92], or graphene [87]. Based on the work of Han et al. [141] on spin injection and detection in monolayer graphene spin valves, one can distinguish between three types of contact interface, namely tunnel (decoupled), pin-hole (intermediate), and transparent (strongly coupled). Spin injection is possible even with transparent contacts, which are strongly coupled to the material, provided that the

contact area is sufficiently reduced in order to achieve higher contact resistances [195]. In an attempt to simplify the device fabrication by avoiding the complicated deposition of tunneling contacts, the spin transport in Bi₂Te₂Se wire-based devices is probed by directly depositing a FM contact onto the TI and taking advantage of the reduced dimensions to achieve spin injection and detection.

5.1.1 Device fabrication and initial characterization

As a first step to barrier-free spin injection, the catalyst-free VS process, as described in **Section 3.1**, is modified in order to obtain Bi₂Te₂Se nanowires. Increased growth time and higher substrate temperature result in long, narrow single crystal wires and ribbons with a width of 80 to 500 nm and a length of 5 to 50 μm . These are transferred mechanically to a marker substrate and EBL is used to define first the NM Ohmic Ti(2 nm)/Au(50 nm) contacts, followed by the FM Co (50 nm)/Au(10 nm) contacts. In both cases, the contact pretreatment and the thermal evaporation are done *in-situ* at low pressure in the 10^{-7} – 10^{-8} mbar range. The NM contact resistances are below 700 Ω , while the FM contact resistances show a slightly larger variation in the range of 700 Ω –2 k Ω .

Prior to the fabrication of the first spin valve devices, it is essential to verify the ferromagnetic properties of the Cobalt film. For this purpose, metallic test structures are fabricated through a standard EBL process and evaporation of Co(50 nm)/Au(10 nm) contacts, as depicted in the SEM micrograph in **Fig. 5.1a**. The four-terminal resistance of the test device is monitored while an external magnetic field applied in-plane along the Cobalt channel is swept from -100 to +100 mT. When the magnetic domains in the Cobalt are reoriented, a resistance peak occurs at the switching field symmetric around $B = 0$. The switching field depends on the lateral size of the Cobalt channel. **Fig. 5.1b,c** illustrate this switching magnetoresistance for two channels of different width (330 nm and 250 nm, respectively). As expected, the switching field is larger for smaller channel width.

5.1.2 Spin transport behavior

Electronic transport experiments are performed in an Oxford cryostat equipped with a 12 T magnet and a rotatable insert for measurements in the range of 1.3-300 K. The applied 13 Hz AC-signal is offset by a home-built differential operational amplifier module running on batteries. The current is monitored by a DLPCA 200 (FEMTO), while the voltage is pre-amplified using a SRS 560 (Stanford) before digitalization.

5.1. Spin valves with $\text{Bi}_2\text{Te}_2\text{Se}$ wires and transparent contacts

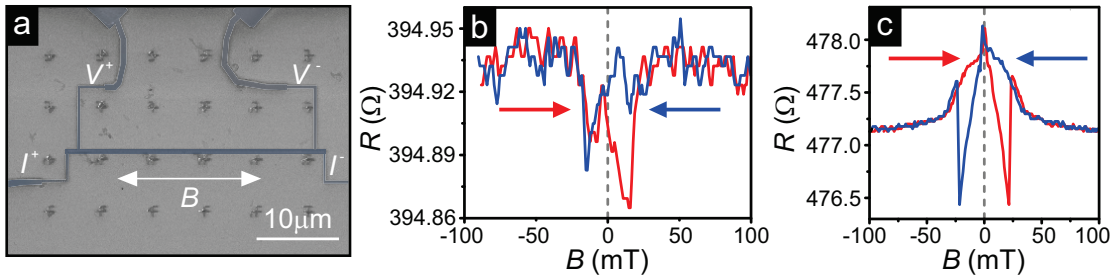


Figure 5.1 – Ferromagnetic switching of a Cobalt channel. **a)** SEM image of the all-metallic Cobalt test structure used to determine the switching field of the thermally evaporated, 50 nm thick Cobalt film. **b, c)** Switching in the four-terminal magnetoresistance for two different channel widths, i.e., 330 nm in panel **b)** and 250 nm in panel **c)**.

The spin valve measurements are carried out by passing a constant AC current (500 nA) mixed with a DC bias ($\pm 100 \mu\text{A}$) current through a pair of electrodes on top of the $\text{Bi}_2\text{Te}_2\text{Se}$ and measuring the voltage drop in a three-terminal non-local or a four-terminal non-local geometry as a function of in-plane magnetic field applied along their easy axis of magnetization and perpendicular to the applied bias current.

As a first step, spin valves are fabricated in only one EBL and one evaporation step, resulting in nanowires electrically contacted by FM Cobalt electrodes only, as shown in **Fig. 5.2a**. The contact pretreatment is done by Argon plasma, as described in **Section 3.7**. Electrical characterization of the $\text{Bi}_2\text{Te}_2\text{Se}/\text{Cobalt}$ contacts reveals contact resistances falling mainly in two groups, i.e., $R_c < 1 \text{ k}\Omega$ and $1 \text{ k}\Omega < R_c < 3 \text{ k}\Omega$. A measurable spin signal could only be observed for the devices with higher R_c , as FM contacts strongly coupled to the TI wire give rise to increased spin scattering and faster spin relaxation [108] [110]. **Fig. 5.2b** shows a SEM image of the measured device, from which the lateral widths of the FM electrodes can be determined in order to estimate the switching field.

The applied external magnetic field can reverse the direction of their magnetization and the applied bias current gives rise to a voltage drop, which is consistent with the detector's magnetization being either parallel or antiparallel to the spin in the TI. Since it is a constant current measurement, the detected voltage can be normalized by dividing it by the current. Thus obtained resistance is plotted as a function of the magnetic field in **Fig. 5.2c** for positive bias and in **Fig. 5.2d** for negative bias. For the present device, the resulting hysteresis was found to be more pronounced for positive currents than for negative ones. This difference can be attributed to a low stability of the $\text{Bi}_2\text{Te}_2\text{Se}/\text{Co}$ interface, and was seen to vary for different devices. As the second measurement (**Fig. 5.2d**) is mirror image-like of the first one (**Fig. 5.2c**), it is tempting to argue that no matter how the FM injector polarizes the current, the topological

insulator only propagates the spin direction locked to the k-vector. However, reaching a more conclusive proof of current-induced spin transport in the $\text{Bi}_2\text{Te}_2\text{Se}$ requires replacing the FM injector contact by a NM one, as described below.

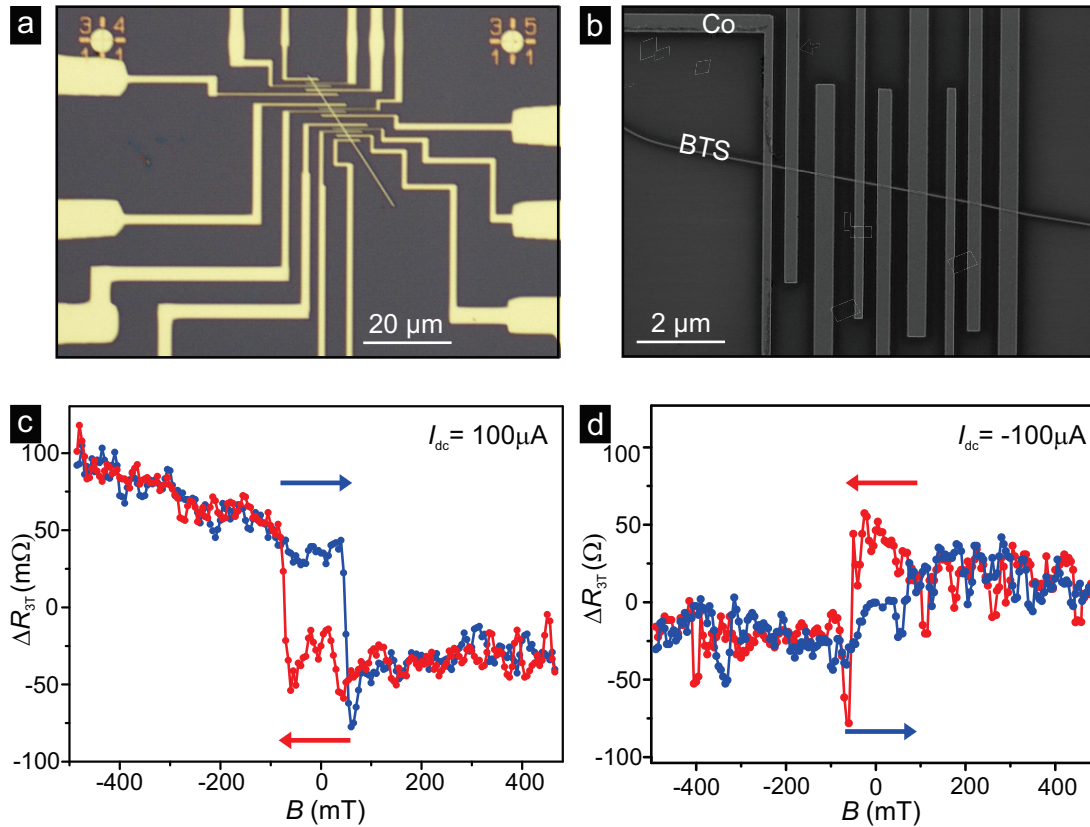


Figure 5.2 – Spin transport in $\text{Bi}_2\text{Te}_2\text{Se}$ nanowires with all-FM transparent contacts. **a)** Optical micrograph of a spin valve device with multiple Co/Au electrodes. **b)** SEM image of the device, showing an electrically contacted wire and the FM Cobalt contacts with different lateral widths. **c)** Single-switch in the magnetoresistance for positive applied bias current detected in a three-terminal non-local configuration. **d)** Mirroring of the single switch for the same device when the bias current polarity is reversed.

In order to confirm that spin-momentum locking related spin polarization of the current is indeed detected, devices with mixed FM and NM contacts are fabricated in a two-step EBL process and two separate evaporation steps. The Ti/Au electrodes are evaporated first, followed by the FM ones. **Fig. 5.3a** shows an optical micrograph of a long $\text{Bi}_2\text{Te}_2\text{Se}$ wire electrically contacted with multiple FM and NM electrodes, such that different geometries can be explored and the contact resistances can be reliably investigated.

The electrical measurements are performed in a non-local geometry, such that constant cur-

5.1. Spin valves with $\text{Bi}_2\text{Te}_2\text{Se}$ wires and transparent contacts

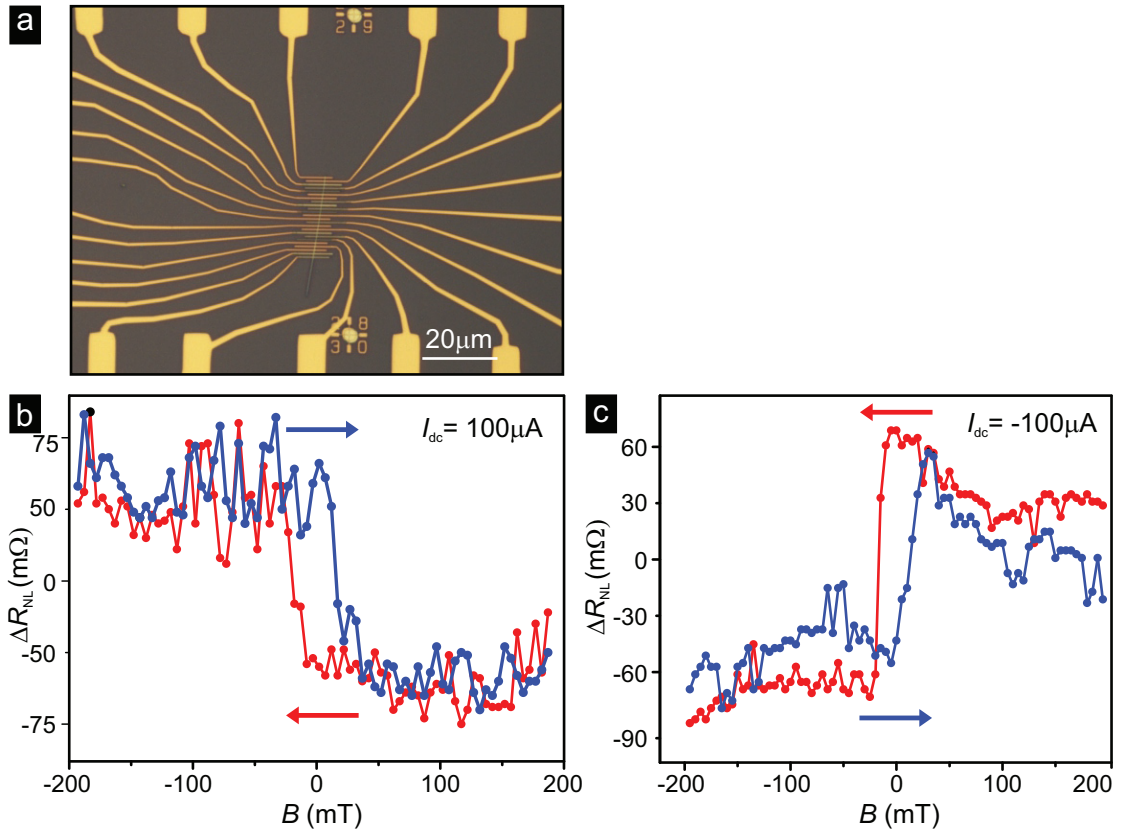


Figure 5.3 – Spin transport in $\text{Bi}_2\text{Te}_2\text{Se}$ nanowires with NM-FM transparent contacts. a) Optical micrograph of a spin valve device with combined Ti/Au and Co/Au) electrodes. **b)** Single-switch in the magnetoresistance for positive bias current applied between NM electrodes. The spin signal is detected via one FM electrode. **c)** Mirroring of the single switch for the same device when the bias current polarity is reversed.

rent is applied between two NM electrodes and one of the voltage probes is a FM. Otherwise the experiment is analogous to the one described above. Again, a single switch is observed and its behavior is consistent with a spin signal that arises from the spin-momentum locking in a TI (**Fig. 5.3b,c**). As expected for strongly coupled contacts, the spin signal is in the sub-100m Ω range, which is an order of magnitude lower than spin signals observed for 3D TIs in the presence of a tunnel barrier [90]. Due to the low stability of the Cobalt contacts, a spin signal with reproducible amplitude could be reliably recorded only at low temperature and bias currents of maximally $\pm 100 \mu\text{A}$. Based on the confirmed electrical detection of spin-polarized current in $\text{Bi}_2\text{Te}_2\text{Se}$, the next step is to improve the device performance by incorporation of a tunnel barrier. To this end, 2D crystalline films, such as graphene or hBN are attractive alternatives to standard oxide films. Graphene has been used as a tunnel barrier with Si [12] and with Bi_2Se_3 [87]. Spin injection into graphene in the presence of a hBN tunnel barrier has

also been demonstrated [196] [197] [198], but such an experiment has not yet been performed with a TI as a transport channel. Here, this gap is closed by combining $\text{Bi}_2\text{Te}_2\text{Se}$ thin platelets with a hBN tunnel barrier, as described in the next section.

5.2 Spin valves with $\text{Bi}_2\text{Te}_2\text{Se}$ platelets and tunneling contacts

In order to improve the quality of the FM/TI interface and enhance the spin signal, a tunnel barrier composed of a 2D hexagonal boron nitride (hBN) thin film is utilized. While thin oxides are a standard choice for the tunnel barrier, their fabrication poses a significant experimental challenge and must be optimized in order to avoid pin-holes, interface trap states, defects and non-uniformity. This problem has been recently addressed by replacing thin oxide barriers with 2D single crystal films, such as graphene [199] and hBN [196] [198] [200] in MTJs and lateral spintronics devices. Incorporating graphene as a tunnel barrier on top of a TI requires additional etching steps, due to its conductive nature in the 2D plane. If exfoliated graphene is used, the TI film can be epitaxially grown on top, followed by flipping of the heterostructure, such that the graphene lies on top of the TI and can be patterned into strips by reactive ion etching (RIE). A FM contact evaporated on top of a graphene strip then serves as a detector for electrically induced spin-polarized current in the TI. A detailed description of the fabrication process developed within this thesis can be found in Appendix A.

Graphene's isomorph, hBN, is a large band gap insulator, which has been utilized as tunnel barrier for spin injection and detection in graphene lateral spin valve devices [196] [200] and as a substrate for graphene, enabling long distance spin transport [201]. As an atomically flat and chemically inert dielectric substrate, hBN is able to significantly enhance charge transport properties such as mobility in graphene [202] [203] and in TIs [65]. A significant advantage of hBN as a tunnel barrier in spintronic devices is the possibility to tune the contact resistance of the tunnel junction, since the resistance-contact area product (RA) scales exponentially with the number of hBN layers [197]. Thus, the influence of the tunnel barrier thickness onto the magnitude and the properties of the spin signal can be investigated. Recently, Kamalakar et al. [204] have demonstrated a spin filtering effect of the hBN tunnel barrier in a single layer graphene spin valve, which depends on the ratio of the resistances of the injector and detector contacts.

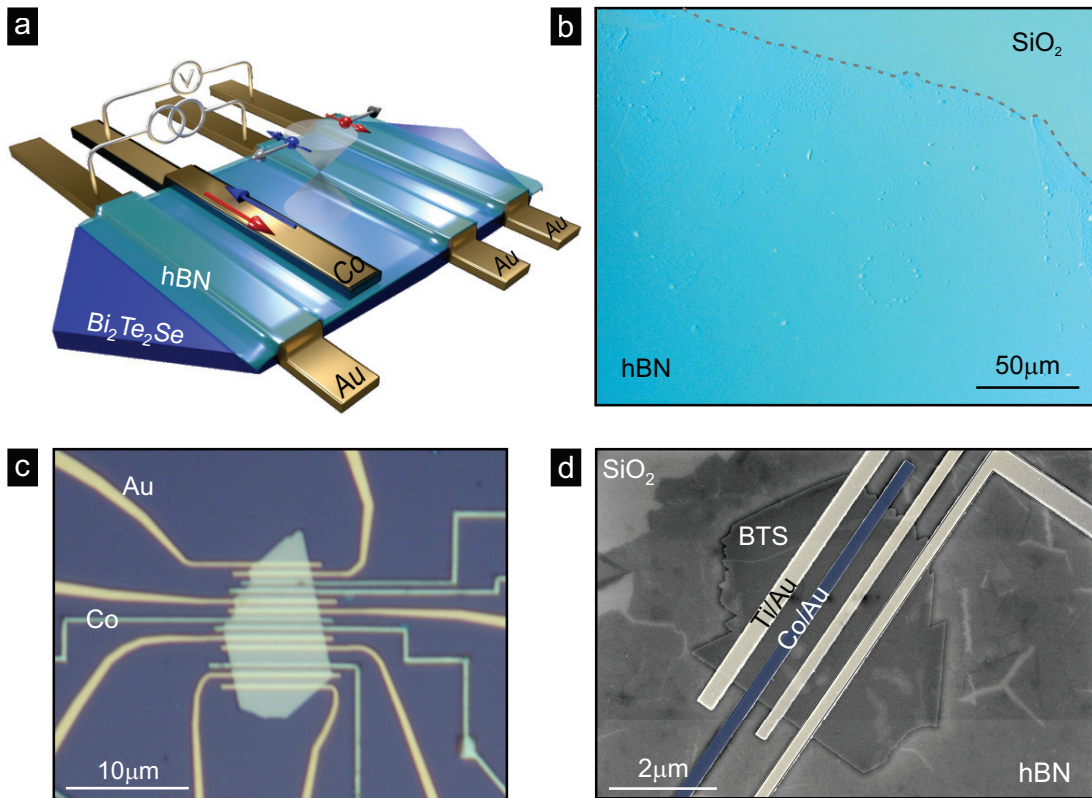


Figure 5.4 – Fabrication of $\text{Bi}_2\text{Te}_2\text{Se}$ lateral spin valve devices with hBN tunnel barriers. **a)** Schematic representation of the experimental concept and the device structure of a TI-based spin valve with three NM contacts and one FM detector decoupled from the TI channel via a hBN sheet. **b)** Optical micrograph of a hBN sheet transferred onto a Si/SiO₂ substrate showing high coverage. **c)** Optical micrograph of a measured device consisting of a $\text{Bi}_2\text{Te}_2\text{Se}$ platelet electrically contacted by Co and Au electrodes. The hBN sheet lies only beneath the Co electrodes, while the Au ones comprise Ohmic interfaces. **d)** SEM image of a device, where the hBN film is clearly visible.

5.2.1 Device fabrication and initial characterization

$\text{Bi}_2\text{Te}_2\text{Se}$ thin platelets are grown in a catalyst-free VS method on Si/SiO₂ substrates, as described in **Section 3.1**. They are subsequently mechanically transferred to marker substrates and electrically contacted via EBL, followed by thermal evaporation of Ti (2 nm)/ Au (50 nm) electrodes and standard lift-off. The contact area is pretreated in an *in-situ* Argon milling process prior to metal evaporation in order to achieve Ohmic contacts. The contacts resistance of these NM electrodes falls within the range of 200-500 Ω. Next, the CVD-grown hBN film on copper is transferred on top of the devices (for more detail, see Appendix A). Atomic force microscopy is used to confirm that the hBN film is intact in the areas where the FM contacts are to be deposited. Finally, in a second lithographic step, FM detector electrodes are defined

and Cobalt (50 nm), capped with Au (10 nm) is thermally evaporated, followed by a final lift-off. The Co/hBN contact resistances fall into the range of 2-20 k Ω and change only little upon cooling from room to base temperature.

Transport measurements are performed in an Oxford superconducting magnet system (15 T) and a sorption pumped HelioxVL ^3He rotatable insert with a base temperature of 230 mK. It is connected to an amplifier stage, providing a mixed AC/DC signal supplied by a lock-in amplifier operated at 13 Hz and a Keithley 2400, respectively. The stage in addition provides a high impedance voltage signal amplification before digitalization. Current-driven spin valve measurements are performed at constant AC currents in the range of 500 nA-1 μA , which are offset by a bias current with varying polarity in the range of -10 to 10 μA . The magnetization of the single FM detector electrode is aligned in-plane by applying an external magnetic field perpendicular to the current direction. Thus, while a constant bias is applied between a pair of NM electrodes, the voltage drop is measured between a FM-NM pair in order to probe the spin signal across the TI channel. The voltage difference between the high- and low-voltage states is normalized by the injection current and plotted as the spin signal, ΔR_s .

5.2.2 Spin filter effect of hBN/Co detector electrodes

$\text{Bi}_2\text{Te}_2\text{Se}$ spin valve with low resistance hBN/Co tunnel contacts The I - V characteristics of the hBN/Cobalt detectors reveal mostly tunneling contacts with varying resistances, but for all measured devices, they are found to be at least an order of magnitude larger than the resistances of the direct Ohmic NM contacts. The slightly non-linear I - V characteristics of one of the devices with low hBN/Co contact resistance ($R_c < 5$ k Ω) is shown in **Fig. 5.5a**. For spin signal detection, a mixed AC/DC constant current is applied between a set of NM electrodes and the voltage drop between a FM-NM pair is measured in a four-terminal geometry (**Fig. 5.4a**), similar to the procedure of Tang et al. [90].

The measured voltage depends on the relative orientation of the spin-polarized current and the magnetization of the Cobalt electrode, resulting in states of high and low resistance, the transition between which occurs at the switching field of the Cobalt electrode. The latter is determined by the lateral dimension of the electrode (width of 170 nm). For the latter, a coercive field of 45 mT is estimated in combination with the magnetoresistance switching behavior of test Cobalt structures (see **Section 5.1.1**).

The measured spin signal is found to be maximal for $I_{dc} = +3.5$ μA and -3 μA for the device shown and exhibits a similar trend for the remaining devices (**Fig. 5.5b**). **Fig. 5.5c,d** show a

5.2. Spin valves with $\text{Bi}_2\text{Te}_2\text{Se}$ platelets and tunneling contacts

current-invertible hysteresis consistent with spin polarization of the TI surface states. The magnitude of the spin signal of $R_s = 1 \Omega$ is one order of magnitude larger compared to the spin signals recorded in the case of transparent contacts (see **Section 5.1**). This difference directly reflects the presence of the hBN sheet, which reduces the coupling at the interface between the TI channel and the FM contact.

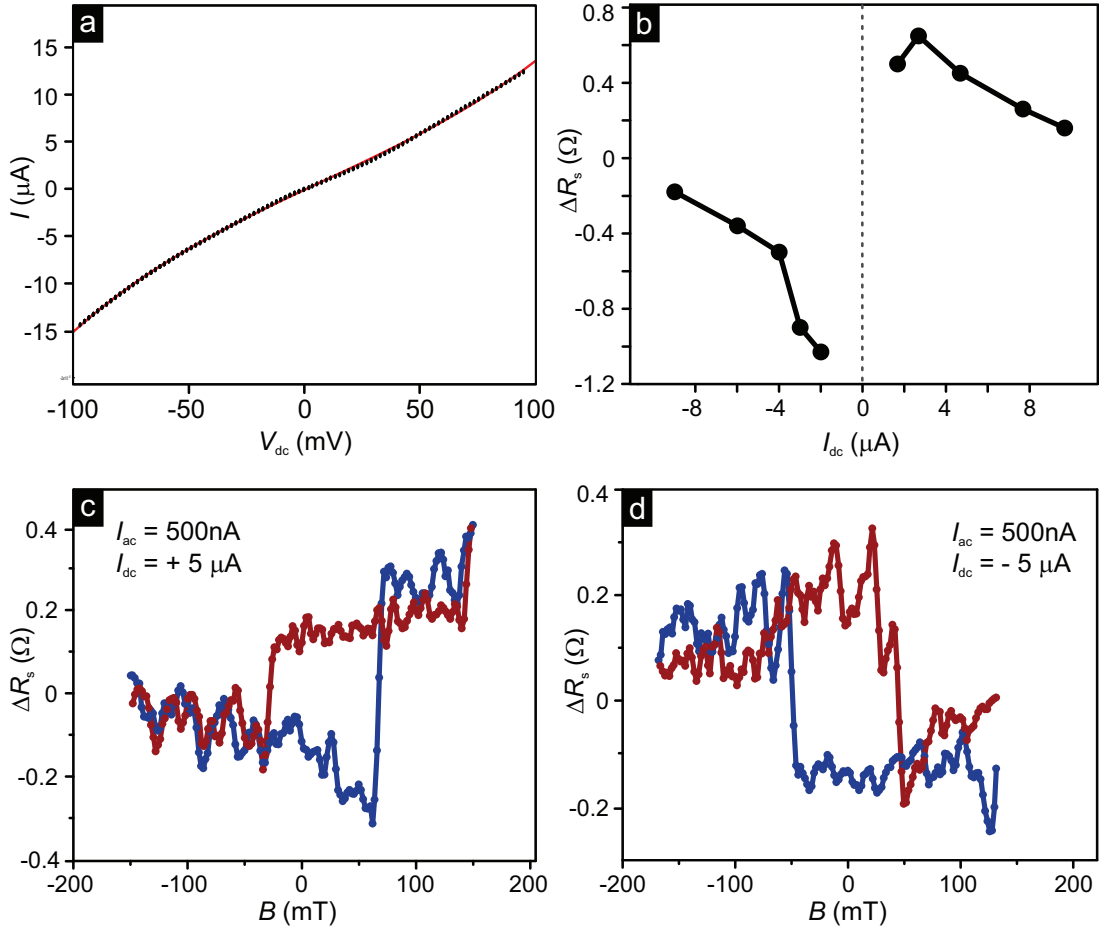


Figure 5.5 – Spin transport in $\text{Bi}_2\text{Te}_2\text{Se}$ spin valve with low resistance hBN/Co tunnel contacts. **a)** Slightly nonlinear $I - V$ characteristics of a hBN/Co contact ($T = 250 \text{ mK}$; the red line is a Simmons model fit to the data). **b)** Bias current dependence of the averaged spin signal for both sweeping directions of the magnetic field, displaying a reversed sign of the spin signal, indicating its origin from the electrically induced spin-polarized current in the TI channel. **c,d)** Hysteresis in the measured resistance as the in-plane magnetic field is swept in both directions for an applied DC bias of $I_{dc} \pm 5 \mu\text{A}$ and an AC amplitude of 500 nA at base temperature $T = 230 \text{ mK}$. A sign reversal of the spin signal occurs for $\pm I_{dc}$.

$\text{Bi}_2\text{Te}_2\text{Se}$ spin valve with high resistance hBN/Co tunnel contacts The hBN/Co detector electrodes of several devices are found to exhibit higher contact resistance ($R_C > 5 \text{ k}\Omega$). The I - V characteristics of one these devices clearly shows a more pronounced tunnel behavior (Fig. 5.5a). For positive bias, as shown in Fig. 5.6c, a resistance hysteresis is recorded, whose amplitude of $\Delta R = 3 \Omega$ exceeds the signal measured in the low-resistance devices. This finding is consistent with the presence of a tunnel barrier, which decouples the contacts from the transport channel and reduces contact-induced effects onto the spin signal.

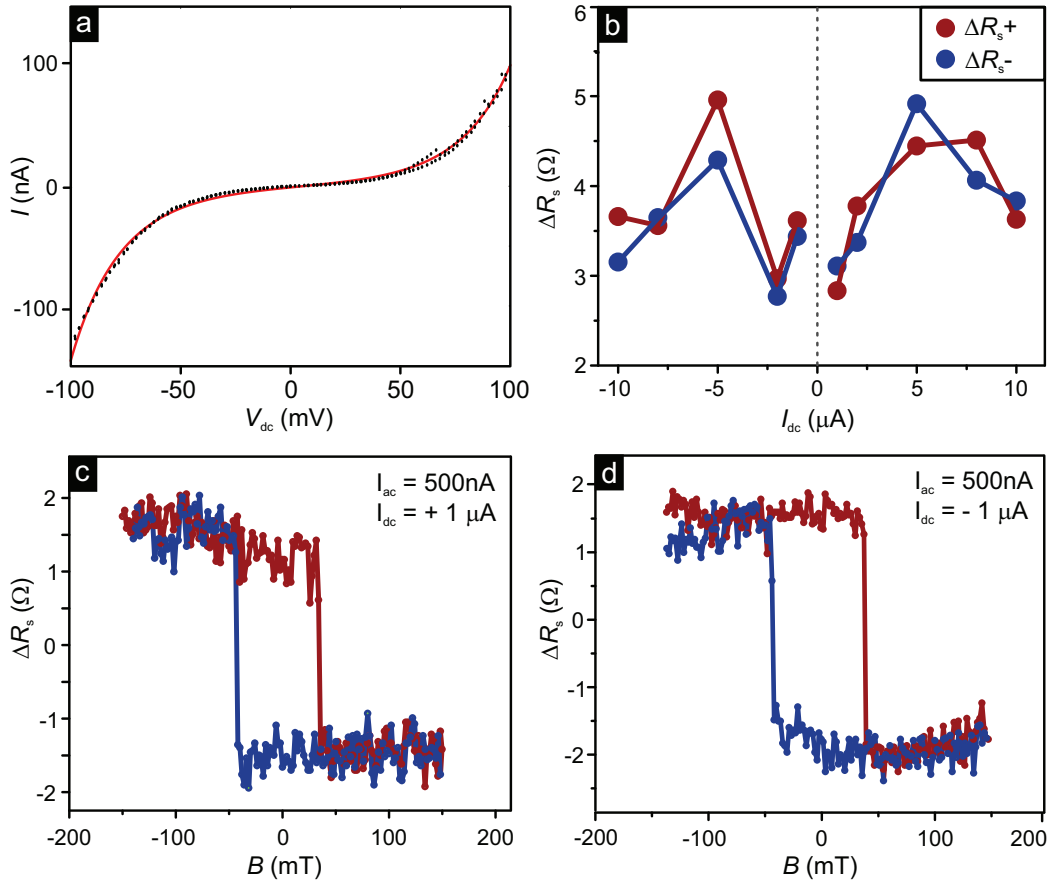


Figure 5.6 – Spin transport in $\text{Bi}_2\text{Te}_2\text{Se}$ spin valve with high resistance hBN/Co tunnel contacts. **a)** Nonlinear $I - V$ characteristics of the hBN/Co contacts ($T = 250 \text{ mK}$; the red line is a Simmons model fit to the data). **b)** Bias current dependence of the spin signal for both sweeping directions of the magnetic field (blue and red data points), revealing a maximum spin signal for $I_{dc} \pm 5 \mu\text{A}$ and a non-reversed sign for both current polarities. **c,d)** Hysteresis in the measured resistance as the in-plane magnetic field is swept in both directions for an applied DC bias of $I_{dc} \pm 1 \mu\text{A}$ and an AC amplitude of 500 nA at base temperature $T = 230 \text{ mK}$. No sign reversal of the spin signal occurs for $\pm I_{dc}$.

The contact resistance of the FM contacts, determined by the hBN layer, has a clear impact onto the magnitude of the spin signal. This observation is consistent with previous studies

5.2. Spin valves with Bi₂Te₂Se platelets and tunneling contacts

of graphene spin valves with hBN tunnel barriers by Yamaguchi et al. [198], who observed spin signals on the order of a few mΩ and short spin lifetimes of 50 ns for low-resistance hBN/Ni₈₁Fe₁₉ contacts in bilayer graphene spin valves.

Spin-momentum locking in a 3D TI requires a reversal of the low- and high-resistance states of the hysteresis when the direction of the bias current is reversed. **Fig. 5.6d** shows the measured hysteresis for the negative bias polarity, which unexpectedly remains unchanged. The bias dependence of the spin signal for both positive and negative bias currents, shown in **Fig. 5.6b** further confirms that the hysteresis remains unchanged up to $I_{dc} \pm 10 \mu\text{A}$. This behavior is reproducibly observed for several devices whose hBN/Co contact resistances fall into the range $5 \text{ k}\Omega < R_c < 20 \text{ k}\Omega$. It can be explained by considering a possible spin filtering effect that might be taking place at the hBN/Co electrode. As previously reported, the properties of the FM contact/tunnel barrier interface can strongly influence and even reverse the polarization of the spin current. Such inversion of the spin signal for graphene spin valves with a few-layer hBN tunnel barrier reported by Kamalakar et al. [204] hints towards spin-filtering properties of the hBN/Co contacts. As in graphene there is no charge current-induced spin polarization, the spin filtering effect manifests itself as a sign reversal of the spin signal detected in a LSV. By comparison, the Bi₂Te₂Se spin valve, the low-resistance value of the spin signal corresponds to parallel orientation between the direction of magnetization of the propagating spin-polarized current in the TI and the magnetization of Cobalt detector, while the high-resistance state corresponds to antiparallel orientation. Hence, unlike the graphene case, the spin-momentum locking property of the TI surface states should reverse the spin signal when the bias current is reversed. However, in the case of the detector contact having an opposed spin polarization, there is an interplay between the spin-momentum locking inversion and the spin filter effect at the hBN/Co detector. As a consequence, when the bias is reversed, the hysteresis would be inverted twice - first by the TI itself and then by the detector electrode. This scenario readily explains the observed non-reversible hysteresis, which exhibits a high-resistance state for parallel orientation and a low-resistance state for antiparallel orientation. Along the same lines, Zou et al. [205] have demonstrated inversion of the spin signal in metallic spin valves consisting of a NM Cu channel and Co (or NiFe) FM electrodes. When a break junction tunnel barrier forms at the detector FM-NM interface, a large negative spin signal is detected, whose magnitude is attributed to the strong spin-charge coupling at the high-resistance interface, while its negative sign is assigned to the atomic structure of the interface, which influences the spin-dependent tunneling.

Temperature and angle dependence of the spin signal Fig. 5.7a shows the temperature-dependent spin signal amplitude of a measured device, which is seen to persist up to 15 K. Other devices have provided detectable signals even up to 25 K. The decreasing signal upon warming testifies a reduction of the effective spin polarization of the applied current, which can be attributed to an increased bulk contribution to the conduction due to thermal activation of bulk dopands or increased phonon scattering [206].

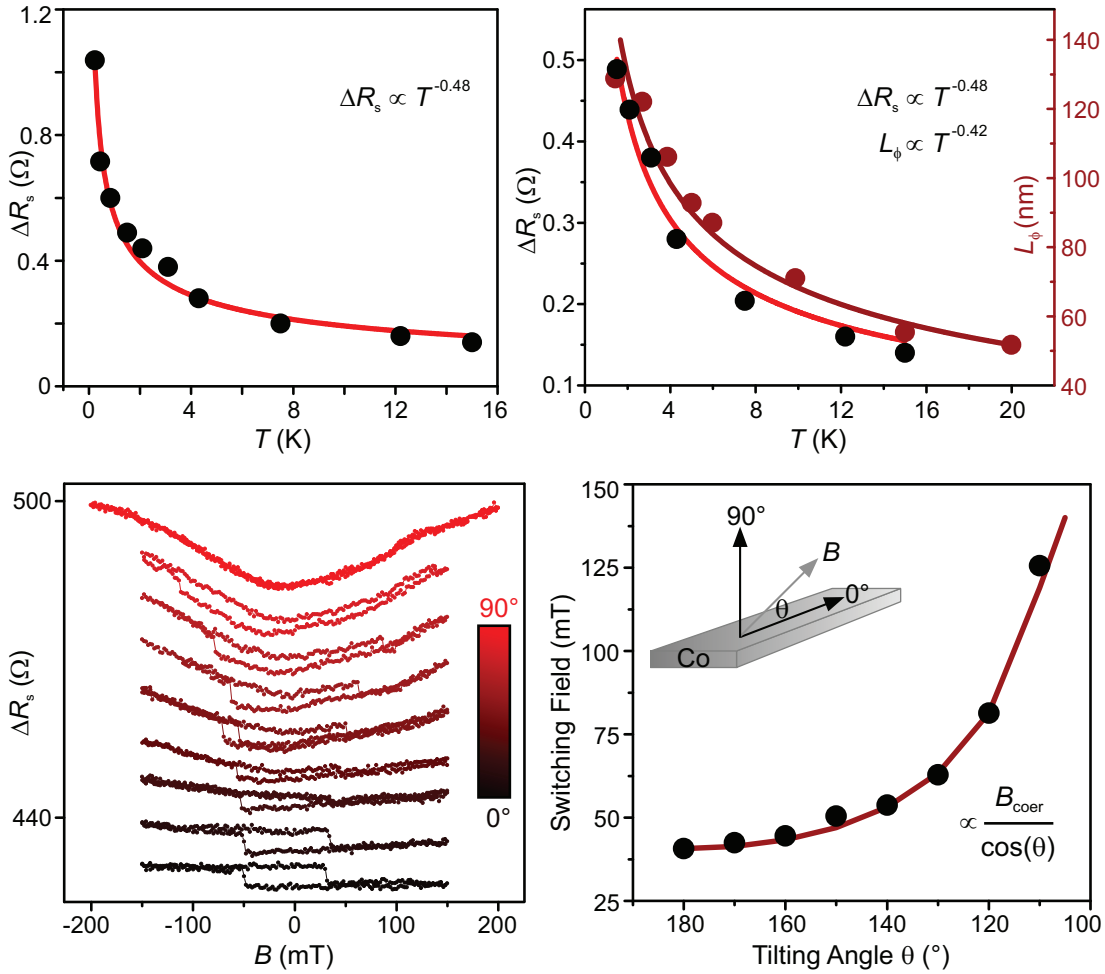


Figure 5.7 – Temperature and angle dependence of the spin signal. a) The spin signal observed up to 15 K for the present device decreases as $T^{-0.48}$ (red fitting curve). b) Comparison of ΔR_s and L_ϕ within the same temperature range. The respective fits (red lines) are as indicated in the inset. c) The dependence of the spin signal on the tilting angle in magnetic field shows that the switching field of the Cobalt detector increases as the rotation angle approaches 90°. d) The spin signal dependence on tilting angle θ can be well fitted with the switching field divided by $\cos(\theta)$ (red line).

The signal decreases as $T^{-0.48}$, which is similar to the behavior of the phase coherence

5.2. Spin valves with Bi₂Te₂Se platelets and tunneling contacts

length $L_\phi \propto T^{-0.42}$ in Bi₂Te₂Se platelets, as extracted from HNL fits of low-field temperature-dependent magnetoconductance data. A direct comparison of the temperature dependence of ΔR_s and L_ϕ is shown in **Fig. 5.7b**.

After the switching hysteresis has been recorded for in-plane magnetic field, the sample is rotated from 0° (in-plane) to 90° (out-of-plane) in order to confirm that the switching is correlated to the switching of the FM detector. The hysteresis is recorded for each rotation angle, as shown in **Fig. 5.7c**. The switching field increases as the rotation angle increases, i.e., the hysteresis becomes wider as the sample is rotated out-of-plane. Furthermore, a more pronounced parabolic magnetoresistance background appears as the out-of-plane component of the magnetic field increases and the spin signal slowly vanishes. The dependence of the switching field on the rotation angle can be well fitted by the coercive field of the FM electrode divided by the cosine of the angle, as shown in **Fig. 5.7d**. This finding confirms that the relative orientation of the spin-polarized current in the TI channel and the magnetization direction of the Co electrode are indeed the origin of the observed hysteresis.

In conclusion, inversion of the spin signal is observed in 3D TI-based LSVs with hBN/Co detector electrodes, whose occurrence depends on the resistance of the TI/hBN/Co interface. Experiments on several devices with different detector contact resistances confirm that the high resistance hBN/Co junctions lead to the unexpected behavior of the spin signal switching hysteresis for different bias polarity. This finding suggests that two counteracting phenomena take place in the operation of the LSV, namely the spin-momentum locking of the surface states and the spin filtering property of the detector. The possibility to manipulate the sign and the magnitude of the spin signal via the thickness of a 2D tunnel barrier underscores the significance of hBN as a spin filter component in heterostructure-based spintronic devices in combination with other 2D materials.

6 Spin-polarized currents in van der Waals graphene/Bi₂Te₂Se heterostructures¹

Further development of the field of all-electric spintronics requires the successful integration of spin transport channels with spin injector/generator elements. While with the advent of graphene and related 2D materials high performance spin channel materials are available, the use of nanostructured spin generators remains a major challenge. Especially promising for the latter purpose are 3D TIs, whose 2D surface states host massless Dirac fermions with spin-momentum locking. Here, we demonstrate injection of spin-polarized current from a topological insulator into graphene, enabled by its intimate coupling to an ultrathin Bi₂Te₂Se nanoplatelet within a van der Waals epitaxial heterostructure. The spin switching signal, whose magnitude scales inversely with temperature, is detectable up to 15 K. Our findings establish TIs as prospective future components of spintronic devices wherein spin manipulation is achieved by purely electrical means.

6.1 Concept and device fabrication

In the devised spin valves, spin injection into graphene occurs from an ultrathin layer of the 3D TI Bi₂Te₂Se, deposited on top of the graphene sheet by van der Waals epitaxy. Epitaxial growth is facilitated by the small lattice constant mismatch of about 1.5% [64] and ensures a close coupling between the two materials, as concluded from an increased carrier mobility of Bi₂Te₂Se nanoplatelets on hBN sheets [65], and corresponding transmission electron microscopy analysis [207]. The compound Bi₂Te₂Se is advantageous due to its relatively high

¹This chapter is based on publication [2] in the CV Publications list, p. 143 (Nano Lett. 16, 4 (2016))

Chapter 6. Spin-polarized currents in van der Waals graphene/Bi₂Te₂Se heterostructures

bulk resistivity [35], large band gap of 310 meV, and reduced n-doping in comparison to Bi₂Se₃. After mechanical exfoliation of highly oriented pyrolytic graphite (HOPG) onto Si substrates covered by a 300 nm thick SiO₂ layer, Bi₂Te₂Se nanoplatelets were grown on top by a catalyst-free vapor-solid process (see **Section 3.1**). To this end, Bi₂Se₃ and Bi₂Te₃ crystal sources (Alfa Aesar, 99.999%) were placed in a tube furnace, close to the homogeneous hot zone. The graphene-covered Si/SiO₂ growth substrates were placed in the colder region, where the temperature gradient can be exploited to adjust the substrate temperature as an important growth parameter. The quartz tube was then evacuated to 80 mbar and the temperature ramped up to 582 °C using well-defined heating rates. As the sources begin to evaporate between 450 and 470 °C a continuous ultrapure Argon flow (6N) of 150 sccm carries the evaporated material over to the deposition substrates where the crystals are formed. In a first lithography step, Ti/Au

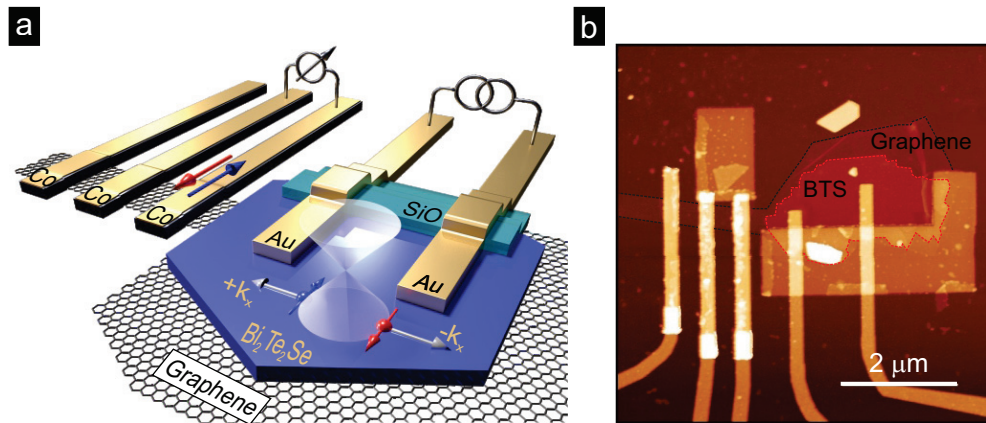


Figure 6.1 – Experimental concept and device structure. **a)** Schematic depiction of the investigated device configuration, with a graphene-TI heterostructure as major component. Due to its spin-momentum coupling, the TI is expected to act as spin polarizer on top of the graphene. The direction of the spin current is determined by the polarity of the applied bias and is detected by a magnetic electrode on top of the graphene channel. **b)** Atomic force microscope image of one of the measured devices.

markers were fabricated and the graphene-TI stacks examined by AFM to determine height profiles and surface morphology. All further patterning was done via e-beam lithography using PMMA resist. The entire device fabrication included four major steps, specifically:

- i)** reactive ion etching to pattern the graphene into strips with widths of 200–300 nm in order to increase the resistance of the graphene/Co interface;
- ii)** thermal evaporation of a 25 nm thick SiO₂ film on a small area covering the edge of the graphene/TI stack, such that later only the TI can be contacted;

iii) pretreatment of the TI contact regions inside a deposition chamber (base pressure of 3×10^{-8} mbar) by 15 sec of argon milling at 10^{-4} mbar in order to remove the surface oxide layer and achieve Ohmic contacts. Subsequently, 2 nm Ti/40 nm Au NM contacts were thermally evaporated at 8×10^{-8} mbar;

iv) definition of FM contacts on the graphene strips by thermal evaporation of 45 nm Co, followed by 10 nm Au as a capping layer to prevent Co oxidation. Prior to the Co/Au deposition, the chamber was evacuated for 2 days and the sample heated up to 70 °C in order to minimize (surface) contaminations and reach the base pressure of the chamber.

Pure metallic Co structures were fabricated in order to confirm the material's ferromagnetic property, as probed by low temperature magnetotransport measurements. The graphene/Co contact resistance was found to fall into the range of 1–5 k Ω , whereas the NM TI/Au contacts displayed values between 200 and 700 Ω . The contact resistances in both cases changed only little upon cooling from RT to 1.3 K. Electrical transport measurements were performed in an Oxford cryostat equipped with a 12 T magnet and a rotatable variable range insert for measurements in the range of 1.3–300 K. The applied 13 Hz AC-signal is offset by a home-built differential operational amplifier module running on batteries. The current is monitored by a DLPCA 200 (FEMTO) and the non-local voltage is pre-amplified using a SRS 560 (Stanford) before digitalization. In total, five devices were characterized for three of which a complete data set was obtained. The spin valve measurements were carried out by passing a constant AC (1 μ A) mixed with a DC (± 5 to ± 20 μ A) current through the NM contacts on top of the Bi₂Te₂Se and measuring the voltage drop between a pair of FM contacts as a function of in-plane magnetic field applied along their easy axis of magnetization perpendicular to the applied bias current.

The device configuration used to detect the spins injected into graphene is schematically illustrated in **Fig. 6.1a**. Importantly, the placement of one NM electrode pair on the Bi₂Te₂Se combined with at least two FM electrodes on the graphene allows for direct comparison between spin injection from a FM Cobalt contact and the TI. Moreover, this configuration allows for non-local 4-terminal measurements, which provide more reliable information compared to local measurements of spin polarization in 3D TIs [208] [209]. The decreased contact area between the Co electrode and the graphene results in increased contact resistance and renders the strongly coupled (transparent) Co contacts suitable as spin probes in the absence of a

tunneling barrier [195]. The electrical transport behavior described below was reproducibly observed for five different devices (see **Fig. 6.1b** for one example).

By using catalyst-free vapor-solid growth, we obtained regularly shaped Bi₂Te₂Se nanoplatelets on mechanically exfoliated graphene, as exemplified in **Fig. 6.2a**. The lateral sizes of as-grown platelets range from 400 nm to 5 μm, depending on the shape of the graphene underneath, while their thickness is between 4 and 15 nm (**Fig. 6.2b**). The growth time is adjusted such that the platelets are still well-separated from each other. In separate magnetotransport experiments on individual Bi₂Te₂Se nanoplatelets grown under similar conditions directly on Si/SiO₂ substrates, we observed weak antilocalization (WAL) features attributable to the 2D surface states of Bi₂Te₂Se for platelet thicknesses above 6 nm.

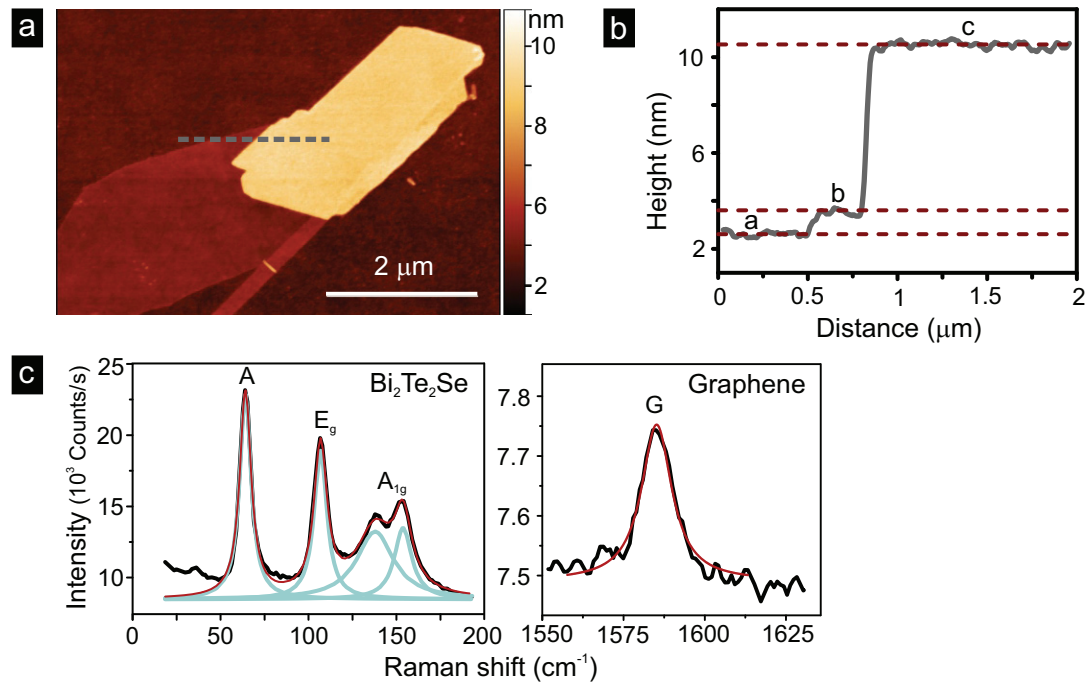


Figure 6.2 – The Bi₂Te₂Se/graphene heterostructure. **a)** AFM image of a graphene-Bi₂Te₂Se nanoplatelet stack on Si/SiO₂ substrate. **b)** Height profile of the heterostructure taken along the dotted line in panel **a)**, where a 6 nm Bi₂Te₂Se platelets (-c-) is grown on top of mechanically exfoliated graphene (-b-) on SiO₂ (-a-). The thickness of as-grown platelets ranges from 4 to 15 nm. **c)** Raman spectrum of a Bi₂Te₂Se nanoplatelet grown on graphene (left) and the G-band in the Raman spectrum of the graphene underneath the same nanoplatelet (right).

6.2 Current-induced spin polarization

Spin injection via a FM contact The first set of experiments addresses spin transport in the narrowed section of the underlying graphene sheet (**Fig. 6.3**). In the used geometry, spin polarized carriers are injected by a Co electrode and detected by a nearby Co contact in a 4-terminal, non-local measurement (**Fig. 6.3a**). The magnetization of both electrodes is governed by the externally applied in-plane magnetic field. The devices display a conventional spin valve effect in the graphene channel, which manifests itself as a change in the non-local voltage/resistance, when the applied current is kept constant (**Fig. 6.3b**). Specifically, the resistance is low when the magnetic injector and detector are magnetized parallel to each other. As one of them reverses its magnetization direction (at a coercive field of 50 mT for an electrode width of 170 nm), the resulting antiparallel alignment causes a sharp resistance increase. Due to the similar lateral width of the injector and detector Co electrodes, the high-resistance plateau is quite narrow, which leads to a peak-like appearance. The sign of the non-local resistance, and therefore the orientation of the switching steps, depends on the sign of the applied bias. No background has been subtracted from the raw data. As a consequence of the suppressed electron-phonon scattering in graphene, the spin signal changes only little up to 40 K (**Fig. 6.3c**). This behavior is in agreement with previous reports on graphene-based spin valves up to room temperature [149]. Back gate-dependent measurements (**Fig. 6.3d**) reveal a minimum of the non-local signal ΔR_{NL} at the charge neutrality point (CNP) which occurs at $V_g = +32$ V for the device shown here. This behavior signifies the presence of transparent ferromagnetic contacts [110], as expected from the direct evaporation of Co onto the graphene strip and can be explained within the one-dimensional (1D) drift-diffusion theory of spin transport [210]. It is furthermore noteworthy that the relatively low resistance at the CNP (8 k Ω) reflects (inhomogeneous) doping of the graphene by PMMA residues accumulated during the device fabrication process [211] and allows for spin detection even at the CNP. For the field-effect mobility, values in the range of 1250–2450 cm²V⁻¹s⁻¹ are extracted from the graphene transfer curves.

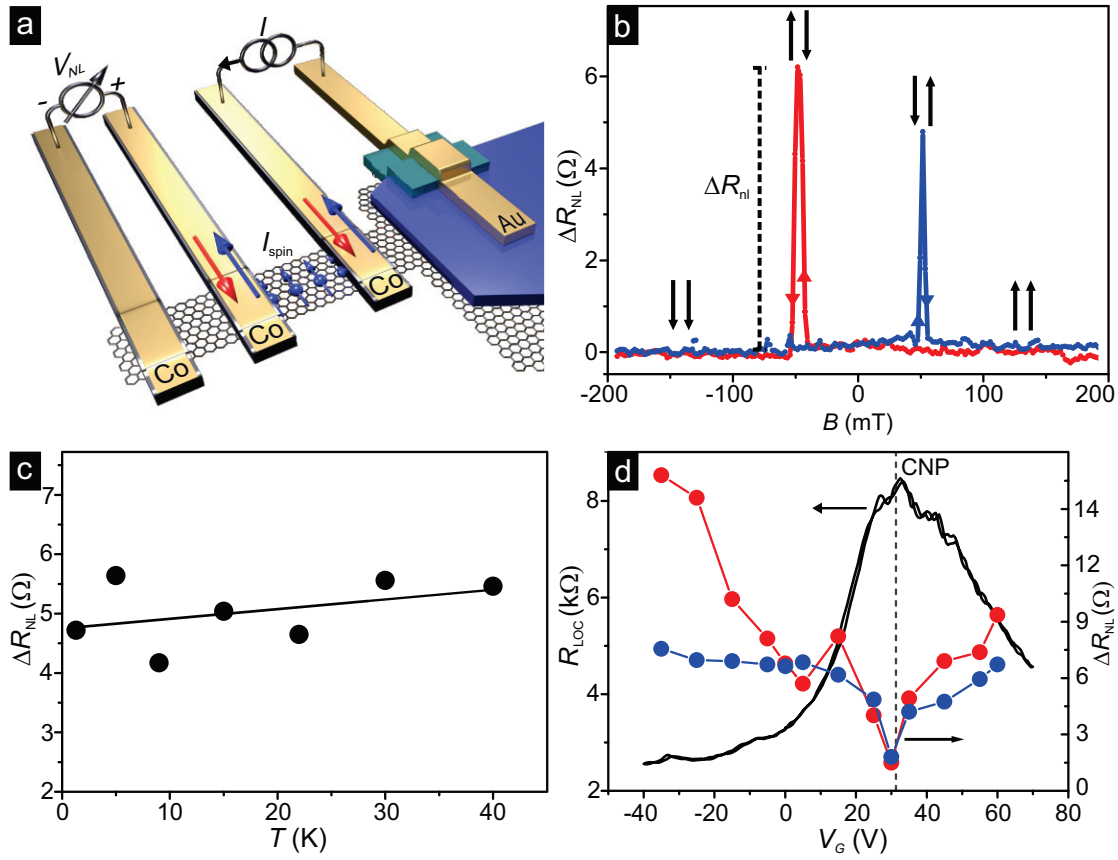


Figure 6.3 – Spin injection into graphene by Co contacts. **a)** Schematic diagram of the spintronic device with 4-terminal non-local measurement geometry. In the present experiments, a magnetic electrode injects spin-polarized carriers into the graphene channel (first Co contact is used as a source, the Au contact as drain), while the neighboring magnetic electrode detects it as a change in the non-local signal (second and third Co electrodes are the voltage probes). **b)** Spin valve effect in graphene, where the non-local resistance change is plotted as a function of in-plane B-field strength. The resistance is low when the injector and detector electrode have the same direction of magnetization, and higher resistance when their magnetizations are antiparallel, as indicated by the arrows. **c)** Non-local resistance change as a function of temperature. The spin valve signal is almost independent of temperature, in accordance with previous studies of graphene-based spin valves. This behavior is due to the fact that electron-phonon interactions in graphene are suppressed even at higher temperatures. **d)** A local resistance measurement reveals graphene’s charge neutrality point (CNP) at $V_g = 32$ V (black curve), consistent with p-type doping during the fabrication process. The gate dependence of the non-local spin valve signal has a minimum close to the CNP (blue and red curve for right and left jump, respectively), indicating that the Cobalt contacts are nearly transparent.

Spin injection via NM/BTS Having established the conventional spin valve operation in the bare graphene section, in the second set of experiments we inject current between two NM Ti/Au electrodes on top of the graphene/Bi₂Te₂Se heterostructure and detect the spin signal

between a pair of FM electrodes on the graphene strip (**Fig. 6.4a**).

Again magnetic field induced resistance switching is observed in the form of a hysteretic step-like voltage signal (**Fig. 6.4c,d**). However, in comparison to the graphene spin valve case, only a single-switch is observed. This difference can be explained by the fact that due to the spin-momentum locking of the TI surface states, the two spin directions parallel to the magnetization axis of the FM electrodes are locked to the two momentum vectors, k_x and $-k_x$, corresponding to positive and negative bias current. For the present devices, this mechanism is confirmed by the effect of reversing the polarity of current injected into the $\text{Bi}_2\text{Te}_2\text{Se}$. For positive bias current, $I_{\text{dc}} = +5\ \mu\text{A}$, the resistance change is consistent with the detector's magnetization being either parallel or antiparallel to the incoming spins (**Fig. 6.4c**). Upon reversing the bias current, $I_{\text{dc}} = -5\ \mu\text{A}$, the resulting hysteresis is mirrored with respect to $B = 0\text{T}$ (**Fig. 6.4d**). Such behavior has likewise been observed in experiments directed toward electrical detection of spin-polarized currents in 3D TIs [87–93]. This finding is consistent with either the injection of spin-polarized current from the $\text{Bi}_2\text{Te}_2\text{Se}$ surface states into the graphene, or the spin Hall effect (SHE) due to proximity-induced SO coupling [160], as both could generate a spin current that is perpendicular to the direction of the charge current imposed onto the BTS. In order to discriminate between the two mechanisms, we performed further experiments addressing the influence of three different parameters, namely the back gate, the temperature, and the thickness of the $\text{Bi}_2\text{Te}_2\text{Se}$ nanoplatelet. The gained results together strongly favor the direct spin injection scenario, as detailed in the following.

Firstly, the spin signal was found to be only little affected and to lack a meaningful physical trend upon application of back gate voltages of up to $\pm 45\text{V}$ (**Fig. 6.5a**). If the SHE were present, the vertical electric field should alter the strength of the interfacial Rashba SO coupling, and thus influence the generated spin imbalance. At the same time, the appreciable n-type doping of the $\text{Bi}_2\text{Te}_2\text{Se}$ sheets accounts for the absence of a sizable gate effect for the spin injection scenario, as the Fermi level can only be slightly shifted even for highest gate voltages [192].

Within the relevant model of 1D spin transport [210] the spin signal ΔR_{NL} is given by

$$\Delta R_{\text{NL}} = 4R_{\text{G}} \exp\left(-\frac{L}{\lambda_{\text{G}}}\right) \left[\left(\left(\frac{P_{\text{J}} \frac{R_{\text{C}}}{R_{\text{G}}} + P_{\text{Co}} \frac{R_{\text{F}}}{R_{\text{G}}}}{1 - P_{\text{J}}^2} + \frac{P_{\text{Co}} \frac{R_{\text{F}}}{R_{\text{G}}}}{1 - P_{\text{Co}}^2} \right) \left(\frac{P_{\text{J}} \frac{R_{\text{C}'}}{R_{\text{G}}} + P_{\text{Co}} \frac{R_{\text{F}}}{R_{\text{G}}}}{1 - P_{\text{J}}^2} + \frac{P_{\text{Co}} \frac{R_{\text{F}}}{R_{\text{G}}}}{1 - P_{\text{Co}}^2} \right) \right] \left[\left(1 + \frac{2 \frac{R_{\text{C}}}{R_{\text{G}}}}{1 - P_{\text{J}}^2} + \frac{2 \frac{R_{\text{F}}}{R_{\text{G}}}}{1 - P_{\text{Co}}^2} \right) \left(1 + \frac{2 \frac{R_{\text{C}'}}{R_{\text{G}}}}{1 - P_{\text{J}}^2} + \frac{2 \frac{R_{\text{F}}}{R_{\text{G}}}}{1 - P_{\text{Co}}^2} \right) \exp\left(-\frac{2L}{\lambda_{\text{G}}}\right) \right]^{-1} \quad (6.1)$$

Chapter 6. Spin-polarized currents in van der Waals graphene/Bi₂Te₂Se heterostructures

where P_J is the polarization of the injected spin current by the Bi₂Te₂Se, P_{Co} is the polarization of the Cobalt contact, R_C and R_C' are the contact resistances, R_G is the graphene channel resistance, L is the distance between injector and detector, λ_G is the spin diffusion length. $R_F = \frac{\rho_{Co}\lambda_{Co}}{A_{Co}}$, where $\rho_{Co} = 115 \text{ n}\Omega\text{m}$ is the Cobalt resistivity at low temperature, $\lambda_{Co} = 6 \times 10^{-8} \text{ m}$ is the spin diffusion length of Cobalt, and A_{Co} is the Cobalt contact area. Using this model, we estimate the spin polarization P_J at the graphene/Bi₂Te₂Se junction to be 10%. Secondly, the resistance change associated with the switching shows a temperature characteristic similar to that of magnetotransport-related phenomena in Bi₂Te₂Se. As apparent from **(Fig. 6.4b)**, the signal decreases significantly with increasing temperature, such that it becomes difficult to detect above 15 K. In the case of WAL [181] in Bi₂Te₂Se, the phase coherence length displays a T^{-n} dependence, where n takes the value $n = 1/2$ for a 2D system and $n = 2/3$ for a 3D system [187]. In previous magnetotransport studies of CVD-grown Bi₂Te₂Se, we have observed WAL features associated with 2D surface states up to about 20 K, which is close to the 15 K mentioned above [192]. Furthermore, in studies of Bi₂Te₂Se and (Bi_{0.53}Sb_{0.47})₂Te₃ devices, where the TI serves as both spin injector and spin transport channel, spin transport has been observed up to 20 K in Bi₂Te₂Se [89] and up to 10 K in (Bi_{0.53}Sb_{0.47})₂Te₃ [90]. These findings have been attributed to an increasing impact of the bulk TI states with increasing temperature. For the present spin valve devices, the extracted spin signal ΔR_{NL} exhibits a T^{-n} dependence with $0.4 < n < 0.7$. This range, obtained from all measured devices, is in close correspondence to the above mentioned WAL dependence, providing additional support that the spin generation occurs within the 2D surface states. **Fig. 6.5b** illustrates the similar dependence of the spin signal and of the phase coherence length, L_Φ , as extracted from the WAL magnetoconductance measurements on Bi₂Te₂Se, analogous to the data published by Tang et al. [90].

Thirdly, the spin signal, acquired at $I_{dc} = 5 \mu\text{A}$ for several different devices with different Bi₂Te₂Se thicknesses, is seen to scale inversely with the thickness of the Bi₂Te₂Se platelets **(Fig. 6.5c)**. This trend underscores that the main contribution to the measured signal stems from the Bi₂Te₂Se surface states, as contributions from the bulk of the nanoplatelets become more significant with increasing Bi₂Te₂Se thickness, analogous to conclusions drawn from spin-polarized current detection experiments on Bi₂Se₃ [87].

We also investigated the dependence of the spin signal on the applied DC bias current for spin injection via the Bi₂Te₂Se. Upon applying bias currents of up to $\pm 20 \mu\text{A}$, a signal maximum is observed at $I_{dc} = \pm 5 \mu\text{A}$, as shown in **Fig. 6.5d**. Previous studies on TI-based spin valves found both linear [87] [92] and non-linear [89] [93] dependence of the measured spin signal on the

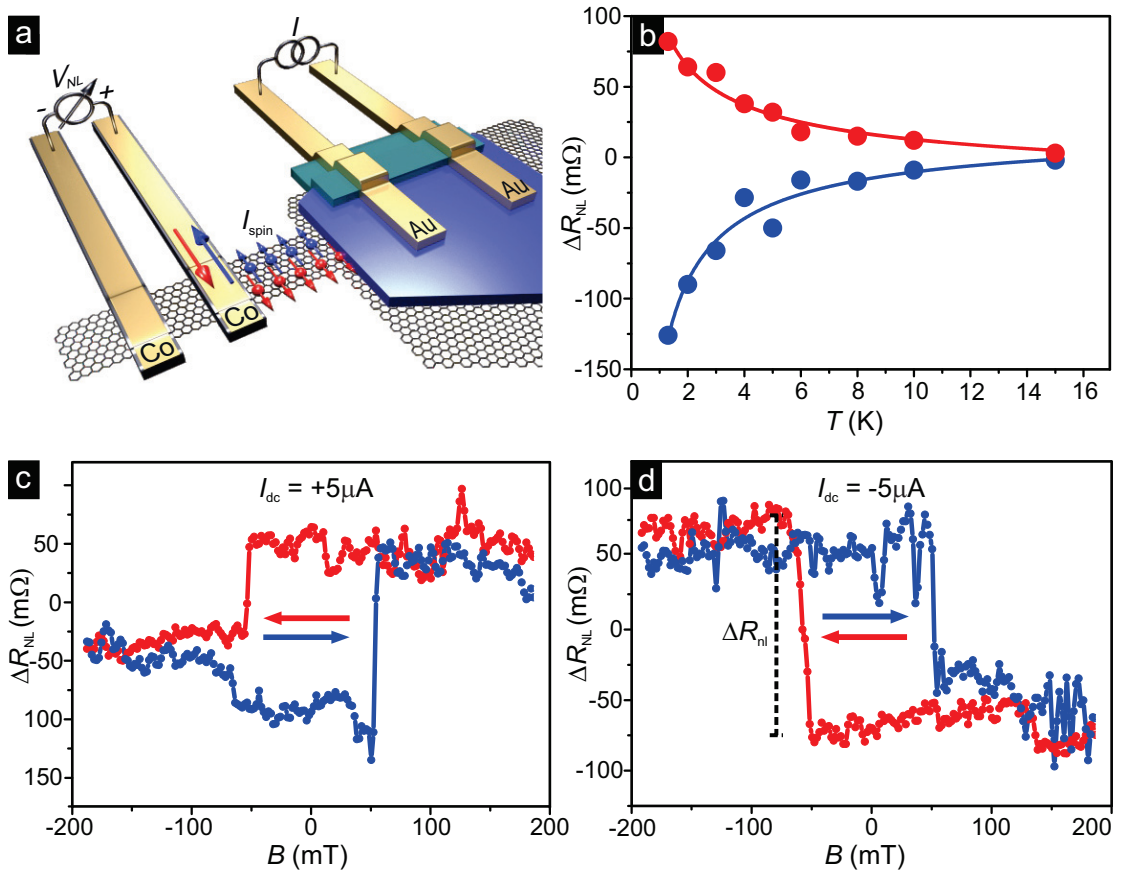


Figure 6.4 – Electrical detection of spin currents in graphene injected from Bi₂Te₂Se as spin polarizer. **a)** Schematic diagram of the spintronic device with 4-terminal non-local geometry. In the present measurement configuration, the net spin current generated in the TI is injected into the graphene channel in a direction depending on the polarity of the applied bias (the left Au electrode serves as a source, the right one as drain). A magnetic Co electrode on the graphene strip serves as spin current detector. **b)** Plot of the spin valve non-local signal in dependence of temperature for positive (blue) and negative (red) B-field. The data closely follow a T^{-n} dependence, where $n = 0.7$ and $n = 0.5$, respectively. **c)** Spin valve non-local signal, detected as electrical resistance change upon reversing the magnetization direction of the magnetic detector electrode with respect to the incoming spin current. The measurement is taken at a bias current of $I_{\text{dc}} = +5 \mu\text{A}$, for which maximum signal was observed. **d)** For reversed sign of applied bias, the hysteresis is mirrored proving that the TI injects spin-polarized current into the graphene channel. No linear magnetoresistance background has been subtracted from the data.

applied bias. For those devices, bias currents on the order of μA to mA have been applied in order to induce spin polarization. By comparison, the Bi₂Te₂Se platelets in our devices have much smaller dimensions (6–15 nm thickness, 1–3 μm lateral size), which leads to substantially higher current densities. On this basis, we attribute the spin signal decrease at larger bias to

Joule heating effects in the Bi₂Te₂Se nanoplatelet.

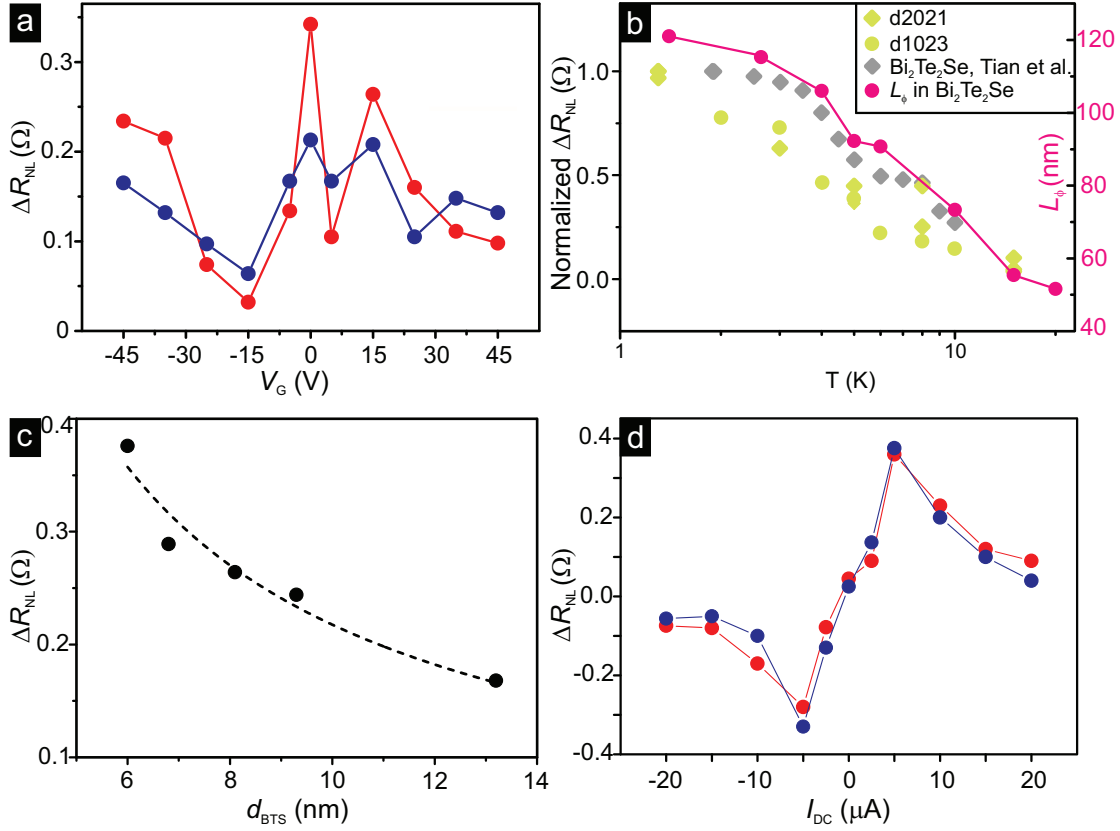


Figure 6.5 – Spin signal dependencies. **a)** No sizable dependence of ΔR_{NL} on the back gate voltage in the range of ± 45 V applied across the 300 nm SiO₂ dielectric layer for positive (blue) and negative (red) B-field. **b)** The temperature dependences of ΔR_{NL} and the phase coherence length, extracted from magnetoconductance measurements of Bi₂Te₂Se, exhibit a similar trend. **c)** ΔR_{NL} acquired at $I_{dc} = +5 \mu A$ for five different Bi₂Te₂Se platelet thicknesses, which scales inversely with the thickness, suggesting that the measured spin signal is very likely to originate from the Bi₂Te₂Se surface states. **d)** ΔR_{NL} , as a function of bias current, I_{dc} in the range $\pm 20 \mu A$. A maximum is observed for $I_{dc} = \pm 5 \mu A$, after which the signal decreases with increasing bias.

6.3 Hanle spin precession measurements

Finally, with the aim of determining the spin relaxation times, we performed Hanle measurements by applying current between the non-magnetic Au electrodes and detecting ΔR_{NL} via the magnetic Co electrodes, while applying an out-of-plane magnetic field. The detector magnetization is first aligned in-plane by an external magnetic field, followed by tilting the device by 90° with respect to the magnetic field axis. This leads to a precession of the spins with the

Larmor frequency, $\omega_L = \frac{g\mu_B B_{\text{perp}}}{\hbar}$, while they propagate toward the detector, as schematically illustrated in **Fig. 6.6a**. For zero magnetic field and positive bias, the spins arrive parallel to the detector and the signal exhibits a maximum. With increasing magnetic field the signal becomes proportional to $\cos(\theta)$, i.e., the projection of the spin direction onto the direction of the detector's magnetization and ΔR_{NL} decreases. Like for the spin valve signal in **Fig. 6.4c,d**, reversing the bias polarity causes a flip of the Hanle curve (**Fig. 6.6b**). In order to extract the spin life times, we fitted the Hanle data to the equation:

$$R_{\text{NL}} \propto \int_0^{\infty} \frac{1}{\sqrt{4\pi Dt}} \exp\left[-\frac{L^2}{4Dt}\right] \cos(\omega_L t) \exp\left[-\frac{t}{\tau_s}\right] dt \quad (6.2)$$

where τ_s is the spin lifetime, L is the contact separation, and D is the spin diffusion constant [110] [151]. The fits yield spin lifetimes in the range of 90–110 ps, spin diffusion lengths on the order of 400 nm for spins propagating in the graphene channel, and corresponding spin diffusion constants between 1.2×10^{-4} and $3.4 \times 10^{-4} \text{ m}^2\text{s}^{-1}$. Previous studies of spin current injected into graphene have found spin lifetimes of up to 6.2 ns in bilayer graphene at 20 K in the presence of an MgO tunnel barrier [212] and diffusion lengths on the order of several microns [213] [146] [147]. Additionally, quite large spin lifetimes of up to 65 ns [214] have been observed for conduction electrons by electron spin resonance (ESR) measurements, attributable to the absence of metallic contacts or substrate effects [215]. Like for the spin valve resistance change, ΔR_{NL} , a fast decay with increasing temperature also occurs for the amplitude of the Hanle curves, which are detectable only up to 10 K (**Fig. 6.6d**). Nonetheless, the diffusion length remains almost constant up to this temperature, which proves that the fading amplitude of the Hanle curves is solely due to diminished spin polarization within the $\text{Bi}_2\text{Te}_2\text{Se}$, rather than processes within the graphene itself.

Hanle curves measured for comparison using the Co injector (**Fig. 6.6c**) reflect similar diffusion lengths on the order of several hundreds of nm, along with a significant signal decrease with increasing temperature. In principle, the Hanle signal should persist up to higher temperatures [149]. However, two factors need to be taken into account in this respect. Firstly, the graphene quality is significantly decreased due to the multiple fabrication steps that leave behind surface contaminations on the graphene. Secondly, the Co contacts are strongly coupled to the graphene, which has previously been considered as an impediment in Hanle experiments. In fact, for transparent contacts, appreciable contact-induced spin relaxation and consequently shorter lifetimes on the order of 100 ps [149] [142] have been reported.

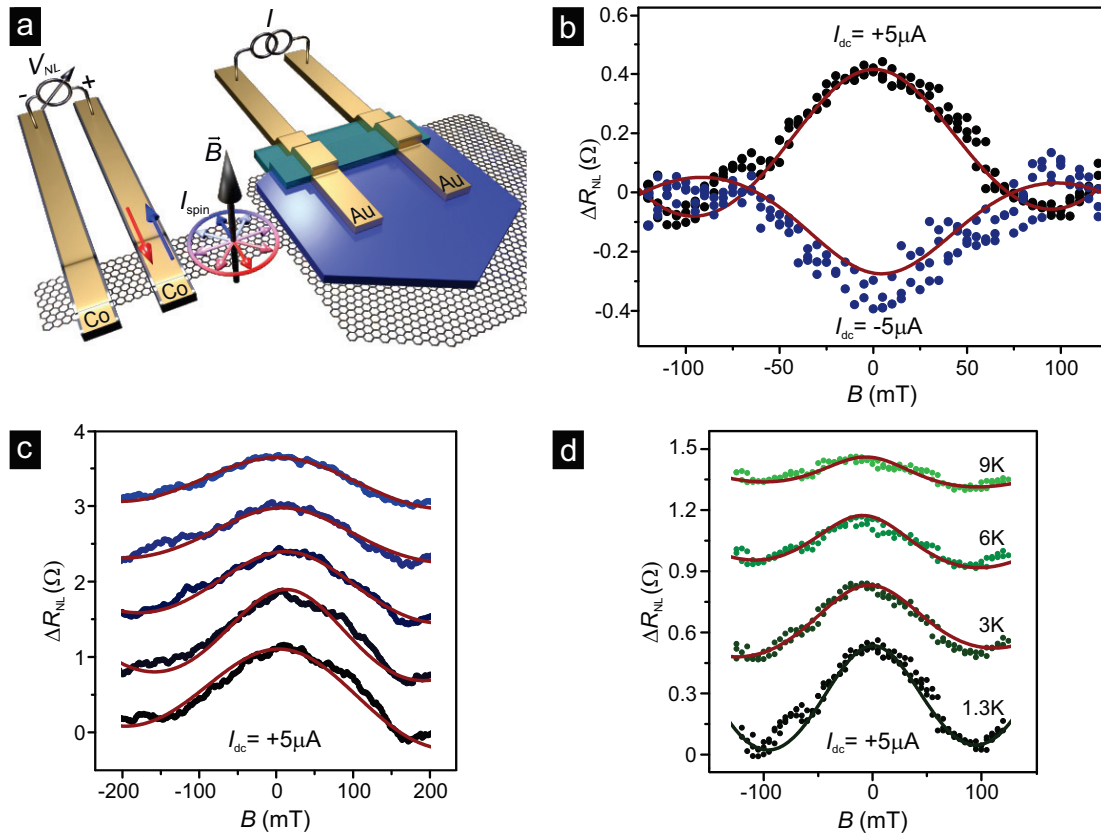


Figure 6.6 – Hanle spin precession. **a)** The Hanle effect is induced in the graphene channel when an external out-of-plane magnetic field is applied. The spins injected by the TI and transported in the graphene start precessing around this field and thus arrive at the detector electrode having a different orientation. The detected signal has a maximum at $B = 0$ T and decreases as the field increases and reorients the spins. **b)** Low temperature ($T = 1.3$ K) Hanle data for positive and negative bias where changing the bias current direction flips the Hanle peak. The solid lines are fits to the data using Eqn. 6.2, which yield a spin life time of 107 ps and a diffusion length of 430 nm. **c)** Temperature dependence of the Hanle curves measured for the Co injector geometry. The similarly small diffusion constant and spin life time are attributed to the resist residues on the graphene after the multiple fabrication steps. **d)** Temperature dependence of the Hanle curves measured for the Bi₂Te₂Se/Au-injector geometry, where the spin signal is seen to decrease as the sample temperature approaches 10 K. The solid lines are fits to the data and the curves are offset for clarity.

In summary, it follows that intimate coupling between a 3D TI and graphene allows for exploiting the SO-induced spin-momentum locking in the TI for injecting spin-polarized currents into the adjacent graphene sheet. Our findings represent a major advancement toward the realization of novel spintronic device designs for energy efficient spin-logic applications. Moreover, the demonstrated devices open perspectives for realizing efficient spin-charge con-

6.3. Hanle spin precession measurements

version by combining spin conserving transport channels with spin generator materials. Due to the non-magnetic character of the TI injectors, the present devices open up novel, intriguing prospects for the development of all-electric spintronics. In future studies, the $\text{Bi}_2\text{Te}_2\text{Se}$ system could be replaced by a TI with improved properties, such as the tetradymite $\text{Bi}_{2-x}\text{Sb}_x\text{Te}_{3-y}\text{Se}_y$, whose Fermi level position favors dominating surface state contribution [39].

7 Summary and Outlook

The significant recent advances in the field of spintronics have been enabled by the improved understanding and control of spin dynamics in novel materials. Of particular interest are non-magnetic materials, in which the presence of SO coupling or symmetry-related properties open up exciting opportunities towards the development of novel nanoscale spintronic devices. The strong SO coupling in Dirac materials, such as 3D TIs, gives rise to topologically non-trivial helical 2D electronic surface states, a property that renders them promising as spin generators. At the same time, 2D TIs host 1D edge states, which open the door to exploration of the QSHE. In real TI materials, the dissipationless surface/edge transport is almost always combined with contributions from bulk charge carriers, as inferred from ARPES measurements and evident from magnetotransport experiments on TIs, in which crystal defects push the Fermi level out of the band gap and pin it to the bulk.

The first part of this thesis addressed the electronic properties of four different Dirac materials by low-temperature magnetotransport experiments. Two 3D TI materials, Sb_2Te_3 and $\text{Bi}_2\text{Te}_2\text{Se}$, were synthesized by a CVD approach. The growth parameters were optimized in order to obtain different morphologies, such as thin platelets, nanoribbons, and nanowires. Additionally, a layered Dirac semimetal, ZrTe_5 was investigated. Its charge transport behavior indicates a significant surface state contribution to the conductance and a higher mobility, as compared to the other studied materials.

Finally, a naturally occurring 3D TI, Aleksite, was studied, in which the presence and behavior of the WAL effect and the pronounced UCFs indicate surface state contributions to the conductance. Coherence lengths much larger than the sample width were recorded that point toward a dimensional crossover. It was established that the nature of the transport changes from 2D to 1D depending on the sample's size.

The second experimental part deals with the detection of current-induced spin polarization generated within the surface states of 3D TI nanowires and platelets. Lateral spin valve devices, based on the ternary $\text{Bi}_2\text{Te}_2\text{Se}$ were fabricated, in which the applied current was spin-polarized by the TI and was detected by a FM electrode for two different cases of contact coupling strength of the FM/TI interface. In the first case, current-induced spin polarization generated within the surface states of thin TI films was demonstrated for transparent contacts in the absence of a tunnel barrier. In the second case, in order to improve the quality of the spin signal, an hBN tunnel barrier was incorporated. The hBN/FM interface of the spin detector contact was found to increase the magnitude and the reproducibility of the measured spin signal, such that also the temperature and bias dependences of the signal could be investigated. Additionally, a spin signal inversion property of the hBN/Co has been observed, which acts as a spin filter in the spin detection process.

The experimental results of the third part demonstrate for the first time spin injection and detection in an epitaxial heterostructure, comprised of $\text{Bi}_2\text{Te}_2\text{Se}$ and graphene. It combines the spin generation properties of a TI with strong SO coupling with the spin conservation properties of graphene, whose long coherence lengths and spin lifetimes are a consequence of its extremely weak SO coupling. The spin-momentum locking of the TI 2D surface states allows for direct control of the spin current via purely electrical means and the graphene serves as a spin transport channel. Additionally, the device allowed for direct comparison between a standard graphene spin valve fabricated with all-FM contacts and a TI injector-based spin valve, where the spin current is generated by the TI. These findings shed light onto spin-charge conversion in heterostructures and open up exciting opportunities for the development of a novel generation of nanoscale spintronic devices.

Based upon these results, various follow-up experiments could provide a deeper insight into the electronic properties of the investigated 3D TI compounds, and lead to better device performance and possible applications. Especially promising is the combination of Dirac materials into heterostructures, whose interface properties need to be further explored. Along these lines, the most important perspectives are outlined in the following.

7.1 Spin-charge conversion properties of TI/2D material interfaces

The experimental observation of spin-polarized currents in a TI/graphene heterostructure opens up the possibility to exploit the spin-momentum locking in 3D TIs in order to efficiently transfer spin-polarized currents into an adjacent 2D system. An exciting perspective is the

7.2. Spin detection in TI/graphene heterostructures with NM electrodes

development of all-electric spintronic devices and gaining a better understanding of the electronic interactions at the interface between 3D TIs and 2D materials.

In order to improve the spin injection efficiency, the problem of the interfering bulk needs to be addressed. In the currently accessible devices, the magnitude and the temperature dependence of the measured spin signal is still compromised by the TI bulk states. In order to overcome this problem, TI materials whose Fermi level can be efficiently tuned into the band gap are required. One promising candidate is Sb-doped $\text{Bi}_2\text{Te}_2\text{Se}$, specifically the quaternary system $\text{Bi}_{2-x}\text{Sb}_x\text{Te}_{3-y}\text{Se}_y$, whose surface states have been reported to make a sizable contribution to the electronic transport [216]. A promising alternative is Sb-doped Bi_2Te_3 , in particular $(\text{Bi}_{1-x}\text{Sb}_x)_2\text{Te}_3$ with x close to 0.9 [217]. Nanoplatelets of both these compounds can be synthesized by the established CVD method (Section 3.1). In the growth experiments, the desired stoichiometry has to be adjusted by controlling the relevant parameters, specifically the mixing ratio of the components, the temperature profile inside the growth furnace, and the gas flow rate. In order to effectively adjust the Fermi level in the above compounds, a top gate could be implemented [218]. In combination with the available bottom gate, it should allow to independently tune the two surfaces into the n- and p-type regime [219].

7.2 Spin detection in TI/graphene heterostructures with NM electrodes

A further step towards the realization of an all-electric spintronic device may be achieved by the fabrication of TI/graphene spin injection devices in which some of the FM detector electrodes are replaced by NM ones. A schematic diagram of such geometry and an optical micrograph of prototype devices are shown in Fig. 7.1. For these devices, a number of configurations are possible, most prominently (i) the distance between the Co and the Au spin detector probes can easily be varied within the same device, allowing to directly probe the spin coherence length; (ii) the Co contacts can be decoupled by a tunneling barrier, thereby increasing the detection efficiency in both spin-valve and Hanle precession measurements; (iii) a top gate can be incorporated, in order to electrostatically tune the Fermi level and decrease the bulk interference with the spin signal that originates from the surface states.

The possibility of spin detection with NM Ti/Au electrodes has been demonstrated for extended graphene sheets in a non-local measurement geometry [158]. The underlying mechanism has been ascribed to a non-linear interaction between spin and charge which leads to a potential difference longitudinal to the spin current. The detection of second harmonics

signals requires a high quality graphene channel. This could be achieved by a solvent-free graphene transfer [148], or through hBN-encapsulated graphene [145] [154] [155]. These approaches are able to preserve the properties of pristine graphene and would lead to larger spin coherence lengths in the graphene channel.

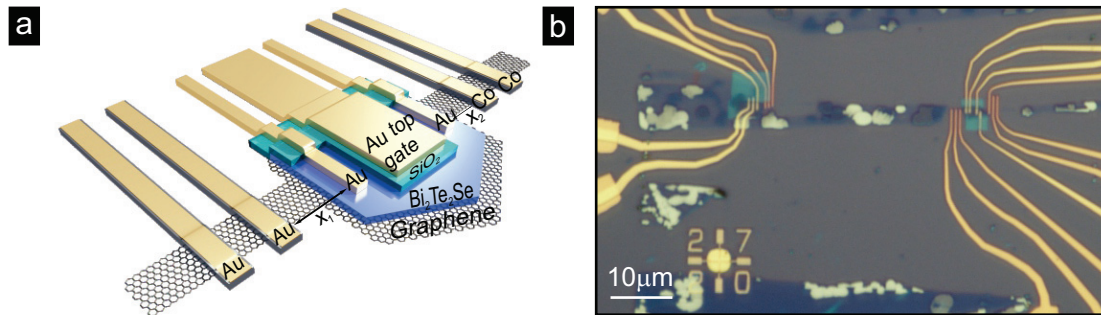


Figure 7.1 – Lateral spin valve geometry patterned onto a $\text{Bi}_2\text{Te}_2\text{Se}$ /graphene heterostructure. **a)** Schematic diagram of the device, where the graphene is etched into a strip on both sides of the $\text{Bi}_2\text{Te}_2\text{Se}$, enabling the deposition of mixed FM and NM electrodes. The distance between the detector contacts can be varied, in order to estimate the spin coherence length. Additionally, non-linear detection of spin signals could be achieved in the absence of a FM detector. **b)** Optical micrograph of ready fabricated devices with NM electrodes for non-linear detection of the net spin polarization in the graphene channel.

7.3 Proximity-induced SO coupling in TI/graphene heterostructures

A TI/graphene heterostructure is an exciting platform for exploring the interaction mechanism between the two materials. Most intriguing is the possibility to exploit the strong SO coupling of the TI in order to enhance the one in graphene. Alternatively, such enhancement has been attempted by chemical modification, such as hydrogenation [159] [160] or fluorination [220], as well as by heavy metal deposition. It has been documented that metallic Pb islands are able to impart strong SO coupling onto graphene, as evidenced by scanning tunneling spectroscopy [221]. Unfortunately, both approaches can lead to disorder and decreased mobility. Proximity-induced SO coupling can also be achieved for example in heterostructures via the proximity of a suitable material with large SO coupling. One such material is the TMD WS_2 and it has been recently shown that when mechanically transferred on top of graphene, it imparts a SO coupling of up to 17 meV onto the graphene [160], which is about three orders of magnitude larger than the intrinsic one. Alternatively, WS_2 has been used as a substrate for graphene. In this case, electronic transport measurements have shown the emergence of WAL

at low temperatures and a strongly reduced spin relaxation time [222].

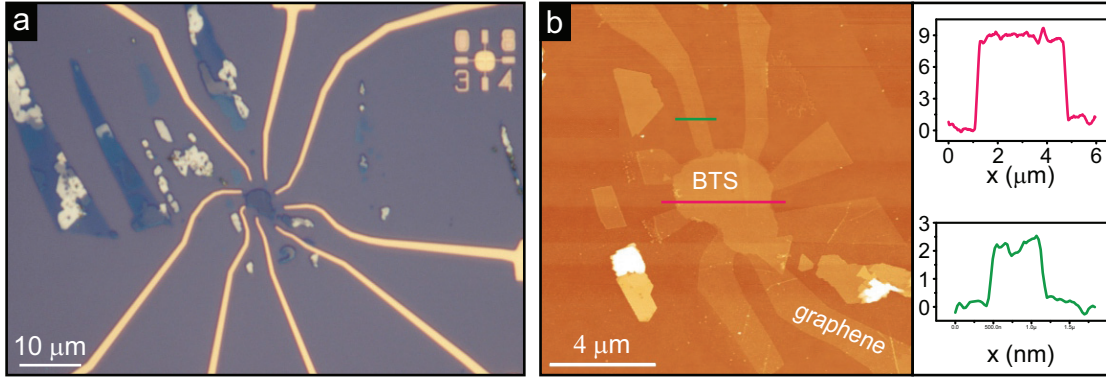


Figure 7.2 – Towards enhanced SO coupling in graphene. **a)** Optical micrograph of a fabricated device, where the graphene in a $\text{Bi}_2\text{Te}_2\text{Se}$ /graphene heterostructure is patterned by RIE into multiple long arms, which are electrically contacted with Ti/Au. **b)** AFM topography of the structure after the RIE step and height profiles of both materials (red: heterostructure, green: graphene).

In the last stage of this thesis, first devices have been fabricated in order to test the possibility to detect interface-induced SO coupling in graphene via its proximity to a TI. For this purpose, the epitaxial 3D TI/graphene heterostructures are especially promising owing to (i) the presence of heavy Bi atoms, (ii) the intimate coupling of the two components, and (iii) the lattice alignment achieved by van der Waals epitaxy, which is not possible in the case of a simple layer transfer that has been used for the TMD/graphene heterostructures mentioned above. **Fig. 7.2a** displays a ready fabricated device, in which a $\text{Bi}_2\text{Te}_2\text{Se}$ thin platelet is epitaxially grown on top of exfoliated graphene. The latter is subsequently patterned into multiple protruding arms, as more clearly seen in the AFM topography image in **Fig. 7.2b**, which are then electrically contacted with Ti/Au. The magnetotransport measurements have been carried out in a Hall bar geometry, as shown in **Fig. 7.3a**. The longitudinal resistance R_{xx} has been recorded by applying current to the contact pair 1-6 and detecting a voltage drop between electrodes 2-3 or 4-5. Its temperature and back-gate voltage dependence was investigated under perpendicular magnetic field (up to 14 T). From the local transport data, the position of the charge neutrality point (doping effects) and the carrier mobility can be determined. The Fermi surface size is commonly determined from the period of the SdH oscillations. SO coupling would give rise to a spin-split Fermi surface with different spin polarizations. It is thus expected that the SdH oscillations exhibit two frequencies that would allow to directly determine the SO interaction parameter α . The gate voltage dependence of the frequencies indi-

Chapter 7. Summary and Outlook

cates for the type of SO splitting (for instance Rashba), as recently reported for graphene/TMD heterostructure devices [223]. Critical for the observation of pronounced SdH oscillations in the present BTS/graphene samples is the preservation of the high graphene quality. The first local measurement of $\text{Bi}_2\text{Te}_2\text{Se}$ /graphene Hall bar devices is shown in **Fig. 7.3b**, where pronounced SdH oscillations are visible at higher fields for different gate voltages.

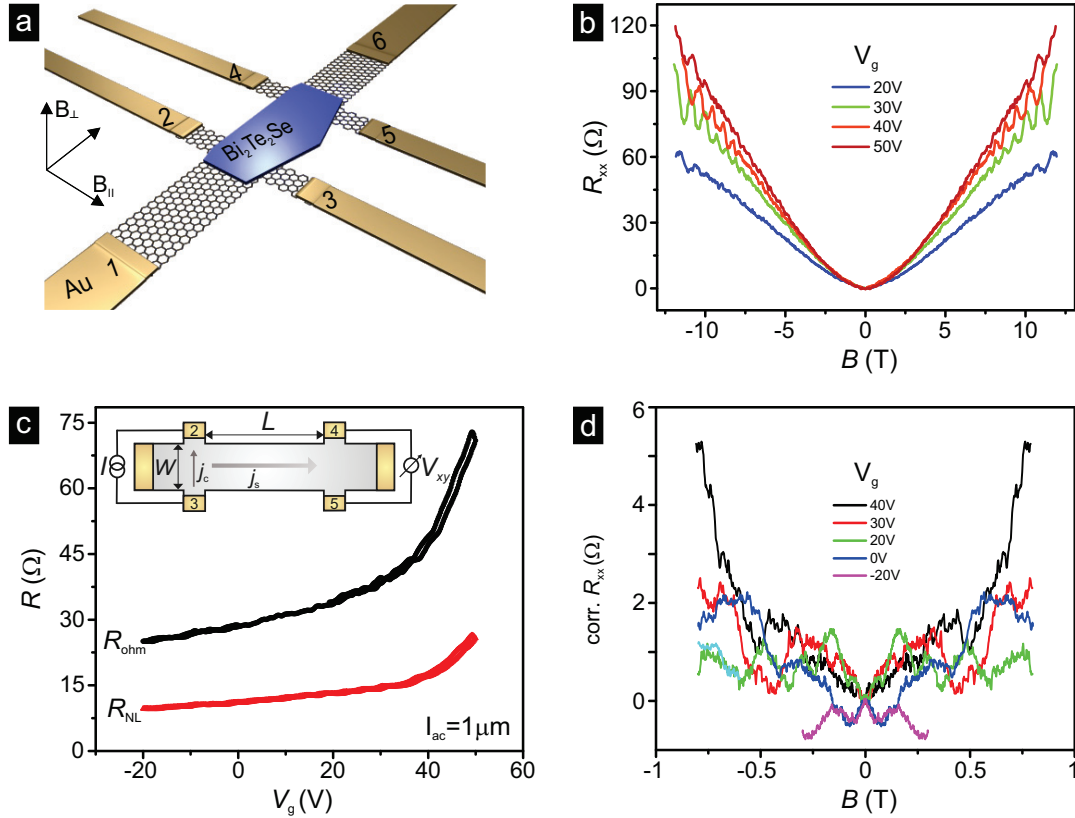


Figure 7.3 – First electronic transport measurements of $\text{Bi}_2\text{Te}_2\text{Se}$ /graphene Hall bar structures. **a)** Schematic diagram a $\text{Bi}_2\text{Te}_2\text{Se}$ /graphene heterostructure patterned into a Hall bar. **b)** First magnetoresistance measurements under perpendicular magnetic field, revealing SdH oscillations at large fields for a range of gate voltages. **c)** Comparison of the Ohmic and the non-local resistances at zero B-field. The inset shows a schematic diagram of a Hall bar sample of width W and length L , where the charge current density j_c generates spin current density j_s , if the SHE is present. **d)** Corrected magnetoresistance at low magnetic fields, exhibiting strong UCF oscillations and a peak at zero B-field, which undergoes a transition from WL to WAL for positive gate voltages.

Furthermore, the non-local resistance R_{NL} is recorded as a function of gate voltage, when current is applied between electrodes 2-3 and voltage drop is measured between electrodes 4-5. In the presence of enhanced SO coupling, it is expected that the non-local resistance R_{NL} magnitude would exceed the Ohmic longitudinal resistance $R_{\text{Ohm}} = \rho_{\text{xx}} \cdot e^{-\pi \cdot L/W}$. A direct

7.3. Proximity-induced SO coupling in TI/graphene heterostructures

comparison of these two quantities is shown in **Fig. 7.3c**, where the zero-field R_{NL} and R_{Ohm} are plotted together. Even at high positive gate voltages up to 50 V, the Dirac point is not visible, suggesting that the graphene in the present device was strongly p-doped during the fabrication process. Here, the Ohmic contribution is larger than the non-local one, suggesting that there is no appreciable enhancement of the SO coupling. However, the conclusions drawn from this comparison depend strongly on the sample geometry, more precisely on the W/L ratio of the graphene H-bar. In the case of large W , like for the present sample, it is hard to clearly distinguish between the local and non-local contributions.

Fig. 7.3c (inset) shows a schematic geometry of a non-local spin-mediated charge transport. The charge current applied between electrodes 2-3 generates a spin current, which diffuses in a direction perpendicular to the applied current, as governed by the mechanism of SHE. The distance it propagates is determined by the spin diffusion length L_s , and the voltage probes 4-5 detect the spin-induced transversal voltage. The non-local contribution only exceeds the Ohmic one, when $W \ll L_s$ [224]. Thus, in future experiments optimization of the device geometry might enhance the non-local contribution, such that it can be distinguished from the Ohmic transport.

Furthermore, for low perpendicular magnetic fields, SO coupling-induced WAL might emerge. Evaluation of the magnetoconductance data yields the spin relaxation time τ_s as a measure of the SO coupling strength [222]. The first magnetoresistance data obtained for a range of gate voltages (**Fig. 7.3d**) exhibits pronounced UCF oscillations, which make it difficult to determine whether or not there is a quantum correction to the magnetoconductance around zero B-field. Interestingly, when recording R_{xx} with a very small step size of 500 μT , a crossover between WL and WAL is observed for positive gate voltages. However, in order to obtain more conclusive results, further devices with optimized geometry need to be investigated. Moreover, to get a clearer picture around zero B-field, ensemble averaging for multiple gate voltages has to be performed in order to suppress the UCFs. Additionally, it would be interesting to study the dependence of the non-local signal under in-plane magnetic field. Since the induced spin current j_s points out of plane, an external in-plane magnetic field parallel to the applied charge current should give rise to Hanle precession. Detection of this precession would give access to the spin relaxation time and the spin diffusion length in the graphene channel.

7.4 The TI/graphene heterostructure for optospintronic experiments

Complementary to the magnetotransport studies, it is of interest whether signatures of the TI surface states can be detected by circularly polarized light. A similar goal has already been approached by a photoconductivity study on Bi_2Se_3 sheets using circularly polarized light [130]. Although the direction of the induced photocurrent could be controlled by the direction of the circular polarization, the interpretation of the obtained data is complicated by the large thickness of the Bi_2Se_3 sheets (≈ 120 nm), which favors bulk contributions to the transport. Additionally, the global laser illumination includes also the regions close to the electrical contacts. Better suited are 3D TI/graphene heterostructures, in which the graphene's atomic layer thickness and close proximity to the TI surface render it into a close-to-ideal detection platform for the generated photocurrent. Moreover, a local laser illumination (using a laser spot size below $1 \mu\text{m}$) would enable the detection of the photoresponse of the TI sheet itself. An additional, intriguing option is to use the circularly polarized light to "optically pump" the spins within the 3D TI and detect them electrically after their lateral diffusion along the graphene.

A Recipes

A.1 CVD graphene/CVD hBN wet etching and transfer process

- (i) Prepare a polystyrene solution by dissolving 50 mg polystyrene into 1 ml toluene.
- (ii) Drop-cast a small amount of the solution on top of the Cu/hBN stack, taking care that the solution does not spread onto the bottom side, and hold the stack above a hot plate for 1–2 min until the film hardens. Place on a hot plate and bake for additional 2 min at 130°C.
- (iii) Prepare an etching solution of DI H₂O, HCl, H₂O₂ (40/7.5/2, v/v/v) and float the Cu/hBN/polystyrene stacks on top for 30–40 min.
- (iv) Transfer the stacks to DI H₂O.
- (v) Transfer to a solution of HCl and DI H₂O (1/30, v/v) followed by 2-3 more transfers to DI H₂O.
- (vi) Fish out the stack with a substrate (Si/SiO₂), which has been pretreated with O₂-plasma in order to achieve better surface adhesion.
- (vii) Carefully dry the bottom of the substrate and blow dry at very low nitrogen gas flow in order to reduce the amount of water trapped between the stack and the substrate. Place onto a hot plate at 40°C and increase the temperature slowly until the water evaporates completely and the stack lies as a smooth film on top of the substrate.

(viii) Place the substrate in a toluene bath at 45°C for 1 hr in order to remove the polystyrene.

The above recipe works for the the Cu etching and transfer of 2D films on top of SiO₂ or other chemically inert materials. Special care needs to be taken, when transferring graphene or hBN on top of TI materials, since they react with acids and water, such that their structural stability and properties are severely altered/damaged. In this case, the hBN/polystyrene stack is transferred to isopropanol after step (v). Subsequently, the substrate containing the TI film on top is used to fish out the hBN/polystyrene stack, which is typically more challenging due to the smaller surface tension of isopropanol in comparison to water.

A.2 Flipping of epitaxial Bi₂Te₂Se/graphene stacks

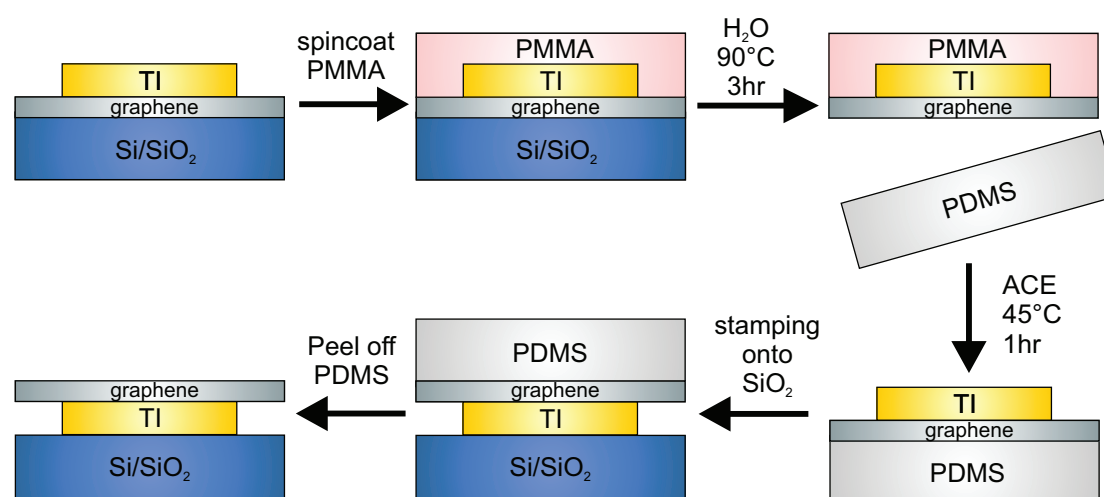


Figure A.1 – Flipping of a TI/Graphene heterostructure via PDMS stamping.

Bibliography

- [1] Moore G.E., Cramming more components onto integrated circuits. *IEEE Solid-State Circuits Society Newsletter* 11, 33–35 (2006), doi:[10.1109/N-SSC.2006.4785860](https://doi.org/10.1109/N-SSC.2006.4785860).
- [2] Baibich M.N., Broto J.M., Fert A., Van Dau F.N., Petroff F., Etienne P., Creuzet G., Friederich A., Chazelas J., Giant Magnetoresistance of (001)Fe/(001)Cr Magnetic Superlattices. *Phys. Rev. Lett.* 61, 2472–2475 (1988), doi:[10.1103/PhysRevLett.61.2472](https://doi.org/10.1103/PhysRevLett.61.2472).
- [3] Binasch G., Grünberg P., Saurenbach F., Zinn W., Enhanced magnetoresistance in layered magnetic structures with antiferromagnetic interlayer exchange. *Phys. Rev. B* 39, 4828–4830 (1989), doi:[10.1103/PhysRevB.39.4828](https://doi.org/10.1103/PhysRevB.39.4828).
- [4] Slonczewski J.C., Conductance and exchange coupling of two ferromagnets separated by a tunneling barrier. *Phys. Rev. B* 39, 6995–7002 (1989), doi:[10.1103/PhysRevB.39.6995](https://doi.org/10.1103/PhysRevB.39.6995).
- [5] Johnson M., Silsbee R.H., Interfacial charge-spin coupling: Injection and detection of spin magnetization in metals. *Phys. Rev. Lett.* 55, 1790–1793 (1985), doi:[10.1103/PhysRevLett.55.1790](https://doi.org/10.1103/PhysRevLett.55.1790).
- [6] Valet T., Fert A., Theory of the perpendicular magnetoresistance in magnetic multilayers. *Phys. Rev. B* 48, 7099–7113 (1993), doi:[10.1103/PhysRevB.48.7099](https://doi.org/10.1103/PhysRevB.48.7099).
- [7] Slonczewski J., Current-driven excitation of magnetic multilayers. *Journal of Magnetism and Magnetic Materials* 159, L1 – L7 (1996), doi:[10.1016/0304-8853\(96\)00062-5](https://doi.org/10.1016/0304-8853(96)00062-5).
- [8] Berger L., Emission of spin waves by a magnetic multilayer traversed by a current. *Phys. Rev. B* 54, 9353–9358 (1996), doi:[10.1103/PhysRevB.54.9353](https://doi.org/10.1103/PhysRevB.54.9353).
- [9] Ralph D., Stiles M., Spin transfer torques. *J. Magn. Magn. Mater.* 320, 1190 – 1216 (2008), doi:[10.1016/j.jmmm.2007.12.019](https://doi.org/10.1016/j.jmmm.2007.12.019).

Bibliography

- [10] Bhat S.G., Kumar P.S.A., Room temperature electrical spin injection into GaAs by an oxide spin injector. *Sci. Rep.* 4 (2014), doi:[10.1038/srep05588](https://doi.org/10.1038/srep05588).
- [11] Dankert A., Dulal R.S., Dash S.P., Efficient Spin Injection into Silicon and the Role of the Schottky Barrier. *Sci. Rep.* 3 (2013), doi:[10.1038/srep03196](https://doi.org/10.1038/srep03196).
- [12] van't Erve O., Friedman A., Cobas E., Li C., Robinson J., Jonker B., Low-resistance spin injection into silicon using graphene tunnel barriers. *Nat Nano* 7, 737–742 (2012), doi:[10.1038/nnano.2012.161](https://doi.org/10.1038/nnano.2012.161).
- [13] Novoselov K.S., Geim A.K., Morozov S.V., Jiang D., Zhang Y., Dubonos S.V., Grigorieva I.V., Firsov A.A., Electric Field Effect in Atomically Thin Carbon Films. *Science* 306, 666–669 (2004), doi:[10.1126/science.1102896](https://doi.org/10.1126/science.1102896).
- [14] Gupta A., Sakthivel T., Seal S., Recent development in 2D materials beyond graphene. *Prog. Mater Sci.* 73, 44–126 (2015), doi:[10.1016/j.pmatsci.2015.02.002](https://doi.org/10.1016/j.pmatsci.2015.02.002).
- [15] Novoselov K.S., Mishchenko A., Carvalho A., Castro Neto A.H., 2D materials and van der Waals heterostructures. *Science* 353 (2016), doi:[10.1126/science.aac9439](https://doi.org/10.1126/science.aac9439).
- [16] Klitzing K.v., Dorda G., Pepper M., New Method for High-Accuracy Determination of the Fine-Structure Constant Based on Quantized Hall Resistance. *Phys. Rev. Lett.* 45, 494–497 (1980), doi:[10.1103/PhysRevLett.45.494](https://doi.org/10.1103/PhysRevLett.45.494).
- [17] Thouless D.J., Kohmoto M., Nightingale M.P., den Nijs M., Quantized Hall Conductance in a Two-Dimensional Periodic Potential. *Phys. Rev. Lett.* 49, 405–408 (1982), doi:[10.1103/PhysRevLett.49.405](https://doi.org/10.1103/PhysRevLett.49.405).
- [18] Kane C.L., Mele E.J., Z_2 Topological Order and the Quantum Spin Hall Effect. *Phys. Rev. Lett.* 95, 146802 (2005), doi:[10.1103/PhysRevLett.95.146802](https://doi.org/10.1103/PhysRevLett.95.146802).
- [19] Hsieh D., Xia Y., Wray L., Qian D., Pal A., Dil J.H., Osterwalder J., Meier F., Bihlmayer G., Kane C.L., Hor Y.S., Cava R.J., Hasan M.Z., Observation of Unconventional Quantum Spin Textures in Topological Insulators. *Science* 323, 919–922 (2009), doi:[10.1126/science.1167733](https://doi.org/10.1126/science.1167733).
- [20] Pesin D., MacDonald A.H., Spintronics and pseudospintronics in graphene and topological insulators. *Nat Mater* 11, 409–416 (2012), doi:[10.1038/nmat3305](https://doi.org/10.1038/nmat3305).
- [21] Kane C.L., Mele E.J., Quantum Spin Hall Effect in Graphene. *Phys. Rev. Lett.* 95, 226801 (2005), doi:[10.1103/PhysRevLett.95.226801](https://doi.org/10.1103/PhysRevLett.95.226801).

-
- [22] Fu L., Kane C.L., Mele E.J., Topological Insulators in Three Dimensions. *Phys. Rev. Lett.* 98, 106803 (2007), doi:[10.1103/PhysRevLett.98.106803](https://doi.org/10.1103/PhysRevLett.98.106803).
- [23] Ashcroft N.W., Mermin N., Solid State Physics. 1st edition, Academic Press (1979).
- [24] Laughlin R.B., Quantized Hall conductivity in two dimensions. *Phys. Rev. B* 23, 5632–5633 (1981), doi:[10.1103/PhysRevB.23.5632](https://doi.org/10.1103/PhysRevB.23.5632).
- [25] Berry M.V., Quantal Phase Factors Accompanying Adiabatic Changes. *Proceedings of the Royal Society of London A: Mathematical, Physical and Engineering Sciences* 392, 45–57 (1984), doi:[10.1098/rspa.1984.0023](https://doi.org/10.1098/rspa.1984.0023).
- [26] Bernevig B.A., Zhang S.C., Quantum Spin Hall Effect. *Phys. Rev. Lett.* 96, 106802 (2006), doi:[10.1103/PhysRevLett.96.106802](https://doi.org/10.1103/PhysRevLett.96.106802).
- [27] König M., Wiedmann S., Brüne C., Roth A., Buhmann H., Molenkamp L.W., Qi X.L., Zhang S.C., Quantum Spin Hall Insulator State in HgTe Quantum Wells. *Science* 318, 766–770 (2007), doi:[10.1126/science.1148047](https://doi.org/10.1126/science.1148047).
- [28] Moore J.E., Balents L., Topological invariants of time-reversal-invariant band structures. *Phys. Rev. B* 75, 121306 (2007), doi:[10.1103/PhysRevB.75.121306](https://doi.org/10.1103/PhysRevB.75.121306).
- [29] Roy R., Topological phases and the quantum spin Hall effect in three dimensions. *Phys. Rev. B* 79, 195322 (2009), doi:[10.1103/PhysRevB.79.195322](https://doi.org/10.1103/PhysRevB.79.195322).
- [30] Hsieh D., Qian D., Wray L., Xia Y., Hor Y.S., Cava R.J., Hasan M.Z., A topological Dirac insulator in a quantum spin Hall phase. *Nature* 452, 970–974 (2008), doi:[10.1038/nature06843](https://doi.org/10.1038/nature06843).
- [31] Xia Y., Qian D., Hsieh D., Wray L., Pal A., Lin H., Bansil A., Grauer D., Hor Y.S., Cava R.J., Hasan M.Z., Observation of a large-gap topological-insulator class with a single Dirac cone on the surface. *Nat. Phys.* 5, 398–402 (2009), doi:[10.1038/nphys1274](https://doi.org/10.1038/nphys1274).
- [32] Chen Y.L., Analytis J.G., Chu J.H., Liu Z.K., Mo S.K., Qi X.L., Zhang H.J., Lu D.H., Dai X., Fang Z., Zhang S.C., Fisher I.R., Hussain Z., Shen Z.X., Experimental Realization of a Three-Dimensional Topological Insulator, Bi₂Te₃. *Science* 325, 178–181 (2009), doi:[10.1126/science.1173034](https://doi.org/10.1126/science.1173034).
- [33] Sato T., Segawa K., Kosaka K., Souma S., Nakayama K., Eto K., Minami T., Ando Y., Takahashi T., Unexpected mass acquisition of Dirac fermions at the quantum phase transition of a topological insulator. *Nat. Phys.* 7, 840–844 (2011), doi:[10.1038/nphys2058](https://doi.org/10.1038/nphys2058).

Bibliography

- [34] Chen Y.L., Liu Z.K., Analytis J.G., Chu J.H., Zhang H.J., Yan B.H., Mo S.K., Moore R.G., Lu D.H., Fisher I.R., Zhang S.C., Hussain Z., Shen Z.X., Single Dirac Cone Topological Surface State and Unusual Thermoelectric Property of Compounds from a New Topological Insulator Family. *Phys. Rev. Lett.* 105, 266401 (2010), doi:[10.1103/PhysRevLett.105.266401](https://doi.org/10.1103/PhysRevLett.105.266401).
- [35] Ren Z., Taskin A.A., Sasaki S., Segawa K., Ando Y., Large bulk resistivity and surface quantum oscillations in the topological insulator Bi₂Te₂Se. *Phys. Rev. B* 82, 241306 (2010), doi:[10.1103/PhysRevB.82.241306](https://doi.org/10.1103/PhysRevB.82.241306).
- [36] Neupane M., Xu S.Y., Wray L.A., Petersen A., Shankar R., Alidoust N., Liu C., Fedorov A., Ji H., Allred J.M., Hor Y.S., Chang T.R., Jeng H.T., Lin H., Bansil A., Cava R.J., Hasan M.Z., Topological surface states and Dirac point tuning in ternary topological insulators. *Phys. Rev. B* 85, 235406 (2012), doi:[10.1103/PhysRevB.85.235406](https://doi.org/10.1103/PhysRevB.85.235406).
- [37] Nishide A., Taskin A.A., Takeichi Y., Okuda T., Kakizaki A., Hirahara T., Nakatsuji K., Komori F., Ando Y., Matsuda I., Direct mapping of the spin-filtered surface bands of a three-dimensional quantum spin Hall insulator. *Phys. Rev. B* 81, 041309 (2010), doi:[10.1103/PhysRevB.81.041309](https://doi.org/10.1103/PhysRevB.81.041309).
- [38] Jozwiak C., Park C.H., Gotlieb K., Hwang C., Lee D.H., Louie S.G., Denlinger J.D., Rotundu C.R., Birgeneau R.J., Hussain Z., Lanzara A., Photoelectron spin-flipping and texture manipulation in a topological insulator. *Nat. Phys.* 9, 293–298 (2013), doi:[10.1038/nphys2572](https://doi.org/10.1038/nphys2572).
- [39] Arakane T., Sato T., Souma S., Kosaka K., Nakayama K., Komatsu M., Takahashi T., Ren Z., Segawa K., Ando Y., Tunable Dirac cone in the topological insulator Bi_{2-x}Sb_xTe_{3-y}Se_y. *Nat. Commun.* 3 (2012), doi:[10.1038/ncomms1639](https://doi.org/10.1038/ncomms1639).
- [40] Checkelsky J.G., Hor Y.S., Liu M.H., Qu D.X., Cava R.J., Ong N.P., Quantum Interference in Macroscopic Crystals of Nonmetallic Bi₂Se₃. *Phys. Rev. Lett.* 103, 246601 (2009), doi:[10.1103/PhysRevLett.103.246601](https://doi.org/10.1103/PhysRevLett.103.246601).
- [41] Hong S.S., Cha J.J., Kong D., Cui Y., Ultra-low carrier concentration and surface-dominant transport in antimony-doped Bi₂Se₃ topological insulator nanoribbons. *Nat. Commun.* 3 (2012), doi:[10.1038/ncomms1771](https://doi.org/10.1038/ncomms1771).
- [42] Zhang G., Qin H., Chen J., He X., Lu L., Li Y., Wu K., Growth of Topological Insulator Bi₂Se₃ Thin Films on SrTiO₃ with Large Tunability in Chemical Potential. *Adv. Funct. Mater.* 21, 2351–2355 (2011), doi:[10.1002/adfm.201002667](https://doi.org/10.1002/adfm.201002667).

- [43] Hoefler K., Becker C., Rata D., Swanson J., Thalmeier P., Tjeng L.H., Intrinsic conduction through topological surface states of insulating Bi_2Te_3 epitaxial thin films. *Proceedings of the National Academy of Sciences* 111, 14979–14984 (2014), doi:[10.1073/pnas.1410591111](https://doi.org/10.1073/pnas.1410591111).
- [44] Trang C.X., Wang Z., Yamada K., Souma S., Sato T., Takahashi T., Segawa K., Ando Y., Metal-insulator transition and tunable Dirac-cone surface state in the topological insulator $\text{TlBi}_{1-x}\text{Sb}_x\text{Te}_2$ studied by angle-resolved photoemission. *Phys. Rev. B* 93, 165123 (2016), doi:[10.1103/PhysRevB.93.165123](https://doi.org/10.1103/PhysRevB.93.165123).
- [45] Köhler H., Conduction Band Parameters of Bi_2Se_3 from Shubnikov-de Haas Investigations. *physica status solidi (b)* 58, 91–100 (1973), doi:[10.1002/pssb.2220580109](https://doi.org/10.1002/pssb.2220580109).
- [46] Cha J.J., Koski K.J., Cui Y., Topological insulator nanostructures. *physica status solidi (RRL) – Rapid Research Letters* 7, 15–25 (2013), doi:[10.1002/pssr.201206393](https://doi.org/10.1002/pssr.201206393).
- [47] Saha B., Chaturvedi P., Yadav A.K., Saha D., Ganguly S., Pulsed laser deposition of highly oriented stoichiometric thin films of topological insulator Sb_2Te_3 . *Journal of Vacuum Science & Technology B* 34, 021806 (2016), doi:[10.1116/1.4943026](https://doi.org/10.1116/1.4943026).
- [48] Le P.H., Wu K.H., Luo C.W., Leu J., Growth and characterization of topological insulator Bi_2Se_3 thin films on SrTiO_3 using pulsed laser deposition. *Thin Solid Films* 534, 659–665 (2013), doi:[10.1016/j.tsf.2013.01.104](https://doi.org/10.1016/j.tsf.2013.01.104).
- [49] Zhang G., Qin H., Teng J., Guo J., Guo Q., Dai X., Fang Z., Wu K., Quintuple-layer epitaxy of thin films of topological insulator Bi_2Se_3 . *Appl. Phys. Lett.* 95, 053114 (2009), doi:[10.1063/1.3200237](https://doi.org/10.1063/1.3200237).
- [50] Jiang Y., Sun Y.Y., Chen M., Wang Y., Li Z., Song C., He K., Wang L., Chen X., Xue Q.K., Ma X., Zhang S.B., Fermi-Level Tuning of Epitaxial Sb_2Te_3 Thin Films on Graphene by Regulating Intrinsic Defects and Substrate Transfer Doping. *Phys. Rev. Lett.* 108, 066809 (2012), doi:[10.1103/PhysRevLett.108.066809](https://doi.org/10.1103/PhysRevLett.108.066809).
- [51] Kong D., Dang W., Cha J.J., Li H., Meister S., Peng H., Liu Z., Cui Y., Few-Layer Nanoplates of Bi_2Se_3 and Bi_2Te_3 with Highly Tunable Chemical Potential. *Nano Lett.* 10, 2245–2250 (2010), doi:[10.1021/nl101260j](https://doi.org/10.1021/nl101260j).
- [52] Kong D., Randel J.C., Peng H., Cha J.J., Meister S., Lai K., Chen Y., Shen Z.X., Manoharan H.C., Cui Y., Topological Insulator Nanowires and Nanoribbons. *Nano Lett.* 10, 329–333 (2010), doi:[10.1021/nl903663a](https://doi.org/10.1021/nl903663a).

Bibliography

- [53] Eschbach M., Młyńczak E., Kellner J., Kampmeier J., Lanius M., Neumann E., Weyrich C., Gehlmann M., Gospodarič P., Döring S., Mussler G., Demarina N., Luysberg M., Bihlmayer G., Schäpers T., Plucinski L., Blügel S., Morgenstern M., Schneider C.M., Grütz-macher D., Realization of a vertical topological p-n junction in epitaxial $\text{Sb}_2\text{Te}_3/\text{Bi}_2\text{Te}_3$ heterostructures. *Nat. Commun.* 6 (2015), doi:10.1038/ncomms9816.
- [54] Lee Y., Punugupati S., Wu F., Jin Z., Narayan J., Schwartz J., Evidence for topological surface states in epitaxial Bi_2Se_3 thin film grown by pulsed laser deposition through magneto-transport measurements. *Curr. Opin. Solid State Mater. Sci.* 18, 279–285 (2014), doi:10.1016/j.cossms.2014.07.001.
- [55] Peng H., Lai K., Kong D., Meister S., Chen Y., Qi X.L., Zhang S.C., Shen Z.X., Cui Y., Aharonov-Bohm interference in topological insulator nanoribbons. *Nat. Mater.* 9, 225–229 (2010), doi:10.1038/nmat2609.
- [56] Ashalley E., Chen H., Tong X., Li H., Wang Z.M., Bismuth telluride nanostructures: preparation, thermoelectric properties and topological insulating effect. *Frontiers of Materials Science* 9, 103–125 (2015), doi:10.1007/s11706-015-0285-9.
- [57] Gehring P., Benia H.M., Weng Y., Dinnebier R., Ast C.R., Burghard M., Kern K., A Natural Topological Insulator. *Nano Lett.* 13, 1179–1184 (2013), doi:10.1021/nl304583m.
- [58] Hsieh D., Xia Y., Qian D., Wray L., Dil J.H., Meier F., Osterwalder J., Patthey L., Checkelsky J.G., Ong N.P., Fedorov A.V., Lin H., Bansil A., Grauer D., Hor Y.S., Cava R.J., Hasan M.Z., A tunable topological insulator in the spin helical Dirac transport regime. *Nature* 460, 1101–1105 (2009), doi:10.1038/nature08234.
- [59] Cheng P., Song C., Zhang T., Zhang Y., Wang Y., Jia J.F., Wang J., Wang Y., Zhu B.F., Chen X., Ma X., He K., Wang L., Dai X., Fang Z., Xie X., Qi X.L., Liu C.X., Zhang S.C., Xue Q.K., Landau Quantization of Topological Surface States in Bi_2Se_3 . *Phys. Rev. Lett.* 105, 076801 (2010), doi:10.1103/PhysRevLett.105.076801.
- [60] Makala R.S., Jagannadham K., Sales B.C., Pulsed laser deposition of Bi_2Te_3 -based thermoelectric thin films. *J. Appl. Phys.* 94, 3907–3918 (2003), doi:10.1063/1.1600524.
- [61] Onose Y., Yoshimi R., Tsukazaki A., Yuan H., Hidaka T., Iwasa Y., Kawasaki M., Tokura Y., Pulsed Laser Deposition and Ionic Liquid Gate Control of Epitaxial Bi_2Se_3 Thin Films. *Appl. Phys Express* 4, 083001 (2011), doi:10.1143/APEX.4.083001.

- [62] Gehring P., Vaklinova K., Hoyer A., Benia H.M., Skakalova V., Argentero G., Eder F., Meyer J.C., Burghard M., Kern K., Dimensional crossover in the quantum transport behaviour of the natural topological insulator Aleksite. *Sci. Rep.* 5 (2015), doi:10.1038/srep11691.
- [63] Chang C.Z., Tang P., Feng X., Li K., Ma X.C., Duan W., He K., Xue Q.K., Band Engineering of Dirac Surface States in Topological-Insulator-Based van der Waals Heterostructures. *Phys. Rev. Lett.* 115 (2015), doi:10.1103/PhysRevLett.115.136801.
- [64] Dang W., Peng H., Li H., Wang P., Liu Z., Epitaxial Heterostructures of Ultrathin Topological Insulator Nanoplate and Graphene. *Nano Lett.* 10, 2870–2876 (2010), doi:10.1021/nl100938e.
- [65] Gehring P., Gao B.F., Burghard M., Kern K., Growth of High-Mobility Bi₂Te₂Se Nanoplatelets on hBN Sheets by van der Waals Epitaxy. *Nano Lett.* 12, 5137–5142 (2012), doi:10.1021/nl3019802.
- [66] Hikami S., Larkin A.I., Nagaoka Y., Spin-Orbit Interaction and Magnetoresistance in the Two Dimensional Random System. *Progress of Theoretical Physics* 63, 707–710 (1980), doi:10.1143/PTP.63.707.
- [67] Yi L., Zheng M., Yan-Fei Z., Singh M., Jian W., Transport properties of topological insulators films and nanowires. *Chin. Phys. B* 22, 067302 (2013), doi:10.1088/1674-1056/22/6/067302.
- [68] Hamdou B., Gooth J., Dorn A., Pippel E., Nielsch K., Aharonov-Bohm oscillations and weak antilocalization in topological insulator Sb₂Te₃ nanowires. *Applied Physics Letters* 102, 223110 (2013), doi:10.1063/1.4809826.
- [69] Lee P.A., Stone A.D., Fukuyama H., Universal conductance fluctuations in metals: Effects of finite temperature, interactions, and magnetic field. *Phys. Rev. B* 35, 1039–1070 (1987), doi:10.1103/PhysRevB.35.1039.
- [70] Trivedi T., Sonde S., Movva H.C.P., Banerjee S.K., Weak antilocalization and universal conductance fluctuations in bismuth telluro-sulfide topological insulators. *J. Appl. Phys.* 119, 055706 (2016), doi:10.1063/1.4941265.
- [71] Li Z., Chen T., Pan H., Song F., Wang B., Han J., Qin Y., Wang X., Zhang R., Wan J., Xing D., Wang G., Two-dimensional universal conductance fluctuations and the electron-phonon interaction of surface states in Bi₂Te₂Se microflakes. *Sci. Rep.* 2 (2012), doi:10.1038/srep00595.

Bibliography

- [72] Li Z., Meng Y., Pan J., Chen T., Hong X., Li S., Wang X., Song F., Wang B., Indications of topological transport by universal conductance fluctuations in $\text{Bi}_2\text{Te}_2\text{Se}$ microflakes. *Appl. Phys Express* 7, 065202 (2014), doi:[10.7567/APEX.7.065202](https://doi.org/10.7567/APEX.7.065202).
- [73] Taylor R.P., Main P.C., Eaves L., Beaumont S.P., McIntyre I., Thoms S., Wilkinson C.D.W., Magnetoresistance effects in laterally confined n-GaAs/(AlGa)As heterostructures. *J. Phys.: Condens. Matter* 1, 10413 (1989), doi:[10.1088/0953-8984/1/51/014](https://doi.org/10.1088/0953-8984/1/51/014).
- [74] Miyazaki T., Tezuka N., Giant magnetic tunneling effect in Fe/ Al_2O_3 /Fe junction. *J. Magn. Magn. Mater.* 139, L231–L234 (1995), doi:[10.1016/0304-8853\(95\)90001-2](https://doi.org/10.1016/0304-8853(95)90001-2).
- [75] Moodera J.S., Kinder L.R., Wong T.M., Meservey R., Large Magnetoresistance at Room Temperature in Ferromagnetic Thin Film Tunnel Junctions. *Phys. Rev. Lett.* 74, 3273–3276 (1995), doi:[10.1103/PhysRevLett.74.3273](https://doi.org/10.1103/PhysRevLett.74.3273).
- [76] Pu Y., Odenthal P.M., Adur R., Beardsley J., Swartz A.G., Pelekhov D.V., Flatté M.E., Kawakami R.K., Pelz J., Hammel P.C., Johnston-Halperin E., Ferromagnetic Resonance Spin Pumping and Electrical Spin Injection in Silicon-Based Metal-Oxide-Semiconductor Heterostructures. *Phys. Rev. Lett.* 115, 246602 (2015), doi:[10.1103/PhysRevLett.115.246602](https://doi.org/10.1103/PhysRevLett.115.246602).
- [77] Baker A.A., Figueroa A.I., Collins-McIntyre L.J., van der Laan G., Hesjedal T., Spin pumping in Ferromagnet-Topological Insulator-Ferromagnet Heterostructures. *Sci. Rep.* 5 (2015), doi:[10.1038/srep07907](https://doi.org/10.1038/srep07907).
- [78] Memory with a spin. *Nat Nano* 10, 185–185 (2015), doi:[10.1038/nnano.2015.50](https://doi.org/10.1038/nnano.2015.50).
- [79] Kawahara T., Ito K., Takemura R., Ohno H., Spin-transfer torque RAM technology: Review and prospect. *Microelectron. Reliab.* 52, 613–627 (2012), doi:[10.1016/j.microrel.2011.09.028](https://doi.org/10.1016/j.microrel.2011.09.028).
- [80] Bourgeois E., Jarmola A., Siyushev P., Gulka M., Hruby J., Jelezko F., Budker D., Nesladek M., Photoelectric detection of electron spin resonance of nitrogen-vacancy centres in diamond. *Nat. Commun.* 6 (2015), doi:[10.1038/ncomms9577](https://doi.org/10.1038/ncomms9577).
- [81] Kato Y.K., Myers R.C., Gossard A.C., Awschalom D.D., Current-Induced Spin Polarization in Strained Semiconductors. *Phys. Rev. Lett.* 93, 176601 (2004), doi:[10.1103/PhysRevLett.93.176601](https://doi.org/10.1103/PhysRevLett.93.176601).

- [82] Stern N.P, Ghosh S., Xiang G., Zhu M., Samarth N., Awschalom D.D., Current-Induced Polarization and the Spin Hall Effect at Room Temperature. *Phys. Rev. Lett.* 97, 126603 (2006), doi:[10.1103/PhysRevLett.97.126603](https://doi.org/10.1103/PhysRevLett.97.126603).
- [83] Silov A.Y., Blajnov P.A., Wolter J.H., Hey R., Ploog K.H., Averkiev N.S., Current-induced spin polarization at a single heterojunction. *Appl. Phys. Lett.* 85, 5929–5931 (2004), doi:[10.1063/1.1833565](https://doi.org/10.1063/1.1833565).
- [84] Garlid E.S., Hu Q.O., Chan M.K., Palmstrøm C.J., Crowell P.A., Electrical Measurement of the Direct Spin Hall Effect in Fe/In_xGa_{1-x}As Heterostructures. *Phys. Rev. Lett.* 105, 156602 (2010), doi:[10.1103/PhysRevLett.105.156602](https://doi.org/10.1103/PhysRevLett.105.156602).
- [85] Dyrdał A., Barnaś J., Dugaev V.K., Current-induced spin polarization in graphene due to Rashba spin-orbit interaction. *Phys. Rev. B* 89, 075422 (2014), doi:[10.1103/PhysRevB.89.075422](https://doi.org/10.1103/PhysRevB.89.075422).
- [86] Dyrdał A., Barnaś J., Current-induced spin polarization and spin-orbit torque in graphene. *Phys. Rev. B* 92, 165404 (2015), doi:[10.1103/PhysRevB.92.165404](https://doi.org/10.1103/PhysRevB.92.165404).
- [87] H. L., van't Erve O., Robinson J., Liu Y., Li L., Jonker B., Electrical detection of charge-current-induced spin polarization due to spin-momentum locking in Bi₂Se₃. *Nat Nano* 9, 218–224 (2014), doi:[10.1038/nnano.2014.16](https://doi.org/10.1038/nnano.2014.16).
- [88] Tian J., Childres I., Cao H., Shen T., Miotkowski I., Chen Y.P., Topological insulator based spin valve devices: Evidence for spin polarized transport of spin-momentum-locked topological surface states. *Solid State Commun.* 191, 1–5 (2014), doi:[10.1016/j.ssc.2014.04.005](https://doi.org/10.1016/j.ssc.2014.04.005).
- [89] Tian J., Miotkowski I., Hong S., Chen Y.P., Electrical injection and detection of spin-polarized currents in topological insulator Bi₂Te₂Se. *Sci. Rep.* 5 (2015), doi:[10.1038/srep14293](https://doi.org/10.1038/srep14293).
- [90] Tang J., Chang L.T., Kou X., Murata K., Choi E.S., Lang M., Fan Y., Jiang Y., Montazeri M., Jiang W., Wang Y., He L., Wang K.L., Electrical Detection of Spin-Polarized Surface States Conduction in (Bi_{0.53}Sb_{0.47})₂Te₃ Topological Insulator. *Nano Lett.* 14, 5423–5429 (2014), doi:[10.1021/nl5026198](https://doi.org/10.1021/nl5026198).
- [91] Ando Y., Hamasaki T., Kurokawa T., Ichiba K., Yang F., Novak M., Sasaki S., Segawa K., Ando Y., Shiraishi M., Electrical Detection of the Spin Polarization Due to Charge

Bibliography

- Flow in the Surface State of the Topological Insulator $\text{Bi}_{1.5}\text{Sb}_{0.5}\text{Te}_{1.7}\text{Se}_{1.3}$. *Nano Lett.* 14, 6226–6230 (2014), doi:[10.1021/nl502546c](https://doi.org/10.1021/nl502546c).
- [92] Dankert A., Geurs J., Kamalakar M.V., Charpentier S., Dash S.P., Room Temperature Electrical Detection of Spin Polarized Currents in Topological Insulators. *Nano Lett.* 15, 7976–7981 (2015), doi:[10.1021/acs.nanolett.5b03080](https://doi.org/10.1021/acs.nanolett.5b03080).
- [93] Liu L., Richardella A., Garate I., Zhu Y., Samarth N., Chen C.T., Spin-polarized tunneling study of spin-momentum locking in topological insulators. *Phys. Rev. B* 91, 235437 (2015), doi:[10.1103/PhysRevB.91.235437](https://doi.org/10.1103/PhysRevB.91.235437).
- [94] Vaklinova K., Hoyer A., Burghard M., Kern K., Current-Induced Spin Polarization in Topological Insulator–Graphene Heterostructures. *Nano Lett.* 16, 2595–2602 (2016), doi:[10.1021/acs.nanolett.6b00167](https://doi.org/10.1021/acs.nanolett.6b00167).
- [95] Fabian J., Matos-Abiague A., Ertler C., Stano P., Zutic I., Semiconductor Spintronics. *Acta Physica Slovaca* 57, 567–907 (2007).
- [96] Shiraishi M., Electrically-Generated Pure Spin Current in Graphene. *Japanese Journal of Applied Physics* 51, 08KA01 (2012), doi:[10.1143/JJAP.51.08KA01](https://doi.org/10.1143/JJAP.51.08KA01).
- [97] Silsbee R. (Editor), Novel Method for the Study of Spin Transport in Conductors, volume 2 of *Bulletin of Magnetic Resonance*, The Franklin Institute Press (1980).
- [98] Dash S.P., Sharma S., Patel R.S., de Jong M.P., Jansen R., Electrical creation of spin polarization in silicon at room temperature. *Nature* 462, 491–494 (2009), doi:[10.1038/nature08570](https://doi.org/10.1038/nature08570).
- [99] Li C., van't Erve O., Jonker B., Electrical injection and detection of spin accumulation in silicon at 500 K with magnetic metal/silicon dioxide contacts. *Nat. Commun.* 2 (2011), doi:[10.1038/ncomms1256](https://doi.org/10.1038/ncomms1256).
- [100] Lou X., Adelman C., Crooker S.A., Garlid E.S., Zhang J., Reddy K.S.M., Flexner S.D., Palmstrom C.J., Crowell P.A., Electrical detection of spin transport in lateral ferromagnet-semiconductor devices. *Nat. Phys.* 3, 197–202 (2007), doi:[10.1038/nphys543](https://doi.org/10.1038/nphys543).
- [101] Jansen R., Dash S.P., Sharma S., Min B.C., Silicon spintronics with ferromagnetic tunnel devices. *Semicond. Sci. Technol.* 27, 083001 (2012), doi:[10.1088/0268-1242/27/8/083001](https://doi.org/10.1088/0268-1242/27/8/083001).
- [102] Jain A., Rojas-Sanchez J.C., Cubukcu M., Peiro J., Le Breton J.C., Prestat E., Vergnaud C., Louahadj L., Portemont C., Ducruet C., Baltz V., Barski A., Bayle-Guillemaud

- P, Vila L., Attané J.P., Augendre E., Desfonds G., Gambarelli S., Jaffrès H., George J.M., Jamet M., Crossover from Spin Accumulation into Interface States to Spin Injection in the Germanium Conduction Band. *Phys. Rev. Lett.* 109, 106603 (2012), doi:10.1103/PhysRevLett.109.106603.
- [103] Reyren N., Bibes M., Lesne E., George J.M., Deranlot C., Collin S., Barthélémy A., Jaffrès H., Gate-Controlled Spin Injection at LaAlO₃/SrTiO₃ Interfaces. *Phys. Rev. Lett.* 108, 186802 (2012), doi:10.1103/PhysRevLett.108.186802.
- [104] Brinkman A., Huijben M., van Zalk M., Huijben J., Zeitler U., Maan J.C., van der Wiel W.G., Rijnders G., Blank D.H.A., Hilgenkamp H., Magnetic effects at the interface between non-magnetic oxides. *Nat. Mater.* 6, 493–496 (2007), doi:10.1038/nmat1931.
- [105] Son J., Moetakef P., Jalan B., Bierwagen O., Wright N.J., Engel-Herbert R., Stemmer S., Epitaxial SrTiO₃ films with electron mobilities exceeding 30,000 cm²V⁻¹s⁻¹. *Nat. Mater.* 9, 482–484 (2010), doi:10.1038/nmat2750.
- [106] Txoperena O., Song Y., Qing L., Gobbi M., Hueso L.E., Dery H., Casanova E., Impurity-Assisted Tunneling Magnetoresistance under a Weak Magnetic Field. *Phys. Rev. Lett.* 113, 146601 (2014), doi:10.1103/PhysRevLett.113.146601.
- [107] Schmidt G., Ferrand D., Molenkamp L.W., Filip A.T., van Wees B.J., Fundamental obstacle for electrical spin injection from a ferromagnetic metal into a diffusive semiconductor. *Phys. Rev. B* 62, R4790–R4793 (2000), doi:10.1103/PhysRevB.62.R4790.
- [108] Rashba E.I., Theory of electrical spin injection: Tunnel contacts as a solution of the conductivity mismatch problem. *Phys. Rev. B* 62, R16267–R16270 (2000), doi:10.1103/PhysRevB.62.R16267.
- [109] Fert A., Jaffrès H., Conditions for efficient spin injection from a ferromagnetic metal into a semiconductor. *Phys. Rev. B* 64, 184420 (2001), doi:10.1103/PhysRevB.64.184420.
- [110] Han W., Pi K., McCreary K.M., Li Y., Wong J.J.I., Swartz A.G., Kawakami R.K., Tunneling Spin Injection into Single Layer Graphene. *Phys. Rev. Lett.* 105, 167202 (2010), doi:10.1103/PhysRevLett.105.167202.
- [111] Han W., Wang W.H., Pi K., McCreary K.M., Bao W., Li Y., Miao F., Lau C.N., Kawakami R.K., Electron-Hole Asymmetry of Spin Injection and Transport in Single-Layer Graphene. *Phys. Rev. Lett.* 102, 137205 (2009), doi:10.1103/PhysRevLett.102.137205.

Bibliography

- [112] Dresselhaus G., Spin-Orbit Coupling Effects in Zinc Blende Structures. *Phys. Rev.* 100, 580–586 (1955), doi:[10.1103/PhysRev.100.580](https://doi.org/10.1103/PhysRev.100.580).
- [113] Winkler R., Spin-orbit Coupling Effects in Two-Dimensional Electron and Hole Systems, volume 191. 1st edition, Springer-Verlag Berlin Heidelberg (2003), doi:[10.1007/b13586](https://doi.org/10.1007/b13586).
- [114] Nishikawa Y., Tackeuchi A., Nakamura S., Muto S., Yokoyama N., All-optical picosecond switching of a quantum well etalon using spin-polarization relaxation. *Appl. Phys. Lett.* 66, 839–841 (1995), doi:[10.1063/1.113439](https://doi.org/10.1063/1.113439).
- [115] Bloch F., Hansen W.W., Packard M., The Nuclear Induction Experiment. *Phys. Rev.* 70, 474–485 (1946), doi:[10.1103/PhysRev.70.474](https://doi.org/10.1103/PhysRev.70.474).
- [116] Torrey H.C., Bloch Equations with Diffusion Terms. *Phys. Rev.* 104, 563–565 (1956), doi:[10.1103/PhysRev.104.563](https://doi.org/10.1103/PhysRev.104.563).
- [117] Elliott R.J., Theory of the Effect of Spin-Orbit Coupling on Magnetic Resonance in Some Semiconductors. *Phys. Rev.* 96, 266–279 (1954), doi:[10.1103/PhysRev.96.266](https://doi.org/10.1103/PhysRev.96.266).
- [118] Yafet Y., g Factors and Spin-Lattice Relaxation of Conduction Electrons. volume 14 of *Solid State Physics*, 1–98, Academic Press (1963), doi:[10.1016/S0081-1947\(08\)60259-3](https://doi.org/10.1016/S0081-1947(08)60259-3).
- [119] Kiss A., Szolnoki L., Simon F., The Elliott-Yafet theory of spin relaxation generalized for large spin-orbit coupling. *Sci. Rep.* 6 (2016), doi:[10.1038/srep22706](https://doi.org/10.1038/srep22706).
- [120] Dyakonov M., Perel V., Spin relaxation of conduction electrons in noncentrosymmetric semiconductors. *Soviet Physics Solid State, Ussr* 13, 3023–3026 (1972).
- [121] Jungwirth T., Wunderlich J., Olejnik K., Spin Hall effect devices. *Nat. Mater.* 11, 382–390 (2012), doi:[10.1038/nmat3279](https://doi.org/10.1038/nmat3279).
- [122] Rojas-Sánchez J.C., Oyarzún S., Fu Y., Marty A., Vergnaud C., Gambarelli S., Vila L., Jamet M., Ohtsubo Y., Taleb-Ibrahimi A., Le Fèvre P., Bertran F., Reyren N., George J.M., Fert A., Spin to Charge Conversion at Room Temperature by Spin Pumping into a New Type of Topological Insulator: α -Sn Films. *Phys. Rev. Lett.* 116, 096602 (2016), doi:[10.1103/PhysRevLett.116.096602](https://doi.org/10.1103/PhysRevLett.116.096602).
- [123] Roth A., Brüne C., Buhmann H., Molenkamp L.W., Maciejko J., Qi X.L., Zhang S.C., Nonlocal Transport in the Quantum Spin Hall State. *Science* 325, 294–297 (2009), doi:[10.1126/science.1174736](https://doi.org/10.1126/science.1174736).

-
- [124] Brune C., Roth A., Buhmann H., Hankiewicz E.M., Molenkamp L.W., Maciejko J., Qi X.L., Zhang S.C., Spin polarization of the quantum spin Hall edge states. *Nat. Phys.* 8, 485–490 (2012), doi:[10.1038/nphys2322](https://doi.org/10.1038/nphys2322).
- [125] Bychkov Y.A., Rashba E.I., Oscillatory effects and the magnetic susceptibility of carriers in inversion layers. *J. Phys. C: Solid State Phys.* 17, 6039 (1984), doi:[10.1088/0022-3719/17/33/015](https://doi.org/10.1088/0022-3719/17/33/015).
- [126] Bychkov Y.A., Rashba É.I., Properties of a 2D electron gas with lifted spectral degeneracy. *ZhETF Pisma Redaktsiiu* 39, 66 (1984).
- [127] Miyahara H., Maegawa T., Kuroda K., Kimura A., Miyamoto K., Namatame H., Taniguchi M., Okuda T., Observation of Peculiar Rashba-Type Spin-Split Band on Bi(111) Surface by High-Resolution Spin- and Angle-Resolved Photoemission Spectroscopy. *e-J. Surf. Sci. Nanotechnol.* 10, 153–156 (2012), doi:[10.1380/ejsnt.2012.153](https://doi.org/10.1380/ejsnt.2012.153).
- [128] Krupin O., Bihlmayer G., Starke K., Gorovikov S., Prieto J.E., Döbrich K., Blügel S., Kaindl G., Rashba effect at magnetic metal surfaces. *Phys. Rev. B* 71, 201403 (2005), doi:[10.1103/PhysRevB.71.201403](https://doi.org/10.1103/PhysRevB.71.201403).
- [129] Ast C.R., Henk J., Ernst A., Moreschini L., Falub M.C., Pacilé D., Bruno P., Kern K., Grioni M., Giant Spin Splitting through Surface Alloying. *Phys. Rev. Lett.* 98, 186807 (2007), doi:[10.1103/PhysRevLett.98.186807](https://doi.org/10.1103/PhysRevLett.98.186807).
- [130] W. M.J., D. H., H. S., P. J.H., N. G., Control over topological insulator photocurrents with light polarization. *Nat Nano* 7, 96–100 (2012), doi:[10.1038/nnano.2011.214](https://doi.org/10.1038/nnano.2011.214).
- [131] Edelstein V., Spin polarization of conduction electrons induced by electric current in two-dimensional asymmetric electron systems. *Solid State Commun.* 73, 233–235 (1990), doi:[10.1016/0038-1098\(90\)90963-C](https://doi.org/10.1016/0038-1098(90)90963-C).
- [132] Aronov A., Lyanda-Geller Y.B., Pikus G., Spin polarization of electrons by an electric current. *JETP* 73, 537 (1991).
- [133] Johansson A., Henk J., Mertig I., Theoretical aspects of the Edelstein effect for anisotropic two-dimensional electron gas and topological insulators. *Phys. Rev. B* 93, 195440 (2016), doi:[10.1103/PhysRevB.93.195440](https://doi.org/10.1103/PhysRevB.93.195440).
- [134] Kondou K., Yoshimi R., Tsukazaki A., Fukuma Y., Matsuno J., Takahashi K.S., Kawasaki M., Tokura Y., Otani Y., Fermi-level-dependent charge-to-spin current conversion

Bibliography

- by Dirac surface states of topological insulators. *Nat. Phys.* 12, 1027–1031 (2016), doi:[10.1038/nphys3833](https://doi.org/10.1038/nphys3833).
- [135] Zhang H.J., Yamamoto S., Gu B., Li H., Maekawa M., Fukaya Y., Kawasuso A., Charge-to-Spin Conversion and Spin Diffusion in Bi/Ag Bilayers Observed by Spin-Polarized Positron Beam. *Phys. Rev. Lett.* 114, 166602 (2015), doi:[10.1103/PhysRevLett.114.166602](https://doi.org/10.1103/PhysRevLett.114.166602).
- [136] Nomura A., Tashiro T., Nakayama H., Ando K., Temperature dependence of inverse Rashba-Edelstein effect at metallic interface. *Appl. Phys. Lett.* 106, 212403 (2015), doi:[10.1063/1.4921765](https://doi.org/10.1063/1.4921765).
- [137] Mellnik A.R., Lee J.S., Richardella A., Grab J.L., Mintun P.J., Fischer M.H., Vaezi A., Manchon A., Kim E.A., Samarth N., Ralph D.C., Spin-transfer torque generated by a topological insulator. *Nature* 511, 449–451 (2014), doi:[10.1038/nature13534](https://doi.org/10.1038/nature13534).
- [138] Shen K., Vignale G., Raimondi R., Microscopic Theory of the Inverse Edelstein Effect. *Phys. Rev. Lett.* 112, 096601 (2014), doi:[10.1103/PhysRevLett.112.096601](https://doi.org/10.1103/PhysRevLett.112.096601).
- [139] Sánchez J.C.R., Vila L., Desfonds G., Gambarelli S., Attané J.P., De Teresa J.M., Magén C., Fert A., Spin-to-charge conversion using Rashba coupling at the interface between non-magnetic materials. *Nat. Commun.* 4 (2013), doi:[10.1038/ncomms3944](https://doi.org/10.1038/ncomms3944).
- [140] Geim A.K., Novoselov K.S., The rise of graphene. *Nat. Mater.* 6, 183–191 (2007), doi:[10.1038/nmat1849](https://doi.org/10.1038/nmat1849).
- [141] Han W., Pi K., Wang W.H., McCreary K.M., Li Y., Bao W., Wei P., Shi J., Lau C.N., Kawakami R.K., Spin transport in graphite and graphene spin valves. *Proc. SPIE* 7398, 739819 (2009), doi:[10.1117/12.826705](https://doi.org/10.1117/12.826705).
- [142] Han W., McCreary K., Pi K., Wang W., Li Y., Wen H., Chen J., Kawakami R., Spin transport and relaxation in graphene. *J. Magn. Magn. Mater.* 324, 369–381 (2012), doi:[10.1016/j.jmmm.2011.08.001](https://doi.org/10.1016/j.jmmm.2011.08.001).
- [143] Cho S., Chen Y.F., Fuhrer M.S., Gate-tunable graphene spin valve. *Appl. Phys. Lett.* 91, 123105 (2007), doi:[10.1063/1.2784934](https://doi.org/10.1063/1.2784934).
- [144] Drögeler M., Volmer F., Wolter M., Terres B., Watanabe K., Taniguchi T., Güntherodt G., Stampfer C., Beschoten B., Nanosecond Spin Lifetimes in Single- and Few-Layer Graphene–hBN Heterostructures at Room Temperature. *Nano Lett.* 14, 6050–6055 (2014), doi:[10.1021/nl501278c](https://doi.org/10.1021/nl501278c).

- [145] Drögeler M., Franzen C., Volmer F., Pohlmann T., Banszerus L., Wolter M., Watanabe K., Taniguchi T., Stampfer C., Beschoten B., Spin Lifetimes Exceeding 12 ns in Graphene Nonlocal Spin Valve Devices. *Nano Lett.* 16, 3533–3539 (2016), doi:[10.1021/acs.nanolett.6b00497](https://doi.org/10.1021/acs.nanolett.6b00497).
- [146] Kamalakar M.V., Groenveld C., Dankert A., Dash S.P., Long distance spin communication in chemical vapour deposited graphene. *Nat. Commun.* 6 (2015), doi:[10.1038/ncomms7766](https://doi.org/10.1038/ncomms7766).
- [147] Dlubak B., Martin M.B., Deranlot C., Servet B., Xavier S., Mattana R., Sprinkle M., Berger C., De Heer W.A., Petroff F., Anane A., Seneor P., Fert A., Highly efficient spin transport in epitaxial graphene on SiC. *Nat. Phys.* 8, 557–561 (2012), doi:[10.1038/nphys2331](https://doi.org/10.1038/nphys2331).
- [148] Drögeler M., Volmer F., Wolter M., Watanabe K., Taniguchi T., Neumaier D., Stampfer C., Beschoten B., Nanosecond spin lifetimes in bottom-up fabricated bilayer graphene spin-valves with atomic layer deposited Al₂O₃ spin injection and detection barriers. *physica status solidi (b)* 252, 2395–2400 (2015), doi:[10.1002/pssb.201552418](https://doi.org/10.1002/pssb.201552418).
- [149] Tombros N., Jozsa C., Popinciuc M., Jonkman H.T., van Wees B.J., Electronic spin transport and spin precession in single graphene layers at room temperature. *Nature* 448, 571–574 (2007), doi:[10.1038/nature06037](https://doi.org/10.1038/nature06037).
- [150] Ohishi M., Shiraishi M., Nouchi R., Nozaki T., Shinjo T., Suzuki Y., Spin Injection into a Graphene Thin Film at Room Temperature. *Japanese Journal of Applied Physics* 46, L605 (2007), doi:[10.1143/JJAP.46.L605](https://doi.org/10.1143/JJAP.46.L605).
- [151] Volmer F., Drögeler M., Pohlmann T., Güntherodt G., Stampfer C., Beschoten B., Contact-induced charge contributions to non-local spin transport measurements in Co/MgO/graphene devices. *2D Mater.* 2, 024001 (2015), doi:[10.1088/2053-1583/2/2/024001](https://doi.org/10.1088/2053-1583/2/2/024001).
- [152] Han W., Pi K., Bao W., McCreary K.M., Li Y., Wang W.H., Lau C.N., Kawakami R.K., Electrical detection of spin precession in single layer graphene spin valves with transparent contacts. *Appl. Phys. Lett.* 94, 222109 (2009), doi:[10.1063/1.3147203](https://doi.org/10.1063/1.3147203).
- [153] Banszerus L., Schmitz M., Engels S., Dauber J., Oellers M., Haupt F., Watanabe K., Taniguchi T., Beschoten B., Stampfer C., Ultrahigh-mobility graphene devices from chemical vapor deposition on reusable copper. *Sci. Adv.* 1 (2015), doi:[10.1126/sciadv.1500222](https://doi.org/10.1126/sciadv.1500222).

Bibliography

- [154] Dauber J., Sagade A.A., Oellers M., Watanabe K., Taniguchi T., Neumaier D., Stampfer C., Ultra-sensitive Hall sensors based on graphene encapsulated in hexagonal boron nitride. *Appl. Phys. Lett.* 106, 193501 (2015), doi:[10.1063/1.4919897](https://doi.org/10.1063/1.4919897).
- [155] Gurram M., Omar S., Zihlmann S., Makk P., Schönenberger C., van Wees B.J., Spin transport in fully hexagonal boron nitride encapsulated graphene. *Phys. Rev. B* 93, 115441 (2016), doi:[10.1103/PhysRevB.93.115441](https://doi.org/10.1103/PhysRevB.93.115441).
- [156] Guimarães M.H.D., Veligura A., Zomer P.J., Maassen T., Vera-Marun I.J., Tombros N., van Wees B.J., Spin Transport in High-Quality Suspended Graphene Devices. *Nano Lett.* 12, 3512–3517 (2012), doi:[10.1021/nl301050a](https://doi.org/10.1021/nl301050a).
- [157] Tang Z., Shikoh E., Ago H., Kawahara K., Ando Y., Shinjo T., Shiraishi M., Dynamically generated pure spin current in single-layer graphene. *Phys. Rev. B* 87, 140401 (2013), doi:[10.1103/PhysRevB.87.140401](https://doi.org/10.1103/PhysRevB.87.140401).
- [158] Vera-Marun I.J., Ranjan V., van Wees B.J., Nonlinear detection of spin currents in graphene with non-magnetic electrodes. *Nat. Phys.* 8, 313–316 (2012), doi:[10.1038/nphys2219](https://doi.org/10.1038/nphys2219).
- [159] Balakrishnan J., Kok Wai Koon G., Jaiswal M., Castro Neto A.H., Özyilmaz B., Colossal enhancement of spin-orbit coupling in weakly hydrogenated graphene. *Nat. Phys.* 9, 284–287 (2013), doi:[10.1038/nphys2576](https://doi.org/10.1038/nphys2576).
- [160] Avsar A., Tan J.Y., Taychatanapat T., Balakrishnan J., Koon G., Yeo Y., Lahiri J., Carvalho A., Rodin A.S., O’Farrell E., Eda G., Castro Neto A.H., Özyilmaz B., Spin-orbit proximity effect in graphene. *Nat. Commun.* 5 (2014), doi:[10.1038/ncomms5875](https://doi.org/10.1038/ncomms5875).
- [161] Liu Z., Zhu M., Zheng Y., Quantum transport properties of graphene in the presence of randomly distributed spin-orbit coupling impurities. *Phys. Rev. B* 92, 245438 (2015), doi:[10.1103/PhysRevB.92.245438](https://doi.org/10.1103/PhysRevB.92.245438).
- [162] Qiao Z., Yang S.A., Feng W., Tse W.K., Ding J., Yao Y., Wang J., Niu Q., Quantum anomalous Hall effect in graphene from Rashba and exchange effects. *Phys. Rev. B* 82, 161414 (2010), doi:[10.1103/PhysRevB.82.161414](https://doi.org/10.1103/PhysRevB.82.161414).
- [163] Tse W.K., Qiao Z., Yao Y., MacDonald A.H., Niu Q., Quantum anomalous Hall effect in single-layer and bilayer graphene. *Phys. Rev. B* 83, 155447 (2011), doi:[10.1103/PhysRevB.83.155447](https://doi.org/10.1103/PhysRevB.83.155447).

-
- [164] Inoue J.i., Bauer G.E.W., Molenkamp L.W., Suppression of the persistent spin Hall current by defect scattering. *Phys. Rev. B* 70, 041303 (2004), doi:[10.1103/PhysRevB.70.041303](https://doi.org/10.1103/PhysRevB.70.041303).
- [165] Mishchenko E.G., Shytov A.V., Halperin B.I., Spin Current and Polarization in Impure Two-Dimensional Electron Systems with Spin-Orbit Coupling. *Phys. Rev. Lett.* 93, 226602 (2004), doi:[10.1103/PhysRevLett.93.226602](https://doi.org/10.1103/PhysRevLett.93.226602).
- [166] Raimondi R., Schwab P., Spin-Hall effect in a disordered two-dimensional electron system. *Phys. Rev. B* 71, 033311 (2005), doi:[10.1103/PhysRevB.71.033311](https://doi.org/10.1103/PhysRevB.71.033311).
- [167] Chang C.Z., Zhang J., Feng X., Shen J., Zhang Z., Guo M., Li K., Ou Y., Wei P., Wang L.L., Ji Z.Q., Feng Y., Ji S., Chen X., Jia J., Dai X., Fang Z., Zhang S.C., He K., Wang Y., Lu L., Ma X.C., Xue Q.K., Experimental Observation of the Quantum Anomalous Hall Effect in a Magnetic Topological Insulator. *Science* 340, 167–170 (2013), doi:[10.1126/science.1234414](https://doi.org/10.1126/science.1234414).
- [168] Sánchez-Barriga J., Golias E., Varykhalov A., Braun J., Yashina L.V., Schumann R., Minár J., Ebert H., Kornilov O., Rader O., Ultrafast spin-polarization control of Dirac fermions in topological insulators. *Phys. Rev. B* 93, 155426 (2016), doi:[10.1103/PhysRevB.93.155426](https://doi.org/10.1103/PhysRevB.93.155426).
- [169] Mogi M., Yoshimi R., Tsukazaki A., Yasuda K., Kozuka Y., Takahashi K.S., Kawasaki M., Tokura Y., Magnetic modulation doping in topological insulators toward higher-temperature quantum anomalous Hall effect. *Appl. Phys. Lett.* 107, 182401 (2015), doi:[10.1063/1.4935075](https://doi.org/10.1063/1.4935075).
- [170] Schmidt P., Binnewies M., Glaum R., Schmidt M., Chemical Vapor Transport Reactions–Methods, Materials, Modeling, Advanced Topics on Crystal Growth. InTech (2013), doi:[10.5772/55547](https://doi.org/10.5772/55547).
- [171] Wang J., Chen X., Zhu B.F., Zhang S.C., Topological p - n junction. *Phys. Rev. B* 85, 235131 (2012), doi:[10.1103/PhysRevB.85.235131](https://doi.org/10.1103/PhysRevB.85.235131).
- [172] Knez I., Du R.R., Sullivan G., Evidence for Helical Edge Modes in Inverted InAs/GaSb Quantum Wells. *Phys. Rev. Lett.* 107, 136603 (2011), doi:[10.1103/PhysRevLett.107.136603](https://doi.org/10.1103/PhysRevLett.107.136603).
- [173] Du L., Knez I., Sullivan G., Du R.R., Robust Helical Edge Transport in Gated InAs/GaSb Bilayers. *Phys. Rev. Lett.* 114, 096802 (2015), doi:[10.1103/PhysRevLett.114.096802](https://doi.org/10.1103/PhysRevLett.114.096802).

Bibliography

- [174] Weng H., Dai X., Fang Z., Transition-Metal Pentatelluride ZrTe_5 and HfTe_5 : A Paradigm for Large-Gap Quantum Spin Hall Insulators. *Phys. Rev. X* 4, 011002 (2014), doi:[10.1103/PhysRevX.4.011002](https://doi.org/10.1103/PhysRevX.4.011002).
- [175] Fjellvåg H., Kjekshus A., Structural properties of ZrTe_5 and HfTe_5 as seen by powder diffraction. *Solid State Commun.* 60, 91–93 (1986), doi:[10.1016/0038-1098\(86\)90536-3](https://doi.org/10.1016/0038-1098(86)90536-3).
- [176] Taguchi I., Grisel A., Levy F., Raman scattering in quasi-one-dimensional ZrTe_5 . *Solid State Commun.* 46, 299–303 (1983), doi:[10.1016/0038-1098\(83\)90656-7](https://doi.org/10.1016/0038-1098(83)90656-7).
- [177] Liu Y., Yuan X., Zhang C., Jin Z., Narayan A., Luo C., Chen Z., Yang L., Zou J., Wu X., Sanvito S., Xia Z., Li L., Wang Z., Xiu F., Zeeman splitting and dynamical mass generation in Dirac semimetal ZrTe_5 . *Nat. Commun.* 7 (2016), doi:[10.1038/ncomms12516](https://doi.org/10.1038/ncomms12516).
- [178] Tang H., Liang D., Qiu R.L.J., Gao X.P.A., Two-Dimensional Transport-Induced Linear Magneto-Resistance in Topological Insulator Bi_2Se_3 Nanoribbons. *ACS Nano* 5, 7510–7516 (2011), doi:[10.1021/nm2024607](https://doi.org/10.1021/nm2024607).
- [179] Qu D.X., Hor Y.S., Xiong J., Cava R.J., Ong N.P., Quantum Oscillations and Hall Anomaly of Surface States in the Topological Insulator Bi_2Te_3 . *Science* 329, 821–824 (2010), doi:[10.1126/science.1189792](https://doi.org/10.1126/science.1189792).
- [180] Gao B.F., Gehring P., Burghard M., Kern K., Gate-controlled linear magnetoresistance in thin Bi_2Se_3 sheets. *Appl. Phys. Lett.* 100, 212402 (2012), doi:[10.1063/1.4719196](https://doi.org/10.1063/1.4719196).
- [181] Bao L., He L., Meyer N., Kou X., Zhang P., Chen Z.g., Fedorov A.V., Zou J., Riedemann T.M., Lograsso T.A., Wang K.L., Tuttle G., Xiu F., Weak Anti-localization and Quantum Oscillations of Surface States in Topological Insulator $\text{Bi}_2\text{Se}_2\text{Te}$. *Sci. Rep.* 2 (2012), doi:[10.1038/srep00726](https://doi.org/10.1038/srep00726).
- [182] Li X.B., Huang W.K., Lv Y.Y., Zhang K.W., Yang C.L., Zhang B.B., Chen Y.B., Yao S.H., Zhou J., Lu M.H., Sheng L., Li S.C., Jia J.F., Xue Q.K., Chen Y.F., Xing D.Y., Experimental Observation of Topological Edge States at the Surface Step Edge of the Topological Insulator ZrTe_5 . *Phys. Rev. Lett.* 116, 176803 (2016), doi:[10.1103/PhysRevLett.116.176803](https://doi.org/10.1103/PhysRevLett.116.176803).
- [183] Wu R., Ma J.Z., Nie S.M., Zhao L.X., Huang X., Yin J.X., Fu B.B., Richard P., Chen G.F., Fang Z., Dai X., Weng H.M., Qian T., Ding H., Pan S.H., Evidence for Topological Edge States in a Large Energy Gap near the Step Edges on the Surface of ZrTe_5 . *Phys. Rev. X* 6, 021017 (2016), doi:[10.1103/PhysRevX.6.021017](https://doi.org/10.1103/PhysRevX.6.021017).

- [184] Silkin I.V., Menshchikova T.V., Otrokov M.M., Ereemeev S.V., Koroteev Y.M., Vergniory M.G., Kuznetsov V.M., Chulkov E.V., Natural sulfur-containing minerals as topological insulators with a wide band gap. *JETP Letters* 96, 322–325 (2012), doi:10.1134/S0021364012170158.
- [185] Aleksite, <http://www.mindat.org/min-108.html>, Date of access: 10/26/2016.
- [186] Altshuler B.L., Aronov A.G., Khmel'nitsky D.E., Effects of electron-electron collisions with small energy transfers on quantum localisation. *J. Phys. C: Solid State Phys.* 15, 7367 (1982), doi:10.1088/0022-3719/15/36/018.
- [187] Altshuler B.L., Aronov A.G., Electron-Electron Interactions in Disordered Systems. North Holland (1985).
- [188] Zhang H., Liu C.X., Qi X.L., Dai X., Fang Z., Zhang S.C., Topological insulators in Bi_2Se_3 , Bi_2Te_3 and Sb_2Te_3 with a single Dirac cone on the surface. *Nat. Phys.* 5, 438–442 (2009), doi:10.1038/nphys1270.
- [189] Richter W., Becker C.R., A Raman and far-infrared investigation of phonons in the rhombohedral V2-VI3 compounds Bi_2Te_3 , Bi_2Se_3 , Sb_2Te_3 and $\text{Bi}_2(\text{Te}_{1-x}\text{Se}_x)_3$ ($0 < x < 1$), $(\text{Bi}_{1-y}\text{Sb}_y)_2\text{Te}_3$ ($0 < y < 1$). *physica status solidi (b)* 84, 619–628 (1977), doi:10.1002/pssb.2220840226.
- [190] Bendt G., Zastrow S., Nielsch K., Mandal P.S., Sanchez-Barriga J., Rader O., Schulz S., Deposition of topological insulator Sb_2Te_3 films by an MOCVD process. *J. Mater. Chem. A* 2, 8215–8222 (2014), doi:10.1039/C4TA00707G.
- [191] Hao G., Qi X., Fan Y., Xue L., Peng X., Wei X., Zhong J., Spiral growth of topological insulator Sb_2Te_3 nanoplates. *Appl. Phys. Lett.* 102, 013105 (2013), doi:10.1063/1.4773587.
- [192] Gehring P., Gao B., Burghard M., Kern K., Two-dimensional magnetotransport in $\text{Bi}_2\text{Te}_2\text{Se}$ nanoplatelets. *Appl. Phys. Lett.* 101, 023116 (2012), doi:10.1063/1.4736404.
- [193] Analytis J.G., McDonald R.D., Riggs S.C., Chu J.H., Boebinger G.S., Fisher I.R., Two-dimensional surface state in the quantum limit of a topological insulator. *Nat. Phys.* 6, 960–964 (2010), doi:10.1038/nphys1861.
- [194] Jia S., Ji H., Climent-Pascual E., Fuccillo M.K., Charles M.E., Xiong J., Ong N.P., Cava R.J., Low-carrier-concentration crystals of the topological insulator $\text{Bi}_2\text{Te}_2\text{Se}$. *Phys. Rev. B* 84, 235206 (2011), doi:10.1103/PhysRevB.84.235206.

Bibliography

- [195] Kimura T., Otani Y., Hamrle J., Enhancement of spin accumulation in a non-magnetic layer by reducing junction size. *Phys. Rev. B* 73, 132405 (2006), doi:[10.1103/PhysRevB.73.132405](https://doi.org/10.1103/PhysRevB.73.132405).
- [196] Kamalakar M.V., Dankert A., Bergsten J., Ive T., Dash S.P., Enhanced Tunnel Spin Injection into Graphene using Chemical Vapor Deposited Hexagonal Boron Nitride. *Sci. Rep.* 4 (2014), doi:[10.1038/srep06146](https://doi.org/10.1038/srep06146).
- [197] Britnell L., Gorbachev R.V., Jalil R., Belle B.D., Schedin F., Katsnelson M.I., Eaves L., Morozov S.V., Mayorov A.S., Peres N.M.R., Castro Neto A.H., Leist J., Geim A.K., Ponomarenko L.A., Novoselov K.S., Electron Tunneling through Ultrathin Boron Nitride Crystalline Barriers. *Nano Lett.* 12, 1707–1710 (2012), doi:[10.1021/nl3002205](https://doi.org/10.1021/nl3002205).
- [198] Yamaguchi T., Inoue Y., Masubuchi S., Morikawa S., Onuki M., Watanabe K., Taniguchi T., Moriya R., Machida T., Electrical Spin Injection into Graphene through Monolayer Hexagonal Boron Nitride. *Appl. Phys Express* 6, 073001 (2013), doi:[10.7567/APEX.6.073001](https://doi.org/10.7567/APEX.6.073001).
- [199] Karpan V.M., Giovannetti G., Khomyakov P.A., Talanana M., Starikov A.A., Zwierzycki M., van den Brink J., Brocks G., Kelly P.J., Graphite and Graphene as Perfect Spin Filters. *Phys. Rev. Lett.* 99, 176602 (2007), doi:[10.1103/PhysRevLett.99.176602](https://doi.org/10.1103/PhysRevLett.99.176602).
- [200] Fu W., Makk P., Maurand R., Bräuninger M., Schönenberger C., Large-scale fabrication of BN tunnel barriers for graphene spintronics. *J. Appl. Phys.* 116, 074306 (2014), doi:[10.1063/1.4893578](https://doi.org/10.1063/1.4893578).
- [201] Zomer P.J., Guimarães M.H.D., Tombros N., van Wees B.J., Long-distance spin transport in high-mobility graphene on hexagonal boron nitride. *Phys. Rev. B* 86, 161416 (2012), doi:[10.1103/PhysRevB.86.161416](https://doi.org/10.1103/PhysRevB.86.161416).
- [202] Zomer P.J., Dash S.P., Tombros N., van Wees B.J., A transfer technique for high mobility graphene devices on commercially available hexagonal boron nitride. *Appl. Phys. Lett.* 99, 232104 (2011), doi:[10.1063/1.3665405](https://doi.org/10.1063/1.3665405).
- [203] Dean C., Young A., Meric I., Lee C., Wang L., Sorgenfrei S., Watanabe K., Taniguchi T., Kim P., Shepard L., Hone J., Boron nitride substrates for high-quality graphene electronics. *Nat Nano* 5, 722–726 (2010), doi:[10.1038/nnano.2010.172](https://doi.org/10.1038/nnano.2010.172).

- [204] Kamalakar M.V., Dankert A., Kelly P.J., Dash S.P., Inversion of Spin Signal and Spin Filtering in Ferromagnet|Hexagonal Boron Nitride-Graphene van der Waals Heterostructures. *Sci. Rep.* 6 (2016), doi:10.1038/srep21168.
- [205] Zou H., Chui S.T., Wang X.J., Ji Y., Large and inverted spin signals in nonlocal spin valves. *Phys. Rev. B* 83, 094402 (2011), doi:10.1103/PhysRevB.83.094402.
- [206] He L., Xiu F., Yu X., Teague M., Jiang W., Fan Y., Kou X., Lang M., Wang Y., Huang G., Yeh N.C., Wang K.L., Surface-Dominated Conduction in a 6 nm thick Bi₂Se₃ Thin Film. *Nano Lett.* 12, 1486–1490 (2012), doi:10.1021/nl204234j.
- [207] Xu S., Han Y., Chen X., Wu Z., Wang L., Han T., Ye W., Lu H., Long G., Wu Y., Lin J., Cai Y., Ho K.M., He Y., Wang N., van der Waals Epitaxial Growth of Atomically Thin Bi₂Se₃ and Thickness-Dependent Topological Phase Transition. *Nano Lett.* 15, 2645–2651 (2015), doi:10.1021/acs.nanolett.5b00247.
- [208] Johnson M., Silsbee R.H., Spin-injection experiment. *Phys. Rev. B* 37, 5326–5335 (1988), doi:10.1103/PhysRevB.37.5326.
- [209] Jedema F.J., Filip A.T., van Wees B.J., Electrical spin injection and accumulation at room temperature in an all-metal mesoscopic spin valve. *Nature* 410, 345–348 (2001), doi:10.1038/35066533.
- [210] Takahashi S., Maekawa S., Spin injection and detection in magnetic nanostructures. *Phys. Rev. B* 67, 052409 (2003), doi:10.1103/PhysRevB.67.052409.
- [211] Pirkle A., Chan J., Venugopal A., Hinojos D., Magnuson C.W., McDonnell S., Colombo L., Vogel E.M., Ruoff R.S., Wallace R.M., The effect of chemical residues on the physical and electrical properties of chemical vapor deposited graphene transferred to SiO₂. *Appl. Phys. Lett.* 99, 122108 (2011), doi:10.1063/1.3643444.
- [212] Han W., Kawakami R.K., Spin Relaxation in Single-Layer and Bilayer Graphene. *Phys. Rev. Lett.* 107, 047207 (2011), doi:10.1103/PhysRevLett.107.047207.
- [213] Han W., Kawakami R.K., Gmitra M., Fabian J., Graphene spintronics. *Nat Nano* 9, 794–807 (2014), doi:10.1038/nnano.2014.214.
- [214] Náfrádi B., Choucair M., Forró L., Spin lifetime of itinerant electrons in chemically synthesized graphene multi-layers. *Carbon* 74, 346–351 (2014), doi:10.1016/j.carbon.2014.03.046.

Bibliography

- [215] Rao S.S., Stesmans A., van Tol J., Kosynkin D.V., Higginbotham-Duque A., Lu W., Sinitskii A., Tour J.M., Spin Dynamics and Relaxation in Graphene Nanoribbons: Electron Spin Resonance Probing. *ACS Nano* 6, 7615–7623 (2012), doi:[10.1021/nn302745x](https://doi.org/10.1021/nn302745x).
- [216] Wang W., Zou W.Q., He L., Peng J., Zhang R., Wu X.S., Zhang F.M., Magnetoresistance and nonlinear Hall effect in quaternary topological insulator $\text{Bi}_{1.5}\text{Sb}_{0.5}\text{Te}_{1.8}\text{Se}_{1.2}$. *J. Phys. D: Appl. Phys.* 48, 205305 (2015), doi:[10.1088/0022-3727/48/20/205305](https://doi.org/10.1088/0022-3727/48/20/205305).
- [217] Zhang J., Chang C.Z., Zhang Z., Wen J., Feng X., Li K., Liu M., He K., Wang L., Chen X., Xue Q.K., Ma X., Wang Y., Band structure engineering in $(\text{Bi}_{1-x}\text{Sb}_x)_2\text{Te}_3$ ternary topological insulators. *Nat. Commun.* 2 (2011), doi:[10.1038/ncomms1588](https://doi.org/10.1038/ncomms1588).
- [218] Yang F., Taskin A.A., Sasaki S., Segawa K., Ohno Y., Matsumoto K., Ando Y., Top gating of epitaxial $(\text{Bi}_{1-x}\text{Sb}_x)_2\text{Te}_3$ topological insulator thin films. *Appl. Phys. Lett.* 104, 161614 (2014), doi:[10.1063/1.4873397](https://doi.org/10.1063/1.4873397).
- [219] Yang F., Taskin A.A., Sasaki S., Segawa K., Ohno Y., Matsumoto K., Ando Y., Dual-Gated Topological Insulator Thin-Film Device for Efficient Fermi-Level Tuning. *ACS Nano* 9, 4050–4055 (2015), doi:[10.1021/acsnano.5b00102](https://doi.org/10.1021/acsnano.5b00102).
- [220] Avsar A., Lee J.H., Koon G.K.W., Özyilmaz B., Enhanced spin-orbit coupling in dilute fluorinated graphene. *2D Mater.* 2, 044009 (2015), doi:[10.1088/2053-1583/2/4/044009](https://doi.org/10.1088/2053-1583/2/4/044009).
- [221] Calleja F., Ochoa H., Garnica M., Barja S., Navarro J.J., Black A., Otrokov M.M., Chulkov E.V., Arnau A., Vazquez de Parga A.L., Guinea F., Miranda R., Spatial variation of a giant spin-orbit effect induces electron confinement in graphene on Pb islands. *Nat. Phys.* 11, 43–47 (2015), doi:[10.1038/nphys3173](https://doi.org/10.1038/nphys3173).
- [222] Wang Z., Ki D.K., Chen H., Berger H., MacDonald A.H., Morpurgo A.F., Strong interface-induced spin-orbit interaction in graphene on WS_2 . *Nat. Commun.* 6 (2015), doi:[10.1038/ncomms9339](https://doi.org/10.1038/ncomms9339).
- [223] Wang Z., Ki D.K., Khoo J.Y., Mauro D., Berger H., Levitov L.S., Morpurgo A.F., Origin and Magnitude of ‘Designer’ Spin-Orbit Interaction in Graphene on Semiconducting Transition Metal Dichalcogenides. *Phys. Rev. X* 6, 041020 (2016), doi:[10.1103/PhysRevX.6.041020](https://doi.org/10.1103/PhysRevX.6.041020).
- [224] Abanin D.A., Shytov A.V., Levitov L.S., Halperin B.I., Nonlocal charge transport mediated by spin diffusion in the spin Hall effect regime. *Phys. Rev. B* 79, 035304 (2009), doi:[10.1103/PhysRevB.79.035304](https://doi.org/10.1103/PhysRevB.79.035304).

Acknowledgements

Going through 3+ years of a PhD project is a turbulent journey of countless ups and downs. But as it always goes in life, there are no shortcuts to success and learning what is really worth and important means walking the hard way. Completing a PhD thesis is not only an academic achievement, but also a personal one and means learning to be patient and to persevere without losing the pinch of curiosity that makes the field of fundamental research so unique. All this would have been nearly impossible without the people who have trusted in me and stood by me in various ways and whom I would hereby like to acknowledge.

I would like to thank **Prof. Klaus Kern** for supervising my thesis and giving me the opportunity to complete my PhD at the Nanoscale Science Department. This project would have hardly been possible without the amount of freedom and the excellent resources available at the department and at Max Planck Institute in general. I am grateful for having the chance to spend my PhD time here.

I would like to thank **Dr. Marko Burghard**, for welcoming me at the Quantum Materials research group. I am grateful for his continuous support and for the invaluable feedback he has always provided in the course of my PhD.

I thank **Dr. Carsten Woltmann**, who has been a source of strength and support in various ways every step of the way and without whom this thesis wouldn't have become reality.

I would like to thank **Prof. Richard Jordan** and **Prof. Shuba Tewari** for being an inspiration to continue doing science at graduate level. I would have hardly taken this path, had I not attended their amazing classes at Mt. Holyoke College.

I thank the Nanostructuring Lab team, namely **Ulli, Marion, Thomas**, and **Achim**, for their continuous support in sample fabrication and process development.

I thank my colleagues and friends **Roberto, Soudabeh**, and **Patrick**, as well as all current and former group members, with whom I had the chance to work with, for the nice times at the lab and the fun lunch and coffee breaks.

Acknowledgements

I thank **Alex, Christian, and Pascal**, who taught me a lot about measurement techniques and supported my efforts in the lab.

I thank my friends and former colleagues **Mahdieh** and **Sibani** for all the nice tea breaks and girl conversations in and outside of the institute and for staying in touch after having moved on professionally.

I thank my friend and colleague **Jone** for being there during emotional hardships and turmoils, for listening to my rants and offering helpful insights. I am immensely grateful for that.

I thank **Sebastian** and **Jörg** for always keeping their door open for me and for being truly amazing.

I thank my friend **Gaurav** for being the best homie one could wish for and for all the fun times we've had in and outside of the institute.

I thank **AJ** for helping me appreciate the beauty of the work we do and for being an inspiration during the final phase of my PhD.

I thank everyone at Department Mannhart and the research group of Dr. Hagen Klauk for their friendship, support, and all the fun times in and outside of the institute.

I thank my friends **Kati, Teddy, Yani, and May** for the amazing four years at Mt. Holyoke, for being supportive, willing to reunite again and again despite all geographical constraints, and last but not least, for being my family.

I thank my dearest friends, **Anna** and **Gery**, for the truly amazing friendship of 18 years. I have been lucky to have a shoulder to lean on anytime, regardless of distance and circumstances.

Last, but not least I am thankful to my parents and family for their love and continuous moral support.

Lausanne, Nov 21, 2016

K. V.

Kristina Vaklinova

CONTACT INFORMATION	Kreuzstr. 9, D-70563 Stuttgart Phone: +49 (157) 34007727 E-mail: kvaklinova@gmail.com	
CITIZENSHIP, DATE OF BIRTH	Bulgarian/German, January 31, 1986	
EDUCATION	M.Sc. in Physics, Grade 1.4/1.0 <i>University of Stuttgart, Stuttgart, Germany</i> (Jan 2012) <ul style="list-style-type: none">Thesis: "Towards Single-Carbon Nanotube/Superconducting Devices with Improved Properties" B.A. in Astronomy and Statistics (double major), GPA 3.5/4.0 <i>Mount Holyoke College, South Hadley, USA</i> (May 2009) <ul style="list-style-type: none">Senior Project: "Spectroscopic Study of Chemically Peculiar Stars"	
RESEARCH INTERESTS	nanotechnology, spintronics, quantum heterostructures, topological insulators, 2D materials, semiconductors, low-temperature magnetotransport, nanofabrication, process development and optimization	
ACADEMIC/PROFESSIONAL EXPERIENCE	PhD Student in Applied Physics <i>Nanoscale Science Department, Max-Planck-Institute for Solid State Research, Stuttgart, Germany</i> <i>Doctoral School in Physics at EPFL, Lausanne, Switzerland</i> (Mar 2013–today) Spin transport in topological insulator-based nanostructures Research Assistant <i>1. Physics Institute, University of Stuttgart; Max-Planck-Institute for Solid State Research, Stuttgart, Germany</i> (Feb 2012–Dec 2012) Optimized single carbon nanotube-based nano-SQUIDs with titanium/niobium electrodes. Fabricated and characterized the behavior of topological insulator-based nanodevices at low temperature.	
PUBLICATIONS	Seifert, P., Vaklinova, K. et al. Surface state-dominated photoconduction and THz-generation in topological $\text{Bi}_2\text{Te}_2\text{Se}$ -nanowires. <i>Nano Lett.</i> , 17, 2 (2017) Vaklinova, K., Hoyer, A. et al. Current-Induced Spin Polarization in Topological Insulator/Graphene Heterostructures. <i>Nano Lett.</i> , 16, 4 (2016) Devender, Gehring, P., Gaul, A., Hoyer, A., Vaklinova, K. et al. Harnessing topological band effects in bismuth telluride selenide for large enhancements in thermoelectric properties through isovalent doping. <i>Adv. Mater.</i> 1521-4095 (2016) Gehring, P., Vaklinova, K. et al. Dimensional crossover in the quantum transport behavior of the natural topological insulator As_2S_3 . <i>Nature Sci. Rep.</i> 5, 11691 (2015)	
TALKS	Invited talk, "Spin transport in topological insulators and in graphene/topological insulator heterostructures", Spin Orbit Coupling and Topology in Low Dimensions Workshop, Spetses, Greece (Jun 2016) Contribution talk, "Single-Carbon Nanotube/Superconducting Devices with Improved Properties" at the 5th International Conference "Control of quantum correlations in tailored matter: Common perspectives of mesoscopic systems and quantum gases", G�unzburg,	

	Germany (Nov, 2011)
AWARDS AND SCHOLARSHIPS	<p>SFB/Transregio 21 Scholarship during Master’s Studies, University of Stuttgart (Mar 2011–Jan 2012)</p> <p>DAAD/Matching Funds Scholarship (Nov 2010)</p> <p>University of Utrecht grant awarded for participation in the Stellar Astrophysics Summer Program 2008, the Netherlands (Aug 2008)</p> <p>Student Government Association Grant for Leadership (Sep 2006)</p> <p>Global Studies Fellowship for Research Abroad awarded by the McCulloh Center of Global Initiatives, Mount Holyoke College (Apr 2008)</p> <p>Four–year full–tuition scholarship awarded for academic excellence by the Mount Holyoke College Board of Trustees (Sep 2005–May 2009)</p>
ADDITIONAL EMPLOYMENT EXPERIENCE	<p>Teaching Assistant <i>1. Physics Institute, University of Stuttgart, Stuttgart, Germany</i> (Oct 2012–Feb 2013) Supervised an NMR–Imaging experiment for the Advanced Physics Laboratory course, designed for Master’s students in Physics. Instructed and assisted the students in performing experimental tasks, evaluating scientific results, and writing scientific reports.</p> <p>Computer Administration and Webdesign <i>Departments of German Studies and Linguistics, University of Stuttgart</i> (Oct 2009–Oct 2012) Provided network, web, and technical support to faculty and staff. Regulated and performed software and hardware upgrades and maintenance.</p> <p>Computer Management System and Web Tech Support Assistant <i>Information and Technology Services</i> (Jan 2006–May 2009) Developed and managed a new interface of the Mount Holyoke College official web page. Collaborated with academic departments on College Web projects as a part of the Web Development team.</p> <p>Teaching Assistant <i>Physics and Astronomy Department, Mount Holyoke College, South Hadley, USA</i>(Jan 2006–May 2006) Lectured laboratory and observational sessions for ”Introduction to Astronomy” undergraduate course and held tutoring sessions.</p>
SKILLS	<p>Technical Competences Programming and Software: Origin, Labview, Python, Mathematica, Raith eLine, CorelDraw, Blender, Photoshop, Dreamweaver, Statistical Analysis (SPSS), CMS RedDot, OpenCMS, L^AT_EX, Microsoft Office Scientific instrumentation: scanning electron microscopy, electron beam lithography, physical vapor deposition, chemical vapor deposition, extensive clean room experience</p> <p>Languages Bulgarian (native fluency), English (native fluency), German (native fluency), Spanish (conversational)</p>
INTERESTS	travel, mountaineering, yoga, foreign languages

